Publishing House ASV

begell house, inc. publishers

Scientific coordination is carried out by the Russian Academy of Architecture and Construction Sciences (RAACS)

Volume 21 • Issue 2 • 2025

ISSN 2588-0195 (Online)
ISSN 2587-9618 (Print) Continues ISSN 1524-5845

International Journal for

Computational Civil and Structural Engineering

Международный журнал по расчету гражданских и строительных конструкций

https://ijccse.iasv.ru/

DOI: 10.22337/2587-9618
GICID: 71.0000.1500.2830

EXECUTIVE EDITOR

Vladimir I. Travush,
Full Member of RAACS, Professor, Dr.Sc.,
Vice-President of the Russian Academy
of Architecture and Construction Sciences;
Urban Planning Institute
of Residential and Public Buildings;
24, Ulitsa Bolshaya Dmitrovka, 107031, Moscow, Russia

EDITOR-IN-CHIEF

Vladimir N. Sidorov,
Full Member of RAACS, Professor, Dr.Sc., National Research Moscow State University of Civil Engineering; Russian University of Transport (RUT – MIIT); Moscow Institute of Architecture (State Academy); Perm National Research Polytechnic University; 26, Yaroslavskoe Shosse, 129337, Moscow, Russia

EDITORIAL DIRECTOR

Valery I. Telichenko,
Full Member of RAACS, Professor, Dr.Sc.,
The First Vice-President of the Russian Academy
of Architecture and Construction Sciences;
Honorary President of National Research
Moscow State University of Civil Engineering;
24, Ulitsa Bolshaya Dmitrovka, 107031, Moscow, Russia

MANAGING EDITOR

Nadezhda S. Nikitina,
Professor, Ph.D.,
Director of ASV Publishing House;
National Research Moscow State University
of Civil Engineering;
26, Yaroslavskoe Shosse, 129337, Moscow, Russia

ASSOCIATE EDITORS

Pavel A. Akimov,
Full Member of RAACS, Professor, Dr.Sc.,
Acting Rector of National Research
Moscow State University of Civil Engineering;
Vice-President of the Russian Academy
of Architecture and Construction Sciences;
Tomsk State University of Architecture and Building;
Russian University of Friendship of Peoples;
26, Yaroslavskoe Shosse, 129337, Moscow, Russia

Alexander M. Belostotsky,
Full Member of RAACS, Professor, Dr.Sc.,
Research & Development Center "STADYO";
National Research Moscow State University of Civil Engineering; Russian University of Transport (RUT – MIIT); Russian University of Friendship of Peoples;
Perm National Research Polytechnic University;
Tomsk State University of Architecture and Building;
Irkutsk National Research Technical University;
8th Floor, 18, ul. Tretya Yamskogo Polya,
125040, Moscow, Russia

Mikhail Belyi, Professor, Dr.Sc.,
Dassault Systèmes Simulia;
1301 Atwood Ave Suite 101W
02919 Johnston, RI, United States

Vitaly Bulgakov, Professor, Dr.Sc.,
Micro Focus;
Newbury, United Kingdom

Nikolai P. Osmolovskii, Professor, Dr.Sc.,
Systems Research Institute, Polish Academy of Sciences;
Kazimierz Pulaski University
of Technology and Humanities in Radom;
29, ul. Malczewskiego, 26-600, Radom, Poland

Gregory P. Panasenko, Professor, Dr.Sc.,
Equipe d'Analise Numerique; NMR CNRS 5585
University Gean Mehnet;
23 rue. P.Michelon 42023, St.Etienne, France

Scientific coordination is carried out by the Russian Academy of Architecture and Construction Sciences (RAACS)

PUBLISHER

ASV Publishing House
(ООО «Издательство АСВ»)
19/1,12, Yaroslavskoe Shosse, 120338, Moscow, Russia
Tel. +7(925)084-74-24; E-mail: iasv@iasv.ru; Интернет-сайт: http://iasv.ru/

ADVISORY EDITORIAL BOARD

Mojtaba Aslami, Ph.D,
Fasa University; Daneshjou blvd,
Fasa, Fars Province, Iran

Klaus-Jurgen Bathe, Professor
Massachusetts Institute
of Technology;
Cambridge, MA 02139, USA

Alexander T. Bekker,
Academician of RAACS,
Professor, Dr.Sc.,
Far Eastern Federal University;
Russian Academy of Architecture
and Construction Sciences;
8, Sukhanova Street, Vladivostok,
690950, Russia

Tomas Bock, Professor, Dr.-Ing.,
Technical University of Munich,
Arcisstrasse 21, D-80333
Munich, Germany

Jan Buynak, Professor, Ph.D.,
University of Žilina;
1, Univerzitná, Žilina, 010 26,
Slovakia

Vladimir T. Erofeev,
Full Member of RAACS,
Professor, Dr.Sc.,
Ogarev Mordovia State University;
68, Bolshevistskaya Str., Saransk
430005, Republic of Mordovia,
Russia

Victor S. Fedorov,
Full Member of RAACS,
Professor, Dr.Sc.,
Russian University of Transport
(RUT – MIIT);
9b9 Obrazcova Street, Moscow,
127994, Russia

Sergey V. Fedosov,
Full Member of RAACS,
Professor, Dr.Sc.,
Russian Academy of Architecture
and Construction Sciences;
24, Ul. Bolshaya Dmitrovka, 107031,
Moscow, Russia

Sergiy Yu. Fialko,
Professor, Dr.Sc.,
Cracow University of Technology;
24, Warszawska Street, Kraków,
31-155, Poland

Vladimir G. Gagarin,
Corresponding Member
of RAACS, Professor, Dr.Sc.,
Research Institute of Building
Physics of Russian Academy
of Architecture and Construction
Sciences;
21, Lokomotivny Proezd,
Moscow, 127238, Russia

Vyatcheslav A. Ilyichev,
Full Member of RAACS,
Professor, Dr.Sc.,
Russian Academy of Architecture
and Construction Sciences;
Podzemproekt Ltd.;
24, Ulitsa Bolshaya Dmitrovka,
Moscow, 107031, Russia

Marek Iwański,
Professor, Dr.Sc.,
Kielce University of Technology;
7, al. Tysiąclecia Państwa Polskiego
Kielce, 25 – 314, Poland

Sergey Yu. Kalashnikov,
Corresponding Member of RAACS,
Professor, Dr.Sc.,
Volgograd State Technical
University; 28, Lenin avenue,
Volgograd, 400005, Russia

Semen S. Kaprielov,
Academician of RAACS,
Professor, Dr.Sc.,
Research Center of Construction;
6, 2nd Institutskaya St., Moscow,
109428, Russia

Nikolay I. Karpenko,
Full Member of RAACS,
Professor, Dr.Sc.,
Research Institute of Building
Physics of Russian Academy
of Architecture and Construction
Sciences; Russian Academy of
Architecture and Construction
Sciences; 21, Lokomotivny Proezd,
Moscow, 127238, Russia

Vladimir V. Karpov,
Professor, Dr.Sc., Saint Petersburg
State University of Architecture and
Civil Engineering;
4, 2-nd Krasnoarmeiskaya Steet,
Saint Petersburg, 190005, Russia

Galina G. Kashevarova,
Corresponding Member
of RAACS, Professor, Dr.Sc.,
Perm National Research
Polytechnic University;
29 Komsomolsky pros., Perm,
Perm Krai, 614990, Russia

John T. Katsikadelis,
Professor, Dr.Eng, PhD, Dr.h.c.,
National Technical University of
Athens; Zografou Campus
9, Iroon Polytechniou str
15780 Zografou, Greece

Vitaly I. Kolchunov,
Full Member of RAACS,
Professor, Dr.Sc., Southwest State
University; Russian Academy of
Architecture and Construction
Sciences; 94, 50 let Oktyabrya,
Kursk, 305040, Russia

Dmitry V. Kozlov, Corresponding
Member of RAACS
Dr. Sc. Engineering, Professor, Head
of the Department of Hydraulics and
Hydrotechnical Construction, NRU
MGSU, 26, Yaroslavskoe Shosse.,
129337, Moscow, Russia

Markus König, Professor
Ruhr-Universität Bochum;
150, Universitätsstraße, Bochum,
44801, Germany

Sergey B. Kositsin,
Advisor of RAACS,
Professor, Dr.Sc.,
Russian University of Transport
(RUT – MIIT); 9b9 Obrazcova
Street, Moscow, 127994, Russia

Sergey B. Krylov,
Full Member of RAACS,
Professor, Dr.Sc.,
Research Center of Construction;
6, 2nd Institutskaya St., Moscow,
109428, Russia

Sergey V. Kuznetsov,
Professor, Dr.Sc.,
Ishlinsky Institute for Problems
in Mechanics of the Russian
Academy of Sciences;
101-1, Prosp. Vernadskogo,
Moscow, 119526, Russia

Vladimir V. Lalin,
Professor, Dr.Sc.,
Peter the Great Saint-Petersburg Polytechnic University;
29, Ul. Politechnicheskaya,
Saint-Petersburg, 195251, Russia

Leonid S. Lyakhovich,
Full Member of RAACS,
Professor, Dr.Sc., Tomsk State University of Architecture and Building; 2, Solyanaya Sq., Tomsk, 634003, Russia

Rashid A. Mangushev,
Corresponding Member of RAACS, Professor, Dr.Sc.,
Saint Petersburg State University of Architecture and Civil Engineering;
4, 2-nd Krasnoarmeiskaya Steet,
Saint Petersburg, 190005, Russia

Ilizar T. Mirsayapov,
Corresponding Member of RAACS,
Professor, Dr.Sc., Kazan State University of Architecture and Engineering; 1, Zelenaya Street,
Kazan, 420043, Republic of Tatarstan, Russia

Vladimir L. Mondrus,
Corresponding Member of RAACS, Professor, Dr.Sc.,
National Research Moscow State University of Civil Engineering;
Yaroslavskoe Shosse 26,
Moscow, 129337, Russia

Valery I. Morozov,
Corresponding Member of RAACS, Professor, Dr.Sc.,
Saint Petersburg State University of Architecture and Civil Engineering;
4, 2-nd Krasnoarmeiskaya Steet,
Saint Petersburg, 190005, Russia

Anatoly V. Perelmuter,
Foreign Member of RAACS,
Professor, Dr.Sc., SCAD Soft;
Office 1,2, 3a Osvity street,
Kiev, 03037, Ukraine

Alexey N. Petrov,
Advisor of RAACS, Professor,
Dr.Sc., Petrozavodsk State University; 33, Lenina Prospect,
Petrozavodsk, 185910,
Republic of Karelia, Russia

Vladilen V. Petrov,
Full Member of RAACS,
Professor, Dr.Sc.,
Yuri Gagarin State Technical University of Saratov;
77 Politechnicheskaya Street,
Saratov, 410054, Russia

Jerzy Z. Piotrowski,
Professor, Dr.Sc.,
Kielce University of Technology;
al. Tysiąclecia Państwa Polskiego 7,
Kielce, 25 – 314, Poland

Chengzhi Qi, Professor, Dr.Sc.,
Beijing University of Civil Engineering and Architecture;
1, Zhanlanlu, Xicheng District,
Beijing, China

Vladimir P. Selyaev,
Full Member of RAACS,
Professor, Dr.Sc., Ogarev Mordovia State University;
68, Bolshevistskaya Str., Saransk
430005, Republic of Mordovia, Russia

Eun Chul Shin,
Professor, Ph.D.,
Incheon National University;
(Songdo-dong)119 Academy-ro,
Yeonsu-gu, Incheon, Korea

D.V. Singh,
Professor, Ph.D,
University of Roorkee;
Roorkee, India, 247667

Wacław Szcześniak,
Foreign Member of RAACS,
Professor, Dr.Sc.,
Lublin University of Technology;
Ul. Nadbystrzycka 40,
20-618 Lublin, Poland

Tadatsugu Tanaka,
Professor, Dr.Sc.,
Tokyo University; 7-3-1 Hongo,
Bunkyo, Tokyo, 113-8654, Japan

Josef Vican,
Professor, Ph.D,
University of Žilina;
1, Univerzitná, Žilina, 010 26,
Slovakia

Zbigniew Wojcicki,
Professor, Dr.Sc.,
Wroclaw University of Technology;
11 Grunwaldzki Sq., 50-377,
Wrocław, Poland

Artur Zbiciak, Professor, Dr.Sc.,
Warsaw University of Technology;
Pl. Politechniki 1, 00-661 Warsaw,
Poland

Segrey I. Zhavoronok, Ph.D.,
Institute of Applied Mechanics of Russian Academy of Sciences;
Moscow Aviation Institute (National Research University);
7, Leningradsky Prt.,
Moscow, 125040, Russia

Askar Zhussupbekov,
Professor, Dr.Sc.,
Eurasian National University;
5, Munaitpassov street, Astana,
010000, Kazakhstan

TECHNICAL EDITOR

Taymuraz B. Kaytukov,
Advisor of RAACS,
Associate Professor, Ph.D.,
Vice-Rector of National Research Moscow State University of Civil Engineering;
Yaroslavskoe Shosse 26,
Moscow, 129337, Russia

EDITORIAL TEAM

Vadim K. Akhmetov, Professor, Dr.Sc., National Research Moscow State University of Civil Engineering; 26, Yaroslavskoe Shosse, 129337 Moscow, Russia

Pavel A. Akimov, Full Member of RAACS, Professor, Dr.Sc., Acting Rector of National Research Moscow State University of Civil Engineering; Vice-President of the Russian Academy of Architecture and Construction Sciences; Tomsk State University of Architecture and Building; Russian University of Friendship of Peoples; 26, Yaroslavskoe Shosse, 129337, Moscow, Russia

Alexander M. Belostotsky, Full Member of RAACS, Professor, Dr.Sc., Research & Development Center "STADYO"; National Research Moscow State University of Civil Engineering; Russian University of Transport (RUT – MIIT); Russian University of Friendship of Peoples; Perm National Research Polytechnic University; Tomsk State University of Architecture and Building; Irkutsk National Research Technical University; 8th Floor, 18, ul. Tretya Yamskogo Polya, 125040, Moscow, Russia

Mikhail Belyi, Professor, Dr.Sc., Dassault Systèmes Simulia; 1301 Atwood Ave Suite 101W 02919 Johnston, RI, United States

Vitaly Bulgakov, Professor, Dr.Sc., Micro Focus; Newbury, United Kingdom

Charles El Nouty, Professor, Dr.Sc., LAGA Paris-13 Sorbonne Paris Cite; 99 avenue J.B. Clément, 93430 Villetaneuse, France

Natalya N. Fedorova, Professor, Dr.Sc., Novosibirsk State University of Architecture and Civil Engineering (SIBSTRIN); 113 Leningradskaya Street, Novosibirsk, 630008, Russia

Darya Filatova, Professor, Dr.Sc., Probability, Assessment, Reasoning and Inference Studies Research Group, EPHE Laboratoire CHART (PARIS) 4-14, rue Ferrus, 75014 Paris

Vladimir Ya. Gecha, Professor, Dr.Sc., Research and Production Enterprise All-Russia Scientific-Research Institute of Electromechanics with Plant Named after A.G. Iosiphyan; 30, Volnaya Street, Moscow, 105187, Russia

Taymuraz B. Kaytukov, Advisor of RAACS, Associate Professor, Ph.D, Vice-Rector of National Research Moscow State University of Civil Engineering; 26, Yaroslavskoe Shosse, 129337, Moscow, Russia

Marina L. Mozgaleva, Professor, Dr.Sc., National Research Moscow State University of Civil Engineering; 26, Yaroslavskoe Shosse, 129337 Moscow, Russia

Nadezhda S. Nikitina, Professor, Ph.D., Director of ASV Publishing House; National Research Moscow State University of Civil Engineering; 26, Yaroslavskoe Shosse, 129337 Moscow, Russia

Nikolai P. Osmolovskii, Professor, Dr.Sc., Systems Research Institute Polish Academy of Sciences; Kazimierz Pulaski University of Technology and Humanities in Radom; 29, ul. Malczewskiego, 26-600, Radom, Poland

Gregory P. Panasenko, Professor, Dr.Sc., Equipe d'Analise Numerique NMR CNRS 5585 University Gean Mehnet; 23 rue. P.Michelon 42023, St.Etienne, France

Andreas Rauh, Prof. Dr.-Ing. habil. Carl von Ossietzky Universität Oldenburg, Germany School II - Department of Computing Science Group Distributed Control in Interconnected Systems D-26111 Oldenburg, Germany

Zhan Shi, Professor LPSM, Université Paris VI 4 place Jussieu, F-75252 Paris Cedex 05, France

Marina V. Shitikova, National Research Moscow State University of Civil Engineering, Advisor of RAACS, Professor, Dr.Sc., Voronezh State Technical University; 14, Moscow Avenue, Voronezh, 394026, Russia

Igor L. Shubin, Corresponding Member of RAACS, Professor, Dr.Sc., Research Institute of Building Physics of Russian Academy of Architecture and Construction Sciences; 21, Lokomotivny Proezd, Moscow, 127238, Russia

Vladimir N. Sidorov, Full Member of RAACS, Professor, Dr.Sc., National Research Moscow State University of Civil Engineering; Russian University of Transport (RUT – MIIT); Moscow Institute of Architecture (State Academy); Perm National Research Polytechnic University; 26, Yaroslavskoe Shosse, 129337, Moscow, Russia

Valery I. Telichenko, Full Member of RAACS, Professor, Dr.Sc., The First Vice-President of the Russian Academy of Architecture and Construction Sciences; National Research Moscow State University of Civil Engineering; 24, Ulitsa Bolshaya Dmitrovka, 107031, Moscow, Russia

Vladimir I. Travush, Full Member of RAACS, Professor, Dr.Sc., Vice-President of the Russian Academy of Architecture and Construction Sciences; Urban Planning Institute of Residential and Public Buildings; 24, Ulitsa Bolshaya Dmitrovka, 107031, Moscow, Russia

INVITED REVIEWERS

Akimbek A. Abdikalikov, Professor, Dr.Sc.,
Kyrgyz State University of Construction, Transport and Architecture n.a. N. Isanov;
34 Maldybayeva Str., Bishkek, 720020, Biskek, Kyrgyzstan

Vladimir N. Alekhin, Advisor of RAACS, Professor, Dr.Sc.,
Ural Federal University named after the first President of Russia B.N. Yeltsin;
19 Mira Street, Ekaterinburg, 620002, Russia

Irina N. Afanasyeva, Ph.D., University of Florida; Gainesville, FL 32611, USA

Ján Čelko, Professor, PhD, Ing., University of Žilina; Univerzitná 1, 010 26, Žilina, Slovakia

Tatyana L. Dmitrieva, Professor, Dr.Sc.,
Irkutsk National Research Technical University; 83, Lermontov street, Irkutsk, 664074, Russia

Petr P. Gaidzhurov, Advisor of RAACS, Professor, Dr.Sc.,
Don State Technical University; 1, Gagarina Square, Rostov-on-Don, 344000, Russia

Jacek Grosel, Associate Professor, Dr inz.
Wroclaw University of Technology; 11 Grunwaldzki Sq., 50-377, Wrocław, Poland

Stanislaw Jemioło, Professor, Dr.Sc.,
Warsaw University of Technology; 1, Pl. Politechniki, 00-661, Warsaw, Poland

Konstantin I. Khenokh, M.Ing., M.Sc.,
General Dynamics C4 Systems; 8201 E McDowell Rd, Scottsdale, AZ 85257, USA

Christian Koch, Dr.-Ing., Ruhr-Universität Bochum;
Lehrstuhl für Informatik im Bauwesen, Gebäude IA, 44780, Bochum, Germany

Gaik A. Manuylov, Professor, Ph.D.,
Moscow State University of Railway Engineering; 9, Obraztsova Street, Moscow, 127994, Russia

Alexander S. Noskov, Professor, Dr.Sc.,
Ural Federal University named after the first President of Russia B.N. Yeltsin;
19 Mira Street, Ekaterinburg, 620002, Russia

Grzegorz Świt, Professor, Dr.hab. Inż.,
Kielce University of Technology; 7, al. Tysiąclecia Państwa Polskiego, Kielce, 25 – 314, Poland

AIMS AND SCOPE

The aim of the Journal is to advance the research and practice in structural engineering through the application of computational methods. The Journal will publish original papers and educational articles of general value to the field that will bridge the gap between high-performance construction materials, large-scale engineering systems and advanced methods of analysis.

The scope of the Journal includes papers on computer methods in the areas of structural engineering, civil engineering materials and problems concerned with multiple physical processes interacting at multiple spatial and temporal scales. The Journal is intended to be of interest and use to researches and practitioners in academic, governmental and industrial communities.

ОБЩАЯ ИНФОРМАЦИЯ О ЖУРНАЛЕ

International Journal for Computational Civil and Structural Engineering

(Международный журнал по расчету гражданских и строительных конструкций)

Международный научный журнал "International Journal for Computational Civil and Structural Engineering (Международный журнал по расчету гражданских и строительных конструкций)" (IJCCSE) является ведущим научным периодическим изданием по направлению «Инженерные и технические науки», издаваемым, начиная с 1999 года (ISSN 2588-0195 (Online); ISSN 2587-9618 (Print) Continues ISSN 1524-5845). В журнале на высоком научно-техническом уровне рассматриваются проблемы численного и компьютерного моделирования в строительстве, актуальные вопросы разработки, исследования, развития, верификации, апробации и приложений численных, численно-аналитических методов, программно-алгоритмического обеспечения и выполнения автоматизированного проектирования, мониторинга и комплексного наукоемкого расчетно-теоретического и экспериментального обоснования напряженно-деформированного (и иного) состояния, прочности, устойчивости, надежности и безопасности ответственных объектов гражданского и промышленного строительства, энергетики, машиностроения, транспорта, биотехнологий и других высокотехнологичных отраслей.

В редакционный совет журнала входят известные российские и зарубежные деятели науки и техники (в том числе академики, члены-корреспонденты, иностранные члены, почетные члены и советники Российской академии архитектуры и строительных наук). Основной критерий отбора статей для публикации в журнале − их высокий научный уровень, соответствие которому определяется в ходе высококвалифицированного рецензирования и объективной экспертизы, поступающих в редакцию материалов.

Журнал входит в Перечень ВАК РФ ведущих рецензируемых научных изданий, в которых должны быть опубликованы основные научные результаты диссертаций на соискание ученой степени кандидата наук, на соискание ученой степени доктора наук по научным специальностям и соответствующим им отраслям науки:

- 1.1.8 – Механика деформируемого твердого тела (технические науки),
- 1.2.2 – Математическое моделирование численные методы и комплексы программ (технические науки),
- 2.1.1 – Строительные конструкции, здания и сооружения (технические науки),
- 2.1.2 – Основания и фундаменты, подземные сооружения (технические науки),
- 2.1.5 – Строительные материалы и изделия (технические науки),
- 05.23.07 – Гидротехническое строительство (технические науки),
- 2.1.9 – Строительная механика (технические науки)

В Российской Федерации журнал индексируется Российским индексом научного цитирования (РИНЦ).

Журнал входит в базу данных Russian Science Citation Index (RSCI), полностью интегрированную с платформой Web of Science. Журнал имеет международный статус и высылается в ведущие библиотеки и научные организации мира.

Издатели журнала – *Издательство Ассоциации строительных высших учебных заведений /АСВ/* (Россия, г. Москва) и до 2017 года *Издательский дом Begell House Inc*. (США, г. Нью-Йорк). Официальными партнерами издания является *Российская академия архитектуры и строительных наук* (РААСН), осуществляющая научное курирование издания, и *Научно-исследовательский центр СтаДиО* (ЗАО НИЦ СтаДиО).

Цели журнала – демонстрировать в публикациях российскому и международному профессиональному сообществу новейшие достижения науки в области вычислительных методов

решения фундаментальных и прикладных технических задач, прежде всего в области строительства.

Задачи журнала:

• предоставление российским и зарубежным ученым и специалистам возможности публиковать результаты своих исследований;

• привлечение внимания к наиболее актуальным, перспективным, прорывным и интересным направлениям развития и приложений численных и численно-аналитических методов решения фундаментальных и прикладных технических задач, совершенствования технологий математического, компьютерного моделирования, разработки и верификации реализующего программно-алгоритмического обеспечения;

• обеспечение обмена мнениями между исследователями из разных регионов и государств.

Тематика журнала. К рассмотрению и публикации в журнале принимаются аналитические материалы, научные статьи, обзоры, рецензии и отзывы на научные публикации по фундаментальным и прикладным вопросам технических наук, прежде всего в области строительства. В журнале также публикуются информационные материалы, освещающие научные мероприятия и передовые достижения Российской академии архитектуры и строительных наук, научно-образовательных и проектно-конструкторских организаций.

Тематика статей, принимаемых к публикации в журнале, соответствует его названию и охватывает направления научных исследований в области разработки, исследования и приложений численных и численно-аналитических методов, программного обеспечения, технологий компьютерного моделирования в решении прикладных задач в области строительства, а также соответствующие профильные специальности, представленные в диссертационных советах профильных образовательных организациях высшего образования.

Редакционная политика. Политика редакционной коллегии журнала базируется на современных юридических требованиях в отношении авторского права, законности, плагиата и клеветы, изложенных в законодательстве Российской Федерации, и этических принципах, поддерживаемых сообществом ведущих издателей научной периодики.

За публикацию статей плата с авторов не взымается. Публикация статей в журнале бесплатная. На платной основе в журнале могут быть опубликованы материалы рекламного характера, имеющие прямое отношение к тематике журнала.

Журнал предоставляет непосредственный открытый доступ к своему контенту, исходя из следующего принципа: свободный открытый доступ к результатам исследований способствует увеличению глобального обмена знаниями.

Индексирование. Публикации в журнале входят в системы расчетов индексов цитирования авторов и журналов. «Индекс цитирования» – числовой показатель, характеризующий значимость данной статьи и вычисляющийся на основе последующих публикаций, ссылающихся на данную работу.

Авторам. Прежде чем направить статью в редакцию журнала, авторам следует ознакомиться со всеми материалами, размещенными в разделах сайта журнала (интернет-сайт Российской академии архитектуры и строительных наук (http://raasn.ru); подраздел «Издания РААСН» или интернет-сайт Издательства АСВ (http://iasv.ru); подраздел «Журнал IJCCSE»): с основной информацией о журнале, его целями и задачами, составом редакционной коллегии и редакционного совета, редакционной политикой, порядком рецензирования направляемых в журнал статей, сведениями о соблюдении редакционной этики, о политике авторского права и лицензирования, о представлении журнала в информационных системах (индексировании), информацией о подписке на журнал, контактными данными и пр. Журнал работает по лицензии Creative Commons типа cc by-nc-sa (Attribution Non-Commercial Share Alike) – Лицензия «С указанием авторства – Некоммерческая – Копилефт».

Рецензирование. Все научные статьи, поступившие в редакцию журнала, проходят обязательное двойное слепое рецензирование (рецензент не знает авторов рукописи, авторы рукописи не знают рецензентов).

Заимствования и плагиат. Редакционная коллегия журнала при рассмотрении статьи проводит проверку материала с помощью системы «Антиплагиат». В случае обнаружения многочисленных заимствований редакция действует в соответствии с правилами COPE.

Подписка. Журнал зарегистрирован в Федеральном агентстве по средствам массовой информации и охраны культурного наследия Российской Федерации. Индекс в общероссийском каталоге РОСПЕЧАТЬ − 18076.

По вопросам подписки на международный научный журнал “International Journal for Computational Civil and Structural Engineering (Международный журнал по расчету гражданских и строительных конструкций)” обращайтесь в Агентство «Роспечать» (Официальный сайт в сети Интернет: http://www.rosp.ru/) или в издательство Ассоциации строительных вузов (АСВ) в соответствии со следующими контактными данными:

ООО «Издательство АСВ»

Юридический адрес: 129337, Россия, г. Москва, Ярославское ш., д. 26, офис 705;

Фактический адрес: 129337, Россия, г. Москва, Ярославское ш., д. 19, корп. 1, 5 этаж, офис 12 (ТЦ Соле Молл);

Телефоны: +7 (925) 084-74-24;

Интернет-сайт: www.iasv.ru. Адрес электронной почты: iasv@iasv.ru.

Контактная информация. По всем вопросам работы редакции, рецензирования, согласования правки текстов и публикации статей следует обращаться к главному редактору журнала академику РААСН *Сидорову Владимиру Николаевичу* (адреса электронной почты: sidorov.vladimir@gmail.com, sidorov@iasv.ru, iasv@iasv.ru, sidorov@raasn.ru) или к техническому редактору журнала советнику РААСН *Кайтукову Таймуразу Батразовичу* (адреса электронной почты: tkaytukov@gmail.com; kaytukov@raasn.ru). Кроме того, по указанным вопросам, а также по вопросам размещения в журнале рекламных материалов можно обращаться к генеральному директору ООО «Издательство АСВ» *Никитиной Надежде Сергеевне* (адреса электронной почты: iasv@iasv.ru, nsnikitina@mail.ru, ijccse@iasv.ru).

Журнал становится технологичнее. Издательство АСВ с сентября 2016 года является членом Международной ассоциации издателей научной литературы (Publishers International Linking Association (PILA)), осуществляющей свою деятельность на платформе CrossRef. Оригинальным статьям, публикуемым в журнале, будут присваиваться уникальные номера (индексы DOI – Digital Object Identifier), что значительно облегчит поиск метаданных и местонахождение полнотекстового произведения. DOI – это система определения научного контента в сети Интернет.

С октября 2016 года стал возможен прием статей на рассмотрение и рецензирование через онлайн систему приема статей Open Journal Systems на сайте журнала (электронная редакция): https://ijccse.iasv.ru.

Автор имеет возможность следить за продвижением статьи в редакции журнала в личном кабинете Open Journal Systems и получать соответствующие уведомления по электронной почте.

В феврале 2018 года журнал был зарегистрирован в Directory of open access journals (DOAJ) (это один из самых известных поисковых сервисов в мире, который предоставляет открытый доступ к материалам и индексирует не только заголовки журналов, но и научные статьи), в сентябре 2018 года включен в продукты EBSCO Publishing.

В ноябре 2020 года журнал начал индексироваться в международной базе Scopus.

International Journal for
Computational Civil and Structural Engineering
(Международный журнал по расчету гражданских и строительных конструкций)
Volume 21, Issue 2 ***2025***

Scientific coordination is carried out by the Russian Academy of Architecture and Construction Sciences (RAACS)

CONTENTS

Assessment the Probability of Failure of a Reinforced Concrete Frame Under a Column Removal Scenario Using the First-Order Reliability Method 14
Vu Ngoc Tuyen, Nataliya V. Fedorova, Duong Thanh Qui

Nonlinear Dynamic Analysis of Reinforced Concrete Large-Panel Building 30
Zaurbek K. Abaev, Azamat D. Valiev

Accounting for the Added Mass of Water of Reservoir in Calculation of Seismic Accelerations for Pressure Hydraulic Structures 43
Alexandra S. Bestuzheva, Georgy P. Gotsiridze

Investigation of Failure of Riverbank Protection Structure: a Case Study in Long an Province, Vietnam 62
Pham Ngoc Thinh, Dang Van Phu

Mathematical Modeling of Swirling Flow in a Vortex Dust Separator 75
Vadim K. Akhmetov

Butt Joint with Meander Outline for Box-Section Column in Frame Moment Connection for Seismic Applications 83
Yurii S. Kost, Tatiana L. Dmitrieva

Structural Behavior of GFRP-Concrete Composite Columns Under Axial Load 99
Mohammed A.M. Khalil, Mohammed M.Salem, Ata El-Kariem Shoeib, Alaa Gamal Sherif

Numerical Assessment of Soil Mass Slope Stability with Regard to Predicted Thawing of Permafrost Soils 116
Nikolay A. Aniskin, Stanislav A. Sergeev, Andrey V. Stupivtsev, Ilia A. Bokov

Experimental Determination of the Total Shrinkage Strain of Reinforced Concrete 129
Valeryia A. Rzhevutskaya, Yuliya G. Maskalkova

Adaptive Neuro-Fuzzy System for Estimation of Biopositivity of Built Environment 138
Valeriy I. Telichenko, Nikita S. Rud

Earth Core Rockfill Dam: Interaction of Water and Soil **149**
Mikhail P. Sainov , Aleksandr A. Boldin

Nonlocal in Time Dynamic Deformation Model and Its Calibration Based on the Beam Vibration Experiment Results **161**
Vladimir N. Sidorov, Elena. S. Badina, Roman O. Tsarev

Assessment of the Distribution of the Soil Deformation Modulus Based on CPT Data **171**
Nune Tigabu Abera, Ludmila V. Kirianova

Deep Beam Analysis with the Use of Discrete-Continual Finite Element Method in the Presence of a Vertical Crack **177**
Marina L. Mozgaleva, Pavel A. Akimov

Numerical Modeling of Cast-in-Place Reinforced Concrete Bubble Deck Floor Slabs Utilized in Earthquake-Prone Regions **187**
Alexander M. Belostotsky, Alexander I. Nagibovich, Sergey V. Scherbina, Tatiana N. Vasileva

3D Concrete Printing: a Study of Printed Structures Durability **200**
Aleksey O. Adamtsevich, Andrey P. Pustovgar, Liubov A. Adamtsevich, Yuriy I. Markov

International Journal for
Computational Civil and Structural Engineering
(Международный журнал по расчету гражданских и строительных конструкций)
Volume 21, Issue 2 ***2025***

Scientific coordination is carried out by the Russian Academy of Architecture and Construction Sciences (RAACS)

СОДЕРЖАНИЕ

Оценка вероятности отказа железобетонной рамы при сценарии удалени колонны методом надежности первого порядка **14**
Ву Нгок Туен, Н.В. Федорова, Зыонг Тхань Куй

Нелинейный динамический анализ крупнопанельного железобетонного здания **30**
З.К. Абаев, А.Д. Валиев

Учёт присоединенной массы воды водохранилища в расчете сейсмических сил для напорных гидротехнических сооружений **43**
А.С. Бестужева, Г.П. Гоциридзе

Анализ разрушения берегозащитной конструкции в провинции Лонг Ан, Вьетнам **62**
Фам Нгок Тхинь, Данг Ван Фу

Математическое моделирование закрученного течения в вихревом пылеотделителе **75**
В.К. Ахметов

Стык с очертанием меандра коробчатой колонны для сейсмостойкого рамного узла **83**
Ю.С. Кость, Т.Л. Дмитриева

Несущая способность железобетонных колонн, армированных GFRP-профилем, при действии продольной силы и огневом воздействии **99**
Мохаммед А.М. Халил, Мохаммед М. Салем, Ата Эль-Карим Шойиб, Алаа Гамаль Шериф

Численная оценка устойчивости откосов грунтового массива с учетом прогнозного растепления многолетнемерзлых грунтов **116**
Н.А. Анискин, С.А. Сергеев, А.В. Ступивцев, И.А. Боков

Экспериментальное определение полных деформаций усадки железобетона **129**
В.А. Ржевуцкая, Ю.Г. Москалькова

Оценка биопозитивности среды жизнедеятельности гражданских зданий на основе адаптивной нейро-нечеткой системы вывода **138**
В.И. Теличенко, Н.С. Рудь

Каменно-земляная плотина: взаимодействие воды и грунта **149**
М.П. Саинов , А.А. Болдин

Нелокальная во времени модель динамического деформирования материала и её калибровка по результатам динамических испытаний изгибаемых балок **161**
В.Н. Сидоров, Е.С. Бадьина, Р.О. Царёв

Оценка распределения модуля деформации грунта на основе данных CPT **171**
Нуне Тигабу Абера, Л.В. Кирьянова

Расчет балки-стенки с использованием дискретно-континуального метода конечных элементов при наличии вертикальной щели **177**
М.Л. Мозгалева, П.А. Акимов

Численное моделирование монолитных железобетонных перекрытий с пустотообразователями, применяемых в сейсмически активных районах **187**
А.М. Белостоцкий, А.И. Нагибович, С.В. Щербина, Т.Н. Васильева

Аддитивное строительное производство: исследование долговечности напечатанных конструкций **200**
А.О. Адамцевич, А.П. Пустовгар, Л.А. Адамцевич, Ю.И. Марков

International Journal for Computational Civil and Structural Engineering, 21(2) 14–29 (2025)

DOI:10.22337/2587-9618-2025-21-2-14-29

ASSESSMENT THE PROBABILITY OF FAILURE OF A REINFORCED CONCRETE FRAME UNDER A COLUMN REMOVAL SCENARIO USING THE FIRST-ORDER RELIABILITY METHOD

Vu Ngoc Tuyen [1], Fedorova Nataliya Vitalyevna [1], Duong Thanh Qui [2]

[1] Moscow State University of Civil Engineering National Research University, Moscow, RUSSIA

[2] Vietnam Institute for building materials, Ha Noi, VIETNAM

Abstract: The article considers issues related to the assessment of survivability of structural reinforced concrete systems in special limit states under the scenario of removal of one of the load-bearing columns within the framework of the probabilistic approach. Probabilistic models of basic (stochastic) variables included in the load and resistance functions are presented. Statistical parameters of the uncertainty of the resistance model and the model of the effect of external actions are obtained and integrated as a basic variable in probabilistic modeling. The functions of the limit state of the structural system in a special calculated situation with a sudden removal of the central column of the first floor are determined. Probabilistic modeling is performed using the first-order reliability method (FORM) for structural reinforced concrete systems designed according to the current standards of the Russian Federation. As a result, the values of the failure probabilities and the corresponding reliability indices are obtained for the considered structural systems.

Keywords: Progressive collapse, probability, structural reliability, first order reliability method, robustness, column removal scenarios, reinforced concrete structures

ОЦЕНКА ВЕРОЯТНОСТИ ОТКАЗА ЖЕЛЕЗОБЕТОННОЙ РАМЫ ПРИ СЦЕНАРИИ УДАЛЕНИЯ КОЛОННЫ МЕТОДОМ НАДЕЖНОСТИ ПЕРВОГО ПОРЯДКА

Ву Нгок Туен [1], Н.В. Федорова [1], Зыонг Тхань Куй [2]

[1] Национальный исследовательский Московский государственный строительный университет, г. Москва, РОССИЯ

[2] Вьетнамский институт строительных материалов, г. Ханой, ВЬЕТНАМ

Аннотация: В рамках вероятностного подхода рассмотрены вопросы связанные с оценкой живучести конструктивных железобетонных систем в особых предельных состояниях при сценарии удалении одной из несущих колонн. Представлены вероятностные модели базисных (стохастических) переменных, входящих в функции нагрузок и сопротивлений. Получены и интегрированы в виде базисной переменной при вероятностном моделировании статистические параметры неопределенности модели сопротивления и модели эффекта от внешних воздействий. Определены функции предельного состояния конструктивной системы в особой расчетной ситуации при внезапном удалении центральной колонны первого этажа. Выполнено вероятностное моделирование по методу расчета надежности первого порядка (FORM) конструктивных железобетонных систем железобетона, запроектированных по действующим нормам РФ. В результате для рассматриваемых конструктивных систем получены значения вероятностей отказа и соответствующих индексов надежности.

Ключевые слова: Прогрессирующее обрушение, вероятность, надежность конструкций, метод надежности первого порядка, прочность, сценарии удаления колонн, железобетонные конструкции

1. INTRODUCTION

Progressive collapse is a catastrophic partial or complete failure of a structure caused by local structural damage [1]. Local failure initiates a chain reaction of failures that propagates vertically or horizontally through the structural system, resulting in widespread partial or complete collapse. The key feature of progressive collapse is that the resulting ultimate damage is disproportionate to the local damage caused by the initiating event. Such collapses may be initiated by specific beyond design basis events (e.g. gas explosions, vehicle collisions, and sabotage, fires, extreme environmental impacts, and human errors in design and construction) [2].

Progressive collapse and stability of structures under such special beyond design loads became an important factor in research and design after the collapse of the Ronan Point apartment tower in 1968. Interest in this topic has recently increased as a result of the terrorist attack on the Murrah Federal Building in Oklahoma City in 1995 and the attack on the World Trade Center in New York in 2001 [3].

At present, although the stability of structures against progressive collapse under special beyond design basis events has become a worldwide research topic, there is no unified theory for assessing structural stability, nor a general methodology for quantitatively assessing the progressive collapse resistance of real complex structures. Below are presented some notable research directions proposed for assessing the stability of reinforced concrete structures against progressive collapse.

One of the main areas of research in assessing the response of structures to beyond design actions is the conduct of experiments on structural models. A number of quasi-static tests have been conducted on various structural models, such as a beam-column and beam-slab substructure, flat frame structures and large-scale buildings, ... [4]. Thanks to these experiments, the load-bearing capacity, as well as the deformation and failure characteristics of the structure, have been studied quite thoroughly. During the deformation of the substructure, various mechanisms of resistance to progressive collapse were discovered with an increase in the quasi-static concentrated load above the removed column.

At early stages, when the applied force is still small, the bending moment in dangerous sections is less than the bearing capacity M_{ult}, the structure operates according to the bending mechanism. The internal forces in the beam are only the transverse force and the bending moment. The longitudinal force is practically equal to zero [5].

When the quasi-static external force applied above the removed column continues to increase, the bending moment reaches the limiting value M_{ult} in the sections near the side columns. At the same time, as the external load increases, the value of the bending moment in these sections no longer increases. The stresses in the reinforcement in the tension zone of the dangerous sections reach the yield point, and the plastic deformation in them increases significantly. The compression zone height of concrete gradually decreases, and numerous cracks appear in the tension zone of concrete. At this stage, it can be observed that the compressed concrete strip forms an arc (arch). The horizontal displacement at the base of the formed arch is limited by the adjacent structures. Due to the work of the compressive concrete arch, the bearing capacity of the system increases significantly. The structure enters the stage according to the arch mechanism [6]. It should be noted that when calculating reinforced concrete structures under the scenario of removing a load-bearing column, the arch mechanism cannot be modeled using bar and plate elements in traditional finite element analysis.

As the quasi-static external force applied above the removed column increases, the displacement of the structure also increases. The height of the compressive concrete arch gradually decreases to zero. At this stage, the arch mechanism completely disappears and is replaced by a catenary mechanism [7]. All reinforcement in dangerous sections is subjected to tension. This also means

that the longitudinal force in the structure begins to manifest itself and increases to a limiting value when the stresses in the reinforcement reach the tensile strength. The structure completely collapses when the longitudinal reinforcement ruptures.

It should be emphasized that the above-mentioned deformation and failure characteristics were discovered as a result of quasi-static experiments. Therefore, it does not fully reflect the dynamic nature of the process of progressive collapse and does not explain the change in the dynamic strength of the material under high-strain-rate conditions. Several dynamic experiments have been conducted so far to overcome the shortcomings of quasi-static experiments [8,9]. However, these experiments are very complex and require expensive equipment.

In parallel with the experiments, many scientists choose the method of predicting the bearing capacity, as well as the deformability and failure characteristics of structures using numerical methods, such as the finite element method [10]. However, the output results of the numerical analysis largely depend on the correctness of the input data, the suitability of the material model, the types of finite elements, as well as the perfection of the calculation algorithm and the skills in using specialized software. It should be noted that the numerical analysis here can be either nonlinear dynamic or nonlinear static. In the case of nonlinear static analysis, a dynamic amplification factor is applied so that the structural system provides equivalent dynamic behavior in the scenario of sudden column failure [11].

Another approach proposed for assessing the dynamic response of structures is the energy approach. Based on the nonlinear relationship between load and displacement in a quasi-static test and assuming that the work of the external force is balanced by the energy stored inside the structure when the column fails, we can find the greatest displacement that the system can achieve [12]. The energy approach is relatively simple, but it does not allow us to assess the effect of strain rate on the dynamic strength of materials in reinforced concrete structures.

Some researchers use the tools of structural dynamics to solve the problem of dynamic behavior of structures under beyond-design actions in the form of sudden failure of load-bearing columns. Jian Weng and his colleagues proposed a linear model with single-degree-of-freedom, which takes into account a fixed damping coefficient and failure time of the column [13]. Jun Yu and his colleagues proposed a nonlinear model with single-degree-of-freedom, in which the system stiffness is described by a trilinear function, which is able to describe various mechanisms of resistance to progressive collapse of the structure [14,15].

Another approach to studying the resistance of building structures to progressive collapse is to use reliability/risk indices [16,17]. The ability of a structure to withstand damage can be determined based on the reliability analysis of the structure and probability assessment. Probabilistic analysis will allow design engineers to decide whether further protective measures are required to prevent the risk of collapse. Izzuddin A. et al. [18] proposed a probabilistic risk assessment system for multi-story steel buildings under beyond design actions. In their work, a simple probabilistic scheme was used, including the basic requirements for describing the uncertainty of hazards, the local damage associated with them, and the consequences of global failure. Xu and Ellingwood assessed the resistance of steel frames to progressive collapse by developing a probabilistic model of failure of beam-column connections [19]. In the proposed model, the load values as well as the load-bearing capacity of the structure are uncertain quantities. Brunesi and Parisi used Monte Carlo simulation to create two-dimensional (2D) and three-dimensional (3D) stochastic realizations of structural models from which an analytically model of progressive failure of reinforced concrete frame structures could be derived [20].

The main objective of this study is to develop an assessment method for predicting the resistance

to progressive collapse of a reinforced concrete frame structure based on the probability principle. In the reliability analysis, a global limit state equation for the bearing capacity of the structural system is first formulated, in which the safety factor is the difference between the ultimate bearing capacity of the structural system and the effects of external loads. An analytical approach (the first-order reliability method (FORM)) is applied to analyze the reliability of multi-story reinforced concrete frame structures subject to column failure based on the structural reliability index.

2. METHODS

Fundamentals of a progressive collapse risk management strategy

In general, the strategy for managing the risks of progressive collapse focuses on calculation methods that assess the ability of a damaged structural system to maintain survivability after a special event associated with the occurrence of a special action.

If each of the threats discussed earlier is represented as a random event, then the total probability of collapse of the structural system can be written as follows:

$$P(F) = \overbrace{\underbrace{P(F|DH)}_{\text{robustness}}\underbrace{P(DH|H)}_{\text{element behaviour}}}^{\text{collapse resistance}}\ \underbrace{P(H)}_{\text{event control}} \begin{matrix} \left.\vphantom{\overbrace{a}^{b}}\right\}\text{maximise} \\ \left.\vphantom{\underbrace{a}_{b}}\right\}\text{minimise,} \end{matrix} \quad \begin{matrix} \\ \\ \text{vulnerability} \quad \text{hazard} \end{matrix} \tag{1}$$

where F is an event defined as a disproportionate or progressive collapse of a structural system;

$P(H)$ is the probability of occurrence of a special event associated with the threat H;

$P(DH|H)$ is the conditional probability of local failure of an individual structural element *D* as a result of the realization of the threat H;

$P(F|DH)$ is the conditional probability of the occurrence of progressive collapse of a structural system *F* under the condition that local failure of an individual element *D* occurs upon the realization of a special event H.

In the case of a progressive collapse, the main consequence of which is loss of life, acceptable reliability $P(F)$ will be achieved if the following condition is met:

$$P(F) \le p_{tag}. \tag{2}$$

The basic question in the approaches adopted by almost all regulatory documents containing requirements for calculations for special actions is the following: what level of probability of collapse of a structural system should be considered acceptable?

Within the framework of the generally accepted concept, it is considered that the central criterion value of the probability of collapse of a structural system is $P_{tag} = 10^{-7} / \text{год}$ for a reference period of 1 year.

It is easy to see that the probability of occurrence of disproportionate progressive collapse of the structural system can be reduced by reducing either each individual or all three probabilities included in (1). In this case, the probability of occurrence of a special event $P(H)$ associated with a threat H is independent during design. It can be controlled by the space-planning solution or placement of the building, reduction of possible risks inside the structure with organized security measures, personnel training, etc. When implementing such measures, many risks can be effectively prevented (e.g., terrorist attacks, improper operation of the building and structure, ...). In addition, these measures include quality control during design to prevent human errors and recommendations for technical maintenance.

The design strategy of key elements aimed at ensuring resistance to local failure is reduced to minimizing the probability $P(DH|H)$. Within the framework of this strategy, a key element is understood to be the load-bearing elements and connections that are necessary to ensure the resistance of the original structural system as a whole. This strategy may be difficult to implement (due to the uncertainty of the magnitude of special actions), contain significant risks, or initially give uneconomical results.

In the case where the alternate load path method is used in assessing survivability, the conditional probability of a local failure of a key element when a special event H occurs is conservatively taken as $P(DH|H) = 1$ (the failure of a key element occurs when a special event occurs, although in the general case a structural element designed in a design traditional calculated situation will have some reliability under the action of special loads). Then expression (1) can be written in the following form:

$$P(F) = P(F|DH)P(H). \quad (3)$$

Thus, the design task in a special calculated situation is reduced mainly to minimizing the probability $P(F|DH)$. This strategy should be implemented in a wide range: from design measures aimed at creating the continuity and structural integrity of the system to a complete calculation of damage to the structural system taking into account various mechanisms of resistance to progressive collapse, which are not taken into account in traditional design (for example, compressive arch and catenary mechanisms, the effect of high-speed deformation of materials, large deformations and displacements, physical and geometric nonlinearity, etc.).

Taking into account that the occurrence of a special event H can be modeled by a Poisson process with an annual average occurrence frequency λ_H, the probability of occurrence of this event during some estimated period T (service life) for small λ_H is approximately $P(H) = \lambda_H T$. From which it follows that:

$$P(F) = P(F|DH)\lambda_H T. \quad (4)$$

Thus, the permissible probability of progressive collapse of the structural system is determined by the formula

$$P(F|DH) \le \frac{p_{tag}}{\lambda_H T}. \quad (5)$$

The value of λ_H is determined by statistical assessment of threats and can be taken in the range of 10^{-6}/year…10^{-5}/year depending on the type of threat. Thus, the target average annual conditional probability of progressive collapse of a damaged structural system can be taken equal to

$$P(F|DH) \le \frac{\frac{10^{-7}}{\text{год}}}{\left(\frac{10^{-6}}{\text{year}}...\frac{10^{-5}}{\text{year}}\right)\text{year}} = \frac{10^{-2}}{\text{year}}...\frac{10^{-1}}{\text{year}}. \quad (6)$$

Limit state function

In order to determine the probability $P(F|DH)$, one must first postulate a mathematical model (limit state function) *G(X)* in accordance with the principles established in reliability theory [21].

From the point of view of reliability theory, the behavior of a structural system or its element at an arbitrary moment in time can be described using a set of inherent limit states that designate the boundary between safe and unsafe states, the transition through which is considered a failure.

The model describing the limit state is represented by the so-called state function *G( )*, which includes all the basic variables *X* necessary for design, describing the effects of external loads *E(X)* and the resistance of the system itself *R(X)*:

$$G(X)=R(X)-E(X)= R(X_1, X_2, \dots, X_n) - \quad (7)$$

$$E(X_1, X_2, \ldots, X_n),$$

where $E(X)$ is a function representing the model of the effect of external loads; R(X) is a function representing the model of the element's resistance; X is a vector of basic (stochastic) variables, which are the parameters of the calculation model $E(\bullet)$ and $R(\bullet)$.

For specific basic variables X, the function $G(X)$ shows the state of the structural element: safe (operational) when $G(X) \geq 0$, or in a state of failure when $G(X)<0$. Progressive collapse of a structural system is a probabilistic event, and the probability of its occurrence $P\left(F\middle|DH\right)$ is determined as follows:

$$P\left(F\middle|DH\right) = Prob\left\{G\left(X\right) < 0\right\}. \quad (8)$$

Reliability index β

The basic stochastic variable has two characteristic numerical values: the mathematical expectation (mean value) and the standard deviation. Let μ_G be the mean value of the limit state function $G(\,)$. σ_G is the standard deviation, then σ_G^2 is the variance of the function $G(\,)$. The reliability index β is defined as the ratio

$$\beta = \mu_G / \sigma_G. \quad (9)$$

If $R(X)$ and $E(X)$ are normally distributed, independent and uncorrelated, we have

$$\beta = \frac{\mu_R - \mu_E}{\sqrt{\sigma_R^2 + \sigma_E^2}}. \quad (10)$$

Let us consider the case when $R(X)$ and $E(X)$ are linear functions of the basic stochastic variables X_i:

$$R = \sum_{i=1}^{n} a_i X_i + a_0; E = \sum_{k=1}^{n} b_k X_k + b_0, \quad (11)$$

where a_i and b_k are constants. Then $G(X)=R(X)-E(X)$ is also a linear function of these variables X_i:

$$G\left(X\right) = \sum_{i=1}^{n} a_i X_i - \sum_{k=1}^{n} b_k X_k + \left(a_0 - b_0\right). \quad (12)$$

Thus, the mean value μ_G of the limit state function has the form

$$\mu_G = \sum_{i=1}^{n} a_i \mu_{X_i} - \sum_{k=1}^{n} b_k \mu_{X_k} + \left(a_0 - b_0\right), \quad (13)$$

and the variance σ_G^2 of the function has the form

$$\sigma_G^2 = \sum_{i=1}^{n} a_i \sigma_{X_i}^2 - \sum_{k=1}^{n} b_k \sigma_{X_k}^2. \quad (14)$$

Then, determining the reliability index β in this case is quite simple, based on formula (9).

If $R(X)$ and $E(X)$ are nonlinear functions of the basic stochastic variables X_i, approximate methods such as linearization methods (e.g., FORM, SORM, FOSM) or the iterative method can be used to find the reliability index β.

Theoretical and experimental studies [22] have shown that the values of the physical and mechanical properties of materials, the geometric dimensions of the structure, and external loads have the properties of random variables and have a normal distribution law. In addition, when calculating the structures of buildings and structures for non-bearing capacity, the limit state function is established using analytical formulas. These are favorable conditions for applying the first-order reliability method (FORM) to determine the probability of progressive collapse of a building or structure under special beyond-design actions.

First-order reliability method (FORM)

To determine the reliability index β, it is necessary to know the analytical expression $G(\,)$ for the basic stochastic variables X_i and determine the mean value μ_G, the standard deviation σ_G of the limit state function $G(\,)$ for these variables. The mean value μ_G is determined by re-

placing the values of these variables X_i with their average values μ_{X_i} in the expression *G(X)*. Determining the standard deviation σ_G requires more complex calculations.

If *G(X)* is a linear function of the basic stochastic variables X_i, then σ_G is calculated using formula (14).

If *G(X)* is a nonlinear function of the basic stochastic variables X_i, then we perform a Taylor expansion of the function *G(X)* around the mean value of the variables. Ignoring the higher-order components in this expansion, we can determine the approximate value of *G(X)* as a linear function of the basic stochastic variables X_i.

For example, the Taylor expansion of the function *G(X)* around the mean value has the form

$$G = G\left(\mu_{X_i}\right) + \sum_{i=1}^{n} \left.\frac{\partial G}{\partial X_i}\right|_{\mu_{\bar{x}}} \left(X_i - \mu_{X_i}\right) + \frac{1}{2}\sum\sum \left.\frac{\partial^2 g}{\partial X_i \partial X_j}\right|_{\mu_{\bar{x}}} \left(X_i - \mu_{X_i}\right)\left(X_j - \mu_{X_j}\right) + ..., \tag{15}$$

where $\left.\frac{\partial G}{\partial X_i}\right|_{\mu_{\bar{x}}}$ is the partial derivative of *G(X)* with respect to X_i at μ_{X_i}. If only first-order terms are retained, *G(X)* is approximated as a linear function of the basis stochastic variables.

$$G \approx G\left(\mu_{\bar{X}}\right) + \sum_{i=1}^{n} \left.\frac{\partial G}{\partial X_i}\right|_{\mu_{\bar{x}}} \left(X_i - \mu_{X_i}\right). \tag{16}$$

By replacing (16) the mean value of the variables X_i, we obtain the average value of the limit state function *G(X)*.

$$\mu_G \approx G\left(\mu_{X_i}, \mu_{X_2}, ..., \mu_{X_n}\right), \tag{17}$$

and variance:

$$\sigma_G^2 = \sum_{i=1}^{n} \left(\frac{\partial G}{\partial X_i}\right)^2 \mathrm{var}\left(X_i\right). \tag{18}$$

Knowing the mean value μ_G and the variance σ_G^2, we can determine the reliability index β using formula (9). Using the table of normalized distribution functions Φ, we find $P\left(F\middle|DH\right)$.

$$P\left(F\middle|DH\right) = \Phi\left(-\beta\right) = 1 - \Phi\left(\beta\right) \tag{19}$$

In the case of using a normal (or lognormal) distribution, the probability of progressive collapse of a damaged structural system is related to the reliability index β by means of the Laplace function:

$$\beta = -\Phi^{-1}\left[P\left(F\middle|DH\right)\right] \tag{20}$$

where $\Phi^{-1}(\,)$ is the inverse function of the standard normal distribution function.

The limiting value of $P\left(F\middle|DH\right)$ is in the range of 10^{-2}/year … 10^{-1}/year, which means that the limiting value of the reliability index will be in the range:

$$\beta_{tag} = \frac{1{,}28}{\text{year}} ... \frac{2{,}33}{\text{year}}. \tag{21}$$

3. RESULTS AND DISCUSSION

To illustrate the proposed calculation method, a multi-story building frame made of monolithic reinforced concrete is used as a visual example (Fig. 1a). A scenario of a special action in the form of a sudden removal of the load-bearing middle column of the first floor is considered. As a result of recent studies by many scientists, it has been shown that the area where progressive collapse can occur is the part of the structure above the damaged column (the local

failure zone). That is, the failure of the structural elements can spread vertically, while adjacent horizontal structures are usually not strongly exposed to the special actions mentioned above. Therefore, the calculation of the stability of the entire building against progressive collapse can be simplified by studying the stress-strain states in time of the local failure zone.

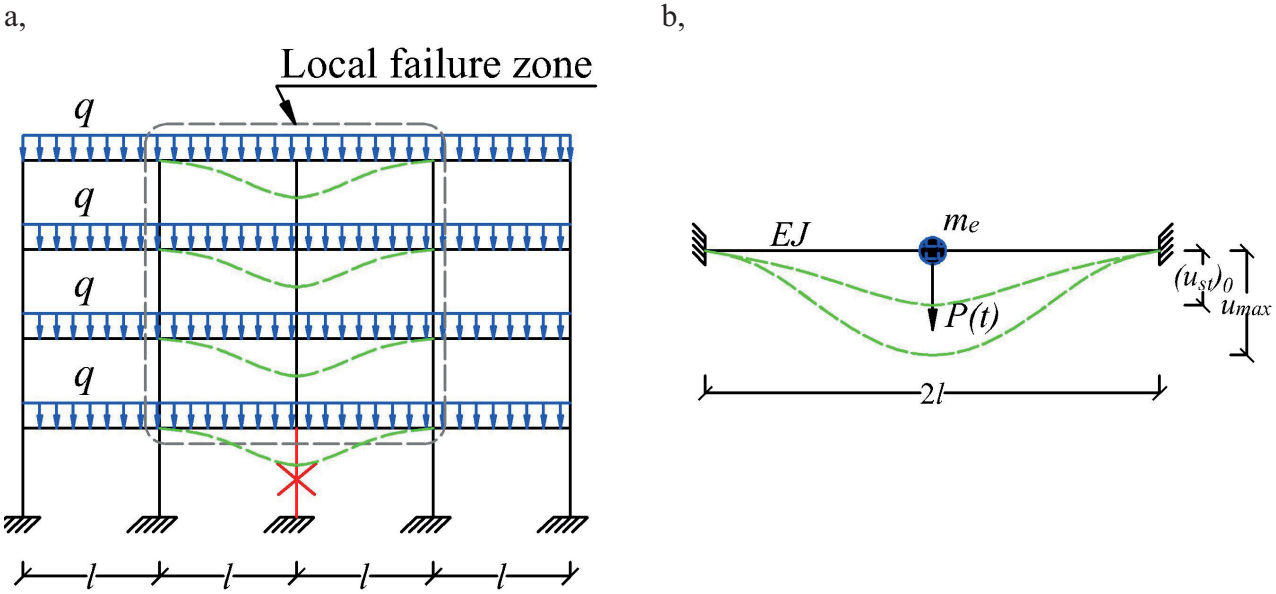


Figure 1. Monolithic reinforced concrete frame of the building in the scenario of sudden removal of the middle column (a) and the calculated scheme of a typical floor (b)

If we assume that the floors above removed supporting column are typical, their design characteristics are the same and under the same operational load, then we can see that their deformations, displacements, vibrations and failure are practically synchronous with each other.

This is the basis for further simplification of the calculated scheme. The study of the stress-strain state in time of the local failure zone is replaced by consideration of only the stress-strain state of one floor in the form of a fixed-ended beam of length *2l*. Fig. 1b shows the calculated scheme of the specified beam.

Figure 2 shows the diagram of bending moments M_{n-1}^{st} in the case of slow column failure (without taking into account the inertia force), and the diagram of bending moments M_{n-1}^{d} in the case of rapid column removal in a short time t_r. In section 1-1, at both ends of the beam, the bending moment has the greatest value. Therefore, it can be concluded that progressive collapse occurs when the moment at the end of the beam exceeds its ultimate value. Reliability calculations in these sections will give us the probability of occurrence or absence of progressive collapse.

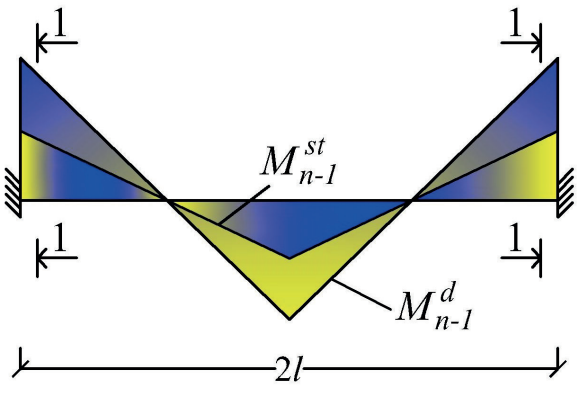


Figure 2. Bending moment diagrams in a beam with slow (M_{n-1}^{st}) and fast (M_{n-1}^{d}) removal of the middle column

As proven in [23], the maximum value of the bending moment in section 1-1 is achieved at time $t_0=t_r/2+T/2$. Where T is the period of free oscillations of the fixed-ended beam, representing the work of a typical floor. This value can be determined based on the maximum displacement of the beam point above the removed column as follows.

$$M_{1-1}^{\max} = -\frac{ql^2}{48} - \frac{24EJ}{l^2}u_{\max}, \qquad (22)$$

where q is the calculated operational load in the form of a distributed force, EJ is the flexural rigidity of the beam, l is the distance between the supporting columns, u_{max} is the maximum displacement that the beam system can achieve at a point above the removed column during the oscillation process.

If the energy absorption capacity of the system is neglected, the maximum displacement u_{max} can be determined by the following formula:

$$u_{\max} = \left(u_{st}\right)_0\left(1+\frac{\sin\pi\frac{t_r}{T_n}}{\pi\frac{t_r}{T_n}}\right) = \left(u_{st}\right)_0\left(1+\frac{\sin\frac{\omega_n t_r}{2}}{\frac{\omega_n t_r}{2}}\right), \qquad (23)$$

where $\left(u_{st}\right)_0 = \frac{ql^4}{384EJ}$ is the static displacement at the midpoint of the beam during slow failure of the column ($t_r \to \infty$), $T_n=2\pi/\omega_n$ and $\omega_n = \frac{1}{l^2}\sqrt{\frac{512EJ}{m}}$ is the period and natural frequency of oscillations of the damaged structural system, $J = bh^3/12$ is the moment of inertia of the rectangular cross-section of the beam.

Substituting the formulas of the given parameters into (23) and substituting (23) into (22), we obtain the final analytical expression for the maximum bending moment in section 1-1 of the structural system depending on the basic variables q, l, t_r, EJ, m.

$$M_{1-1}^{\max} = -\frac{ql^2}{48} - \frac{ql^2}{16}\left(1+\frac{\sin\frac{t_r}{2l^2}\sqrt{\frac{512EJ}{m}}}{\frac{t_r}{2l^2}\sqrt{\frac{512EJ}{m}}}\right). \qquad (24)$$

Determination of the total variance of the maximum displacement of a structural system

To determine the influence of the basic variables on the maximum value of the bending moment $M_{1-1}^{\max}$, we determine the partial derivative of the function $M_{1-1}^{\max}$ with respect to each variable.

$$\begin{aligned}
\frac{\partial M_{1-1}^{\max}}{\partial q} &= \frac{\sqrt{2}l^4}{256t_r}\sqrt{\frac{m}{EJ}}\sin\left(\frac{8\sqrt{2}t_r}{l^2}\sqrt{\frac{EJ}{m}}\right)+\frac{l^2}{24},\\
\frac{\partial M_{1-1}^{\max}}{\partial l} &= \frac{\sqrt{2}l^3 q}{64t_r}\sqrt{\frac{m}{EJ}}\sin\left(\frac{8\sqrt{2}t_r}{l^2}\sqrt{\frac{EJ}{m}}\right)+\frac{lq}{12}-\frac{lq}{8}\cos\left(\frac{8\sqrt{2}t_r}{l^2}\sqrt{\frac{EJ}{m}}\right),\\
\frac{\partial M_{1-1}^{\max}}{\partial t_r} &= -\frac{\sqrt{2}l^4 q}{256t_r^{\,2}}\sqrt{\frac{m}{EJ}}\sin\left(\frac{8\sqrt{2}t_r}{l^2}\sqrt{\frac{EJ}{m}}\right)+\frac{l^2 q}{32EJ}\cos\left(\frac{8\sqrt{2}t_r}{l^2}\sqrt{\frac{EJ}{m}}\right),\\
\frac{\partial M_{1-1}^{\max}}{\partial EJ} &= \frac{\sqrt{2}l^4 q}{512t_r EJ}\sqrt{\frac{m}{EJ}}\sin\left(\frac{8\sqrt{2}t_r}{l^2}\sqrt{\frac{EJ}{m}}\right)+\frac{l^2 q}{32EJ}\cos\left(\frac{8\sqrt{2}t_r}{l^2}\sqrt{\frac{EJ}{m}}\right),\\
\frac{\partial M_{1-1}^{\max}}{\partial m} &= \frac{\sqrt{2}l^4 q}{512t_r m}\sqrt{\frac{m}{EJ}}\sin\left(\frac{8\sqrt{2}t_r}{l^2}\sqrt{\frac{EJ}{m}}\right)-\frac{l^2 q}{32m}\cos\left(\frac{8\sqrt{2}t_r}{l^2}\sqrt{\frac{EJ}{m}}\right).
\end{aligned} \qquad (25)$$

The standard deviation of the maximum bending moment depending on each variable separately is determined by the formula:

$$\sigma'_q = \left|\frac{\partial M^{\max}_{1-1}}{\partial q}\right|\sigma_q, \sigma'_l = \left|\frac{\partial M^{\max}_{1-1}}{\partial l}\right|\sigma_l,$$
$$\sigma'_{t_r} = \left|\frac{\partial M^{\max}_{1-1}}{\partial t_r}\right|\sigma_{t_r}, \sigma'_{EJ} = \frac{\partial M^{\max}_{1-1}}{\partial EJ}\sigma_{EJ}, \quad (26)$$
$$\sigma'_m = \left|\frac{\partial M^{\max}_{1-1}}{\partial m}\right|\sigma_m.$$

where σ_q, σ_l, σ_{t_r}, σ_{EJ}, σ_m is the standard deviation of the variables, determined from the statistical data of actual measurements or experimental results.

Using the property of independence of variables, we determine the total variance of the maximum bending moment:

$$\sigma^2_{M^{\max}_{1-1}} = \left(\sigma'_q\right)^2 + \left(\sigma'_l\right)^2 + \left(\sigma'_{t_r}\right)^2 + \left(\sigma'_{EJ}\right)^2 + \left(\sigma'_m\right)^2. \quad (27)$$

Similar to the calculation process described above, we can determine the total variance of the ultimate bending moment of reinforced concrete elements during bending. Depending on the location of the longitudinal reinforcement, two cases are distinguished: bending reinforced concrete elements with single and double reinforcement.

Determination of the total variance of the ultimate bending moment of reinforced concrete elements with single reinforcement

The stress diagram of a rectangular reinforced concrete section with single reinforcement is shown in Figure 3.

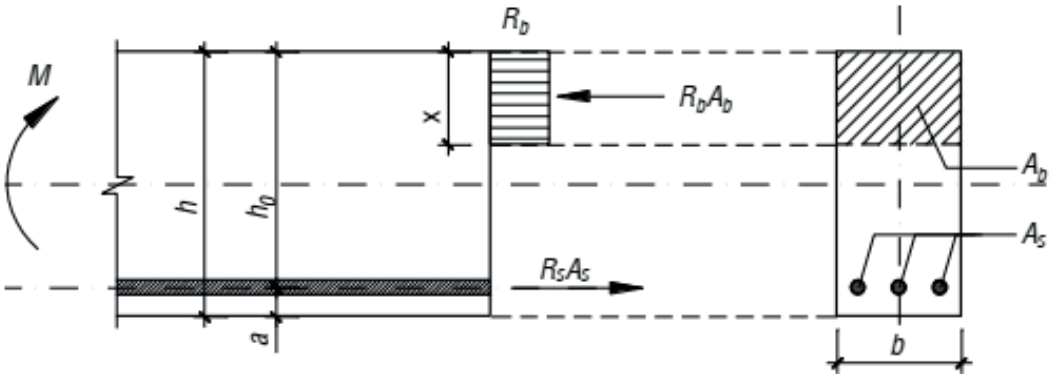


Figure 3. Internal force diagram and stress diagram of a rectangular section with single reinforcement

The calculation of bending concrete elements should be made based on the strength condition:

$$M \le M_{ult} \to M \le R_b bx\left(h_0 - \frac{x}{2}\right). \quad (28)$$

From the condition of equilibrium of the projections of internal forces in the section on the beam axis, it is possible to determine the compression zone height of concrete:

$$R_b bx = R_s A_s \Rightarrow x = \frac{R_s A_s}{R_b b}. \quad (29)$$

From (28) and (29) we can rewrite the expression for the ultimate bending moment:

$$M_{ult} = R_b b\frac{R_s A_s}{R_b b}\left(h_0 - \frac{R_s A_s}{2R_b b}\right) = R_s A_s h_0 - \frac{R_s^2 A_s^2}{2R_b b} \quad (30)$$

Let us determine the partial variance of the ultimate bending moment for each basic variable:

$$\sigma'_{R_b} = \left|\frac{\partial M_{ult}}{\partial R_b}\right|\sigma_{R_b} = \left|\frac{R_s^2 A_s^2}{2R_b^2 b}\right|\sigma_{R_b};$$

$$\sigma'_{R_s} = \left|\frac{\partial M_{ult}}{\partial R_s}\right|\sigma_{R_s} = \left|A_s h_0 - \frac{R_s A_s^2}{R_b b}\right|\sigma_{R_s};$$

$$\sigma'_{A_s} = \left|\frac{\partial M_{ult}}{\partial R_s}\right|\sigma_{A_s} = \left|R_s h_0 - \frac{R_s A_s^2}{R_b b}\right|\sigma_{A_s}; \qquad (31)$$

$$\sigma'_{h_0} = \left|\frac{\partial M_{ult}}{\partial h_0}\right|\sigma_{h_0} = \left|R_s A_s\right|\sigma_{h_0};$$

$$\sigma'_b = \left|\frac{\partial M_{ult}}{\partial b}\right|\sigma_b = \left|\frac{R_s^2 A_s^2}{2R_b b^2}\right|\sigma_b,$$

where σ_{R_b}, σ_{R_s}, σ_{A_s}, σ_{h_0}, σ_b is the standard deviation of the variables, determined from the statistical data of actual measurements or experimental results.

The total variance is equal to the following sum

$$\sigma^2_{M_{ult}} = \left(\sigma'_{R_b}\right)^2 + \left(\sigma'_{R_s}\right)^2 + \left(\sigma'_{A_s}\right)^2 + \left(\sigma'_{h_0}\right)^2 + \left(\sigma'_b\right)^2. \qquad (32)$$

Determination of the total variance of the ultimate bending moment of reinforced concrete elements with double reinforcement

The stress diagram of a reinforced concrete rectangular section with double reinforcement is shown in Figure 4.

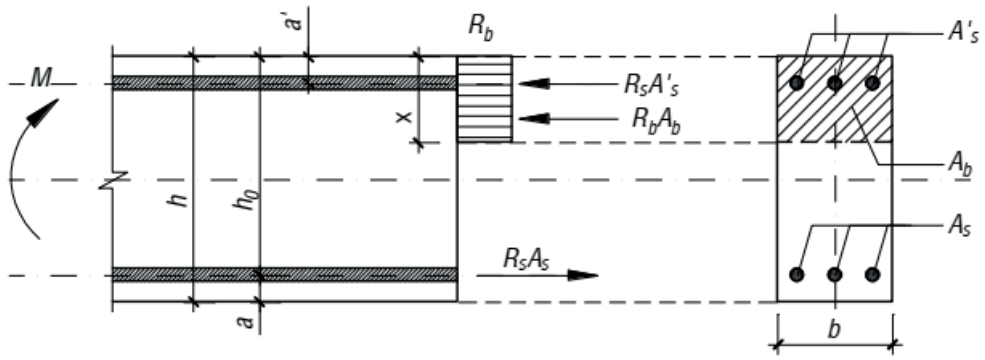


Figure 4. Internal force diagram and stress diagram of a rectangular cross-section with double reinforcement

The calculation of bending concrete elements should be made based on the strength condition:

$$M \le M_{ult} \rightarrow M \le R_b b x\left(h_0 - \frac{x}{2}\right) + R_{sc}A'_s\left(h_0 - a'\right). \qquad (33)$$

From the condition of equilibrium of the projections of internal forces in the section on the beam axis, it is possible to determine the compression zone height of concrete:

$$R_b b x + R_{sc}A'_s = R_s A_s \Rightarrow x = \frac{R_s A_s}{R_b b} - \frac{R_{sc}A'_s}{R_b b} \qquad (34)$$

Substituting the value of x into (33) and performing the transformation, we obtain:

$$M_{ult} = R_b b\frac{R_s A_s}{R_b b}\left(h_0 - \frac{R_s A_s}{2R_b b}\right) = R_s A_s h_0 - \frac{R_s^2 A_s^2}{2R_b b} - \frac{R_{sc}^2 A_s'^2}{2R_b b} + \frac{R_s A_s R_{sc} A'_s}{R_b b} - R_{sc}A'_s a'. \qquad (35)$$

To determine the influence of individual variables on the overall standard deviation of M_{ult}, we determine the partial derivative of M_{ult} with respect to each basis variable. From (35) we have

$$\frac{\partial M_{ult}}{\partial R_s} = A_s h_0 - \frac{R_s A_s^2}{R_b b} + \frac{A_s R_{sc} A'_s}{R_b b};$$

$$\frac{\partial M_{ult}}{\partial A_s} = R_s h_0 - \frac{R_s A_s^2}{R_b b} + \frac{R_s R_{sc} A'_s}{R_b b}; \qquad (36)$$

$$\frac{\partial M_{ult}}{\partial h_0} = R_s A_s;$$
$$\frac{\partial M_{ult}}{\partial R_{sc}} = -\frac{R_{sc} A_s^{'2}}{R_b b} + \frac{R_s A_s A_s^{'}}{R_b b} - A_s^{'} a^{'};$$
$$\frac{\partial M_{ult}}{\partial a^{'}} = -R_{sc} A_s^{'};$$
$$\frac{\partial M_{ult}}{\partial R_b} = \frac{R_s^2 A_s^2}{2R_b^2 b} + \frac{R_{sc}^2 A_s^{'2}}{2R_b^2 b} - \frac{R_s A_s R_{sc} A_s^{'}}{R_b^2 b};$$
$$\frac{\partial M_{ult}}{\partial b} = \frac{R_s^2 A_s^2}{2R_b b^2} + \frac{R_{sc}^2 A_s^{'2}}{2R_b b^2} - \frac{R_s A_s R_{sc} A_s^{'}}{R_b b^2};$$
$$\frac{\partial M_{ult}}{\partial R_{sc}} = -\frac{R_{sc} A_s^{'2}}{R_b b} + \frac{R_s A_s A_s^{'}}{R_b b} - A_s^{'} a^{'};$$
$$\frac{\partial M_{ult}}{\partial A_s^{'}} = -\frac{R_{sc}^2 A_s^{'}}{R_b b} + \frac{R_s A_s R_{sc}}{R_b b} - R_{sc} a^{'};$$

Based on the measurement data and experimental studies, the standard deviation of the parameters R_s, A_s, R_{sc}, A_s', R_b, b, h_0, a' can be determined as σ'_{R_s}, σ'_{A_s}, $\sigma'_{R_{sc}}$, $\sigma'_{A_s^{'}}$, σ'_{R_b}, σ'_b, σ'_{h_0}, $\sigma'_{a'}$.

$$\begin{aligned}
\sigma'_{R_s} &= \left|\frac{\partial M_{ult}}{\partial R_s}\right|\sigma_{R_s}; \sigma'_{A_s} = \left|\frac{\partial M_{ult}}{\partial A_s}\right|\sigma_{A_s};\\
\sigma'_{R_b} &= \left|\frac{\partial M_{ult}}{\partial R_b}\right|\sigma_{R_b}; \sigma'_{R_{sc}} = \left|\frac{\partial M_{ult}}{\partial R_{sc}}\right|\sigma_{R_{sc}};\\
\sigma'_{A'_S} &= \left|\frac{\partial M_{ult}}{\partial A_S^{'}}\right|\sigma_{A'_S}; \sigma'_b = \left|\frac{\partial M_{ult}}{\partial b}\right|\sigma_b;\\
\sigma'_{h_0} &= \left|\frac{\partial M_{ult}}{\partial h_0}\right|\sigma_{h_0}; \sigma'_{a'} = \left|\frac{\partial M_{ult}}{\partial a^{'}}\right|\sigma_{a'}.
\end{aligned} \tag{37}$$

The total variance of the ultimate bending moment of a reinforced concrete section is determined by the formula:

$$\begin{aligned}
\sigma^2_{M_{ult}} &= \left(\sigma'_{R_s}\right)^2 + \left(\sigma'_{A_s}\right)^2 + \left(\sigma'_{R_{sc}}\right)^2 +\\
&+\left(\sigma'_{A'_s}\right)^2 + \left(\sigma'_{R_b}\right)^2 + \left(\sigma'_{h_0}\right)^2 + \left(\sigma'_b\right)^2 + \left(\sigma'_{a'}\right)^2.
\end{aligned} \tag{38}$$

After determining the total variance of M_{ult} and $M_{1-1}^{\max}$, we can determine the reliability index using the following formula:

$$\beta = \frac{\mu_{M_{ult}} - \mu_{M_{1-1}^{\max}}}{\sqrt{\sigma^2_{M_{ult}} + \sigma^2_{M_{1-1}^{\max}}}} \tag{39}$$

By comparing the value of the calculated reliability index with its limit value according to formula (21), we can draw conclusions about the reliability of monolithic reinforced concrete structures in the scenario of sudden removal of load-bearing structural elements.

5. CONCLUSIONS

In this article, a quantitative assessment of the stability of monolithic reinforced concrete frame structures against progressive collapse is presented using a probabilistic approach. The distinctive feature of the proposed approach is that the probabilistic models take into account the basic variable loads and resistances of factors caused by the phenomenon of progressive collapse. Using the first-order reliability method (FORM), the conditional probabilities of progressive collapse and reliability index of the monolithic structural system are obtained under the scenario of removing one of the load-bearing structural elements.

ACKNOWLEDGMENTS

The research described in this paper was financially supported by the Russian Science Foundation grant No. 24-49-10010, https://rscf.ru//project/24-49-10010/.

REFERENCES

1. **Kiakojouri F., De Biagi V., Chiaia B., Sheidaii M.R.** (2020) Progressive collapse of framed building structures: Current

knowledge and future prospects. *Engineering Structures*, no. 206. doi:10.1016/J.ENGSTRUCT.2019.110061.

2. **Ellingwood B.R., Dusenberry D.O.** (2005) Building Design for Abnormal Loads and Progressive Collapse. *Computer-Aided Civil and Infrastructure Engineering*, vol. 3, no. 20, pp. 194–205. doi:10.1111/J.1467-8667.2005.00387.X.
3. **Adam J.M., Parisi F., Sagaseta J., Lu X.** (2018) Research and practice on progressive collapse and robustness of building structures in the 21st century. *Engineering Structures*, no. 173, pp. 122–149. doi:10.1016/j.engstruct.2018.06.082.
4. **Alshaikh I.M.H., Bakar B.H.A., Alwesabi E.A.H., Akil H.M.** (2020) Experimental investigation of the progressive collapse of reinforced concrete structures: An overview. *Structures*, no. 25, pp. 881–900. doi:10.1016/J.ISTRUC.2020.03.018.
5. **Wang Y., Zhang B., Gu X.L., Lin F.** (2022) Experimental and numerical investigation on progressive collapse resistance of RC frame structures considering transverse beam and slab effects. *Journal of Building Engineering*, no. 47. doi:10.1016/J.JOBE.2021.103908.
6. **Azim I., Yang J., Farjad Iqbal M., Faisal Javed M., Nazar S., Wang F., Liu Q. feng.** (2020) Semi-analytical model for compressive arch action capacity of RC frame structures. *Structures*, no. 27, pp. 1231–1245. doi:10.1016/J.ISTRUC.2020.06.011.
7. **Kang S.B., Wang S., Gao S.** (2020) Analytical study on one-way reinforced concrete beam-slab sub-structures under compressive arch action and catenary action. *Engineering Structures*, no. 206. doi:10.1016/J.ENGSTRUCT.2019.110032.
8. **Pham A.T., Tan K.H.** (2018) Static and Dynamic Responses of Reinforced Concrete Structures under Sudden Column Removal Scenario Subjected to Distributed Loading. *Journal of Structural Engineering*, vol. 1, no. 145. doi:10.1061/(ASCE)ST.1943-541X.0002214.
9. **Kai Q., Li B.** (2012) Dynamic performance of RC beam-column substructures under the scenario of the loss of a corner column—Experimental results. *Engineering Structures*, no. 42, pp. 154–167. doi:10.1016/J.ENGSTRUCT.2012.04.016.
10. **Wang H., Li S., Zhai C.** (2023) Experimental and numerical investigation on progressive collapse of self-centering precast concrete frame with infill walls. *Journal of Building Engineering*, no. 78. doi:10.1016/J.JOBE.2023.107472.
11. **Amiri S., Saffari H., Mashhadi J.** (2018) Assessment of dynamic increase factor for progressive collapse analysis of RC structures. *Engineering Failure Analysis*, no. 84, pp. 300–310. doi:10.1016/J.ENGFAILANAL.2017.11.011.
12. **Liu M., Pirmoz A.** (2016) Energy-based pulldown analysis for assessing the progressive collapse potential of steel frame buildings. *Engineering Structures*. no. 123, pp. 372–378. doi:10.1016/J.ENGSTRUCT.2016.05.020.
13. **Weng J., Lee C.K., Tan K.H.** (2020) Simplified Dynamic Assessment for Reinforced-Concrete Structures Subject to Column Removal Scenarios. *Journal of Structural Engineering*, vol. 12, no. 146. doi:10.1061/(ASCE)ST.1943-541X.0002833.
14. **Yu J., Guo Y.** (2016) Nonlinear SDOF model for dynamic response of structures under progressive collapse. *Journal of Engineering Mechanics*, vol. 142, no. 3.
15. **Yu J., Yin C., Guo Y.** (2017) Nonlinear SDOF Model for Progressive Collapse Responses of Structures with Consideration of Viscous Damping. *Journal of Engineering Mechanics*, vol. 9, no. 143. C. 04017108. doi:10.1061/(ASCE)EM.1943-7889.0001339.
16. **Ellingwood B.R.** (2006) Mitigating Risk from Abnormal Loads and Progressive Collapse. *Journal of Performance of Constructed Facilities*, vol. 4, no. 20, pp. 315–323.

doi:10.1061/(ASCE)0887-3828(2006)20:4(315).
17. **Ellingwood B.R.** (2007) Strategies for mitigating risk to buildings from abnormal load events. *International Journal of Risk Assessment and Management*, vol. 6, no. 7, pp. 828–845. doi:10.1504/IJRAM.2007.014662.
18. **Izzuddin B.A., Pereira M.F., Kuhlmann U., Rölle L., Vrouwenvelder T., Leira B.J.** (2012) Application of Probabilistic Robustness Framework: Risk Assessment of Multi-Storey Buildings under Extreme Loading. *Structural Engineering International*, vol. 1, no. 22, pp. 79–85. doi:10.2749/101686612X13216060213518.
19. **Xu G., Ellingwood B.R.** (2011) Probabilistic Robustness Assessment of Pre-Northridge Steel Moment Resisting Frames. *Journal of Structural Engineering*, vol. 9, no. 137, pp. 925–934. doi:10.1061/(ASCE)ST.1943-541X.0000403.
20. **Brunesi E., Parisi F.** (2017) Progressive collapse fragility models of European reinforced concrete framed buildings based on pushdown analysis. *Engineering Structures*, no. 152, pp. 579–596. doi:10.1016/J.ENGSTRUCT.2017.09.043.
21. **Chen C.H., Zhu Y.F., Yao Y., Huang Y., Long X.** (2016) An evaluation method to predict progressive collapse resistance of steel frame structures. *Journal of Constructional Steel Research*, no. 122, pp. 238–250. doi:10.1016/J.JCSR.2016.03.024.
22. **Beck A.T., Ribeiro L. da R., Valdebenito M.** (2020) Risk-based cost-benefit analysis of frame structures considering progressive collapse under column removal scenarios. *Engineering Structures,* no. 225. doi:10.1016/J.ENGSTRUCT.2020.111295.
23. **Tuyen V.N., Ivanovich K.V., Vitalyevna F.N.** (2024) Dynamic response model of reinforced concrete building frame under column removal scenario. *Structures*, vol. 63. doi:10.1016/J.ISTRUC.2024.106356.

СПИСОК ЛИТЕРАТУРЫ

1. **Kiakojouri F., De Biagi V., Chiaia B., Sheidaii M.R.** Progressive collapse of framed building structures: Current knowledge and future prospects // Engineering Structures. 2020. № 206. DOI:10.1016/J.ENGSTRUCT.2019.110061.
2. **Ellingwood B.R., Dusenberry D.O.** Building Design for Abnormal Loads and Progressive Collapse // Computer-Aided Civil and Infrastructure Engineering. 2005. № 3(20). С. 194–205. DOI:10.1111/J.1467-8667.2005.00387.X.
3. **Adam J.M., Parisi F., Sagaseta J., Lu X.** Research and practice on progressive collapse and robustness of building structures in the 21st century // Engineering Structures. 2018. № 173. С. 122–149. DOI:10.1016/j.engstruct.2018.06.082.
4. **Alshaikh I.M.H., Bakar B.H.A., Alwesabi E.A.H., Akil H.M.** Experimental investigation of the progressive collapse of reinforced concrete structures: An overview // Structures. 2020. № 25. С. 881–900. DOI:10.1016/J.ISTRUC.2020.03.018.
5. **Wang Y., Zhang B., Gu X.L., Lin F.** Experimental and numerical investigation on progressive collapse resistance of RC frame structures considering transverse beam and slab effects // Journal of Building Engineering. 2022. № 47. DOI:10.1016/J.JOBE.2021.103908.
6. **Azim I., Yang J., Farjad Iqbal M., Faisal Javed M., Nazar S., Wang F., Liu Q. feng.** Semi-analytical model for compressive arch action capacity of RC frame structures // Structures. 2020. № 27. С. 1231–1245. DOI:10.1016/J.ISTRUC.2020.06.011.
7. **Kang S.B., Wang S., Gao S.** Analytical study on one-way reinforced concrete beam-slab sub-structures under compressive arch action and catenary action // Engineering Structures. 2020. № 206. DOI:10.1016/J.ENGSTRUCT.2019.110032.
8. **Pham A.T., Tan K.H.** Static and Dynamic Responses of Reinforced Concrete Struc-

tures under Sudden Column Removal Scenario Subjected to Distributed Loading // Journal of Structural Engineering. 2018. № 1(145). DOI:10.1061/(ASCE)ST.1943-541X.0002214.
9. **Kai Q., Li B.** Dynamic performance of RC beam-column substructures under the scenario of the loss of a corner column—Experimental results // Engineering Structures. 2012. № 42. C. 154–167. DOI:10.1016/J.ENGSTRUCT.2012.04.016.
10. **Wang H., Li S., Zhai C.** Experimental and numerical investigation on progressive collapse of self-centering precast concrete frame with infill walls // Journal of Building Engineering. 2023. № 78. C. 107472. DOI:10.1016/J.JOBE.2023.107472.
11. **Amiri S., Saffari H., Mashhadi J.** Assessment of dynamic increase factor for progressive collapse analysis of RC structures // Engineering Failure Analysis. 2018. № 84. C. 300–310. DOI:10.1016/J.ENGFAILANAL.2017.11.011.
12. **Liu M., Pirmoz A.** Energy-based pulldown analysis for assessing the progressive collapse potential of steel frame buildings // Engineering Structures. 2016. № 123. C. 372–378. DOI:10.1016/J.ENGSTRUCT.2016.05.020.
13. **Weng J., Lee C.K., Tan K.H.** Simplified Dynamic Assessment for Reinforced-Concrete Structures Subject to Column Removal Scenarios // Journal of Structural Engineering. 2020. № 12(146). DOI:10.1061/(ASCE)ST.1943-541X.0002833.
14. **Yu J., Guo Y.** Nonlinear SDOF model for dynamic response of structures under progressive collapse // Journal of Engineering Mechanics. 2016. № 142(3).
15. **Yu J., Yin C., Guo Y.** Nonlinear SDOF Model for Progressive Collapse Responses of Structures with Consideration of Viscous Damping // Journal of Engineering Mechanics. 2017. № 9(143). DOI:10.1061/(ASCE)EM.1943-7889.0001339.
16. **Ellingwood B.R.** Mitigating Risk from Abnormal Loads and Progressive Collapse // Journal of Performance of Constructed Facilities. 2006. № 4(20). C. 315–323. DOI:10.1061/(ASCE)0887-3828(2006)20:4(315).
17. **Ellingwood B.R.** Strategies for mitigating risk to buildings from abnormal load events // International Journal of Risk Assessment and Management. 2007. № 6–7(7). C. 828–845. DOI:10.1504/IJRAM.2007.014662.
18. **Izzuddin B.A., Pereira M.F., Kuhlmann U., Rölle L., Vrouwenvelder T., Leira B.J.** Application of Probabilistic Robustness Framework: Risk Assessment of Multi-Storey Buildings under Extreme Loading // Structural Engineering International. 2012. № 1(22). C. 79–85. DOI:10.2749/101686612X13216060213518.
19. **Xu G., Ellingwood B.R.** Probabilistic Robustness Assessment of Pre-Northridge Steel Moment Resisting Frames // Journal of Structural Engineering. 2011. № 9(137). C. 925–934. DOI:10.1061/(ASCE)ST.1943-541X.0000403.
20. **Brunesi E., Parisi F.** Progressive collapse fragility models of European reinforced concrete framed buildings based on push-down analysis // Engineering Structures. 2017. (152). C. 579–596. DOI:10.1016/J.ENGSTRUCT.2017.09.043.
21. **Chen C.H., Zhu Y.F., Yao Y., Huang Y., Long X.** An evaluation method to predict progressive collapse resistance of steel frame structures // Journal of Constructional Steel Research. 2016. № 122. C. 238–250. DOI:10.1016/J.JCSR.2016.03.024.
22. **Beck A.T., Ribeiro L. da R., Valdebenito M.** Risk-based cost-benefit analysis of frame structures considering progressive collapse under column removal scenarios // Engineering Structures. 2020. № 225. DOI:10.1016/J.ENGSTRUCT.2020.111295.
23. **Tuyen V.N., Ivanovich K.V., Vitalyevna F.N.** Dynamic response model of reinforced concrete building frame under column removal scenario // Structures, 2024, № 63.

Vu Ngoc Tuyen — Candidate of Technical Sciences, Associate Professor, Department of Fundamental Education, National Research Moscow State University of Civil Engineering, 26, Yaroslavskoe Shosse, Moscow, 129337, Russia, WuNgokTuen@gic.mgsu.ru, +7 (495)-287-49-14*1751

Fedorova Natalia Vitalievna - Doctor of Technical Sciences, Professor, Head of the Department of Industrial and Civil Engineering, National Research Moscow State University of Civil Engineering, 26, Yaroslavskoye Shosse, Moscow, 129337, Russia, FedorovaNV@gic.mgsu.ru, +7(495) 583-79-04

Duong Thanh Quy, PhD, Researcher, Vietnam Institute of Building Materials - Ministry of Construction of Vietnam, N235, Nguyen Trai, Thanh Xuan, Hanoi, 180000, Vietnam. quiduongthanh@gmail.com, +84 98 615 00 15

Ву Нгок Туен — кандидат технических наук, доцент кафедры Фундаментального образования, Федеральное государственное бюджетное образовательное учреждение высшего образования «Национальный исследовательский Московский государственный строительный университет» (НИУ МГСУ), д. 26, Ярославское шоссе, г. Москва, 129337, Россия, WuNgokTuen@gic.mgsu.ru, +7 (495)-287-49-14*1751

Федорова Наталия Витальевна — доктор технических наук, профессор заведующий кафедрой Промышленного и гражданского строительства, Федеральное государственное бюджетное образовательное учреждение высшего образования «Национальный исследовательский Московский государственный строительный университет» (НИУ МГСУ), д. 26, Ярославское шоссе, г. Москва, 129337, Россия, FedorovaNV@gic.mgsu.ru, +7(495) 583-79-04

Зыонг Тхань Куй, кандидат технических наук, научный сотрудник, Вьетнамский институт строительных материалов - министерство строительства Вьетнама, д.235, Нгуенчай, ТханьСуан, г. Ханой, 180000, Вьетнам. quiduongthanh@gmail.com., +84 98 615 00 15

DOI:10.22337/2587-9618-2025-21-2-30-42

NONLINEAR DYNAMIC ANALYSIS OF REINFORCED CONCRETE LARGE-PANEL BUILDING

Zaurbek K. Abaev [1], Azamat D. Valiev [2]

[1] Vladikavkaz Scientific Centre of the Russian Academy of Sciences, Vladikavkaz, RUSSIA
[2] North Caucasian Institute of Mining and Metallurgy (State Technological University), Vladikavkaz, RUSSIA

Abstract: A nonlinear dynamic analysis of large-panel reinforced concrete building (LPB) using LIRA-SAPR software is presented. LPBs, which became prevalent in the mid-20th century, have generally demonstrated good seismic performance during past earthquakes. However, the connection regions and specific structural characteristics still present challenges in accurately modeling and predicting their behavior under seismic loading. Conventional linear models often inadequately represent the complex nonlinear behavior such as strength and stiffness degradation and connection failures inherent in LPBs, highlighting the need for more sophisticated analytical approaches. A detailed nonlinear analysis methodology was applied to a full-scale reinforced concrete precast LPB, investigating various parameters including material properties, damping variation, and their effects on interstory drift ratios and displacement patterns. The analysis revealed significant differences in seismic response, particularly for lower concrete grades, emphasizing the critical role of accurate material characterization. Displacement and acceleration distributions exhibited directional dependencies, aligning with results from existing literature and full-scale testing. Despite the strengths of the LIRA-SAPR software, certain limitations were identified, such as the inability to modify the standard hysteresis model, which lowers the accuracy of the simulation of strength and stiffness degradation. The findings suggest the necessity of modifying existing building codes to include specific acceptance criteria and updated analysis procedures tailored to the unique behaviors of LPBs. Such modifications are essential for developing effective tools for seismic performance evaluation and enhancing the resilience of these structures.

Keywords: Large-Panel Buildings, Nonlinear Dynamic Analysis, Seismic Performance Evaluation

НЕЛИНЕЙНЫЙ ДИНАМИЧЕСКИЙ АНАЛИЗ КРУПНОПАНЕЛЬНОГО ЖЕЛЕЗОБЕТОННОГО ЗДАНИЯ

З.К. Абаев [1], А.Д. Валиев [2]

[1] Владикавказский научный центр Российской академии наук, г. Владикавказ, РОССИЯ
[2] Северо-Кавказский горно-металлургический институт (государственный технологический университет), г. Владикавказ, РОССИЯ

Аннотация: Представлен нелинейный динамический анализ крупнопанельного железобетонного здания (КПЗ) с использованием программного комплекса ЛИРА-САПР. Крупнопанельные здания, получившие широкое распространение в середине прошлого века, в целом продемонстрировали хорошую сейсмостойкость во время прошедших землетрясений. Однако соединения панелей и специфические конструктивные особенности по-прежнему создают проблемы для точного моделирования и прогнозирования их поведения при сейсмических воздействиях. Обычные линейные модели часто неадекватно отражают сложное нелинейное поведение, такое как деградация свойств и разрушение соединений, присущее КПЗ, что подчеркивает необходимость применения более сложных аналитических подходов. Детальная методология нелинейного анализа была применена к железобетонному КПЗ с учетом различных факторов, включая свойства материалов, вариацию демпфирования и их влияние на значения междуэтажных перекосов и характер деформации. Анализ выявил значительные различия в сейсмической реакции, особенно для более низких марок бетона, что подчеркивает критическую роль точного определения характеристик материала. Распределения перемещений и ускорений демонстрируют зависимость от направления воздействия, что согласуется с результатами, представленными в литературе и натурными испытаниями. Несмотря на сильные стороны программного

обеспечения ЛИРА-САПР, были выявлены некоторые ограничения, такие как невозможность модификации модели гистерезиса, что ограничивает точное моделирование деградации прочности и жесткости, характерной для данного типа сооружений. Полученные результаты свидетельствуют о необходимости модификации существующих строительных норм и правил для включения в них специальных критериев оценки сейсмостойкости и улучшенных аналитических процедур, учитывающих уникальные особенности поведения КПЗ. Такие изменения важны для разработки эффективных инструментов прогнозирования сейсмической повреждаемости данных сооружений.

Ключевые слова: крупнопанельные здания, нелинейный динамический анализ, оценка сейсмостойкости

INTRODUCTION

Large Panel Buildings (LPBs) have been a significant advancement in construction technology since their inception in the mid-20th century [1,2]. Originally developed to meet the urgent post-war housing demands, LPBs revolutionized the construction industry with their modular approach, enabling rapid assembly and cost-effective production [3,4]. The precast concrete panels used in LPBs offered numerous advantages, including enhanced durability, improved thermal performance, and consistent quality control. Over the decades, LPBs have evolved to incorporate advancements in materials science and construction techniques, solidifying their place in both residential and commercial architecture.

Despite their widespread use, LPBs have faced scrutiny regarding their seismic performance, particularly in regions prone to earthquakes. The connection regions and large precast panels characteristic of LPBs pose unique challenges under earthquake loading [5,6]. Historical seismic events have demonstrated varying degrees of structural vulnerability, highlighting the need for a deeper understanding and enhancement of LPB seismic resilience [7,8]. Studies have shown that the performance of LPBs during earthquakes is influenced by factors such as panel connections, overall structural configuration, and the quality of construction materials [9,10].

The analytic study of LPB seismic performance has become a crucial area of research, aiming to predict and mitigate potential failures. Advanced analytical methods, including nonlinear dynamic analysis, have been employed to simulate the behavior of LPBs under seismic loads [11,12]. These studies provide insights into the stress distribution, deformation patterns, and potential failure modes of LPB structures.

To accurately assess and improve the seismic performance of LPBs, the development of relevant and reliable analytical models is essential. These models must account for the complex interactions between panels, connections, and the overall structural system. They should incorporate nonlinear material properties, dynamic loading conditions, and potential degradation. The use of sophisticated software tools, such as LIRA-SAPR [13], enables the creation of detailed and robust models that can simulate real-world seismic scenarios. These models serve as a foundation for developing effective retrofitting strategies and informing building codes and standards.

This study aims to conduct a comprehensive nonlinear dynamic analysis of a reinforced concrete precast large-panel building using the LIRA-SAPR software. By simulating the seismic response of the LPB structure, this research seeks to identify critical stress points, deformation behaviors, and potential failure mechanisms. The findings will contribute to the ongoing efforts to develop robust tools for seismic performance evaluation, such as fragility curves, and calls for modifications to existing building codes [14].

METHODS

The object of the study is a typical residential apartment building of large-panel type series 1-092, located in Vladikavkaz city (Figure 1): 9-

story 1-section building. The story height is 3 meters. External nonbearing walls are 300 mm thick panels, internal bearing walls are 160 mm thick single-layer panels, partitions are 80 mm thick. Floor panels 160 mm thick. Concrete grade – B15 (f'_c = 8.5 MPa, E_c = 24000 MPa), reinforcement – A-I (R_s = 240 MPa, E_s = 200000 MPa).

A visual inspection of the building revealed several characteristic defects, including partial absence of joint filling, corrosion of joint metal, and poor or complete lack of joint filling (as shown in Figure 3). To account for these defects within the limitations of the software, a concrete grade of B7.5 (f'_c = 4.5 MPa, E_c = 16000 MPa) was also employed in the analyses for the joint regions.

The horizontal and vertical panel joints are shown in Figure 2.

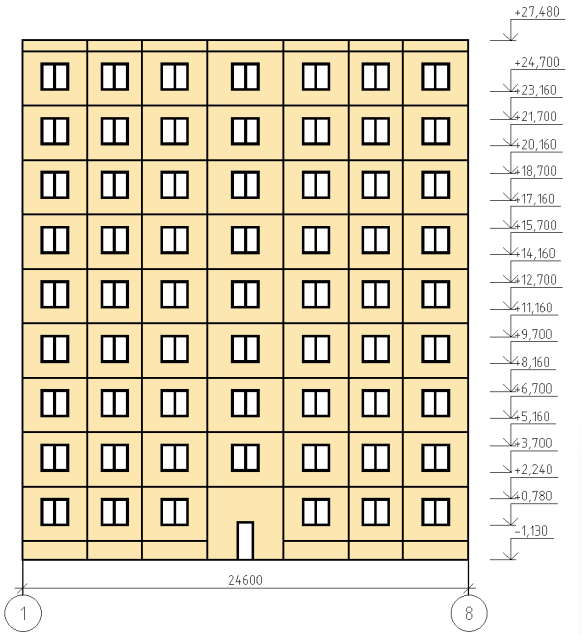


Figure 1. Object of study

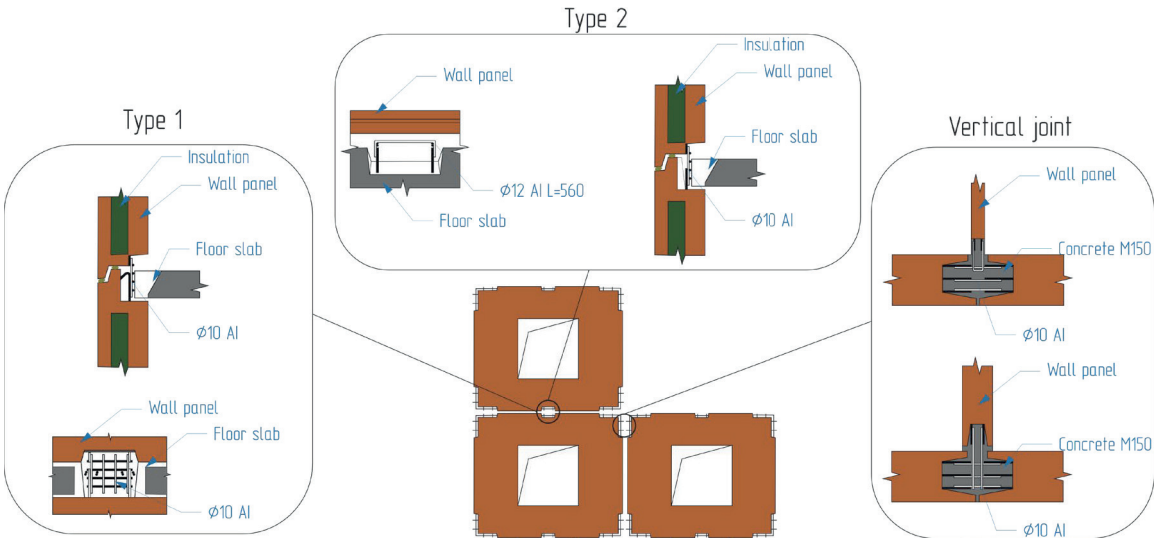


Figure 2. Details of the building



Figure 3. Defects of the building

Modeling assumptions

In the modeling of large-panel precast structures, it is conventional to assume that the solid panels exhibit linear elastic behavior. This assumption is justified by the anticipated function of these elements within the structure's overall seismic response. Typically, wall panels are considered to behave in an elastic-brittle manner with respect to in-plane normal forces. Any potential nonlinear or inelastic behavior is often deemed negligible in the panels themselves and is concentrated in the connection regions, where it can be more effectively modeled and analyzed [11].

The following assumptions are made for the joint element [15]:

– all points of the horizontal section remain in one plane after the force is applied (plane sections remain plane);

– for the tensile zone of the section the tensile strength of concrete is not taken into account;

– normal compressive stresses distribution along the section is linear or bilinear.

LIRA-SAPR implementation

The finite element method software LIRA-SAPR is used for numerical analysis.

Nonlinear behavior of the connection region is modeled by a combination of two finite elements (FE) (Figure 4) [16]:

– Shell Element (FE 259) representing stress distribution in the connection region,

– 2-mode link element (FE 255) for modeling shear keys.

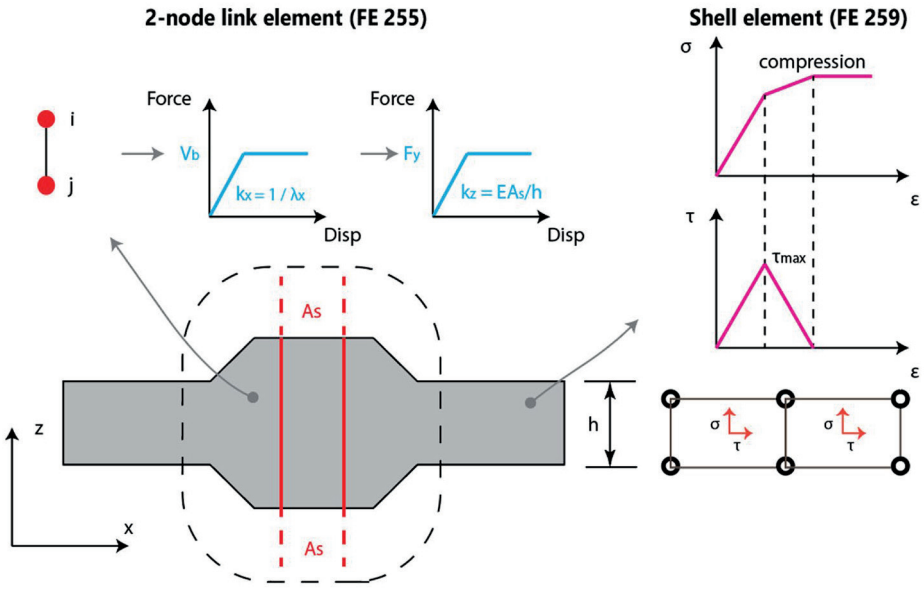


Figure 4. Finite element implementation of the connection region

The precast walls and floor panels are modeled with elastic shell element FE 44.

2-mode link element (FE 255) parameters

According to section B4 of SP 335.1325800.2017 [17,18], the design shear strength V_{kb} of one shear key of the is taken equal to the smallest of the force values $V_{sh,b}$; $V_{c,b}$; $V_{crc,b}$, corresponding to the destruction of the shear key, respectively, from shear, crushing and shear cracks opening:

$$V_{sh,b} = 1.5 R_{bt} A_{sh} \quad (1)$$

$$V_c = R_{b,loc} A_c \quad (2)$$

$$V_{crc,b} = 0.7 R_{bt} A_j \quad (3)$$

where R_{bt} is design tensile strength of grouting concrete; $R_{b,loc}$ is crushing strength, taken equal $1.5R_b$ – for single keys, $0.8R_b$ – for multikey connections; A_{sh} is shear area; A_c is crushing area; A_j – cross-sectional area of the connection tributary to each shear key:

$$A_j = s_{bt} b_{mon} \tag{4}$$

where s_{bt} is distance between shear keys; b_{mon} is wall thickness of the grouting area.

Stiffness along *Z*-axis is represented by bilinear elastoplastic force-displacement relationship, elastic stiffness is determined by:

$$k_z = EA_s / h \tag{5}$$

where E is elastic modulus of the rebar; A_s is rebar cross-sectional area; h is rebar length (equal to the joint height).

Stiffness along *X*-axis is represented by bilinear elastoplastic force-displacement relationship, elastic pliability is determined by:

$$\lambda_x^1 = \frac{l_{loc}\left(\frac{1}{E_{b,\omega}} + \frac{1}{E_{b,mon}}\right)}{A_{loc}} \tag{7}$$

where A_{loc} is loaded area; l_{loc} is shear key height (recommended l_{loc} = 250 mm); E_b is elastic modulus of concrete precast element; $E_{b,mon}$ is elastic modulus of grouting concrete.

The pliability after shear cracks occurring (exceeding the shear force $V_{crc,b}$):

$$\lambda_x^2 = \frac{6}{d_s n_s}\left(\frac{1}{E_{b,\omega}} + \frac{1}{E_{b,mon}}\right) \tag{8}$$

where d_s is connection rebars diameter; n_s is number of the connection rebars.

Shell Element (FE 259) parameters [19,20]

During short-term compression for a mortar with a compressive strength of 1 MPa or more, with a joint thickness of 10–20 mm, pliability coefficient of the mortar bed joint λ_m, mm^3/N:

$$\text{for } \sigma_m \le 1.15R_m^{2/3} \quad \lambda_m = 1.5\cdot 10^{-3} R_m^{-2/3} t_m \tag{9}$$

$$\text{for } 2R_m^{2/3} \ge 1.15R_m^{2/3} \quad \lambda_m = 5\cdot 10^{-3} R_m^{-2/3} t_m \tag{10}$$

Pliability coefficient of the joint:

$$\lambda_{c,pl} = (\lambda_m + \lambda_m^{'} + \frac{h_{sl}}{E_b})\frac{B_{pl}}{B_{pl} - h_v} \tag{11}$$

where $\lambda_m^{'}$ and λ_m are upper and lower mortar bed joint pliability coefficients; h_{sl} is floor panel height; B_{pl} is contact areas width; h_v is joint width between floor panels.

Strain:

$$\varepsilon = \frac{\lambda_i \sigma_i}{h_v} \tag{12}$$

Stresses:

$$\sigma_m^1 = 1.15R_m^{2/3} \tag{13}$$

$$\sigma_m^2 = 2R_m^{2/3} \tag{14}$$

$$\sigma_m^y = 1.01\sigma_m^2 \tag{15}$$

To reduce the computational time the optimal finite element mesh size was determined by considering three mesh configurations: 0.1 m, 0.2 m, and 0.4 m. In the case of panels with openings, which complicate the computation by inducing stress concentrations – these panels were replaced with solid panels of reduced stiffness. The reduction factor was calculated as the ratio of the wall area with openings to the wall area without the openings. As a result, the finite element mesh of the wall panels was set to 0.4 × 0.4 m, and the finite element mesh of the connections was set to 0.4 × 0.1 m.

The resulting finite element model in LIRA-SAPR is presented in the Figure 5.

Self-weight and live load according to Russian codes were applied.

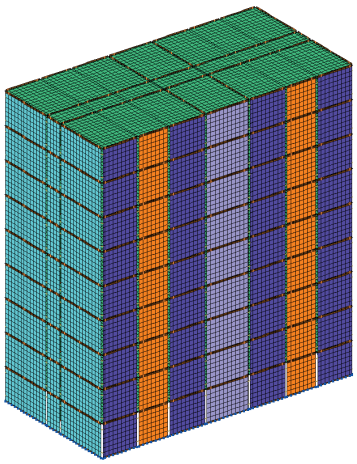


Figure 5. Finite element model of the building

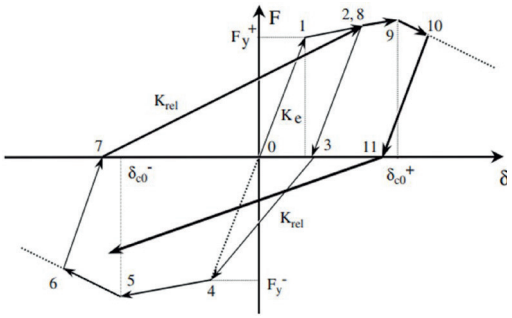


Figure 6. Basic rules for peak-oriented hysteretic model

The analysis was performed using an explicit integration of the equation of motion [21]:

$$M\ddot{x} + C\dot{x} + Kx = p(t) \qquad (21)$$

where $x = u$ is the unknown vector of nodal displacements; $\dot{x} = v$ is the nodal velocity vector; $\ddot{x} = a$ is the nodal acceleration vector; M is the mass matrix; C is the damping matrix; K is the stiffness matrix; $p(t)$ is the vector of applied loads.

Analysis parameters:

– Newmark-beta method (average constant acceleration with $\gamma = 0.5$ and $\beta = 0{,}25$) is used for direct integration of the equations of motion.

– Modified Newton-Raphson method is used for solving nonlinear equations at each time step.

– The results from the natural dynamic testing of the full-scale LPB reveal considerable temporal variations in the structure's damping characteristics [15]. To examine the sensitivity of the structural response, damping ratios ξ of 2%, 3%, 4%, and 5% were employed in the analyses.

– LIRA-SAPR's standard peak-oriented hysteretic model (Figure 6) is applied. The detail description of the employed model is presented in [22].

It is important to note that in the LIRA-SAPR software, the parameters of the standard hysteresis models cannot be modified or changed. While this limitation may be adequate for typical structures, it represents a significant shortcoming when analyzing precast panel structures, which exhibit specific strength and stiffness degradation behaviors. The inability to customize hysteresis rules restricts the accuracy of the simulation, particularly for structures with unique dynamic characteristics. Future releases of the software should address this issue by incorporating flexible hysteresis options, enabling more precise modeling of the complex behaviors inherent in precast panel systems.

– Total integration time is 20 sec.

– Integration step is 0.01 sec.

The model is subjected to two component of ground motion of the 1988 Spitak, Armenia earthquake (Figure 7–8). An earthquake registering a surface wave magnitude of 6.8 and a maximum MSK-64 intensity of X (Devastating) hit the northern part of the Armenian Republic of the Soviet Union on 7 December 1988, resulting in thousands of deaths and injuries [23].

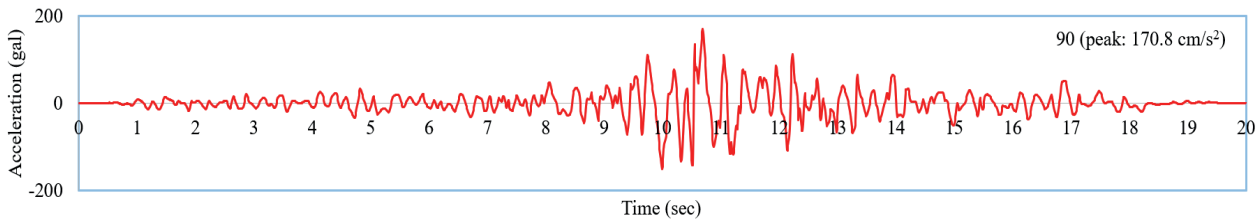


Figure 7. Ground acceleration record (Spitak, Armenia, 1988, Gukasian, component 000)

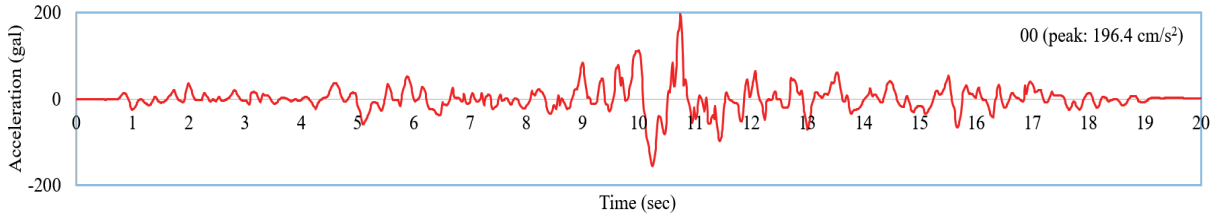


Figure 8. Ground acceleration record (Spitak, Armenia, 1988, Gukasian, component 090)

RESULTS AND DISCUSSION

The natural period of the structure is 0.37 s in Y-direction.

The maximum displacements, shown in Figure 9, occur in the Y-direction for both materials: 24 mm for B7.5 and 20 mm for B15, compared to 7.31 and 4.59 mm in the X direction, respectively. Figure 10 shows the distribution of the maximum acceleration, with peaks of 3.1 m/s² in the X direction and 2.44 m/s² in the Y direction at the top story.

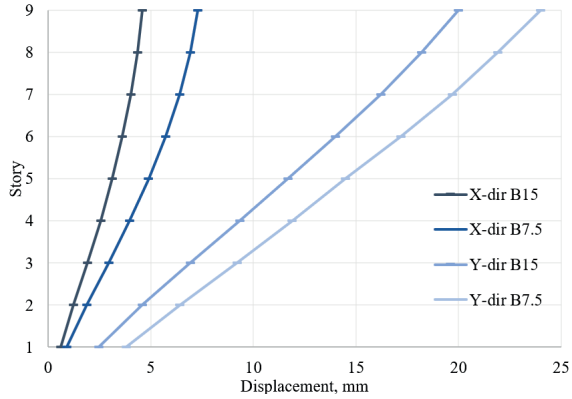


Figure 9. Maximum displacements (ξ = 5%)

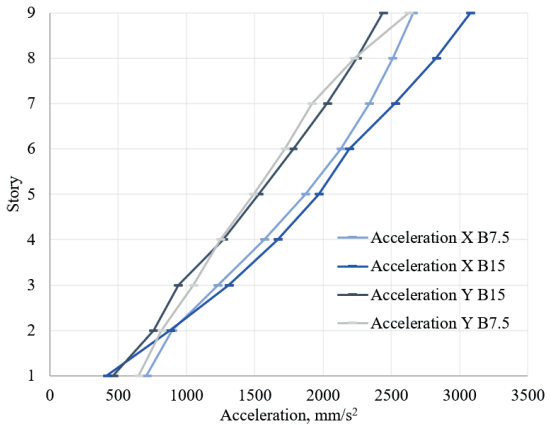


Figure 10. Maximum accelerations (ξ = 5%)

These results are consistent with findings reported in the literature and with the outcomes of natural testing conducted on full-scale buildings [15,24].

The corresponding graph of the interstory drift ratio (Figure 11) exhibits a similar pattern across different damping values, with the maximum drift occurring at the first story. However, the differences in these values are significant, with variations up to 25%. This notable discrepancy underscores the importance of accurately determining the appropriate damping ratio, which necessitates thorough investigation in future research.

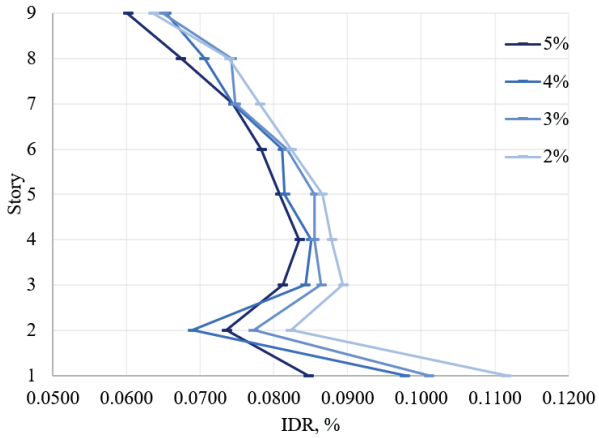


Figure 11. IDR for different damping ratios

The interstory drift ratio (IDR), which measures the relative horizontal displacement between adjacent floors of a building, is a critical indicator of structural damage [25]. The IDR for different concrete grades is illustrated in Figure 12. The analysis reveals that the seismic response for the lower concrete grade is significantly higher, with an IDR of 0.132 % compared to 0.085 % for the higher grade. This notable difference underscores the critical

importance of meticulously investigating the material parameters of buildings in future research. Despite the disparity in IDR values, the overall response in both cases remains relatively low when compared to the commonly accepted ranges for performance-based design as specified by building codes [26]. However, it is important to note that there are currently no established acceptance criteria specifically tailored for LPBs, highlighting the urgent need for the development of such criteria. These should account for the unique behavior and fragility characteristics of this structural type.

The findings presented in Figure 12 are consistent with post-earthquake investigations of LPBs following the Spitak earthquake, where none of these buildings were destroyed or suffered significant damage [27]. This correlation further emphasizes the necessity for a comprehensive framework to evaluate and enhance the seismic resilience of LPBs

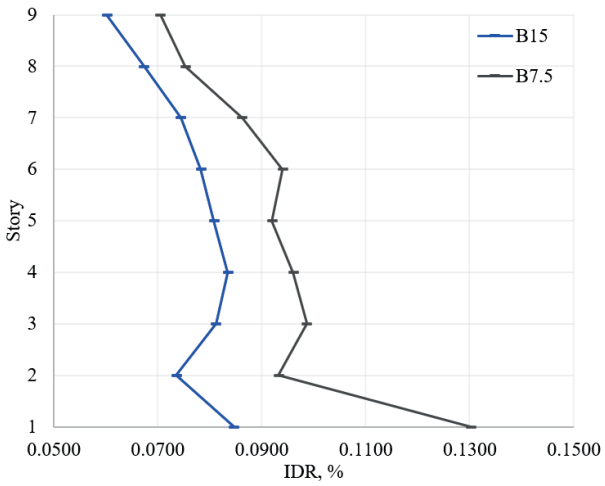


Figure 12. IDR for B7.5 and B15 concrete grades

One effective approach for such an evaluation is the development of fragility curves, which depict the probability of reaching various performance levels at different ground motion intensity levels [28]. These curves are crucial in quantifying the seismic vulnerability of structures, as they provide a statistical relationship between seismic demand and structural performance. Fragility curves are typically developed through a statistical analysis of the results obtained from Incremental Dynamic Analysis (IDA) [29].

In IDA, the structure is subjected to a suite of ground motions that are incrementally scaled in intensity, allowing for a detailed assessment of its nonlinear response and failure modes. An example of IDA for a selected ground motion scaled for 6 levels of intensity (from 0.1 g to 0.6 g) is presented in Figure 13. This figure illustrates how the structural response evolves with increasing ground motion intensity, highlighting critical thresholds where performance levels transition from minor damage to potential collapse.

It is important to note that as the intensity level increases, the dispersion in the response also becomes more pronounced. These factors contribute to longer computational time and may introduce inaccuracies if not carefully managed. Therefore, it is imperative that the analysis parameters of the IDA, including mesh size, time step, and convergence criteria, are meticulously calibrated beforehand to ensure reliable results.

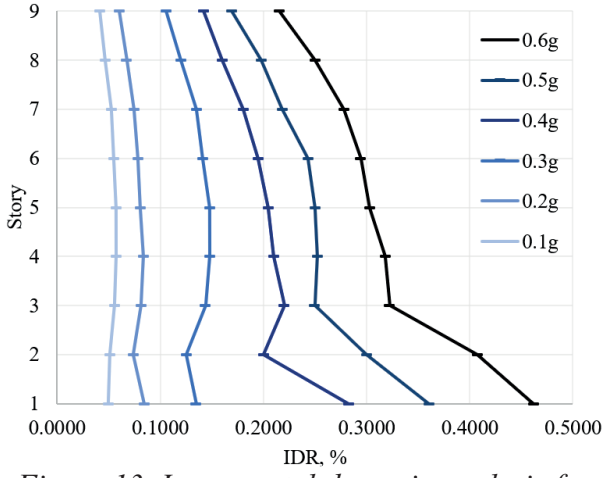


Figure 13. Incremental dynamic analysis for selected ground motion (B15, ξ = 5%)

To successfully implement these findings and develop robust tools for seismic performance evaluation, targeted modifications to existing building codes are necessary [14,30]. These modifications should include the establishment of specific acceptance criteria for large-panel

buildings (LPBs) that account for their unique structural behavior and fragility under seismic loading.

CONCLUSION

This study has undertaken a detailed nonlinear dynamic analysis of large-panel buildings (LPBs) using the LIRA-SAPR software, focusing on accurately modeling the seismic response of precast concrete structures. The methodology developed in this research allowed for the simulation of complex behavior inherent in LPBs, particularly under seismic loading. The analysis revealed key insights into the seismic performance of these structures, with significant differences observed in the interstory drift ratios and displacement patterns depending on the material properties.

One of the critical findings was the considerable variation in seismic response based on different concrete grades of the connections, with lower-grade concrete exhibiting significantly higher interstory drift ratios. In addition, the notable discrepancy in response for different damping ratios (up to 25%) was observed for the model. These variations highlight the importance of precise material characterization in predicting structural behavior of LPBs. The results align well with previous studies and the outcomes of natural testing on full-scale buildings, providing a strong validation of the analysis conducted.

However, the study also identified limitations within the LIRA-SAPR software that could impact the accuracy of such analyses. Notably, the inability to modify or change standard hysteresis models posed challenges in accurately representing the strength and stiffness degradation specific to precast panel structures. Despite these constraints, the overall findings of the study offer valuable insights into the seismic behavior of LPBs, emphasizing the importance of detailed nonlinear analysis in understanding and predicting their performance.

In summary, the research successfully applied a nonlinear analysis methodology to LPBs using LIRA-SAPR, yielding critical findings on the seismic response of these structures. While some software limitations were identified, the results contribute to the understanding of LPB behavior under seismic loads and underscore the necessity of code modifications to support the development of effective seismic performance evaluation tools.

ACKNOWLEDGEMENTS

The research was supported by the Russian Science Foundation (Project No. 24-79-00087).

REFERENCES

1. **Malazdrewicz S., Ostrowski K.A., Sadowski L.** Large Panel System Technology in the Second Half of the Twentieth Century – Literature Review, Recycling Possibilities and Research Gaps // Buildings. 2022. Vol. 12, No. 11. 1822 p.
2. **Rozanov N.** Large-panel construction. M.: Stroyizdat, 1982. 224 p. (in Russian).
3. **Malaia K.** A Unit of Homemaking: The Prefabricated Panel and Domestic Architecture in the Late Soviet Union // Architectural Histories. 2020. Vol. 8, No. 1. 12 p.
4. **Wardach M., Krentowski J.R.** Current perspective on large-panel buildings – A review // Structures. 2023. Vol. 58. 105537 p. https://doi.org/10.1016/j.istruc.2023.105537
5. **Shapiro G., Gasanov A.** Numerical solution of the problem of stability of the prefabricated building against progressive collapse // International Journal for Computational Civil and Structural Engineering. 2016. No. 12 (2). pp. 158–166. (in Russian).
6. **Harris H.G.** Full-Scale Tests on Horizontal Joints of Large Panel Precast Concrete Buildings // PCIJ. 1980. Vol. 25, No. 2. pp. 72–92. https://doi.org/10.15554/pcij.03011980.72.92
7. **Guri M., Brzev S., Lluka D.** Performance of Prefabricated Large Panel Reinforced

Concrete Buildings in the November 2019 Albania Earthquake // Journal of Earthquake Engineering. 2022. Vol. 26, No. 11. pp. 5799–5825. https://doi.org/10.1080/13632469.2021.1887010

8. **Velkov M.** Behaviour of large panel building during the Romania earthquake of March 4, 1977. 1978. pp. 32–42. https://doi.org/10.5169/seals-24183.
9. **Caccese V., Harris H.G.** Seismic resistance of precast concrete shear walls // Earthq Engng Struct Dyn. 1987. Vol. 15, No. 6. pp. 661–677. https://doi.org/10.1002/eqe.4290150602
10. **Clough R.W., Malhas F., Oliva M.G.** Seismic Behavior of Large Panel Precast Concrete Walls: Analysis and Experiment // PCIJ. 1989. Vol. 34, No. 5. pp. 42–66. https://doi.org/10.15554/pcij.09011989.42.66
11. **Becker J.M., Llorente C., Mueller P.** Seismic response of precast concrete walls // Earthq Engng Struct Dyn. 1980. Vol. 8, No. 6. pp. 545–564. https://doi.org/10.1002/eqe.4290080605
12. **Kianoush M.R., Scanlon A.** Analytical modelling of large panel coupled walls for seismic loading // Can. J. Civ. Eng. 1988. Vol. 15, No. 4. pp. 623–632. https://doi.org/10.1139/l88-084
13. **Abaev Z., Valiev A., Kodzaev M.** Methodology of the reinforced concrete large panel buildings modeling with SAPFIR-generator visual programming tool // AIP Conference Proceedings. 2023. Vol. 2833, No. 1. https://doi.org/10.1063/5.0151656
14. **Abaev Z., Valiev A., Kodzaev M.** Development of recommendations for the implementation of seismic risk mitigation policy in the Russian Federation based on world experience // Earthquake Engineering. Construction Safety. 2023. No. 3. pp. 48–72. https://doi.org/10.37153/2618-9283-2023-3-48-72 (in Russian).
15. **Ashkinadze G., Sokolov M., Martynova L.** Reinforced concrete walls of earth-resistant buildings. M.: Stroyizdat, 1988. 504 p. (in Russian).
16. **Abaev Z., Valiev A., Kodzaev M.** Large Panel Reinforced Concrete Buildings Inelastic Behavior Modeling Approach for Nonlinear Seismic Analysis // Proceedings of the 7th International Conference on Construction, Architecture and Technosphere Safety / ed. Radionov A.A. et al. Cham: Springer Nature Switzerland, 2024. Vol. 400. pp. 162–174. https://doi.org/10.1007/978-3-031-47810-9_16
17. SP 335.1325800.2017 Large-panel construction systems. Design rules. 2017. (in Russian).
18. Handbook for calculating large-panel buildings. Vol 1. Characteristics of stiffnesses. M.: Stroyizdat, 1974. 42 p. (in Russian).
19. **Gubchenko E.** Work with the 'Joint' tool of software package LIRA-CAD // Housing construction. 2018. No. 3. pp. 30–35. (in Russian).
20. **Vodopyanov R.** Simulation and computation of large-panel buildings in PC LIRA–SAPR 2017 // Housing construction. 2017. No. 3. pp. 42–48. (in Russian).
21. **Chopra A.K.** Dynamics of structures: theory and applications to earthquake engineering. Fifth edition. Hoboken, NJ: Pearson, 2017. 960 p.
22. **Ibarra L.F., Medina R.A., Krawinkler H.** Hysteretic models that incorporate strength and stiffness deterioration // Earthquake Engng Struct. Dyn. 2005. Vol. 34, No. 12. pp. 1489–1511. https://doi.org/10.1002/eqe.495
23. **Noji E.K.** The 1988 Earthquake in Soviet Armenia: Implications for Earthquake Preparedness // Disasters. 1989. Vol. 13, No. 3. pp. 255–262. https://doi.org/10.1111/j.1467-7717.1989.tb00715.x
24. **Zhunusov T. et al.** Vibration tests of a 5–story experimental large–panel building series 69 // Proceedings of the institute

KazNIISSA. Alma–Ata: Kazakhstan, 1977. pp. 56–69. (in Russian).
25. **Yu X., Li X., Bai Y.** Evaluating maximum inter-story drift ratios of building structures using time-varying models and Bayesian filters // Soil Dynamics and Earthquake Engineering. 2022. Vol. 162. 107496 p. https://doi.org/10.1016/j.soildyn.2022.107496
26. **Magliulo G. et al.** Nonstructural Seismic Loss Analysis of Traditional and Innovative Partition Systems Housed in Code-conforming RC Frame Buildings // Journal of Earthquake Engineering. 2022. Vol. 26, No. 15. pp. 7715–7742. https://doi.org/10.1080/13632469.2021.1983488
27. **Fintel M.** Performance of Buildings with Shear Walls in Earthquakes of the Last Thirty Years // PCIJ. 1995. Vol. 40. pp. 62–80. https://doi.org/10.15554/pcij.05011995.62.80
28. **Souheyla S., Yahiaoui D., Demagh R.** Seismic fragility evaluation of soil-pile-structure interaction effects subjected to mainshock-aftershock records // IJCCSE. 2023. Vol. 19, No. 3. pp. 92–113. https://doi.org/10.22337/2587-9618-2023-19-3-92-113
29. **Vamvatsikos D., Cornell C.A.** Incremental dynamic analysis // Earthq Engineering Struct Dyn. 2002. Vol. 31, No. 3. pp. 491–514. https://doi.org/10.1002/eqe.141
30. **Abaev Z.K., Sulthan F.** Seismic Performance Evaluation of Multi-Storey Residential Building with Friction Pendulum Bearings: Indonesia case study // Struct. Mech. of Eng. Const. and Build. 2024. Vol. 20, No. 1. pp. 57–72. https://doi.org/10.22363/1815-5235-2024-20-1-57-72 (in Russian).

СПИСОК ЛИТЕРАТУРЫ

1. **Malazdrewicz S., Ostrowski K.A., Sadowski L.** Large Panel System Technology in the Second Half of the Twentieth Century – Literature Review, Recycling Possibilities and Research Gaps // Buildings. 2022. Vol. 12, № 11. 1822 p.
2. **Розанов Н.П.** Крупнопанельное домостроение. М.: Стройиздат, 1982. 224 с.
3. **Malaia K.** A Unit of Homemaking: The Prefabricated Panel and Domestic Architecture in the Late Soviet Union // Architectural Histories. 2020. Vol. 8, № 1. 12 p.
4. **Wardach M., Krentowski J.R.** Current perspective on large-panel buildings – A review // Structures. 2023. Vol. 58. 105537 p.
5. **Шапиро Г.И., Гасанов А.А.** Численное решение задачи устойчивости панельного здания против прогрессирующего обрушения // International Journal for Computational Civil and Structural Engineering. 2016. № 12 (2). С. 158–166.
6. **Harris H.G.** Full-Scale Tests on Horizontal Joints of Large Panel Precast Concrete Buildings // PCIJ. 1980. Vol. 25, № 2. pp. 72–92.
7. **Guri M., Brzev S., Lluka D.** Performance of Prefabricated Large Panel Reinforced Concrete Buildings in the November 2019 Albania Earthquake // Journal of Earthquake Engineering. 2022. Vol. 26, № 11. pp. 5799–5825.
8. **Velkov M.** Behaviour of large panel building during the Romania earthquake of March 4, 1977. 1978. pp. 32–42.
9. **Caccese V., Harris H.G.** Seismic resistance of precast concrete shear walls // Earthq Engng Struct Dyn. 1987. Vol. 15, No. 6. pp. 661–677.
10. **Clough R.W., Malhas F., Oliva M.G.** Seismic Behavior of Large Panel Precast Concrete Walls: Analysis and Experiment // pcij. 1989. Vol. 34, No. 5. pp. 42–66.
11. **Becker J.M., Llorente C., Mueller P.** Seismic response of precast concrete walls // Earthq Engng Struct Dyn. 1980. Vol. 8, No. 6. pp. 545–564.
12. **Kianoush M.R., Scanlon A.** Analytical modelling of large panel coupled walls for

seismic loading // Can. J. Civ. Eng. 1988. Vol. 15, No. 4. pp. 623–632.
13. **Abaev Z., Valiev A., Kodzaev M.** Methodology of the reinforced concrete large panel buildings modeling with SAPFIR-generator visual programming tool // AIP Conference Proceedings. 2023. Vol. 2833, No. 1.
14. **Абаев З.К., Валиев А.Д., Кодзаев М.Ю.** Разработка рекомендаций политики снижения сейсмического риска в Российской Федерации на основе мирового опыта // Сейсмостойкое строительство. Безопасность сооружений. 2023. № 3. С. 48–72.
15. Железобетонные стены сейсмостойких зданий / под ред. Ашкинадзе Г.Н., Соколов М.Е. М.: Стройиздат, 1988. 504 с.
16. **Abaev Z., Valiev A., Kodzaev M.** Large Panel Reinforced Concrete Buildings Inelastic Behavior Modeling Approach for Nonlinear Seismic Analysis // Proceedings of the 7th International Conference on Construction, Architecture and Technosphere Safety / ed. Radionov A.A. et al. Cham: Springer Nature Switzerland, 2024. Vol. 400. pp. 162–174.
17. СП 335.1325800.2017 Крупнопанельные конструктивные системы. Правила проектирования. 2017.
18. Пособие по расчету крупнопанельных зданий Выпуск 1. Жесткостные характеристики. М.: Стройиздат, 1974. 42 с.
19. **Губченко Е.В.** Работа с инструментом “Стык” ПК ЛИРА-САПР // Жилищное строительство. 2018. № 3. С. 30–35.
20. **Водопьянов Р.Ю.** Моделирование и расчет крупнопанельных зданий в ПК ЛИРА-САПР // Жилищное строительство. 2017. № 3. С. 42–48.
21. **Chopra A.K.** Dynamics of structures: theory and applications to earthquake engineering. Fifth edition. Hoboken, NJ: Pearson, 2017. 960 p.
22. **Ibarra L.F., Medina R.A., Krawinkler H.** Hysteretic models that incorporate strength and stiffness deterioration // Earthquake Engng Struct. Dyn. 2005. Vol. 34, No. 12. pp. 1489–1511.
23. **Noji E.K.** The 1988 Earthquake in Soviet Armenia: Implications for Earthquake Preparedness // Disasters. 1989. Vol. 13, No. 3. pp. 255–262.
24. **Жунусов Т.Ж. и др.** Вибрационные испытания 5-этажного экспериментального крупнопанельного жилого дома серии 69 // Труды института КазНИИССА. Алма-Ата: Казахстан, 1977. С. 56–69.
25. **Yu X., Li X., Bai Y.** Evaluating maximum inter-story drift ratios of building structures using time-varying models and Bayesian filters // Soil Dynamics and Earthquake Engineering. 2022. Vol. 162. 107496 p.
26. **Magliulo G. et al.** Nonstructural Seismic Loss Analysis of Traditional and Innovative Partition Systems Housed in Code-conforming RC Frame Buildings // Journal of Earthquake Engineering. 2022. Vol. 26, No. 15. pp. 7715–7742.
27. **Fintel M.** Performance of Buildings with Shear Walls in Earthquakes of the Last Thirty Years // PCIJ. 1995. Vol. 40. pp. 62–80.
28. **Souheyla S., Yahiaoui D., Demagh R.** Seismic fragility evaluation of soil-pile-structure interaction effects subjected to mainshock-aftershock records // IJCCSE. 2023. Vol. 19, No. 3. pp. 92–113.
29. **Vamvatsikos D., Cornell C.A.** Incremental dynamic analysis // Earthq Engng Struct Dyn. 2002. Vol. 31, No. 3. pp. 491–514.
30. **Абаев З.К., Султан Ф.** Оценка сейсмостойкости многоэтажного жилого здания с фрикционно-маятниковыми опорами на примере Индонезии // Строительная механика инженерных конструкций и сооружений. 2024. Т. 20, № 1. С. 57–72.

Abaev Zaurbek K. – PhD (technical sciences), Associate Professor, Researcher, Vladikavkaz Scientific Centre of the Russian Academy of Sciences (VSC RAS), 1, Vil'yamsa street, Mikhaylovskoe, 363110, Russia. +7 (8672) 72-67-88, zaurbek_a@yahoo.com,
ORCID: https://orcid.org/0000-0002-6932-2740

Valiev Azamat D. – postgraduate student, North Caucasian Institute of Mining and Metallurgy (State Technological University), NCIMM (STU), 44, Nikolaeva st., Vladikavkaz, 362021, Russia, +7 (8672) 40-71-01, azamat99valiev@gmail.com, ORCID: https://orcid.org/0000-0002-9436-3691

Абаев Заурбек Камболатович – кандидат технических наук, доцент, научный сотрудник комплексного научно-исследовательского отдела, Федеральное государственное бюджетное учреждение науки Федеральный научный центр «Владикавказский научный центр Российской академии наук» (ВНЦ РАН), 363110, РСО-Алания, Пригородный район, с. Михайловское, ул. Вильямса, 1, +7 (8672) 72-67-88, zaurbek_a@yahoo.com, SPIN-код: 2843-1586
ORCID: https://orcid.org/0000-0002-6932-2740

Валиев Азамат Джониевич – аспирант, Федеральное государственное бюджетное образовательное учреждение высшего образования «Северо-Кавказский горно-металлургический институт (государственный технологический университет)», СКГМИ (ГТУ), 362021, Республика Северная Осетия, г. Владикавказ, ул. Николаева, 44, +7 (8672) 40-71-01, azamat99valiev@gmail.com, SPIN-код: 1662-8941
ORCID: https://orcid.org/0000-0002-9436-3691

International Journal for Computational Civil and Structural Engineering, 21(2) 43–61 (2025)

DOI:10.22337/2587-9618-2025-21-2-43-61

ACCOUNTING FOR THE ADDED MASS OF WATER OF RESERVOIR IN CALCULATION OF SEISMIC ACCELERATIONS FOR PRESSURE HYDRAULIC STRUCTURES

Alexandra S. Bestuzheva, Georgy P. Gotsiridze

National Research Moscow State University of Civil Engineering, Moscow, RUSSIA

Abstract: The analysis of domestic and foreign studies on the issue of hydrodynamic pressure of water on the pressure face of hydraulic structures under dynamic influences is carried out. The authors have developed an alternative method for numerically analytical solution of the problem of seismic water pressure on the inclined pressure face of the dam. Based on the grapho-analytical solution of the Laplace equation under specified boundary conditions, hydrodynamic grids and diagrams of the distribution of the coefficient of the attached mass of water for pressure faces with a vertical angle of 0...75 degrees are constructed, the obtained solution is compared with the reference solution of Westergaard, Zangar, as well as recommendations of relevant regulatory documentation. Based on the conducted research, a nomogram was constructed to determine the coefficient of the attached mass of water. The obtained results are approximated by a quadratic function, which allows us to obtain the values of the coefficients of the combined mass of water depending on the vertical angle of inclination of the pressure face and the relative depth of the element location on the pressure face, which is used in the algorithm of the calculation program for computers. A graph of the change in the hydrodynamic force acting on the structure, depending on the vertical angle of inclination of the pressure face, is given, the accuracy of plotting is investigated depending on the number of elements on the pressure face. On the basis of the linear spectral method, accelerations in the elements of the pressure face of dams of various designs are calculated, both taking into account the attached mass of water and without. The results obtained indicate a significant effect of the attached mass of water on seismic accelerations not only on the crest of a concrete gravity dam, but also in the zone of the upper slope of groundwater dams. The increase in accelerations in these zones is up to 30% for concrete dams and about 10% for ground dams.

Keywords: hydrodynamic pressure, Laplace equation, attached water mass, pressure structure, seismic acceleration, linear spectral method

УЧЕТ ПРИСОЕДИНЕННОЙ МАССЫ ВОДЫ ВОДОХРАНИЛИЩА В РАСЧЕТЕ СЕЙСМИЧЕСКИХ СИЛ ДЛЯ НАПОРНЫХ ГИДРОТЕХНИЧЕСКИХ СООРУЖЕНИЙ

А.С. Бестужева, Г.П. Гоцiридзе

Национальный исследовательский Московский государственный строительный университет, г. Москва, РОССИЯ

Аннотация: Произведен анализ отечественных и зарубежных исследований по вопросу гидродинамического давления воды на напорную грань гидротехнических сооружений при динамических воздействиях. Авторами разработан альтернативный метод численно-аналитического решения задачи о сейсмическом давлении воды на наклонную напорную грань плотины. На основе графоаналитического решения уравнения Лапласа в заданных граничных условиях построены гидродинамические сетки и эпюры распределения коэффициента присоединенной массы воды для напорных граней с вертикальным углом 0…75 градусов, проведено сопоставление полученного решения с эталонным решением Вестергарда, Зангара, а также рекомендациями актуальной нормативной документации. На основе проведенных исследований построена номограмма для определения коэффициента присоединенной массы воды. Полученные результаты аппроксимированы квадратичной функцией, позволяющей получить значения коэффициентов присоединенной массы воды в зависимости от вертикального угла наклона напорной

грани и относительной глубины расположения элемента на напорной грани, что использовано в алгоритме расчетной программы для ЭВМ. Приводится график изменения гидродинамической силы, действующей на сооружение, в зависимости от вертикального угла наклона напорной грани, исследована точность построения эпюры в зависимости от числа элементов на напорной грани. На основе линейно-спектрального метода вычислены ускорения в элементах напорной грани плотин различной конструкции как с учетом присоединенной массы воды, так и без. Полученные результаты говорят о существенном влиянии присоединенной массы воды на сейсмические ускорения не только на гребне бетонной гравитационной плотины, но и в зоне верхового откоса грунтовых плотин. Увеличение ускорений в этих зонах составляет до 30% для бетонных плотин и около 10% для грунтовых плотин.

Ключевые слова: гидродинамическое давление, уравнение Лапласа, присоединенная масса воды, напорное сооружение, сейсмическое ускорение, линейно-спектральный метод

INTRODUCTION

One of the most difficult and unresolved issues of designing ground dams in the high seismicity zone is the interaction of the structure with the reservoir's water environment during an earthquake. In the modern regulatory literature (SP 358.1325800.2017 " Hydraulic structures. Rules of design and construction in seismic areas", SP 14.13330.2018 "Construction in seismic areas", hereinafter-SP) regulates the determination of hydrodynamic loads at the contact of a structure with water as additional seismic loads during earthquakes. Despite a large amount of scientific research on the hydrodynamic pressure of water on the pressure face of structures under dynamic impacts, in the current standards for plotting the seismic water pressure, there are only provisions on the "attached mass of water" with the determination of the coefficients of the attached mass according to the solution of Westergaard [1], obtained for the vertical pressure face. The Westergaard solution obtained analytically is a reference one (hereinafter referred to as the Westergaard problem) and underlies the applied methods for calculating hydraulic structures. It is based on the following assumptions about: - an ideal, incompressible fluid; - a rigid, non-deformable, interacting with water body; - non-eddy motion of the liquid; - absence of the phenomenon of wave formation on the water surface; - horizontal translational vibrations with a small amplitude, which are performed by the "dam (with base)" system- reservoir"; - a flat problem in the assumption of an infinite length of the reservoir with a horizontal bottom line.

In further works of Russian [2-7] and foreign scientists [8-12], the problems of hydroelasticity were solved taking into account the viscous properties of a compressible liquid and the elastic properties of a solid, taking into account wave formation on the water surface, the special geometry of the reservoir bed, and other factors that specify the solutions.

Of particular importance in the practice of hydraulic engineering construction are structures with a slope profile, often with a broken pressure face, for which the definition of seismic pressure in the current regulatory documentation during an earthquake is limited to taking into account the angle of the upper slope (vertical angle) of 15°.

However, for the vast majority of structures of ground dams, many structures of concrete buttresses, dams made of rolled concrete, berthing and enclosing structures, the upper pressure faces have an angle significantly greater than 15 degrees, which must be taken into account when designing structures in the zone of high seismicity.

The problem of the distribution of the seismic water pressure on the inclined pressure face of the dam was solved in the 50s of the XX century in the works of Sh. G. Napetvaridze on the basis of the conformal mapping method [13], where he gave an approximate formula for determining the seismic water pressure on the inclined face in the form:

$$p_\alpha(z) = p_w(y)\cos^2(\alpha) \quad (1)$$

where α is the vertical angle of inclination of the pressure face.

$p_w(y)$ - seismic water pressure on the vertical pressure face at a depth y from the water level (Westergaard's solution), $p_\alpha(z)$ - seismic water pressure on the inclined pressure face at the length *z* from the water edge along the face.

In the Reference manual of I. S. Sheinin [3], based on the solution of hydroelasticity problems, a similar formula is given for the coefficient of the attached mass of water μ_α taking into account the angle of inclination of the pressure face (vertical) in the form:

$$\mu_\alpha = \mu C(\alpha)\cos^2(\alpha) \quad (2)$$

where is the coefficient of attached mass for the vertical pressure face;

$C(\alpha)$ - coefficient depending on the angle of inclination of the pressure face (Figure 1)

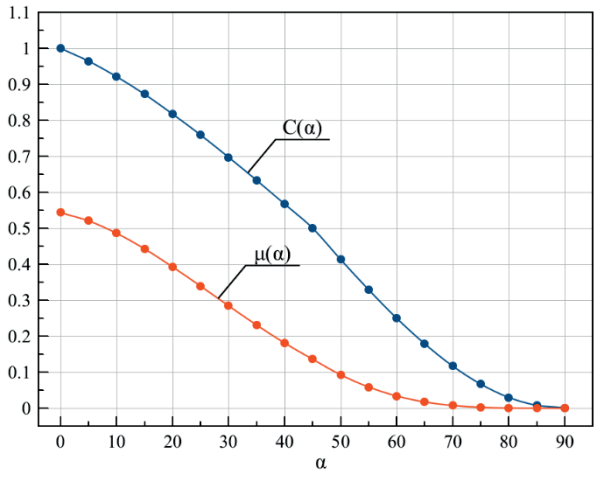


Figure 1. Coefficient of attached water mass

In [14], an experimental solution was obtained for determining the seismic pressure of water on the inclined face of a dam based on the electrodynamic analogy method (EGDA), given in the form of plots of coefficients of the attached mass of water. Comparison of the obtained values of the attached mass coefficients with the values obtained by the authors of the work is given below.

The authors have developed an alternative grapho-analytical method for solving the prob-lem of seismic water pressure on the inclined pressure face of an underground dam in the formulation of the "Westergaard problem" (hereinafter referred to as the GAM) [15,16], compared with known solutions, and compiled calculation programs for determining seismic forces in the body of a ground dam, taking into account the forms of natural vibrations, the seismic pressure of the reservoir, and the direction of approach of the seismic waves to the dam alignment [17].

METHODS

During an earthquake, the dam oscillates and shifts towards the upstream, while hydrodynamic pressure will act on it from the water side, depending on the speed of movement, the elastic properties of interacting bodies, and the geometry of the calculated area. The solution of the contact problem of hydroelasticity for a hydraulic structure is based on the provisions of continuum mechanics and the theory of small deformations, and the prerequisites are used to simplify the problem without losing the accuracy of the solution for a particular structure. For the massive body of a ground dam, small values of the amplitudes of seismic vibrations can be noted, which are measured in centimeters in the most severe earthquakes. Taking into account the fact that the dam dimensions are much larger than the amplitudes of its displacements during seismic vibrations, we can neglect the shape of the deformed axis of the pressure face of the dam during vibrations and take it as a displacement plot uniform in height, which corresponds to the model of "translational movement of a rigid wall". Due to the insignificant speed of water movement in the reservoir during an earthquake, the viscous properties of water can be ignored. Due to the minimal oxygen content in the deep

layers of the reservoir, the water medium can be considered as a homogeneous and incompressible liquid with a constant density $p = const$.

The solution of the problem of pressure distribution in a liquid under given boundary conditions and a known displacement on the contour (the pressure face of the dam) is based on dynamic equilibrium equations in the Euler form, one of which can be written as:

$$\rho \frac{dv}{dt} = \rho X - \frac{\partial p}{\partial x} \tag{3}$$

where $v(x,z,t)$ is a function of the velocity of the water medium particle, m/s

$p(x,z,t)$ – pressure function, kPa

X – projection of volumetric forces on the x-axis, kN

ρ - density of liquid (water), t/m3[3]

The Euler equation in the form (3) is written for volume forces assigned to a unit of volume.

Assuming that there is no rotation in the motion of particles, we can write down the following relative to the velocity components:

$$\frac{\partial v_x}{\partial z} - \frac{\partial v_z}{\partial x} = 0 \tag{4}$$

what happens if v_x both v_z are coordinate derivatives of the same function, i.e. we can write:

$$\begin{cases} v_x = \dfrac{\partial u_x}{\partial t} = \dfrac{\partial \varphi}{\partial x} \\ v_z = \dfrac{\partial u_z}{\partial t} = \dfrac{\partial \varphi}{\partial z} \end{cases} \tag{5}$$

The function is usually called the velocity potential, and the irrotational motion is called the potential.

The Euler equation in the absence of external forces, when the fluid motion is related to the pressure difference at points in a continuous medium caused only by seismic action, taking into account (5), in projections on the axes x and z is written as:

$$\begin{cases} \dfrac{\partial P_0}{\partial x} = -\rho \dfrac{\partial v_x}{\partial t} \\ \dfrac{\partial P_0}{\partial z} = -\rho \dfrac{\partial v_z}{\partial t} \end{cases} \tag{6}$$

where P_0 is the excess hydrodynamic pressure caused by dam vibrations, kPa.

v_x, v_z - horizontal and vertical velocity components.

The solution of problem (6) involves determining the vector velocity field of fluid particles and the scalar pressure field at each moment of time t according to the law of base motion during an earthquake.

The solution of the dynamic problem is constructed based on a series of quasi-stationary states, for which the velocity and pressure functions are determined. The harmonic function can be taken as a regularity of the change in acceleration over time in the given problem:

$$\ddot{u}(t) = \ddot{U}_0 \cos \omega t \tag{7}$$

where is the maximum acceleration of the base corresponding to the earthquake score and local ground conditions, m/s[2], according to the SP is set as a coefficient;

ω - the frequency of forced vibrations during an earthquake, in harmonic vibrations, T - the period closest to the frequency of natural vibrations of the dam, for local earthquakes the period does not exceed $T \le 1...1,2\,s$.

Substituting expressions (5) into (6) and integrating the full differentials of the functions: $dP_0(x,z)$ and $d\varphi(x,z)$ [15], we obtain that the hydrodynamic pressure function is related to the velocity potential by the relation:

$$P_0 = -\rho \frac{\partial \varphi}{\partial t} + C \tag{8}$$

The resulting expression indicates that the pressure function is also a potential function, therefore, its distribution in space obeys the Laplace equation and can be written:

$$\frac{\partial^2 P_0}{\partial x^2}+\frac{\partial^2 P_0}{\partial z^2}=0 \text{ or } \Delta P_0=0 \qquad (9)$$

The solution of the Laplace equation under given boundary conditions is called the Dirichlet problem and is completely determined by the boundary conditions, i.e. it is a boundary value problem. The desired function in equation (9) is the overpressure function, the distribution of which in space can be represented as a family of equipotentials, lines of equal pressure

Often, when solving hydraulic (filtration) problems, the solution of the Laplace equation is presented as a family of two potential functions – the velocity (pressure) potential function and the current line function. Potential functions of current and pressure (velocity potential) they are complex conjugate harmonic functions connected by the Cauchy-Riemann relations:

$$\begin{cases}\dfrac{\partial\varphi}{\partial x}=\dfrac{\partial\psi}{\partial z}\\ \dfrac{\partial\varphi}{\partial z}=-\dfrac{\partial\psi}{\partial x}\end{cases} \qquad (10)$$

In this case, the system of equipotentials $\varphi=const$ and current lines $\psi=const$ form an orthogonal hydrodynamic grid, in which the position of one of the functions uniquely determines the position of the other. Thus, the solution of the Laplace equation for the current function, represented as a family of streamlines, allows graphoanalytically constructing a hydrodynamic grid with determining the position of equipotentials for the velocity potential function (hydrodynamic pressure). This property of orthogonality of two functions allows us to use the boundary conditions of one of the functions when integrating the other (9).

Based on physical representations of the pressure distribution in a liquid during translational (horizontal) motion of a solid wall located at an angle α to the vertical, the following boundary conditions can be determined for the design scheme shown in Figure 2:

1) the boundary of the reservoir bed is non-deformable, impenetrable and stationary, which means that there is no gradient of the velocity potential function along the normal to the boundary ($\frac{\partial\varphi}{\partial n}=0$) and the boundary position for the current line function ($\psi=1$);

2) the vertical boundary of the design area at a great distance from the moving wall is stationary, watertight and does not experience hydrodynamic pressure from wall vibrations, along it it can be assumed $\varphi=0$, however, in the case of consider-ing the problem with a limited reservoir length, or if the slope of the reservoir bottom line is taken into account, the boundary conditions should be set differently: $\psi=1$ and $\frac{\partial\varphi}{\partial n}=0$;

3) there are no wave formation phenomena on the reservoir surface, the pressure is constant: $\varphi=const$ therefore, the current lines are orthogonal to the water surface;

4) on the mobile impenetrable pressure face of the dam, the points of which move at the same horizontal speed, the boundary values of the hydrodynamic pressure function are not determined and are the desired ones. At the same time, for the function of streamlines, the boundary conditions can be defined as follows. At the lower point of the pressure face (A), the intersection with the boundary current line is

set, where $\psi = 1$. At the upper point of the pressure face (D) , at the upstream water cut, the value for the current line function is: $\psi = 0$. The assumption of a uniform "penetrating-reflecting" capacity of the movable pressure face of the structure determines a uniform distribution of flow rates of "current tubes" over the height of the dam. Based on the latter assumption, you can specify a linear distribution of current lines along the length of the pressure face with a step $\Delta\psi$ that corresponds to the accuracy of the problem solution. The constant gradient for the current functions over the height of the pressure face $\Delta\psi$ was assumed to be equal 5...10% h to, where h is the height of the pressure face of the dam.

Determining the boundary conditions for the potential current function allows us to solve the problem of its distribution in the domain (Figure 2) by integrating the Laplace equation for this function:

$$\frac{\partial^2\psi}{\partial x^2} + \frac{\partial^2\psi}{\partial z^2} = 0 \qquad (11)$$

Determination of the hydrodynamic pressure function from the obtained solution for the function with the condition of orthogonality of these functions can be obtained graphoanalytically based on the construction of hydrodynamic grids.

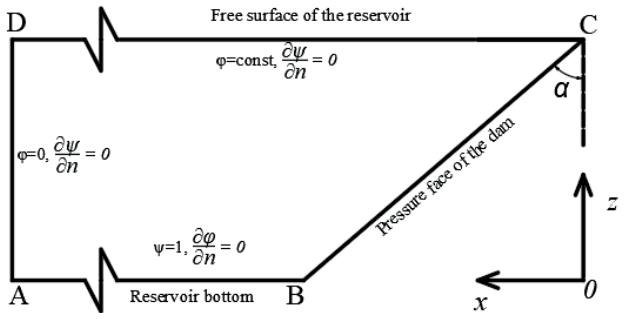


Figure 2. Design scheme with boundary conditions

Based on the principle of quasi-stationary states, it is possible to determine the maximum value of the hydrodynamic pressure function that will occur at the points of the pressure face of the dam, provided that the external impact is given by the maximum acceleration amplitude according to the earthquake score. For $\cos\omega t = 1$, according to (7), $\ddot{u}(t) = \ddot{U}_0 = A_0 g$ The distribution of the maximum pressure along the pressure face will be determined by the nature of the change in the function, which, according to the accepted boundary conditions, varies from 0 to 1 and determines the normalized values of hydrodynamic pressure.

When determining hydrodynamic loads on a structure due to the influence of reservoir water, the concept of "attached mass" of water is used as a body that performs joint vibrations with the structure, changing the inertial properties of the structure.

The force of hydrodynamic water pressure on the pressure face of the dam (P_w) can be represented on the basis of Newton's Second law as the maximum acceleration caused by wall vibrations ($\ddot{U}_0$), multiplied by the mass of water" attached" to the pressure face in the form:

$$P_w = m_w \ddot{U}_0 \qquad (12)$$

where m_w is the "attached mass" involved in the joint vibrations of the dam, which can be used to describe the hydrodynamic pressure on the structure during an earthquake as inertial.

The volume of the attached mass of water per 1 sq. m. of the width of the dam can be described by the area of the plot of the attached mass of water:

$$V_w = H \cdot \int_0^H \mu(Z) dZ \qquad (13)$$

where H is the height of the pressure face, m.
$\mu(Z)$ - function of the coefficient of the attached mass of water;
Z - the height of the element on the pressure face from the bottom of the reservoir, m
Thus, the attached mass of water for the entire structure can be defined by the expression:

$$m_w = \rho H \cdot \int_0^H \mu(Z) dZ \qquad (14)$$

In the solution of Westergaard for the vertical pressure face, it was assumed that the area of the plot of the attached mass of water in the conditions of the problem is determined by the expression:

$$\int_0^H \mu(Z) dZ = \mu_{eq} H \qquad (15)$$

where $\mu_{eq} = 0,544$ is the value of the coefficient of the attached mass of water obtained by the total area of the plot of the attached mass of water according to the accepted calculation scheme of Westergaard.

If in expression (15) we assume that $z = \frac{Z}{H}$ is the relative coordinate of the node on the pressure face ($0 \le z \le h$), and replace the integration variable, then the integral for the function of the coefficient of the attached mass (15) can be rewritten as:

$$\int_0^H \mu(Z) dZ = H \cdot \int_0^h \mu(z) dz = \mu_{eq} H \qquad (16)$$

To determine the coefficient of the attached mass of water μ_{eq} in the works of I. S. Sheinin [3], graphs and tables are given depending on the problem statement, their calculation schemes, and the conditions of movement of the structure. For the calculation schemes considered in this paper with different angles of inclination of the pressure face, the coefficient μ_{eq} can be determined from the plot in the form:

$$\mu_{eq} = \int_0^h \mu(z) dz \qquad (17)$$

Using the concept of the coefficient of attached mass, the value of the attached mass of water for the entire structure can be determined, considering it as an average mass of water evenly distributed over the pressure face of the structure, attributed to the unit area of the pressure face. Based on (14) and (15), for the attached mass of water, we can write:

$$m_{eq} = \frac{\rho \mu_{eq} H^2 \cdot 1 r.m.}{H \cdot 1 r.m.} = \rho \mu_{eq} H \qquad [\frac{kg}{m^2}] \qquad (18)$$

Accordingly, the hydrodynamic force of water pressure, which falls on the entire area of the pressure face of the dam (horizontal component), can be defined as:

$$P_{\Sigma} = \rho H \ddot{U}_0 \int_0^H \mu(Z) dZ = \rho H^2 \ddot{U}_0 \mu_{экв} \qquad (19)$$

Since the distribution of the attached mass of water over the height of the pressure face is uneven, the hydrodynamic pressure acting in the k-element of the pressure face of the dam can be written as:

$$\begin{aligned} p_k &= \rho H \ddot{U}_0 \cdot \mu_k(z) \\ p_k &= \gamma H \cdot \mu_k(z) \cdot A_0 \end{aligned} \qquad (20)$$

where is the ordinate on the plot of coefficients of the attached mass of water in the k-element of the pressure face of the dam, located at a relative height $z = \frac{Z}{H}$ from the bottom of the reservoir.

In the modern regulatory literature, the definition of hydrodynamic pressure is differentiated for different elements by the

height of the pressure face using the table for the coefficient of attached mass $\mu = f(\frac{y}{H})$, where it determines the depth of the calculated element under the water level. However, there are no such reference data for structures of hydraulic structures with an inclined pressure face, which led to the need for research in this area.

To determine the coefficient of attached mass μ_k, it is necessary to solve the problem of the distribution of hydrodynamic pressure over the height of the pressure face of the dam. Taking the seismic acceleration of the base, the water density, and the reduced reservoir depth as unit values, we can conclude that the plot of the distribution of the coefficient of the attached water mass over the height of the pressure face will be identical to the plot of the hydrodynamic water pressure, which is determined by the expression:

$$\mu_k(Z) = \frac{p_k(Z)}{\gamma^* h^* A_0^*} \tag{21}$$

Where A_0^* is the unit seismic acceleration of the base in fractions of g, γ^* is the unit volume weight of water, h^* is the relative depth of the reservoir, reduced to unity in the calculation scheme ($h = 1$).

The character of the distribution of the hydrodynamic pressure function in the calculated area with an inclined pressure face of the dam is determined by integrating the Laplace equation (9).

RESULTS AND DISCUSSING

For the numerical solution of (11), we used the apparatus of numerical methods in the MATLAB software package [18,19]. Design schemes for dams with different angles of inclination of the pressure face are constructed in relative coordinates XOZ, in which the height of the pressure face of the dam is taken as $h = 1$. In relative coordinates, the ordinate of an element on the pressure face z_k is defined as

$$z_k = \frac{Z}{H}$$

The boundary conditions for solving the problem of the distribution of the potential function in the computational domain "dam-reservoir" are set by the interface of the MATLAB software package on each of the sections of the figure ABCD, for the segments AB, BC, CD, DA (Figure 2). According to [MATLAB], two types of boundary conditions are given at the boundaries of the domain: Dirichlet conditions and Neumann conditions:

- the Dirichlet condition (or a condition of the 1st kind) is a method for setting a boundary condition when the value of the desired function is set explicitly, for example;
- the Neumann condition (or condition of the 2nd kind) is a method for setting a boundary condition when the desired function is given by its derivative, for example, $\frac{\partial V(x)}{\partial n} = 0$ which indicates that the equipotentials of the desired function are orthogonal to the selected boundary.

In the MATLAB PC interface, when solving elliptic equations, the boundary conditions for a potential function are set using the equation:

$$r(x) = V(x) \cdot a \tag{22}$$

where a is a variable that can take any valid values, including a null value.

$r(x)$ - a function defined analytically by an equation.

At the same time, the potential function can take any values.

Within the scope of this task, the following conditions will be met at the boundaries of the calculation scheme (Figure 2):

1. AB – reservoir bed, set for all of them

$$a = 1;\ r(x) = 1$$

what creates the conditions for a potential function:

$$V(x,z)\big|_{z=0} = 1 \text{ (Dirichlet condition)}$$

2. BC – conditional watertight boundary of the reservoir, which is a current line where the condition can be set:

$$\frac{\partial V}{\partial n} = 0 \text{ (Neumann condition)}$$

3. CD is the free surface of the reservoir, which is a line of equal pressure, which determines the orthogonality of the function of streamlines at this boundary:

$$\frac{\partial V}{\partial n} = 0 \text{ (Neumann condition)}$$

4. DA is the pressure face of the dam. The pressure at each point of the boundary is defined as a function of the height and angle α between the pressure face and the vertical.

$$a = 1; r(x) = \frac{1}{h \cdot tg(\alpha)} x$$

what defines a potential function:

$$V(x) = r(x) \text{ (Dirichlet condition)}$$

5. To exclude the influence of the length of the reservoir on the solution of the Laplace equation, the following condition was fulfilled in the calculations:

$$L_{res} \geq 3h \qquad (23)$$

Numerical solutions of the Laplace equation for the potential function $\psi(x,z)$ in design schemes with different angles of inclination of the pressure face, in the range of vertical angles from 0° to 75° degrees, are presented in the form of a family of equipotentials for some design schemes in Figure 3, where the blue equipotentials are a function of current lines , the red equipotentials are a function of the hydrodynamic pressure level.

The family of equipotentials representing a solution for the current line distribution function allows, in compliance with the orthogonality principle, to construct a hydrodynamic grid with equipotentials corresponding to the distribution law of the hydrodynamic pressure function in the calculated domain (Figure 4). The plots of the hydrodynamic pressure distribution along the inclined pressure face of the dam are given in the form of function values $P_0 = \varphi(x,z)$, which allows them to be considered as plots of the coefficients of the attached water mass according to (17).

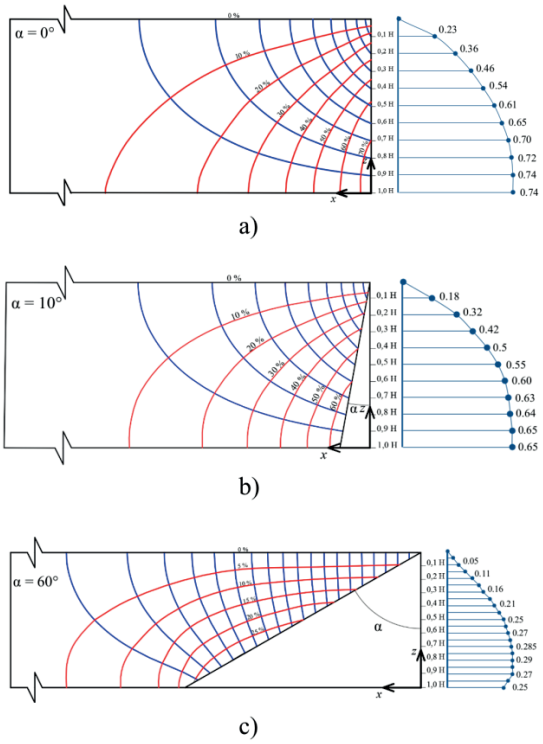


Figure 3. Hydrodynamic grid and plot for the coefficient of the attached mass of water at the angle of inclination of the pressure face: a) $\alpha = 0°$ b) $\alpha = 10°$ c) $\alpha = 60°$

Comparison of the obtained results for the coefficients of the added mass of water was carried out in 3 directions:

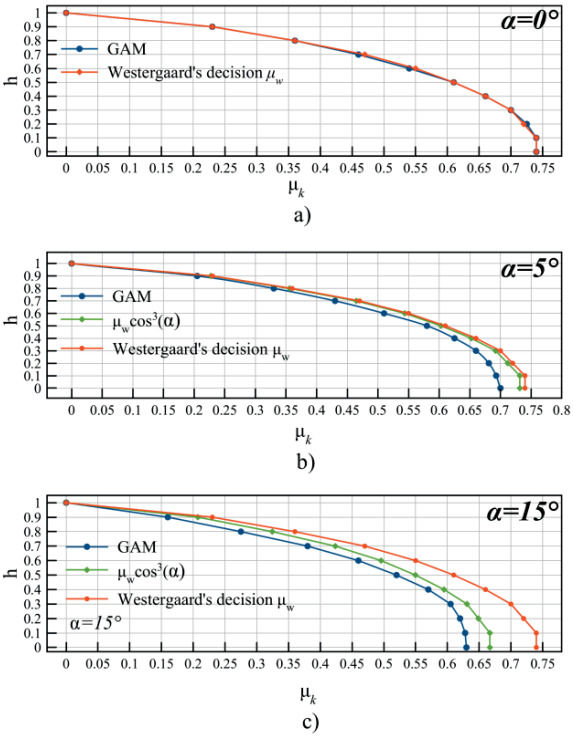
1. Comparison of the obtained functions $\mu(\alpha, z)$ with the Westergaard solution for the vertical pressure face (Figure 4a).
2. Comparison of the obtained functions $\mu(\alpha, z)$ with the recommendations of the SP for taking into account the angle of inclination of the pressure face (15° do) in the form:

$$\mu = \mu_w \cos^3(\alpha) \qquad (24)$$

where α is the angle of inclination of the pressure face relative to the vertical, deg.

μ_w - coefficient of the attached mass of water for the vertical face according to the solution of Westergaard.

3. Comparison of the obtained functions $\mu(\alpha, z)$ with the results of the Zangar experiment (Figure 4e)



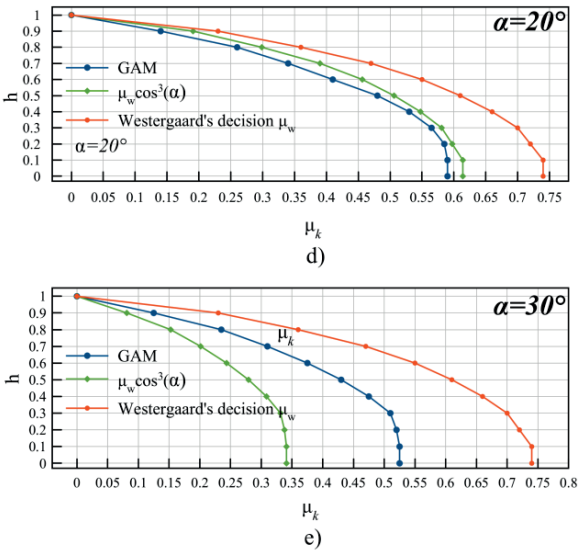


Figure 4. Comparison of results:
a) with the decision of Westergaard,
b) - e) with the recommendations of the SP for the corresponding angles

As can be seen from the comparison, for the angle, there is a high accuracy of matching the analytical solution of Westergaard. At the same time, the difference between the received decision and the JV recommendation reaches 10%, and for, obviously, the recommendations are no longer applicable.

The results of computational studies on the values of the coefficient of attached water mass obtained on the basis of constructed hydrodynamic grids for different angles of inclination of the pressure face of the dam, in the range, are summarized in a nomogram (Figure 5).

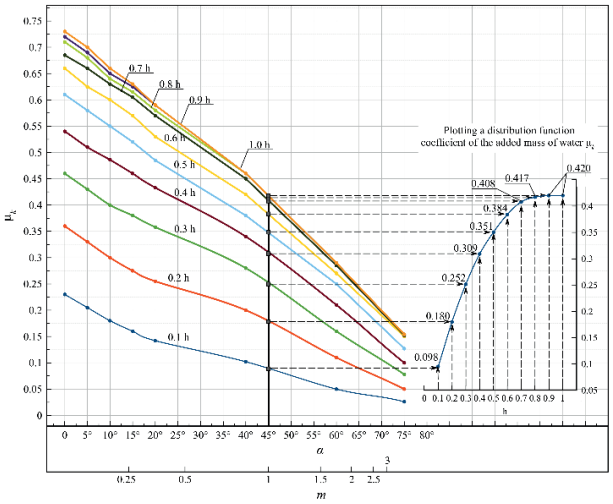


Figure 5. Nomogram

However, for convenient use in calculations, these curves are best represented as mathematical functions that depend on the corresponding arguments. Using the approximation method, we represent each experimental dependence $\mu = f(\alpha)$ as a linear function of the form:

$$\mu(z,\alpha) = a_{zi}\alpha + b_{zi} \tag{25}$$

The approximation functions are found by the least squares method using the Levenberg-Marquardt algorithm [20-22].

Further, representing families of angular coefficients $a_{zi}(z)$ and free terms $b_{zi}(z)$ as square parabolas:

$$\begin{aligned} a_{zi} &= f_\alpha(z) = m_1 z^2 + n_1 z + k_1 \\ b_{zi} &= f_b(z) = m_2 z^2 + n_2 z + k_2 \end{aligned} \tag{26}$$

you can express expression (25) in the following form:

$$\begin{aligned} \mu(z,\alpha) = (0.0073z^2 - 0.0132z - 0.0015)\alpha \\ -0.8448z^2 + 1.4894z + 0.0747 \end{aligned} \tag{27}$$

The value of the coefficient of the attached mass of water in the k-element of the pressure face of the dam can be calculated using expression (26) when $z = z_k$:

$$z_k = \frac{Z_k}{H} \tag{28}$$

where Z_k is the absolute height mark of the k-element, H is the absolute depth of the reservoir.

In accordance with the obtained approximation solution, expression (27) gives the values of the coefficients of the attached mass of water μ only over the interval $z_k = 0{,}1...1$. The function $\mu(z,\alpha)$ on the interval $z_k = 0...0{,}1$ can be approximated in a similar way:

$$\begin{cases} \mu(0,\alpha) \equiv 0 \\ \mu(0.1,\alpha) = a\alpha + b \end{cases} \tag{29}$$

In general, the function for finding the coefficient of the attached mass of water as a function of the relative depth of the element and the vertical angle of the pressure face is the following piecewise linear function with variable coefficients:

$$\mu(z,\alpha) = \begin{cases} 0,\ z \in \{0\} \\ -0.0026\alpha + 0.2103,\ z \in (0,0.1) \\ (0.0073z^2 - 0.0132z - 0.0015)\alpha - \\ -0.8448z^2 + 1.4894z + 0.0747, \\ z \in [0.1,1] \end{cases} \tag{30}$$

The equation of the values of the coefficients of the attached mass of water obtained using the approximation function (30) with the author's nomogram data and the results of experiments [14] for some angles α is shown in Figure 6.

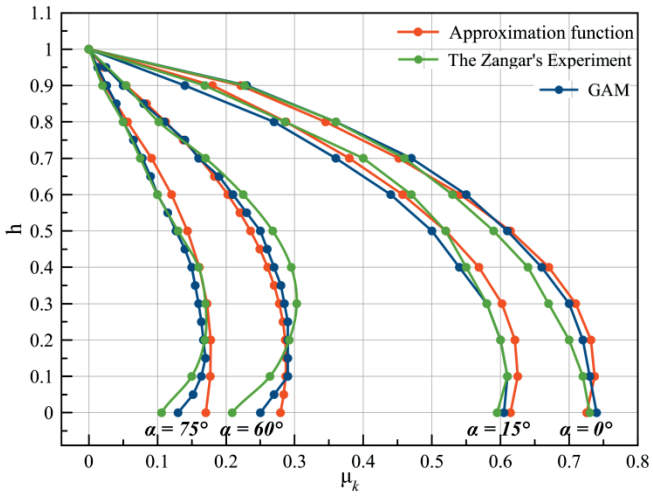


Figure 6. Comparison of results

The hydrodynamic pressure force according to (19) can be calculated by the formula:

$$P_{\Sigma} = \gamma_0 H^2 A_0 \int_0^h \mu(z,\alpha)dz \qquad (31)$$

where-the maximum relative acceleration of the base, - the volume weight of water, h- the relative depth of the reservoir, $\mu(z,\alpha)$– the function of the coefficient of the attached mass of water, constructed for the relative height of the pressure face z, varying from 0 to h

Calculation of hydrodynamic forces based on the obtained solutions for functions $\mu(z,\alpha)$ at different angles of inclination of the pressure face of the dam made it possible to plot changes in the hydrodynamic force $P_{hd} = f(\alpha)$. For this purpose, the integrals $\int_0^h \mu(z,\alpha)$ of the obtained plots $\mu(z,\alpha)$ were calculated. By analogy with (17), the obtained integrals determine the value of the coefficient of the equivalent attached mass of water for a dam with an inclined pressure face, and all other things being equal, the solutions of the problem depend only on the angle of inclination of the face.

For the resulting function, we introduce the following notation:

$$M(\alpha) = \int_0^h \mu(z,\alpha)dz \qquad (32)$$

The function graph $M(\alpha)$ is constructed based on the results of graphoanalytical plotting of the attached mass coefficients (Figure 7) and the approximating function constructed on their basis $\mu(z,\alpha)$.

The integral of the approximating function (30) can be obtained analytically in the form:

$$M(\alpha) = \int_0^h \mu(z,\alpha)dz = \int_0^{0.1} (-0.0026\alpha + 0.2103)dz + \int_{0.1}^1 ((0.0073z^2 - 0.0132z - 0.0015)\alpha - 0.8448z^2 + 1.4894z + 0.0747)dz$$

Performing direct integration, we get:

$$M(\alpha) = (0.021 - 0.00026\alpha) + (0.523 - 0.00545\alpha)$$
$$M(\alpha) = 0.544 - 0.00571\alpha \qquad (32)$$

Traditionally, it is interesting to represent the hydrodynamic pressure force as a fraction of the hydrostatic pressure force W (per 1 nm):

$$W = \frac{\gamma_0 H}{2}$$

Taking into account (30) and (31), we can write:

$$P_{\Sigma}(\alpha) = 2M(\alpha)WA_0 \qquad (33)$$

The obtained expression shows that for a strong earthquake ($A_0 = 0.4g$ for a 9-point earthquake) and a vertical pressure face ($M(0°) = 0.544$ - Westergaard's solution), the seismic pressure of

water on the pressure face of the dam will be $P_{\Sigma}(0°) = 0.435W$. When the pressure face is laid 1:1 ($\alpha = 45°$), which can occur for dams with reinforced concrete screens, the seismic water pressure will be $P_{\Sigma}(45°) = 0.23W$ almost a quarter of the hydrostatic pressure. The results obtained indicate a significant seismic pressure of water on the pressure face of the dam, including the slope profile.

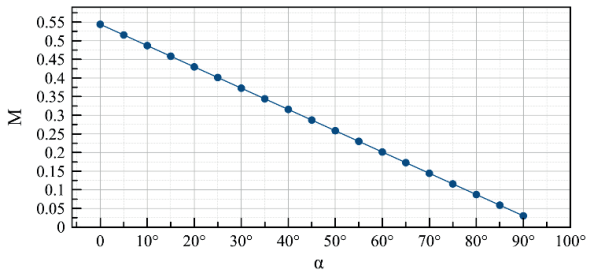


Figure 7. Graph of changes in hydrodynamic pressure from the slope of the pressure face

The obtained quadratic polynomials for the cefficients of the function depend on the height position of the element on the pressure face (23). Therefore, the number of elements forming the hydrodynamic pressure plot will affect the accuracy of plotting the coefficients of the attached water mass and the magnitude of seismic loads.

To assess the effect of the density of the FEM design grid on the hydrodynamic pressure force, calculations were performed with different numbers of elements on the pressure face. A model of a 100-meter dam with a 1:2 upper slope (vertical angle $\alpha = 63.43°$) was considered in 8 variants of breakdown: with 5, 10...70 elements on the pressure face.

As a result of analytical integration of the function of the coefficient of the added mass of water (32), an expression was obtained that can be taken as an exact solution:

$$M(63.43°) = 0.544 - 0.00571 \cdot 63.43 = 0.182$$

In each of the 8 calculation variants, for the center of gravity of the element located on the pressure face, the values of the coefficients of the attached mass of water were determined, according to the approximating function $\mu(z, \alpha)$, and a plot was constructed from them. Determining the area of the plot (using Autocad tools) allowed us to compare the obtained values for the $\alpha = 63.43°$ following parameters. The results of the comparison are shown at Figure 8.

The obtained results allow us to conclude that when forming the FEM grid, it is necessary to provide for at least 20 elements in height on the pressure face of the dam. When dividing the pressure face into 20÷30 elements, the error will be less than 5% of the value obtained by direct integration, which is a satisfactory result for engineering calculations.

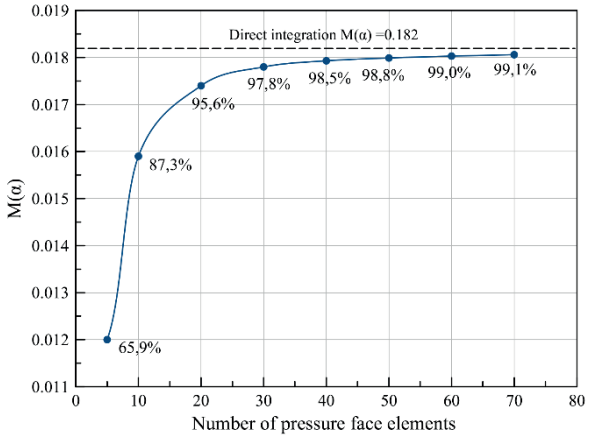


Figure 8. Comparison of numerical and direct integration results

In this problem, a method is developed for determining the hydrodynamic water pressure for a dam with an inclined pressure face, as a reaction to the horizontal component of dam vibrations during an earthquake. Taking into account

the horizontal hydrodynamic pressure of water in the attached mass of water involved in the horizontal vibrations of the dam, it is important to assess this effect in the magnitude of seismic forces that occur in dams during an earthquake, at different angles of inclination of the pressure face of the dam.

The linear-spectral method (hereinafter referred to as LSM), regulated by SP for determining seismic loads in hydraulic structures, involves solving the problem of natural dam vibrations and using calculation forms in determining seismic forces. When solving the problem of plane deformation for a momentless system, there are two components in the components of displacements according to the forms of natural vibrations-horizontal and vertical displacements, which will participate in the formation of both components of seismic forces – both horizontal $S_{k,x}$ and vertical $S_{k,z}$, while the attached mass of water affects only the inertial properties of the dam in the horizontal direction.

The study determined the seismic forces that occur in the dam elements in the horizontal direction, taking into account the horizontal hydrodynamic water pressure from the upstream side and the horizontal direction of propagation of the seismic wave. The considered problem statement determines the greatest seismic loads in the dam along the horizontal component. Studies were carried out for different dam structures: concrete, ground, combined, having different outlines of the pressure face.

The author's program "Seismic_Force_2D" was used to calculate and visualize the distribution of seismic forces in the dam [17]. As part of the calculation, the FEM grid is set, the properties of materials in the calculated area are calculated, the forms of natural vibrations are calculated, and seismic forces and accelerations are determined within the LSM with the calculated earthquake score.

Seismic forces in the dam elements were determined according to the linear-spectral method, taking into account the forms of natural dam vibrations by the formula:

$$S_{k,x} = k_f k_2 Q_{k\mu} \frac{A_0}{g} \sqrt{\sum_{i=1}^{12} ((k_\psi \beta)_i \eta_{ikx}))^2} \quad (34)$$

where k_f, k_2, k_ψ, β - coefficients are determined in accordance with SP, η_{ikx} - coefficient of the oscillation form in the k-element of the dam, according to the i-form of natural vibrations, in the horizontal direction:

$$\eta_{ikx} = \Gamma_{i\beta} x_{ik,x} \quad (35)$$

$$\Gamma_{i\beta} = \frac{\sum_{k=1}^{K} (Q_{k\mu} x_{ik} \cos\beta + Q_k z_{ik} \sin\beta)}{\sum_{k=1}^{K} (Q_{k\mu} x_{ik}^2 + Q_k z_{ik}^2)} \quad (36)$$

where $\Gamma_{i\beta}$ is the coefficient of participation of the i-form of vibrations in the oscillatory process (free vibrations) in the direction of propagation of the seismic wave, β is the angle of approach of the seismic wave with respect to the x-axis.

The change in the participation coefficient $\Gamma_{i\beta}$ when taking into account the attached mass of water for the model of the dam considered earlier is shown in Figure 9. As can be seen from the figure, for waveforms other than horizontal, in the horizontal direction, the coefficient $\Gamma_{i\beta}$ value is close to 0. Thus, there are not so many forms contributing to the seismic vibrations of the dam along the direction of wave propagation, they include 1,3,5 FGC, and the coefficient value of 5,6.9 FGC is not more than 10% $\Gamma_{i\beta}$ of 1 form, at high frequencies (more than 3.5 Hz) significant fluctuations of the dam in the direction of the seismic wave it is not observed, there are no significant fluctuations of the dam in the direction of the seismic wave, and the effect of the attached mass of water on the coefficient $\Gamma_{i\beta}$ for higher forms is minimal.

The weight of elements on the pressure face of the dam taking into account the attached weight of water, is determined by: $Q_{k\mu} = Q_k + Q_\mu$,

where Q_k - the weight of the element without taking into account the attached mass of water;

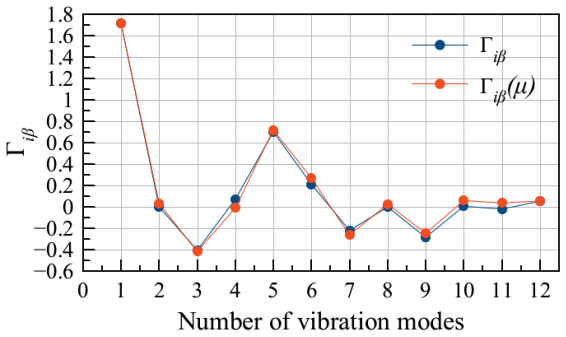


Figure 9. Effect of accounting for the added mass of water on the coefficient $\Gamma_{i\beta}$

x_{ik} and z_{ik} -normalized values of displacements of the k-nodes of the calculation scheme according to the i-form of natural vibrations (hereinafter referred to as FGC) in the horizontal and vertical directions, respectively.

The weight of the attached mass of water on the section of the pressure face of the dam height is determined as follows:

$$Q_\mu = \mu_k(z_k, \alpha_k)\gamma_w H \psi \Delta h_k \qquad (37)$$

where γ_w is the specific gravity of water, H is the depth of the reservoir, ψ and is a coefficient that takes into account the influence of the reservoir length.

The coefficient of the attached mass of water $\mu_k(z_k, \alpha_k)$ is determined by the formula (29), taking into account the change in angle α_k for each element separately.

The study examined three 100-meter-high dams located on the same base, experiencing seismic effects of the same intensity with an estimated base acceleration of 0.4g. The following dams are considered: a gravity concrete dam with a vertical pressure face, a ground dam with a 1:2 pressure face and an asphalt-concrete diaphragm, a combined dam with a concrete pedestal in the lower part of the pressure face and a reinforced concrete screen on the slope with a 1:1.5 foundation (Figure 10). For the correctness of the study, the number of elements on the pressure face in all calculated variants was assumed to be the same (n=30).

For each of the dam variants, according to the obtained function $\mu_k(z_k, \alpha_k)$, plots of the distribution of the coefficients of the attached mass along the pressure face were constructed (Figure 11).

For the design structures of dams, seismic accelerations were calculated using the linear-spectral method [23], taking into account the attached mass of water and without it. For a clear comparison of the effect of the added mass of water on acceleration, the set of coefficients is assumed to be the same.

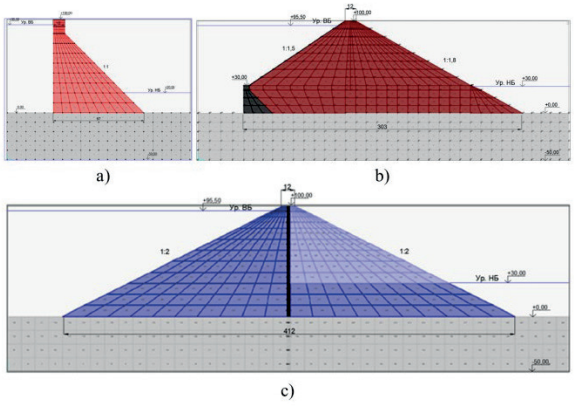


Figure 10. Structures of the considered dams (FEM grids).
a) concrete gravity dam
b) combined dam
c) ground dam

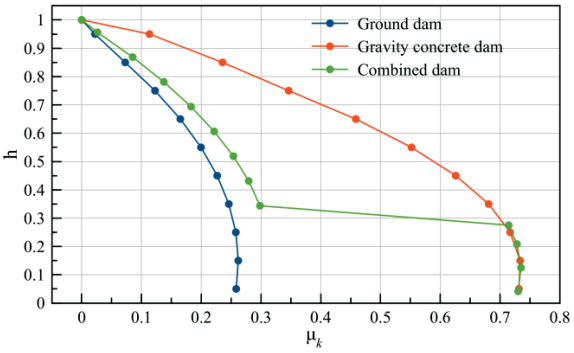


Figure 11. Plots of the distribution of the coefficient of attached water mass

As can be seen in Figure 12, the seismic accelerations of the ground and combined dams are comparable and do not exceed 0.3g in a 9-point earthquake. Accelerations on the crest of a concrete gravity dam are almost 0.7g.

Taking into account the added mass of water increases the acceleration of the elements of the pressure face of the dam over the entire height of the dam, reaching a difference of up to 10 % on the ridge. For a vertical pressure face, taking into account the added mass of water leads to an increase in acceleration on the ridge by almost 30%.

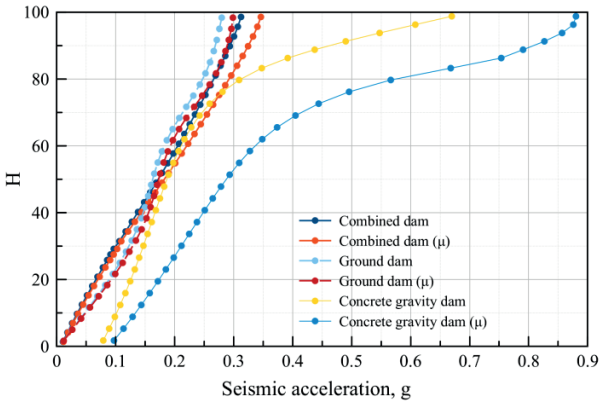


Figure 12. Seismic accelerations on the dam crest

CONCLUSIONS

1. A graph-analytical method for plotting plots of the attached mass of water for water structures with an inclined pressure face are developed for all possible angles of inclination in the range $\alpha = 0°...75°$, including when the slope is variable in height and when there are berms at ground dams.
2. The results of calculations are compared with the results of experimental studies, as well as with the well-known results of domestic and Western scientists, which showed good accuracy of the results.
3. For practical use, a nomogram is constructed with calculated values of the coefficients of the attached water mass, which allows determining the additional seismic pressure of the reservoir water on the structure during an earthquake.
4. An analysis of the accuracy of plotting epigrams of the attached water mass for different density of FEM grids is performed, based on which it is recommended that the maximum size of the element on the pressure face (in height) should not exceed 5% of the height of the dam.
5. The effect of the attached water mass on seismic accelerations for various dam designs is analyzed. The effect of the added mass of water increases the seismic acceleration at the crest of dams from 10% for ground dams to 30% for concrete dams with a vertical pressure face, which must be taken into account when designing hydraulic structures in seismically active areas.

ACKNOWLEDGEMENTS

The research was founded by the National Research Moscow State University of Civil Engineering (grant for fundamental and applied scientific research, project No. 34-392/130)

REFERENCES

1. **Westergaard H.M.** (1931) Water Pressures on Dams during Earthquakes, Proc. Am. Soc. *Civ. Engs*., vol. 57, 9.
2. **Napetvaridze Sh. G.** Seismic resistance of hydraulic structures. - M.: Gosstroyizdat, 1959, - 215p
3. **Sheinin I.S.** Oscillations of hydraulic structures in liquid. - M.: Energia, 1967, - 215 p.
4. **Kulmach P.P.** Seismic resistance of port hydraulic structures. - M.: Transport, 1970, - 312 p.
5. **Shulman S.G.** Calculations of seismic resistance of hydraulic structures taking into account the influence of the aquatic environment. - M.: Energy, 1976, - 190 p.
6. **Kaufman B. D.** Taking into account the influence of uncertain factors when

determining the hydrodynamic pressure on a dam // Magazine of Civil Engineering. 2012. No. 9

7. **Abdikarimov R.A., Eshmatov H., Bobanazarov Sh.P., Khodjaev D.A., Eshmatov B.Kh.** Mathematical modeling and calculation of hydraulic structures of the dam-plate type taking into account seismic loads and hydrodynamic water pressure // Magazine of Civil Engeneering, 2011, No. 3.
8. **Zhang C., Feng J., Pan J., Long Y.** Seismic safety evaluation of high concrete dams. Part 2. Earthquake behavior of arch dams // Proceedings 14th World Conference on Earthquake Engineering. Paper №S13-81, Beiging, China, 2008. Pp. 1-15.
9. **Zhang W., Ren X., Geng X., Zhang Y., Yang W**. Study on influence coefficients of hydrodynamic force on dynamic response of deep-water pier under earthquake // Ocean Engineering. - Elsevier, 2024, V. 299
10. **Qiu Y., Wang J., Zhang C.** An internal input framework of earthquake motions for dam-water-foundation rock systems // Soil Dynamics and Earthquake Engineering. - Elsevier, 2022, V. 156
11. **Ye. J., Zhou H., Zhou X.** Hydrodynamic pressure on lateral side of dam excited by harmonic seismic vibration: A novel formulation // Soil Dynamics and Earthquake Engineering. - Elsevier, 2023, V. 164
12. **Moghaddam A., Mozaheri H., Bidgoli M.** Mathematical modelling, numerical analysis and damage of dams subjected to hydrodynamic pressure // Ocean Engineering. - Elsevier, 2022, V. 253
13. **Napetvaridze Sh.G.** Hydrodynamic pressure under seismic impact // Works of the Institute of Construction of the Academy of Sciences of the Georgian SSR, 1955, v.5. Publishing house of the Academy of Sciences of the Georgian SSR
14. **Zangar C.N.** Hydrodynamic Pressures on Dams due to Horizontal Earthquake Effects, 1952, Denver: U.S. Bureau of Reclamation
15. **Bestuzheva A.S., Gotsiridze G.P**. Coefficient of added water mass for dams with a slope profile taking into account the direction of approach of a seismic wave // Hydrotechnical construction, 2024. No. 2.
16. **Bestuzheva A.S., Gotsiridze G.P**. Hydrodynamic pressure of water on the head face of an earth dam during an earthquake //E3S Web of Conferences - EDP Sciences, 2023. – V. 456
17. Certificate of state registration of the computer program RU 2024666923. Seismic_Force_2D/ A. S. Bestuzheva, G. P. Gotsiridze (RU); copyright holder FGBOU VO "National Research Moscow State University of Civil Engineering".; declared 10.07.2024; published 17.07.2024
18. **Chernyavskaya S.A., Matuzaeva O.V., Tsarev V.G.** Differential equations for solving applied problems in the MATLAB environment. // Power plants and technologies, 2022. Vol.8
19. **Bakhshalyeva M.N., Khalilov E.G.** Justification of the collocation method for the integral equation of the external Dirichlet boundary value problem for the Laplace equation // Journal of Computational Mathematics and Mathematical Physics, 2021. Vol. 61
20. **Levenberg K**. A Method for the Solution of Certain Non-Linear Problems in Least Squares // The Quarterly of Applied Mathematics, 1944, V.2
21. **Marquardt D.W.** An algorithm for least-squares estimation pf nonlinear parameters // Journal of the Society for Industrial and Applied Mathematics, 1963, V.11(2)
22. **Butyrsky E.Yu., Kuvaldin I.A., Chalkin V.P.** Approximation of multidimensional functions // Scientific instrument-making, 2010, Vol. 20, No. 2
23. **Bestuzheva A.S., Gotsiridze G.P.** Spectral methods for calculating earth dams for seismic loads // Izvestiya VNIIG im. B.E. Vedenev, 2022. V. 305

СПИСОК ЛИТЕРАТУРЫ

1. **Westergaard H.M**. (1931) Water Pressures on Dams during Earthquakes, Proc. Am. Soc. *Civ. Engs*., vol. 57, 9.
2. **Напетваридзе Ш.Г.** Сейсмостойкость гидротехнических сооружений. - М.: Госстройиздат, 1959, - 215с
3. **Шейнин И.С.** Колебания конструкций гидросооружений в жидкости. - М.: Энергия, 1967, - 215с
4. **Кульмач П.П.** Сейсмостойкость портовых гидротехнических сооружений. - М.: Транспорт, 1970, - 312с
5. **Шульман С.Г.** Расчеты сейсмостойкости гидросооружений с учетом влияния водной среды. -М.: Энергия, 1976,- 190с
6. **Кауфман Б. Д.** Учет влияния неопределенных факторов при определении гидродинамического давления на плотину // Magazine of Civil Engineering. 2012. №9
7. **Абдикаримов Р.А., Эшматов Х., Бобаназаров Ш.П., Ходжаев Д.А., Эшматов Б.Х.** Математическое моделирование и расчет гидротехнических сооружений типа плотины-пластины с учетом сейсмической нагрузок и гидродинамического давления воды // Инженерно-строительный журнал, 2011, № 3.
8. **Zhang C., Feng J., Pan J., Long Y.** Seismic safety evaluation of high concrete dams. Part 2. Earthquake behavior of arch dams // Proceedings 14th World Conference on Earthquake Engineering. Paper №S13-81, Beiging, China, 2008. Pp. 1-15.
9. **Zhang W., Ren X., Geng X., Zhang Y., Yang W**. Study on influence coefficients of hydrodynamic force on dynamic response of deep-water pier under earthquake // Ocean Engineering. - Elsevier, 2024, V. 299
10. **Qiu Y., Wang J., Zhang C.** An internal input framework of earthquake motions for dam-water-foundation rock systems // Soil Dynamics and Earthquake Engineering. - Elsevier, 2022, V. 156
11. **Ye. J., Zhou H., Zhou X.** Hydrodynamic pressure on lateral side of dam excited by harmonic seismic vibration: A novel formulation // Soil Dynamics and Earthquake Engineering. - Elsevier, 2023, V. 164
12. **Moghaddam A., Mozaheri H., Bidgoli M.** Mathematical modelling, numerical analysis and damage of dams subjected to hydrodynamic pressure // Ocean Engineering.- Elsevier, 2022, V. 253
13. **Напетваридзе Ш.Г.** Гидродинамическое давление при сейсмическом воздействии, // Труды Института строительного дела АН Грузинской ССР, 1955, т.5. Изд-во АН ГССР.
14. **Zangar C.N.** Hydrodynamic Pressures on Dams due to Horizontal Earthquake Effects, 1952, Denver: U.S. Bureau of Reclamation
15. **Бестужева А.С., Гоциридзе Г.П**. Коэффициент присоединённой массы воды для плотин откосного профиля с учётом направления подхода сейсмической волны // Гидротехническое строительство, 2024. № 2.
16. **Bestuzheva A.S., Gotsiridze G.P**. Hydrodynamic pressure of water on the head face of an earth dam during an earthquake //E3S Web of Conferences - EDP Sciense, 2023. – V. 457
17. Свидетельство о государственной регистрации программы для ЭВМ RU 2024666923. Seismic_Force_2D/ А. С. Бестужева, Г. П. Гоциридзе (RU); правообладатель ФГБОУ ВО «Национальный исследовательский Московский государственный строительный университет».; заявл. 10.07.2024; опубл. 17.07.2024
18. **Чернявская С.А., Матузаева О.В., Царев В.Г.** Дифференциальные уравнения к решению прикладных задач в среде MATLAB. // Энергетические установки и технологии, 2022. Т.8
19. **Бахшалыева М.Н., Халилов Э.Г.** Обоснование метода коллокации для интегрального уравнения внешней краевой задачи Дирихле для уравнения

Лапласа // Журнал вычислительной математики и математической физики, 2021. Т.61
20. **Levenberg K**. A Method for the Solution of Certain Non-Linear Problems in Least Squares // The Quarterly of Applied Mathematics, 1944, V.2
21. **Marquardt D.W.** An algorithm for least-squares estimation pf nonlinear parameters // Journal of the Society for Industrial and Applied Mathematics, 1963, V.11(2)
22. **Бутырский Е.Ю. Кувалдин И.А., Чалкин В.П.** Аппроксимация многомерных функций // Научное приборостроение, 2010, Т. 20, № 2
23. **Бестужева А.С., Гоциридзе Г.П**. Спектральные методы расчетов грунтовых плотин на сейсмические нагрузки // Известия ВНИИГ им. Б.Е. Веденеева, 2022. Т. 305

Bestuzheva Alexandra Stanislavovna, Associate Professor, Candidate of Technical Sciences, Associate Professor of the Institute of Hydrotechnical and Power Engineering (IGES) of the National Research Moscow State University of Civil Engineering (NRU MGSU) 129337, Moscow, Yaroslavskoye sh., 26, phone +7 (495) 287-49-14, email: alex_bestu@mail.ru

Gotsiridze Georgy Paatovich, postgraduate student of the Institute of Hydrotechnical and Power Engineering (IGES) of the National Research Moscow State University of Civil Engineering (NRU MGSU) 129337, Moscow, Yaroslavskoye sh., 26, phone +7 (495) 287-49-14, email: gia19952@gmail.com

Гоциридзе Георгий Паатович, аспирант кафедры «Гидравлики и Гидротехнического строительства (ИГЭС) Национального исследовательского Московского государственного строительного университета (НИУ МГСУ) 129337, г. Москва, Ярославское ш., д. 26, тел. +7 (495) 287-49-14, email: gia19952@gmail.com

Бестужева Александра Станиславовна, доцент, кандидат технических наук, доцент кафедры «Гидравлики и Гидротехнического строительства (ИГЭС) Национального исследовательского Московского государственного строительного университета (НИУ МГСУ) 129337, г. Москва, Ярославское ш., д. 26, тел. +7 (495) 287-49-14, email: alex_bestu@mail.ru

DOI:10.22337/2587-9618-2025-21-2-62-74

INVESTIGATION OF FAILURE OF RIVERBANK PROTECTION STRUCTURE: A CASE STUDY IN LONG AN PROVINCE, VIETNAM

Pham Ngoc Thinh, Dang Van Phu
Thuyloi University, 175 Tay Son, Dong Da, Hanoi, VIETNAM

Abstract: The riverbank protection structure is an essential structure constructed to protect the riverbank from the natural and human impact. Therefore, ensuring safety for this project is very important. However, this structure can still have technical failures during construction or working stages. The failure of riverbank protection structures poses significant challenges to infrastructure stability and environmental sustainability, particularly in regions with complex geotechnical conditions. Thus, this study aims to investigate the causes of the failure with the case study is the Long Hau riverbank protection project in Long An Province, Vietnam. In doing so, a combination of on-site observations and numerical simulations using PLAXIS 2D was employed to analyze the stability of the structure and identify potential failure mechanisms. The results revealed a displacement of 8.7 cm in the bearing pile and a total structural displacement of 19.2 cm obtained from the numerical analysis, which agree well with those from field observations. Key factor contributing to the failure is the selection of the structure position, consequently leading to insufficient soil compaction, uneven settlement, and underestimated lateral forces during design. The study highlights the critical need for comprehensive site assessments, detailed numerical modeling, and regular maintenance to ensure long-term stability. In addition, the findings provide valuable insights into riverbank protection practices and provide a basis for proposing appropriate solutions for future work.

Keywords: Riverbank erosion; Riverbank protection structure; Structural failure analysis; PLAXIS 2D simulation; Long Hau embankment; Structural displacement; Bearing pile; Lateral earth pressure

АНАЛИЗ РАЗРУШЕНИЯ БЕРЕГОЗАЩИТНОЙ КОНСТРУКЦИИ В ПРОВИНЦИИ ЛОНГ АН, ВЬЕТНАМ

Фам Нгок Тхинь, Данг Ван Фу
Университет Туйлой, 175 Тай Сон, Донг Да, г. Ханой, ВЬЕТНАМ

Аннотация: Сооружения для защиты берегов рек являются важными конструкциями, предназначенными для защиты береговой линии от естественного и антропогенного воздействия. Поэтому обеспечение безопасности для данного проекта имеет первостепенное значение. Тем не менее, эти сооружения могут иметь технические отказы во время строительства или эксплуатации. Разрушение берегоукрепительных сооружений создает серьезные проблемы для стабильности инфраструктуры и экологической устойчивости, особенно в регионах со сложными геотехническими условиями.

В связи с этим данное исследование направлено на изучение причин разрушения на примере проекта защиты берега реки Лонг Хау в провинции Лонг Ан, Вьетнам. Для этого была использована комбинация натурных наблюдений и численного моделирования с использованием PLAXIS 2D для анализа устойчивости сооружения и выявления потенциальных механизмов разрушения. Результаты показали смещение опорной сваи на 8,7 см и общее смещение конструкции на 19,2 см, полученные в результате численного анализа, которые хорошо согласуются с данными натурных наблюдений. Ключевым фактором, способствующим разрушению, является выбор положения конструкции, что приводит к недостаточному уплотнению грунта, неравномерной осадке и недооценке поперечных сил при проектировании.

В исследовании подчеркивается критическая необходимость комплексной оценки площадки, детального численного моделирования и регулярного технического обслуживания для обеспечения долгосрочной

стабильности. Кроме того, полученные результаты дают ценную информацию о практике защиты берегов рек и служат основой для предложения соответствующих решений для будущих работ.

Ключевые слова: Разрушение берегов рек; Берегоукрепительное сооружение; Анализ разрушения конструкции; Моделирование в PLAXIS 2D; Стена берегоукрепления Лонг Хау; Смещение конструкции; Опорная свая; Боковое давление грунта

1 INTRODUCTION

Riverbank protection structures are the essential structures that use technical solutions to stabilize and protect riverbanks from the impact of currents, waves, and other impacts. This structure system is especially important in areas prone to erosion. In areas with rapid urbanization and industrialization, such as in many developing countries, riverbank protection becomes extremely urgent because if erosion or bank subsidence is not well controlled, it can lead to serious consequences both economically and ecologically. Therefore, the design of protection structures must take into account the topographic, geological, and hydrological characteristics of the site. Specifically, morphology, soil composition, sediment loading, and flow velocity are factors that significantly influence the stresses and forces acting on the structure. Typical structural components of riverbank protection structures include reinforced concrete, retaining walls, anchor piles, and stone armor layers. These elements work together to resist natural erosional forces while ensuring minimal impact on the surrounding ecosystem. However, engineering challenges can arise when design specifications are flawed or environmental assessments are inadequate, which can compromise the effectiveness of the structure and lead to serious failures.

The failure of riverbank protection structures is a pressing issue that has garnered significant attention within the disciplines of geotechnical engineering, environmental science, and hydrology. Riverbank failures arise from a multifaceted interplay of natural and anthropogenic factors, including hydrodynamic forces, soil properties, and human interventions. Leng [1] highlights the critical role of geomorphological factors in the failure of riverbank protection structures, emphasizing the necessity for detailed site-specific assessments. Similarly, Akter et al. [2] underscore the importance of understanding hydrodynamic forces acting on geo-bag revetments, noting that these forces significantly influence failure mechanisms. Anthropogenic activities, such as sediment dredging and vegetation removal, exacerbate riverbank instability, as evidenced by Arora [3]. The geotechnical properties of soil play a pivotal role in riverbank stability. Chen and Wen [4] identify soil saturation caused by extreme rainfall and flooding as a primary factor increasing susceptibility to erosion and structural failure. Furthermore, Duong et al. [5] employed numerical modeling to demonstrate how hydraulic conductivity and rainfall intensity interact to destabilize riverbanks. Specific failure mechanisms, such as cantilever collapses resulting from undercutting, are particularly prevalent in cohesive soils [6], [7]. Patsinghasanee et al. [8] reveal through experimental investigations the significance of tension cracks and beam failures in cohesive riverbanks, highlighting the need for tailored engineering interventions to mitigate these risks. Vegetation is a critical factor in enhancing riverbank stability. Research by Abernethy and Rutherfurd [9] shows that even low root densities can substantially improve soil shear strength, thereby reducing failure risks. Conversely, the removal of vegetation contributes to increased erosion and instability, as demonstrated by Docker and Hubble [10], who found a strong correlation between devegetation and mass failure events. The broader implications of riverbank failures extend beyond immediate

structural concerns, as they pose significant environmental and economic challenges. Patsinghasanee et al. [11] investigated the fluvial erosion and overhanging failure of cohesive riverbank and reported that this is one of the significant problem of river engineering. Mamun et al. [12] highlights the adverse impact of erosion on agricultural productivity and food security in vulnerable regions. Economic consequences are particularly pronounced in urban settings, where infrastructure and cultural heritage are at risk. Weissgerber et al. [13] note that modifications to riverbanks often disrupt riparian ecosystems Morelli et al. [14] documented riverbank failures affecting historical sites in Florence, Italy, emphasizing the need for integrated management strategies that balance infrastructure protection with environmental sustainability.

In this study, the damage incident of the Long Hau riverbank protection structure in Long An Province is analyzed and evaluated. From there, the cause of the damage will be discussed through the results from observation and numerical simulation. The results of this paper can be a basis for proposing solutions to reinforce this riverbank protection structure in the future.

2 DAMAGE SITUATION OF THE INVESTIGATED RIVERBANK PROTECTION STRUCTURE

Fig. 1 shows the location of the project studied in this paper. The project is located in Long An Province, Vietnam. It aims to prevent riverbank erosion and maintain the stability of nearby infrastructure, which is vulnerable to seasonal fluctuations of the river flow and sedimentation. The project was scheduled to be completed in December 2023.



Figure 1. Location of Long Hau embankment

As shown in Fig. 2, this riverbank protection structure consists of a reinforced concrete retaining wall approximately 1.1 meters high and an average thickness of 20 cm. The retaining wall is designed to withstand significant lateral forces exerted by the river, especially during rainy seasons. Behind the wall, a compacted sand layer with a compactness K of 90% provides a support layer to minimize movement and displacement by evenly distributing the pressure load on the retaining wall. The retaining wall is connected to a series of 400 mm diameter and 28 m long prestressed concrete piles, which form the foundation of the structure, ensuring both vertical and horizontal stability. The piles are arranged in a grid pattern, with 3.0 m spacing both vertically and horizontally, each sector consisting of two vertical piles and one inclined pile. This configuration is intended to maximize load distribution and to counteract forces caused by land subsidence, flow, and sediment movement.

The foundation of the structure is reinforced with a layer of geotextile fabric under the sand layer to increase stability and prevent erosion phenomena, along with a series of tightly packed PVC-coated gabions at a depth of -6 meters along the riverbed. These gabions, dimensions of 200 cm x 100 cm x 50 cm, act as a protective barrier against erosion, creating a buffer zone that protects the foundations from direct hydrodynamic impact.

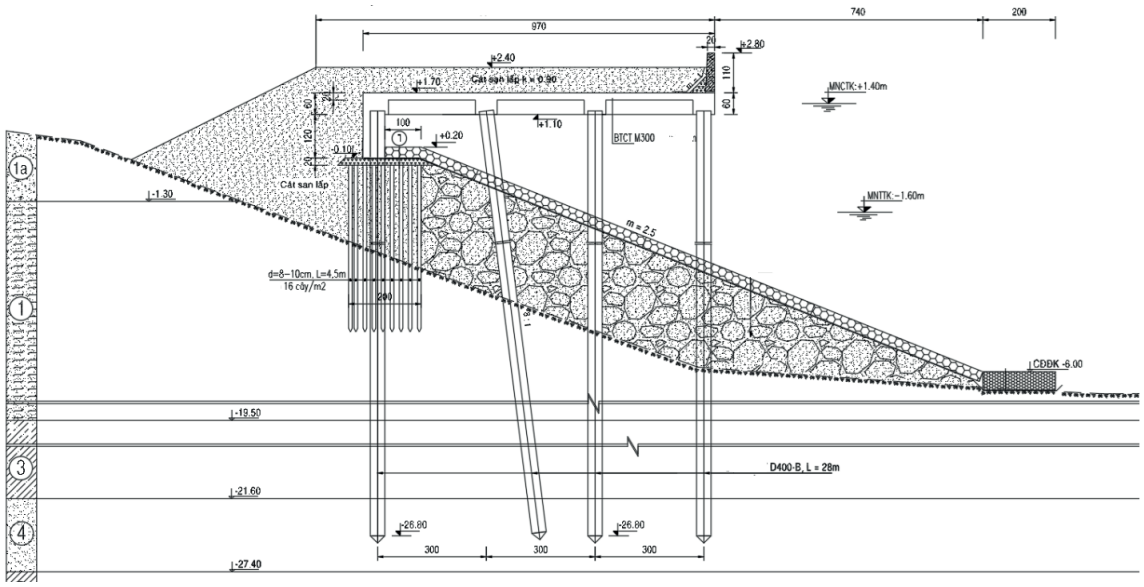


Figure 2. Long Hau embankment cross-section

As shown in Figs. 3 and 4, the Long Hau embankment began to show signs of failure soon after completion. Major issues included a displacement of approximately 20cm toward the river, visible cracks in the concrete piles, and settlement of the compacted sand layer behind the wall. These issues raised concerns about the long-term stability and resilience of the structure and posed potential risks to adjacent infrastructure and the ecosystem if not addressed promptly.



Figure 3. Settlement of the compacted sand layer after construction completion



Figure 4. Cracks on piles

These failures may be due to design or construction method deficiencies. The presence of cracks may indicate that the piles are not sufficiently resistant to surcharge load and lateral force. Similarly, lateral displacement towards the river may indicate a deviation in the safety system or a lack of force components in the calculation. The settlement of the sand layer behind the wall is due to uneven compaction. Solving these problems requires a comprehensive analysis of design and construction factors, focusing on soil interactions and material selection. Therefore, a safety assessment analysis for this structure is

required to find the main causes that may lead to displacement and subsequent pile cracking.

3 ASSESSMENT OF THE CURRENT STATUS OF THE PROJECT

3.1 Project Position

Fig. 5 shows the clear transformation of the regional riverbank from 2014 to 2024. The colored contours represent the positions of the riverbank in a specific timeline, such as 2014 (blue line), 2020 (red line), and 2024 (yellow line). These lines represent the progress of the riverbank movement through each stage. The 2014 riverbank is located close to the riverbed, representing the initial state of the riverbank before being greatly impacted by natural or human factors. The blue line shows that the extent of the riverbank remains relatively stable, without significant changes, indicating that the level of erosion or artificial intervention is still very limited. By 2020, the riverbank changes became more evident as the red line moved toward the landside compared to that observed in 2014. This can be explained by natural erosion or interference from construction and land exploitation activities near the riverbank area. This shift suggests a possible reduction in natural land area and also shows the impact of hydrological or human factors on the topographic structure of the area. The shoreline in 2024 (represented by the yellow line) is currently the newly designed embankment line. Noticeably, the position of the project is about 23.68 m from the shoreline. Choosing the centerline position far from the existing shoreline with this distance can create certain deviations in the calculation of loads and pressures on the embankment, especially the soil pressure from the backfilling foundation (highlighted in red color) after the completion of the project. The observation also shows that the incident occurred mostly in this area. It might be due to the fact that, during the design process, the impact of the backfilling foundation may not have been considered carefully, leading to the omission or underestimation of important impact forces. Specifically, the earth pressure and displacement of the foundation after backfilling are likely to put great pressure on the embankment, requiring additional reinforcement measures or appropriate structural solutions to maintain the stability of the structure. Therefore, it is necessary to carefully analyze the cause of this incident, from which appropriate solutions can be proposed to reinforce the structure at this location.

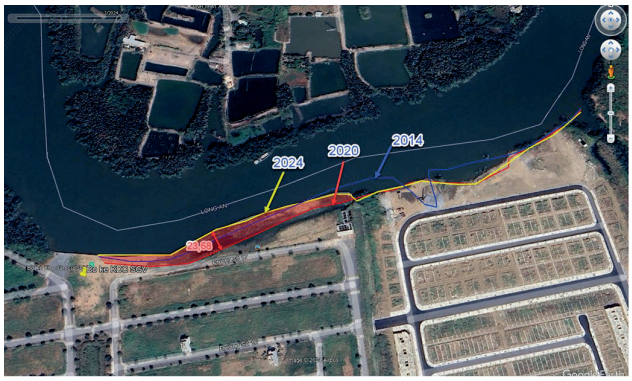


Figure 5. Location of shoreline in 2014 and 2020 and embankment in 2024

3.2 On-Site Observation

The field observation, which took place from August to September 2023, included 29 specific locations illustrated by the red area in Figure 5 and the red spot illustrated explicitly in Figure 6. The main objective of the observation was to systematically collect and observe at each location after the backfilling work, thereby assessing the actual condition of the project during construction. From there, it is possible to assess the safety level or detect the damage of the Long Hau embankment project.

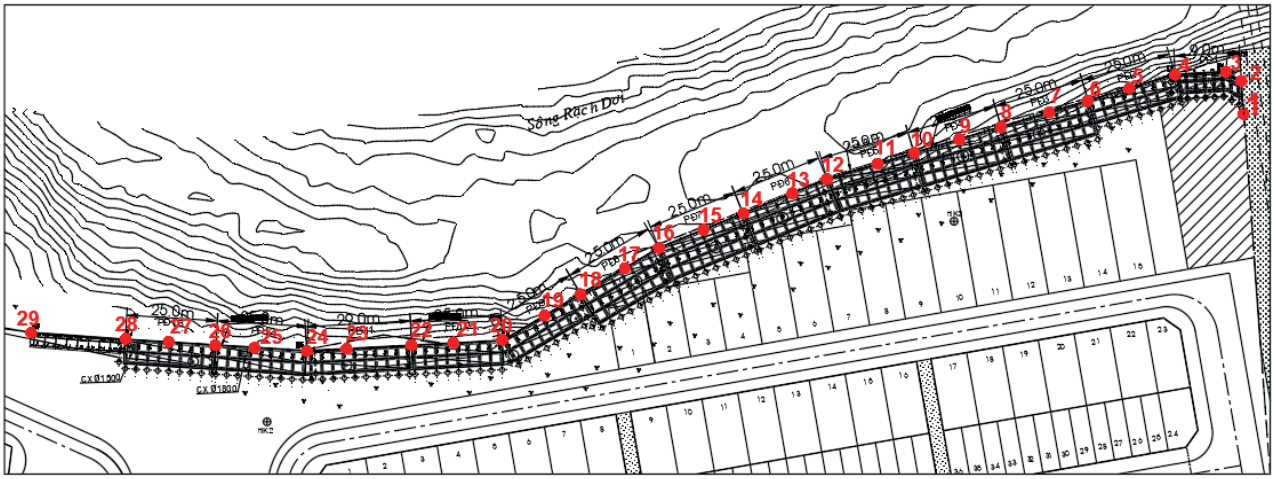


Figure 6. Locations for displacement observation

The results collected from the field observation have been summarized and presented in Fig.7. It can be seen that, after the backfilling on August 16, 2023, the project experienced displacement at 29 measurement points for the first observation. Especially at positions 10-16, the displacement value is quite large, about 11-16cm. After that, there were 10 more observations and the displacement value continued to increase to about 20cm for measurement positions 12 and 13. In addition, cracks have gradually appeared on the concrete piles and can cause unsafety for the project. From this, it can be seen that the design and construction work were not proper when not fully assessing the impact of backfilling on the project. This displacement may be due to horizontal soil pressure as well as the increased load of machinery and equipment during the backfilling process. In addition, the displacement is great at positions 10-16 due to the considerable area of backfilling compared to the other positions. Thus, the impact of the lateral active earth pressure at these positions is more significant. To verify the cause of this problem, numerical simulation analysis needs to be performed, as shown in the following section.

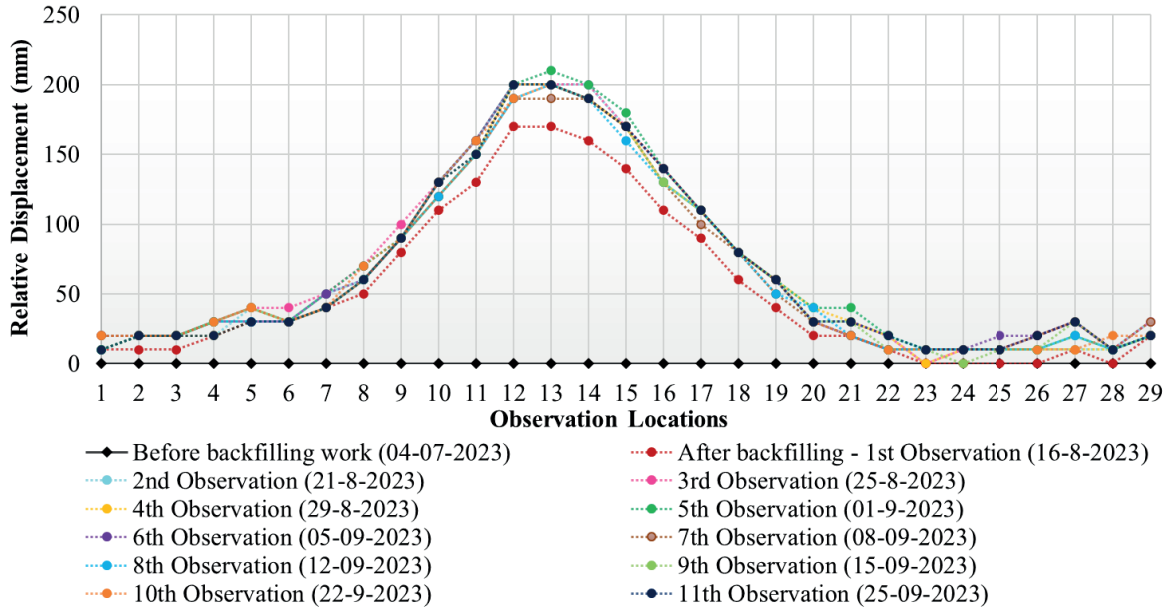


Figure 7. Relative displacement of the riverbank protection structure from the observation

3.3 Numerical analysis

Numerical analysis is widely employed to solve the engineering problem by various researchers [15, 16]. In this study, PLAXIS 2D software – a tool widely used by engineers and researchers to solve geotechnical problems [17, 18, 19] – was applied as a design tool to analyze the stability and determine the cause of geotechnical failures. The mechanical properties of the embankment together with the geotechnical properties of the embankment and foundation, were collected for analysis using the finite element method. To ensure the accuracy of the simulation, the boundary conditions were specifically set as follows: the bottom of the model was assumed to be completely fixed (fixed boundary), while the longitudinal boundaries only allowed vertical displacement to reflect the actual conditions at the site, as shown in Fig. 8.

The soil parts are modeled using six-node triangular isoperimetric elements with three Gaussian points per element as presented in Fig. 8. The Mohr-Coulomb (MC) model, an elastic-plastic model commonly used to simulate the general behavior of soils, requires five parameters: Young's modulus (E′), friction angle (φ'), Poisson's ratio (ν′), cohesion (c′), and dilatation angle (ψ′). For the case $\varphi' > 30^o$, dilatation angle (ψ′) is approximately $\varphi' - 30^o$ [20]. The material parameters are based on field data collected from geotechnical surveys and previous studies at the study site. The typical geological layers at the site include filling sand, silty clay, and soft clay. Field tests such as SPT (Standard Penetration Test) and laboratory tests, including triaxial compression and direct shear, are performed to determine important geotechnical parameters.

The Mohr-Coulomb model was chosen because of the relatively homogeneous geological characteristics in the study area. This model is simple but still meets the analysis requirements. However, to increase accuracy, the parameters were calibrated through comparison with field observations, ensuring that the model fully reflects actual conditions.

The connection between the embankment and the filling soil was also taken into account in the analysis by the rectangular interface elements, which consist of six nodes used between the soils and the structural elements [21]. The material properties used in the finite element simulation are detailed in Tables 1 and 2.

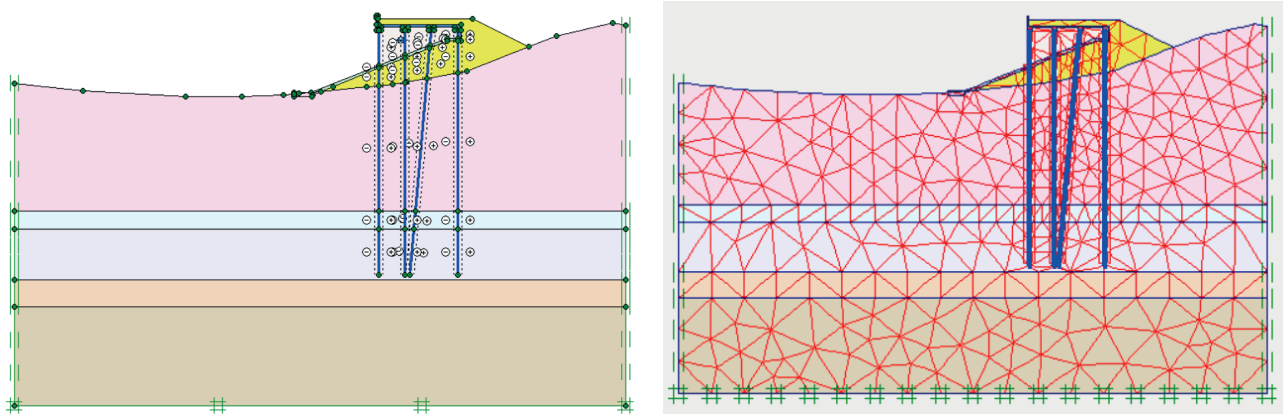


Figure 8. Numerical analysis in Plaxis 2D

Table 1. Parameters of the soil used in PLAXIS 2D

No.	Parameters	Units	Value							
1	Name		Fill sand	Rockfill	Layer 1	Layer 3	Layer 4	Layer 5	Layer 6	Concrete
2	Describe				Claye y silt	Silty clay	Sandy	Clay	Sandy	
3	Material model		MC	MC	MC	MC	MC	MC	MC	LE
4	Type of material behaviour		Drained (D)	Non porous	D	D	D	D	D	Non porous
5	Unsaturated weight	kN/m³	17.0	22.0	15.3	20.3	20.8	19.2	20.4	25.0
6	Saturated weight	kN/m³	18.0		15.5	20.8	21.1	19.6	20.8	
7	Horizontal Permeabilities	m/day	1.0		1.0	1.0	1.0	1.0	1.0	
8	Vertical Permeabilities	m/day	1.0		1.0	1.0	1.0	1.0	1.0	
9	SPT (N)	-			0÷3	5÷10	11÷22	13÷25	19÷26	
10	Stiffness	kN/m²								
	E_{50}^{ref}		7500.0	7500.0						2.15E+07
	E_{SPT}				678.9	3237.1	9723.8	3112.0	9293.3	
11	Poisson's ratio		0.3	0.3	0.4	0.4	0.4	0.4	0.3	0.2
12	Cohesion	kN/m²	1.0		5.6	14.6	6.2	34.1	5.7	0.2
	Friction angle	Deg.	30.0	45.0	3.4	10.1	24.0	14.2	24.2	
13	Angle of dilatancy	Deg.			0.0	0.0	0.0	0.0	0.0	
14	R_{int}			1.0	0.7	0.7	0.8	0.7	0.8	1.0

Table 2. Parameters of plate elements

Ord.	Parameters	Symbol	Units	D400-B
1	Material grade			*M800*
2	Young's Modulus	E_{ref}	kN/m²	4.00E+07
3	Dimension	h	m	0.40
4	Section area	A	m²	0.1257
5	Moment of inertial	I	m^4	1.26E-03
6	Spacing	s	m	3
7	Axial stiffness	EA	kN/m	1.68E+06
8	Flexural rigidity	EI	kNm²/m	1.68E+04
9	Equivalent plate thickness	d'	m	0.346
10	Weight	w	kN/m/m	1.19
11	Poisson's ratio	ν (nu)		0.2
12	Length	L	m	13.00
13	Allowable displacement	[d]	cm	-
14	Crack bending moment	$[M]_{kn}$	KN.m	75.00

The results of the pile displacement and the overall displacement are shown in Figure 9. It can be seen that the simulation results are quite close to the results from the field observations. The overall displacement value from the numerical analysis, which is 19.2 cm, agrees well with that from the field observation, which is 20.1 cm. The relative difference is only about 4.5%. This proves that the PLAXIS 2D model, with the calibrated material parameters and boundary conditions, is capable of reflecting the actual conditions in the study area quite accurately. However, a larger error was recorded in the pile displacement, which is 8.7 cm from the numerical analysis compared to 7.5 cm from the field observation. This may be due to the inaccuracy in simulating the connection between the pile and the ground or other nonlinear factors that have not been included in the model.

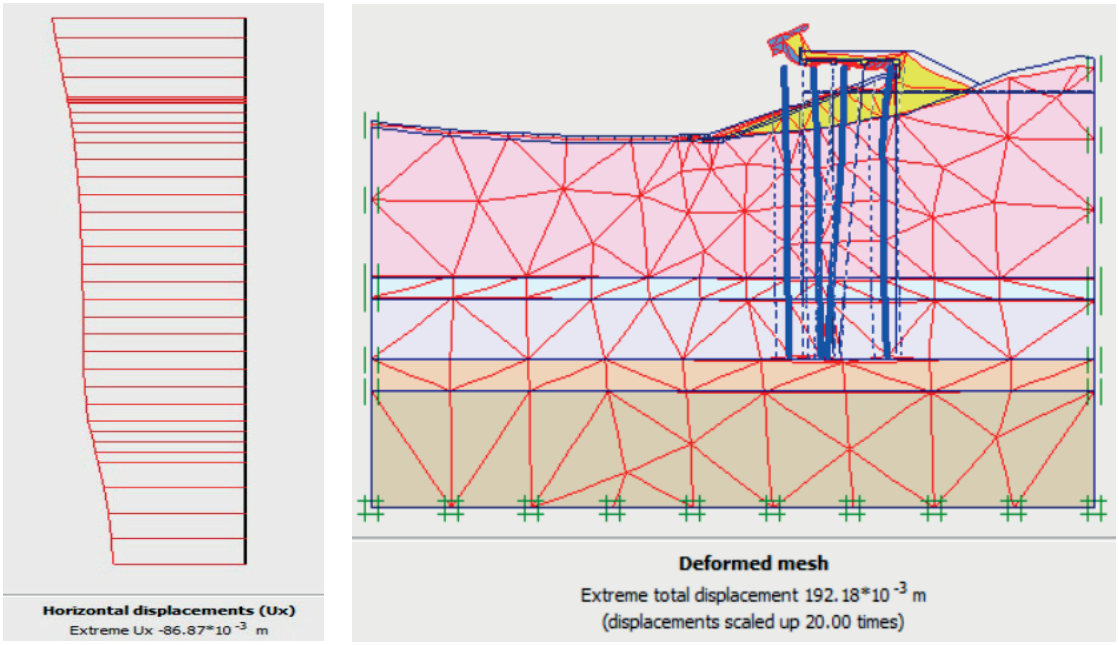


Figure 8. Pile displacement and total displacement.

The findings from this study provide important information to guide future design and maintenance practices for riverbank protection structures in Long An province, Vietnam. The detection of excessive displacement at critical locations, such as the center area of the embankment, indicates that additional reinforcement measures, such as increasing the cushion sand or using piles with higher resistance to lateral loads, are needed. At the same time, field observations demonstrate the importance of periodic inspections to detect early signs of deterioration and take corrective action before serious problems occur.

4 CONCLUSIONS

This study aims to assess the damage status of the embankment protection structure through observation and numerical analysis. In addition, this study also aims to detect the causes of the observed damage. From the analysis results, some conclusions can be drawn as follows:

The integrated approach of field observations and numerical simulations, as in this study, can become powerful methods to evaluate design performance and detect potential problems early in riverbank protection works.

The selection of the structure system position far away from the existing shoreline is one of the significant causes of failure. Because the

great lateral force from the backfill soil might not be carefully considered in the design stage or due to a not proper construction process. Thus, the structure is displaced by around 20 cm toward the riverside and the cracks patterns occur on the bearing piles as shown by the observed results. This result was confirmed by the numerical analysis using PLAXIS 2D.

In the context of globalization and climate change, increasingly affecting riverside areas, expanding similar studies internationally will provide more diverse data, helping to develop new design standards that are more suitable for different natural and economic conditions. This is a potential research direction and should be further developed in the future.

Future research should focus on integrating advanced simulation techniques and eco-engineering solutions to enhance the resilience of riverbank protection systems.

REFERENCES

1. **S. Leng**, "Riverbank protection structure failure factors and remedial approach: a case study in kelantan malaysia", Planning Malaysia, vol. 21, 2023. https://doi.org/10.21837/pm.v21i30.1397
2. **A. Akter, G. Pender, G. Wright, & M. Crapper,** "Predicting the hydrodynamic forces on geobag revetments", Journal of Flood Risk Management, vol. 4, no. 4, p. 328-338, 2011. https://doi.org/10.1111/j.1753-318x.2011.01117.x
3. **S. Arora**, "The riverbank vegetation for mitigating the adverse effects of sediment dredging", Ecohydrology, vol. 17, no. 5, 2024. https://doi.org/10.1002/eco.2656
4. **C. Chen and S. Wen**, "Failure mechanism of jinjiang riverbank based on geotechnical properties of soil", Advanced Materials Research, vol. 261-263, p. 1559-1562, 2011. https://doi.org/10.4028/www.scientific.net/amr.261-263.1559
5. **T. Duong, M. Do, & K. Yasuhara**, "Assessing the effects of rainfall intensity and hydraulic conductivity on riverbank stability", Water, vol. 11, no. 4, p. 741, 2019. https://doi.org/10.3390/w11040741
6. **S. Patsinghasanee, I. Kimura, Y. Shimizu, & M. Nabi,** "Cantilever failure investigations for cohesive riverbanks", Proceedings of the Institution of Civil Engineers - Water Management, vol. 170, no. 2, p. 93-108, 2017. https://doi.org/10.1680/jwama.15.00033
7. **T. Thi and D. Minh,** "Riverbank stability assessment under river water level changes and hydraulic erosion", Water, vol. 11, no. 12, p. 2598, 2019. https://doi.org/10.3390/w11122598
8. **S. Patsinghasanee, I. Kimura, & Y. Shimizu**, "Experimental and numerical study on overhanging failure of river bank", Journal of Japan Society of Civil Engineers Ser B1 (Hydraulic Engineering), vol. 71, no. 4, p. I_127-I_132, 2015. https://doi.org/10.2208/jscejhe.71.i_127
9. **B. Abernethy and I. Rutherfurd**, "The effect of riparian tree roots on the mass-stability of riverbanks", Earth Surface Processes and Landforms, vol. 25, no. 9, p. 921-937, 2000. https://doi.org/10.1002/1096-9837(200008)25:93.0.co;2-7
10. **B. Docker and T. Hubble**, "River bank collapse on the nepean river in the wallacia valley: assessing possible causes by historical and geomechanical methods", Journal and Proceedings of the Royal Society of New South Wales, vol. 134, no. 3-4, p. 65-78, 2001. https://doi.org/10.5962/p.361483
11. **S. Patsinghasanee, I. Kimura, & Y. Shimizu**, "Coupled study of fluvial erosion and overhanging failure for cohesive riverbanks", Journal of Japan Society of Civil Engineers Ser A2 (Applied Mechanics (Am)), vol. 71, no. 2, p. I_533-I_544, 2015. https://doi.org/10.2208/jscejam.71.i_533
12. **A. Mamun, A. Islam, E. Alam, S. Pal, & G. Alam,** "Assessing riverbank erosion and livelihood resilience using traditional approaches in northern bangladesh",

Sustainability, vol. 14, no. 4, p. 2348, 2022. https://doi.org/10.3390/su14042348

13. **M. Weissgerber, R. Jaunatre, F. Dommanget, F. Jacob, G. Huyghe, & A. Évette,** "Seeding dynamics from a local seed mixture on a bioengineered riverbank protection structure", Environmental Management, vol. 64, no. 2, p. 178-189, 2019. https://doi.org/10.1007/s00267-019-01180-9
14. **S. Morelli, V. Pazzi, L. Tanteri, M. Nocentini, L. Lombardi, G. Gigliet al.,** "Characterization and geotechnical investigations of a riverbank failure in florence, italy, unesco world heritage site", Journal of Geotechnical and Geoenvironmental Engineering, vol. 146, no. 10, 2020. https://doi.org/10.1061/(asce)gt.1943-5606.0002305
15. **Perelmuter, A.V., & Kabantsev, O.V.** (2018). About the problem of analysis resistance bearing systems in failure of a structural element. *International Journal for Computational Civil and Structural Engineering*, *14*(3), 103-113. https://doi.org/10.22337/2587-9618-2018-14-3-103-113
16. **Nikolay A. Aniskin, Stanislav A. Sergeev, Andrey V. Stupivtsev, Ilia A. Bokov**. (2024). Numerical solution of the filtration-deformation problem in the case of phased construction of a storage dam. *International Journal for Computational Civil and Structural Engineering, 20(3) 45–55*. https://doi.org/10.22337/2587-9618-2024-20-3-45-55
17. **C.-C. Fan and Y.-S. Fang,** "Numerical solution of active earth pressures on rigid retaining walls built near rock faces," *Computers and Geotechnics*, vol. 37, no. 7, pp. 1023–1029, 2010. http://dx.doi.org/10.1016/j.compgeo.2010.08.004
18. **Y. Yu, I. P. Damians, and R. J. Bathurst**, "Influence of choice of FLAC and PLAXIS interface models on reinforced soil–structure interactions," *Computers and Geotechnics*, vol. 65, pp. 164–174, 2015. https://doi.org/10.1016/j.compgeo.2014.12.009
19. **Khoirunisaa, T., Setiawan, B., & Purwana, Y. M.** (2023). Comparative study of axial bearing capacity for pile foundation based on empirical, numerical method and pile driving analyzer test . *International Journal for Computational Civil and Structural Engineering*, *19*(4), 196-207. https://doi.org/10.22337/2587-9618-2023-19-4-196-207
20. **M. Bolton, "**The strength and dilatancy of sands," *Géotechnique*, vol. 36, no. 1, pp. 65–78, 1986.
21. **R. Brinkgreve and W. Broere**, *PLAXIS 2D Reference Manual 2015*. Delft, Netherlands: Plaxis, 2010.

СПИСОК ЛИТЕРАТУРЫ

1. **S. Leng**, "Riverbank protection structure failure factors and remedial approach: a case study in kelantan malaysia", Planning Malaysia, vol. 21, 2023. https://doi.org/10.21837/pm.v21i30.1397
2. **A. Akter, G. Pender, G. Wright, & M. Crapper,** "Predicting the hydrodynamic forces on geobag revetments", Journal of Flood Risk Management, vol. 4, no. 4, p. 328-338, 2011. https://doi.org/10.1111/j.1753-318x.2011.01117.x
3. **S. Arora**, "The riverbank vegetation for mitigating the adverse effects of sediment dredging", Ecohydrology, vol. 17, no. 5, 2024. https://doi.org/10.1002/eco.2656
4. **C. Chen and S. Wen**, "Failure mechanism of jinjiang riverbank based on geotechnical properties of soil", Advanced Materials Research, vol. 261-263, p. 1559-1562, 2011. https://doi.org/10.4028/www.scientific.net/amr.261-263.1559
5. **T. Duong, M. Do, & K. Yasuhara**, "Assessing the effects of rainfall intensity and hydraulic conductivity on riverbank

stability", Water, vol. 11, no. 4, p. 741, 2019. https://doi.org/10.3390/w11040741

6. **S. Patsinghasanee, I. Kimura, Y. Shimizu, & M. Nabi,** "Cantilever failure investigations for cohesive riverbanks", Proceedings of the Institution of Civil Engineers - Water Management, vol. 170, no. 2, p. 93-108, 2017. https://doi.org/10.1680/jwama.15.00033
7. **T. Thi and D. Minh,** "Riverbank stability assessment under river water level changes and hydraulic erosion", Water, vol. 11, no. 12, p. 2598, 2019. https://doi.org/10.3390/w11122598
8. **S. Patsinghasanee, I. Kimura, & Y. Shimizu**, "Experimental and numerical study on overhanging failure of river bank", Journal of Japan Society of Civil Engineers Ser B1 (Hydraulic Engineering), vol. 71, no. 4, p. I_127-I_132, 2015. https://doi.org/10.2208/jscejhe.71.i_127
9. **B. Abernethy and I. Rutherfurd**, "The effect of riparian tree roots on the mass-stability of riverbanks", Earth Surface Processes and Landforms, vol. 25, no. 9, p. 921-937, 2000. https://doi.org/10.1002/1096-9837(200008)25:93.0.co;2-7
10. **B. Docker and T. Hubble**, "River bank collapse on the nepean river in the wallacia valley: assessing possible causes by historical and geomechanical methods", Journal and Proceedings of the Royal Society of New South Wales, vol. 134, no. 3-4, p. 65-78, 2001. https://doi.org/10.5962/p.361483
11. **S. Patsinghasanee, I. Kimura, & Y. Shimizu**, "Coupled study of fluvial erosion and overhanging failure for cohesive riverbanks", Journal of Japan Society of Civil Engineers Ser A2 (Applied Mechanics (Am)), vol. 71, no. 2, p. I_533-I_544, 2015. https://doi.org/10.2208/jscejam.71.i_533
12. **A. Mamun, A. Islam, E. Alam, S. Pal, & G. Alam,** "Assessing riverbank erosion and livelihood resilience using traditional approaches in northern bangladesh", Sustainability, vol. 14, no. 4, p. 2348, 2022. https://doi.org/10.3390/su14042348
13. **M. Weissgerber, R. Jaunatre, F. Dommanget, F. Jacob, G. Huyghe, & A. Évette,** "Seeding dynamics from a local seed mixture on a bioengineered riverbank protection structure", Environmental Management, vol. 64, no. 2, p. 178-189, 2019. https://doi.org/10.1007/s00267-019-01180-9
14. **S. Morelli, V. Pazzi, L. Tanteri, M. Nocentini, L. Lombardi, G. Gigliet al.,** "Characterization and geotechnical investigations of a riverbank failure in florence, italy, unesco world heritage site", Journal of Geotechnical and Geoenvironmental Engineering, vol. 146, no. 10, 2020. https://doi.org/10.1061/(asce)gt.1943-5606.0002305
15. **Perelmuter, A.V., & Kabantsev, O.V.** (2018). About the problem of analysis resistance bearing systems in failure of a structural element. *International Journal for Computational Civil and Structural Engineering*, *14*(3), 103-113. https://doi.org/10.22337/2587-9618-2018-14-3-103-113
16. **Nikolay A. Aniskin, Stanislav A. Sergeev, Andrey V. Stupivtsev, Ilia A. Bokov**. (2024). Numerical solution of the filtration-deformation problem in the case of phased construction of a storage dam. *International Journal for Computational Civil and Structural Engineering, 20(3) 45–55*. https://doi.org/10.22337/2587-9618-2024-20-3-45-55
17. **C.-C. Fan and Y.-S. Fang,** "Numerical solution of active earth pressures on rigid retaining walls built near rock faces," *Computers and Geotechnics*, vol. 37, no. 7, pp. 1023–1029, 2010. http://dx.doi.org/10.1016/j.compgeo.2010.08.004
18. **Y. Yu, I. P. Damians, and R. J. Bathurst**, "Influence of choice of FLAC and PLAXIS interface models on reinforced soil–

structure interactions," *Computers and Geotechnics*, vol. 65, pp. 164–174, 2015. https://doi.org/10.1016/j.compgeo.2014.12.009

19. **Khoirunisaa, T., Setiawan, B., & Purwana, Y. M.** (2023). Comparative study of axial bearing capacity for pile foundation based on empirical, numerical method and pile driving analyzer test. *International Journal for Computational Civil and Structural Engineering*, *19*(4), 196-207. https://doi.org/10.22337/2587-9618-2023-19-4-196-207
20. **M. Bolton, "**The strength and dilatancy of sands," *Géotechnique*, vol. 36, no. 1, pp. 65–78, 1986.
21. **R. Brinkgreve and W. Broere**, *PLAXIS 2D Reference Manual 2015*. Delft, Netherlands: Plaxis, 2010.

Ngoc Thinh, Pham – Ph.D., Thuyloi University, 175 Tay Son, Dong Da, Hanoi, Vietnam, thinhtls@tlu.edu.vn. Tel: +84947231186

Van Phu, Dang – Ph.D., Thuyloi University, 175 Tay Son, Dong Da, Hanoi, Vietnam, phudv@tlu.edu.vn

Фам Нгок Тхинь – Университет Туйлой, 175 Тай Сон, Донг Да, Ханой (Вьетнам). E-mail: thinhtls@tlu.edu.vn. Номер телефона: +84947231186;

Данг Ван Фу – Университет Туйлой, 175 Тай Сон, Донг Да, Ханой (Вьетнам). E-mail: phudv@tlu.edu.vn.

International Journal for Computational Civil and Structural Engineering, 21(2) 75–82 (2025)

DOI:10.22337/2587-9618-2025-21-2-75-82

MATHEMATICAL MODELING OF SWIRLING FLOW IN A VORTEX DUST SEPARATOR

Vadim K. Akhmetov

Moscow State University of Civil Engineering, Moscow, RUSSIA

Abstract. The problem of swirling flow motion in an axisymmetric channel is numerically investigated. The results of flow field calculation are obtained by solving the Navier-Stokes equations. Various flow regimes with formation of axial recirculation zones are presented. A convective diffusion model is used to determine the concentration of flow particles and the formation of characteristic sedimentation zones. The obtained numerical solutions are compared with the results of available experimental data.

Keywords: swirling flows, two-phase flow, finite-difference method, convection-diffusion model, particle sedimentation

МАТЕМАТИЧЕСКОЕ МОДЕЛИРОВАНИЕ ЗАКРУЧЕННОГО ТЕЧЕНИЯ В ВИХРЕВОМ ПЫЛЕОТДЕЛИТЕЛЕ

В.К. Ахметов

Национальный исследовательский Московский государственный строительный университет, Москва, РОССИЯ

Аннотация. Численно исследована задача о движении закрученного потока в осесимметричном канале. Результаты расчета поля течения получены решением системы уравнений Навье-Стокса. Представлены различные режимы течения с образованием осевых зон рециркуляции. Для определения концентрации частиц потока и формирования характерных зон осаждения использована модель конвективной диффузии. Проведено сравнение полученных численных решений с результатами имеющихся экспериментальных данных.

Ключевые слова: закрученные течения, двухфазный поток, метод конечных разностей, конвективно-диффузионная модель, осаждение частиц

1. INTRODUCTION

Swirling flows have a wide usage in various technical applications. They can be observed in natural phenomena and are the object of theoretical and experimental study. The most important properties of swirling flows are described in [1, 2]. The structure of swirling flows in channels limited by solid walls was investigated numerically in [3-5]. Free flows in an unlimited medium were studied numerically in [6, 7]. Experimental data on the flow structure were presented in [8-10]. The stability of swirling flows was studied in [11-14].

Many engineering applications utilize swirling flows that contain particulate admixtures. The properties of swirling flow are used in cyclone-type devices for gas cleaning against dust, separation of particles, separation of liquid mixtures, in particular for purification of produced oil, in swirl nozzles for atomization of liquids, in drying chambers for removal of moisture from polydisperse products, in chemical, food, construction industries and in agricultural production.

This study considers swirling two-phase flow in a straight-flow cyclone dust separator. Devices of this type are used in air cleaning plants. The principle of operation of the dust separator is as follows. Dusty gas through the tangential swirler 1 enters the pre-separation chamber 2 (figure 1). Here coarse dust is separated. It is

then ejected through tangentially located outlets 3. Fine dust together with the gas moves further in radial direction to the axis of the vortex chamber 5. Due to the action of centrifugal forces, the dust is separated and removed through a number of annular slits 6 in the side surface of the channel.

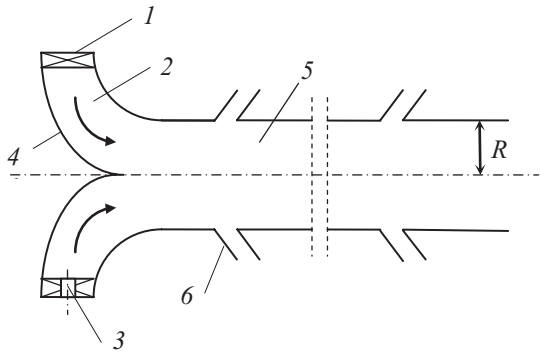


Figure 1. Flow diagram

Experimental studies of the considered device were carried out in [15]. The objective of this study is to develop a mathematical model and investigate the process of particle deposition under the action of swirling flow.

2. PROBLEM STATEMENT AND RESEARCH METHOD

A model problem of two-phase swirling flow in a cylindrical channel of radius R is examened. Finely dispersed particles are considered as a discrete system, which is carried by the flow without affecting it inversely. In cylindrical coordinate system r, φ, z, the Navier-Stokes equations can be represented with respect to the flow function ψ, vorticity Ω and azimuthal velocity V_φ as follows:

$$\frac{1}{r}\frac{\partial^2\psi}{\partial z^2}+\frac{\partial}{\partial r}\left(\frac{1}{r}\frac{\partial\psi}{\partial r}\right)=-\Omega, \qquad (1)$$

$$\frac{\partial\Omega}{\partial t}+\frac{\partial}{\partial z}\left(V_z\Omega\right)+\frac{\partial}{\partial r}\left(V_r\Omega\right)=$$
$$=\frac{1}{\mathrm{Re}}\left[\frac{\partial^2\Omega}{\partial z^2}+\frac{\partial^2\Omega}{\partial r^2}+\frac{\partial}{\partial r}\left(\frac{\Omega}{r}\right)\right]+G^2\frac{1}{r}\frac{\partial\left(V_\varphi\right)^2}{\partial z}, \qquad (2)$$

$$\frac{\partial V_\varphi}{\partial t}+\frac{\partial}{\partial z}\left(V_zV_\varphi\right)+\frac{1}{r}\frac{\partial}{\partial r}\left(rV_rV_\varphi\right)+\frac{V_rV_\varphi}{r}=$$
$$=\frac{1}{\mathrm{Re}}\left[\frac{\partial^2V_\varphi}{\partial z^2}+\frac{1}{r}\frac{\partial}{\partial r}\left(r\frac{\partial V_\varphi}{\partial r}\right)-\frac{V_\varphi}{r^2}\right], \qquad (3)$$

$$V_r=-\frac{1}{r}\frac{\partial\psi}{\partial z},\ V_z=\frac{1}{r}\frac{\partial\psi}{\partial r},\ \Omega=\frac{\partial V_r}{\partial z}-\frac{\partial V_z}{\partial r}\ . \qquad (4)$$

The system of equations (1)-(4) is written in the conservative dimensionless form. Axial V_z and radial V_r velocities are related with the characteristic value U, azimuthal velocity V_φ is related with the value W_0, coordinates are related with radius R, time is related with the ratio R/U. The equation system (1)-(4) contains two dimensionless parameters: Reynolds number $\mathrm{Re}=UR/\nu$, where ν is the kinematic viscosity, and swirl parameter $G=W_0/U$.

The solution of the problem under consideration was defined in the domain $D(0\le z\le z_k,\ 0\le r\le 1)$. The velocity distribution in the initial cross section was assumed to be as follows:

$$V_{z0}=1,\quad V_{r0}=0,$$
$$V_{\varphi0}=\frac{b_1}{r}(1-\exp(-b_2r^2)),\quad 0\le r\le 1,\quad z=0,$$

where $b_1=0.554$, $b_2=8$.

At the lateral surface $r=1$, the adhesion conditions were specified. At the axis $r=0$, the symmetry conditions were specified. At the exit from the channel for $z=z_k$, soft boundary conditions were assigned. The set of boundary conditions in the variables flow function ψ and vorticity Ω is represented in dimensionless form as follows:

$$\psi = \frac{r^2}{2}, V_\varphi = V_{\varphi 0}(r), \quad \frac{\partial \psi}{\partial z} = 0, 0 \le r \le 1, z = 0,$$
$$\psi = \frac{1}{2}, \; V_\varphi = 0, \; \frac{\partial \psi}{\partial r} = 0, \; 0 \le z \le z_k, \; r = 1, \quad (5)$$
$$\psi = 0, \quad V_\varphi = 0, \quad \Omega = 0, \quad 0 \le z \le z_k, \quad r = 0,$$
$$\frac{\partial \psi}{\partial z} = \frac{\partial \Omega}{\partial z} = \frac{\partial V_\varphi}{\partial z} = 0, \quad 0 \le r \le 1, \quad z = z_k .$$

To solve the boundary value problem (1)-(4) at boundary conditions (5), the block iteration method was employed, which was successfully used, for example, in [16, 17] to analyze swirling flows of various types. A uniform 81x256 grid was utilized. The time step was chosen in the range from 0.05 to 0.2.

3. CONVECTION-DIFFUSION MODEL

Among all the forces acting on a particle in a vortex dust separator, the most significant is the Stokes viscous resistance force. In cylindrical coordinates, the equations of particle motion under the action of this force have a dimensionless form:

$$\frac{dV_{zs}}{dt} = \frac{1}{2\,\mathrm{St}}(V_z - V_{zs}), \quad (6)$$

$$\frac{dV_{rs}}{dt} = G^2 \frac{V_{\varphi s}^2}{r} + \frac{1}{2\,\mathrm{St}}(V_r - V_{rs}), \quad (7)$$

$$\frac{dV_{\varphi s}}{dt} = -\frac{V_{rs} V_{\varphi s}}{r} + \frac{1}{2\,\mathrm{St}}(V_\varphi - V_{\varphi s}). \quad (8)$$

Where $\mathrm{St} = (\rho_s r_s^2 U)/(9\nu\rho R)$ is the Stokes number, and the index s is associated with particles. According the equations (6), (8) axial V_{zs} and azimuthal $V_{\varphi s}$ particle velocities coincide with the corresponding velocities of the main flow for $\mathrm{St} << 1$. Радиальная скорость частиц V_{rs} определяется уравнением (7), из которого при условиях $\mathrm{St} << 1$, $G^2\,\mathrm{St} = O(1)$ получаем

If the conditions $\mathrm{St} << 1$, $G^2\,\mathrm{St} = O(1)$ are met, the radial velocity of particles V_{rs} can be determined using equation (7) as follows:

$$V_{rs} - V_r = 2\,\mathrm{St}\,G^2 \frac{V_{\varphi s}^2}{r}. \quad (9)$$

Since the considered flow includes a recirculation zone and significantly inhomogeneous velocity and concentration fields, two approaches were also investigated using averaging procedures with respect to r for the calculation of the V_{rs}. In the first one, the deposition velocity was determined as a function by averaging (9) with respect to r as follows:

$$V_{rs}(z) = 2StG^2 \left\langle V_{\varphi s}^2 / r \right\rangle + \left\langle V_{rs} \right\rangle. \quad (10)$$

In the second approach, the effective deposition velocity V_{rs}^* was introduced by the following relation:

$$\frac{1}{r}\int_0^r V_{rs}\, c r\, dr = V_{rs}^* \int_0^r c\, dr. \quad (11)$$

where the left part is the averaged flow $V_{rs}cr$ at the range $[0, r]$, and the right part is the effective flow calculated for velocity $V_{rs}^* = V_{rs}^*(z,t)$ and total partial concentration at the range $[0, r]$.

Consider the process of particle transportation for the calculated flows. Following the method based on the convection-diffusion model for mixtures of gas with small low-inertia particles, we can neglect the inverse effect of particles on the fluid flow (passive admixture approximation). The velocity field is found using equations (6)-(8). The equation of conservation of mass of particles is transformed to the diffusion equation for a passive scalar

$$\frac{\partial c}{\partial t}+\frac{\partial}{\partial z}(V_z c)+\frac{1}{r}\frac{\partial}{\partial r}(rV_{rs} c)= \\ =\frac{1}{\mathrm{Re}\,\mathrm{Sc}}\left[\frac{\partial^2 c}{\partial z^2}+\frac{1}{r}\frac{\partial}{\partial r}\left(r\frac{\partial c}{\partial r}\right)\right], \quad (12)$$

where c is the particle concentration, $\mathrm{Sc} = \nu/D$ is the Schmidt number, D is the diffusion factor. The convection-diffusion equation (12) has been used to simulate flows of mixtures with particle mass loss by deposition on walls, e.g., in [18, 19].

To determine V_{rs}, we shall consider three models in which the deposition velocity is defined by (12) similarly to $V_{rs}(z)$ by (10), or similarly to $V_{rs}^*(z,t)$ by (11), or by solving equation (7) with the condition $V_{rs}(z,0,t)=0$.

The boundary conditions for equation (12) can be written as follows:

$$z=0: c=1,\ r_1\le r\le r_2;\ c=0,\ r<r_1, r>r_2, \quad (13)$$

$$z=z_k:\ \frac{\partial c}{\partial z}=0,\quad 0\le r\le 1, \quad (14)$$

$$r=0,\ r=1:\ \frac{\partial c}{\partial r}=0,\quad 0\le z\le z_k. \quad (15)$$

In the calculations, $r_1=0.1$, $r_2=0.9$, $z_k=10$ were assumed according to [15].

By integrating equation (12) over the initial volume, taking into account boundary conditions (13)-(15), we obtain

$$2\pi\frac{\partial}{\partial t}\int_0^1\int_0^{z_k} r\,c\,dr\,dz+2\pi\int_0^1 (rV_z c)\big|_{z=z_k}dr+ \\ +2\pi\int_0^{z_k}(rV_{rs} c)\big|_{r=1}dz=0. \quad (16)$$

In accordance with (16), the following integral characteristics have been introduced: the particle flow rates Q_k and Q_b through the outlet section of the tube at $z=z_k$ and the side surface at $r=1$, respectively, as well as the particle mass m_f located in the volume under consideration:

$$Q_k(t)=2\pi\int_0^1 r(V_z c)\big|_{z=z_k}dr,$$

$$Q_b(t)=2\pi\int_0^{z_k} r(V_{rs} c)\big|_{r=1}dz,$$

$$m_f(t)=2\pi\int_0^{z_k}\int_0^1 cr\,dr\,dz.$$

According to these notations, equation (16) will take the form:

$$\frac{\partial}{\partial t}(m_f(t))+Q_k(t)+Q_b(t)=0. \quad (17)$$

By integrating equation (17) over time, we can determine the mass of particles m_k, which came out through the exit section, and the mass of particles m_b, which remained on the side surface:

$$m_k=\int_0^T Q_k(t)\,dt,\quad m_b=\int_0^T Q_b(t)\,dt.$$

The effects of particle reflection during deposition on the lateral surface $r=1$ are not considered. It is assumed that the particle flow $j=D\,\partial c/\partial r+V_{rs}\,c$ is determined only by the convective component, and the influence of diffusion is not taken into account, i.e., $(\partial c/\partial r=0)$.

The boundary value problem (12)-(15) was solved using the difference scheme applied to the transportation equations (2), (3). The main calculations were carried out using the relation (10).

4. RESULTS

In [15], a straight-flow vortex dust separator with the following parameters was investigated.

The length of the channel working part L was 1 m, the Reynolds number calculated from the average flow velocity and channel radius of 0.05 m was Re ~ 10^5, and the swirl parameter G was varied from 0 to 4.

In the present study, the flow fields corresponding to the boundary value problem (1)-(5) were calculated for values of Reynolds numbers Re = 1000, 2000, 2500 and swirl parameter G = 3.6. In this case, a region of return flow was formed in the channel, which started in the vicinity of the inlet section and extended to the channel exit. The axial velocity profiles along the cross-sections practically did not change and weakly depended on the Reynolds number.

The typical profile $V_z(r)$ obtained by solving the boundary value problem (1)-(5) at Re = 1000 in section z = 2.5 is shown in figure 2 (curve *4*). Symbols 5-7 in this figure correspond to the measurement data [15] for flow rates Q = 0.3, 0.25, 0.2 kg/s and show the auto modeling of the profiles by flow rate.

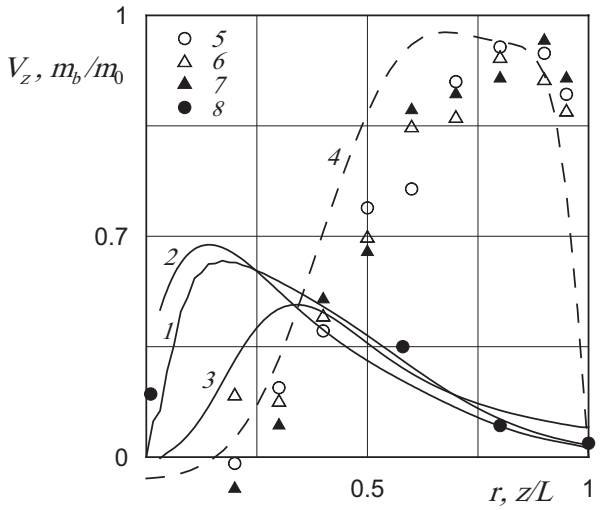


Figure 2. Comparison of computational models with experiments. Mass mb /m0 at r = 1 (models 1-3 for Vrs), data [15] (8), axial velocity $V_z(r)$ (4), flow rate [15] Q = 0.3; 0.25; 0.2 kg/s (5-7)

Generally, the obtained numerical results qualitatively correctly describe the structure of the investigated flow, including the diameter of the near-axis recirculation zone.

To investigate the dust separation process we will use the found velocity field at Re = 1000, G = 3.6.

In experiments [15], quartz dust with a particle diameter of $d'_s = 5.5$ μm and density of $\rho'_s = 2000$ kg/m3 (respectively $\rho_s = \rho'_s / \rho = 1550$) were used. The dimensionless particle radius for the calculations is determined as follows. If $\mathrm{Re}_s < 1$, where $\mathrm{Re}_s = V_{rs}\, r_s / \nu$ is the Reynolds number for the particles, the resistance coefficient is expressed by Stokes' law $c_d = 12 / \mathrm{Re}_s$. Hence, the calculated particle radius is related to the particle radius in the experiment by the expression

$$r_s = r_s^* \sqrt{\mathrm{Re}^* / \mathrm{Re}}\,, \qquad (18)$$

where the values with asterisks refer to the experiment. In [15], the value Re_s was in the transition from laminar to turbulent regime $1 < \mathrm{Re}_s < 500$. In this case, the resistance coefficient is $c_d = 12 / \mathrm{Re}_s^{0,6}$, and the relation (18) for r_s takes the form:

$$r_s = r_s^* (\mathrm{Re}^* / \mathrm{Re})^{3/8}. \qquad (19)$$

Substituting the above parameter values into (19), we obtain $r_s = (0.2 - 0.3) \cdot 10^{-4}$.

Figure 2 (curves 1-3) presents results for mass m_b/m_0, where $m_0 = m_f(0)$, of particles deposited on the lateral surface as a function of length distribution z/L which have been obtained by solving the boundary value problem (12)-(15) at Re =1000, G = 3.6, ρ_s = 1550, r_s = 0.2 104 for all three approaches of finding V_{rs}. Maximum particle deposition is observed at z/L = 0.22-0.35 (z/L = 0.3 in the experiment). At $z/L \geq 0.3$, relations 1-3 practically coincide. Comparison of the obtained data with the experiment [15] (symbols 8) confirms the suitability of the proposed approach using the convective diffusion equation (12) for modeling the transport and deposition of particles in swirlers.

The total mass of particles m_k/m_0, passed through the exit section $z = z_k$, as well as in [15], is about 0.04.

5. CONCLUSIONS

These calculations give a sufficiently detailed view of the dust separation process using the properties of swirled flow. The used mathematical model allows to describe accurately enough the main properties of the flow, such as: the formation of recirculation zones, the emergence of rarefaction in the vicinity of the flow axis under the action of the swirler, the drift of fine dispersed particles by the flow through the side surface of the straight-flow dust separator. There is a general agreement of the calculations with the experimental data.

REFERENCES

1. **Gupta A.K, Lilley D.G, Syred N.** Swirl Flows 1984 (Abacus Press)
2. **Alekseenko S.V., Kuibin P.A., Okulov V.L.** Introduction to theory of concentrated vortices. Moskow–Izhevsk: Institute of Computer Science. 2005. 504 p.
3. **Wang Y., Xingjian Wang X., Yang V.** Evolution and transition mechanisms of internal swirling flows with tangential entry // Physics of Fluids. 2018. Vol. 30. 013601.
4. **Ogus G., Baelmans M., Vanierschot M.** On the flow structures and hysteresis of laminar swirling jets // Physics of Fluids. 2016. Vol. 28. 123604.
5. **Akhmetov V.K., Shkadov V.Ya., Shkadova V.P.** Mixing of hot gases in an axisymmetric channel with a pre-swirled flow // Fluid Dynamics. 2006. Vol. 41. Pp. 504-513.
6. **Orlandi P.** Two-dimensional and three-dimensional direct numerical simulation of co-rotating vortices // Physics of Fluids. 2007. Vol. 19. 013101.
7. **Akhmetov V.K., Shkadov V.Ya.** Ustoychivost svobodnykh i ogranichennykh zakruchennykh techeniy s zonami retsirkulyatsii // Inzhenernaya fizika. 2008. № 6. S. 6-13 (in Russian).
8. **Oberleithner K., Paschereit C., Seele R., Wygnanski T.** Formation of turbulent vortex breakdown: intermittency, criticality, and global instability // AIAA Journal. 2012. Vol. 50. № 7**.** Pp. 1437-1452.
9. **Escudier M.P., Nickson A.K., Poole R.J.** Influence of outlet geometry on strongly swirling turbulent flow through a circular tube // Physics of Fluids. 2006. Vol. 18. 125103.
10. **Mergheni M.A., Riahi Z., Sautet J.C., Nasrallah S.B.** Swirl effects on dynamics characteristics of a coaxial jet // Thermal Science. 2017. Vol. 21. № 6. Pp. 2543-2552.
11. **Blanco-Rodríguez F.J., Rodríguez-García J.O., Parras L., del Pino C.** Optimal response of Batchelor vortex // Physics of Fluids. 2017. Vol. 29. 064108.
12. **Yadav N.K., Samanta A.** The stability of compressible swirling pipe flows with density stratification // Journal of Fluid Mechanics. 2017. Vol. 823. Pp. 689-715.
13. **Delbende I., Rossi M.** Nonlinear evolution of a swirling jet instability // Physics of Fluids. 2005. Vol. 17. 044103.
14. **Akhmetov V.K.** Gidrodinamicheskaya ustojchivost' kontrvihrevyh techenij // Gidrotekhnicheskoe stroitel'stvo. 2018. № 2. S. 13-18 (in Russian).
15. **Kutateladze S.S., Volchkov E.P., Terekhov V.I.** Aerodynamics and heat and mass exchange in bounded vortex flows. Novosibirsk: Institute of thermophysics, 1987. 283 p. (in Russian).
16. **Akhmetov V.K., Shkadov V.Ya.** Chislennoe issledovanie recirkulyacionnyh zon v vihrevoj kamere // Aeromekhanika i gazovaya dinamika. 2003. № 3. S. 39-45 (in Russian).
17. **Akhmetov V.K., Volshanik V.V.** Investigation of the propagation an aerated submerged jet // Hydrotechnical

Construction. 1994. Vol. 28. № 10. C. 605-609.
18. **Mang J., Minkov E., Schaflinger U., Ungarish M.** Particle entrainment in a bounded rotating flow with a drain // Trans. ASME. J. Fluids Eng. 1998. Vol. 120. Pp. 676–679.
19. **Tsai R., Chang Y.P., Lin T.Y.** Combined effects of thermophoresis and electrophoresis on particle deposition onto a wafer // J. Aerosol Sci. 1998. V. 29. № 7. Pp. 811-825.

СПИСОК ЛИТЕРАТУРЫ

1. **Гупта А., Лилли Д., Сайред Н.** Закрученные потоки. М.: Мир, 1987. 588 с.
2. **Алексеенко С.В., Куйбин П.А., Окулов В.Л.** Введение в теорию концентрированных вихрей. Москва–Ижевск: Институт компьютерных исследований, 2005. 504 с.
3. **Wang Y., Xingjian Wang X., Yang V.** Evolution and transition mechanisms of internal swirling flows with tangential entry // Physics of Fluids. 2018. Vol. 30. 013601.
4. **Ogus G., Baelmans M., Vanierschot M.** On the flow structures and hysteresis of laminar swirling jets // Physics of Fluids. 2016. Vol. 28. 123604.
5. **Ахметов В.К., Шкадов В.Я., Шкадова В.П.** Смешение нагретых газов в осесимметричном канале с предварительной закруткой потока // Известия РАН. Механика жидкости и газа. 2006. № 3. С. 19-29.
6. **Orlandi P.** Two-dimensional and three-dimensional direct numerical simulation of co-rotating vortices // Physics of Fluids. 2007. Vol. 19. 013101.
7. **Ахметов В.К., Шкадов В.Я.** Устойчивость свободных и ограниченных закрученных течений с зонами рециркуляции // Инженерная физика. 2008. № 6. С. 6-13.
8. **Oberleithner K., Paschereit C., Seele R., Wygnanski T.** Formation of turbulent vortex breakdown: intermittency, criticality, and global instability // AIAA Journal. 2012. Vol. 50. № 7**.** Pp. 1437-1452.
9. **Escudier M.P., Nickson A.K., Poole R.J.** Influence of outlet geometry on strongly swirling turbulent flow through a circular tube // Physics of Fluids. 2006. Vol. 18. 125103.
10. **Mergheni M.A., Riahi Z., Sautet J.C., Nasrallah S.B.** Swirl effects on dynamics characteristics of a coaxial jet // Thermal Science. 2017. Vol. 21. № 6. Pp. 2543-2552.
11. **Blanco-Rodríguez F.J., Rodríguez-García J.O., Parras L., del Pino C.** Optimal response of Batchelor vortex // Physics of Fluids. 2017. Vol. 29. 064108.
12. **Yadav N.K., Samanta A.** The stability of compressible swirling pipe flows with density stratification // Journal of Fluid Mechanics. 2017. Vol. 823. Pp. 689-715.
13. **Delbende I., Rossi M.** Nonlinear evolution of a swirling jet instability // Physics of Fluids. 2005. Vol. 17. 044103.
14. **Ахметов В.К.** Гидродинамическая устойчивость контрвихревых течений // Гидротехническое строительство. 2018. № 2. С. 13-18.
15. **Кутателадзе С.С., Волчков Э.П., Терехов В.И.** Аэродинамика и тепломассообмен в ограниченных вихревых потоках. Новосибирск: Институт теплофизики, 1987. 283 с.
16. **Ахметов В.К., Шкадов В.Я.** Численное исследование рециркуляционных зон в вихревой камере // Аэромеханика и газовая динамика. 2003. № 3. С. 39-45.
17. **Ахметов В.К., Волшаник В.В.** Исследование распространения аэрированной затопленной струи // Гидротехническое строительство. 1994. № 10. С. 24-26.
18. **Mang J., Minkov E., Schaflinger U., Ungarish M.** Particle entrainment in a bounded rotating flow with a drain // Trans. ASME. J. Fluids Eng. 1998. Vol. 120. Pp. 676-679.

19. **Tsai R., Chang Y.P., Lin T.Y.** Combined effects of thermophoresis and electrophoresis on particle deposition onto a wafer // J. Aerosol Sci. 1998. V. 29. № 7. Pp. 811-825.

Vadim K. Akhmetov, Doctor of Science, Professor, Department of Computer Science and Applied Mathematics, Moscow State University of Civil Engineering, 26, Yaroslavskoe Shosse, Moscow, 129337, Russia, tel. +7(499) 183-59-94, e-mail: vadim.akhmetov@gmail.com

Ахметов Вадим Каюмович, доктор технических наук, профессор кафедры информатики и прикладной математики Национального исследовательского Московского государственного строительного университета, 129337, г. Москва, Ярославское шоссе, д. 26, тел. +7(499) 183-59-94, e-mail: vadim.akhmetov@gmail.com

International Journal for Computational Civil and Structural Engineering, 21(2) 83–98 (2025)

DOI:10.22337/2587-9618-2025-21-2-83-98

BUTT JOINT WITH MEANDER OUTLINE FOR BOX-SECTION COLUMN IN FRAME MOMENT CONNECTION FOR SEISMIC APPLICATIONS

Yurii S. Kost [1], Tatiana L. Dmitrieva [2]

[1] North-Eastern State University, Magadan, RUSSIA
[2] Irkutsk National Research Technical University, Irkutsk, RUSSIA

Abstract: A steel moment frame is a design solution that effectively withstands seismic impact. In National Standards of various countries, box-section columns are recommended for use in moment frame, while this requirement is mandatory in the Russian Federation. Therefore, it is necessary to have a frame moment connection between an I-beam and such column. Most existing solutions involve many welds which reduce reliability under dynamic loads or low temperature conditions. Solutions with fewer welds require special cast components. This article proposes a solution to this problem by introducing a butt joint for box-section columns that creates a frame moment connection with minimal welds, without using any special cast components, and complies with the requirements of National Standards on earthquake-resistant construction in Russia.
Based on calculations performed in ANSYS for extracted frame moment connection in static formulation as well as pseudo-plane single-story moment frame and multi-story moment frame in dynamic formulations using accelerograms from earthquakes, a comparative analysis was conducted regarding stress-strain state of the frame moment connection without butt joints and with different types the outline of butt joints.
It has been found that a butt joint with the outline like a meander is equivalent to a solid column without cutout, allowing calculations of entire design model without detailed modeling of the frame moment connection, simply by applying fixed joint of column and beam. Additionally, one advantage of this type of butt joint is its ability to solve the issue of installing diaphragm plates in the box-section column body.

Keywords: butt joint, steel frame moment connection, box-section column, seismic, low temperature, weld, ANSYS

СТЫК С ОЧЕРТАНИЕМ МЕАНДРА КОРОБЧАТОЙ КОЛОННЫ ДЛЯ СЕЙСМОСТОЙКОГО РАМНОГО УЗЛА

Ю.С. Кость [1], Т.Л. Дмитриева [2]

[1] Северо-Восточный государственный университет, г. Магадан, РОССИЯ
[2] Иркутский Национальный Исследовательский Технический Университет, г. Иркутск, РОССИЯ

Аннотация: Стальной рамный полный каркас представляет собой конструктивное решение, которое эффективно воспринимает сейсмическое воздействие. В национальных стандартах различных стран для полных рамных каркасов рекомендуется применять колонны коробчатого профиля, а в Российской Федерации это требование является обязательным. В связи с этим необходим жёсткий узел крепления ригеля из двутавра к такой колонне. В большинстве существующих решений присутствует много сварных соединений, которые снижают надежность конструкций при динамическом воздействии или эксплуатации в условиях низких температур, а в тех, где сварных соединений мало, необходимо использование специальных литых деталей. Предложено решение данной проблемы в виде стыкового соединения колонн коробчатого сечения, позволяющее в месте стыка создать жёсткий рамный узел с минимальным количеством узлов, без специальных литых деталей и соответствующий требованиям нормативных документов в области сейсмостойкого строительства Российской Федерации.
По результатам расчёта в ANSYS вырезанных узлов в статической постановке, а также псевдо-плоской одноэтажной рамы и многоэтажного полного рамного каркаса в динамической постановке по акселерограммам землетрясений, был проведён сравнительный анализ напряженно-деформированного состояния рамного узла без стыка и со стыками разного очертания.

Было выяснено, что стык с очертанием меандра эквивалентен цельной колонне без разреза, что даёт возможность проводить расчеты всей схемы каркаса без детального моделирования узла, используя жесткое крепление колонны и ригеля. Помимо этого, к достоинствам такого стыка можно отнести возможность решения проблемы установки поперечных рёбер жесткости в теле колонны коробчатого сечения.

Ключевые слова: стыковое соединение, стальной рамный узел, коробчатое сечение, сейсмика, низкие температуры, сварной шов, ANSYS

INTRODUCTION

Taking into account the fact that certain territories of Russia are seismically active, the design engineer is required to analyze the behavior of the structure from seismic impact. To prevent the collapse of the building frame during a seismic impact, it is necessary to dissipate the energy of the seismic impact, for which you can use both the plastic properties of the material of the load-bearing structures and the use of special seismic base isolation and energy dissipation devices. (1, 2). This may also involve addressing the effects of a "soft story", which could allow improvement of the frame's dynamic parameters or its utilization as an energy dissipation device. (3, 4). However, this approach requires the use of a moment frame in both planes of the column. For these purposes, a steel frame is best suited, which has sufficient strength and the possibility of prolonged residual plastic deformation. In National Standards of various countries, box-section columns are recommended for use in moment frame, while this requirement is mandatory in the Russian Federation. In Russian State Standard SP 14.13330.2018 (including supplement 2-4) the following requirements for the moment frames:

1) The cross section of the columns should be box-section or circular section;
2) diaphragm plates should be installed in the columns at the level of the beam.

Since the column has a closed cross-section, the main design problem is the installation of diaphragm plates in the body of the column.

The existing concepts of design solutions for the frame moment connection of an I-beam and a box-section column used in Russia and abroad can be roughly divided into:

1) Using a welded column (1, 5-11);
2) Using elements as diaphragm plates outside the column cavity (5, 13-15, 18);
3) Using an insert that breaks the column or a butt joint at the level of the upper belt of the beam (5, 12, 16-17);
4) The use of special cast components (6, 18-21)

Most existing solutions involve many welds which reduce reliability under dynamic loads (22-27) or low temperature conditions (28). Solutions with fewer welds require special cast components. Since the Russian State Standard does not prohibit the butt joint of columns at the place where the beam is attached, a butt joint of box-section column is considered in this work (with different cut shapes), which makes it possible to create a frame moment connection beam attachment unit at the butt joint that meets the requirements of Russian State Standard of earthquake-resistant construction of the Russian Federation. The essence of the butt joint is to reduce the welds in the moment frame of the I-beam and box-section column. It is assumed that such a column will be made of hot rolled square pipe and, due to this, it will be possible to do only factory full penetration weld joints of diaphragm plates, which will increase the reliability of the structure. (fig. 1).

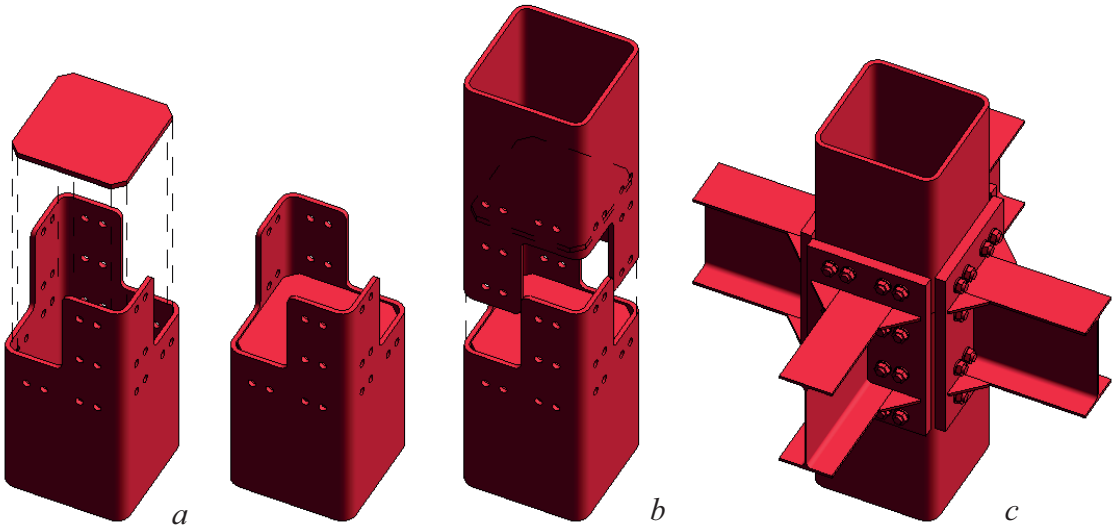


Figure 1. The concept of the butt joint and the frame moment connection whole: a – a jointed square pipe with a meander-shaped trim and a place where the diaphragm plates, b – combining two square pipe, c – the final assembly of the butt joint and the frame moment connection as a whole using metal plates and (or) beam flanges, tightened with pretensioned studs or bolts passing through the profile

METHODS

To obtain reliable data on the behavior of the frame moment connection an earthquake, it is necessary to calculate the entire structure using solid finite elements (hereinafter FE) using an accelerogram, with physical and geometric non-linearity in time. Such a task is quite resource-intensive. In addition, increased control is needed at the level of the source data assignment. To avoid possible errors, the calculation should begin with a simple analysis of the frame in a linear formulation using the Response Spectrum Analysis (hereinafter RSM) without modeling frame moment connection, and then gradually complicate it.

RESULTS AND DISCUSSION

The first example – a pseudo-flat single-story pivotally supported 5x5 m frame, fixed from the bottom of the plane in the column heads (fig.2). The columns are made from 250x8 rolled square pipe according to Russian State Standard GOST 32931-2015, and the beam is made from a 20Ш2 I/H-beam according to Russian State Standard GOST R 57837-2017.

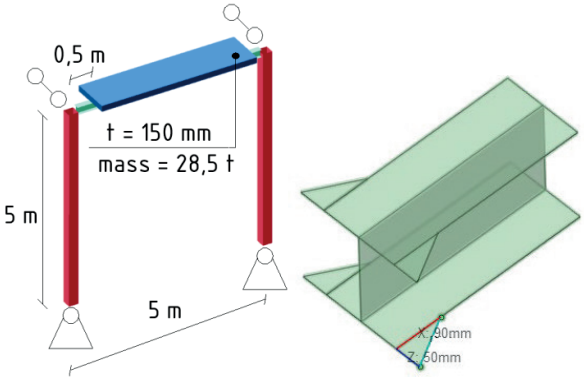


Figure 2. Scheme of pseudo-flat single-story frame and shell moment connection sections

At a distance of 0.5 m from the column, a monolithic reinforced concrete floor slab is fixed attached to the beam, which will not allow the beam to buckling failure. A plastic hinge is expected in the beam. In addition to its own weight of the structure, a uniformly distributed mass of 28.5 tons is applied to the beam. The scheme consists of beam elements, with the exception of the shell support parts of the 0.5 m long beam with additional shelf widening.

Step 1 consists in determining the maximum bending moment in the columns, total deformation and base shear without modeling the frame moment connection, representing it as a fixed joint, from a given artificial single-component accelerogram with a damping coefficient of 0.027. The material of steel structures is S345 steel, set by multilinear kinematic hardening model (fig.3). The calculation is carried out by direct integration of equation of motion in time into ANSYS Transient with geometry and physical linear and nonlinear, and also RSM in ANSYS Response Spectrum from response spectrum plot based on accelerogram. The results are shown in the figures 4-6.

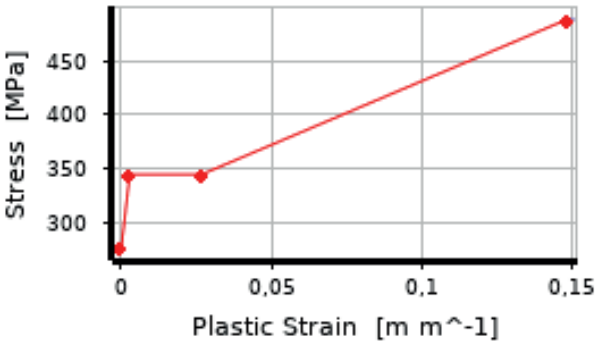


Figure 3. Chart of properties row S345 at multilinear kinematic hardening

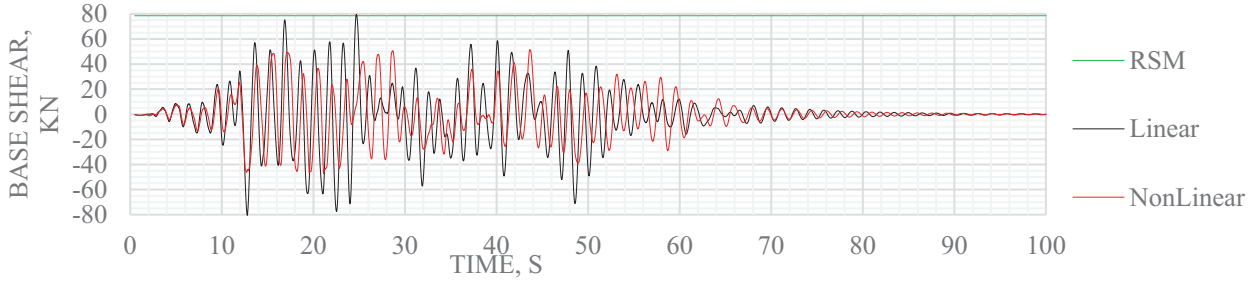


Figure 4. Base shear single-story frame without modeling the frame moment connection

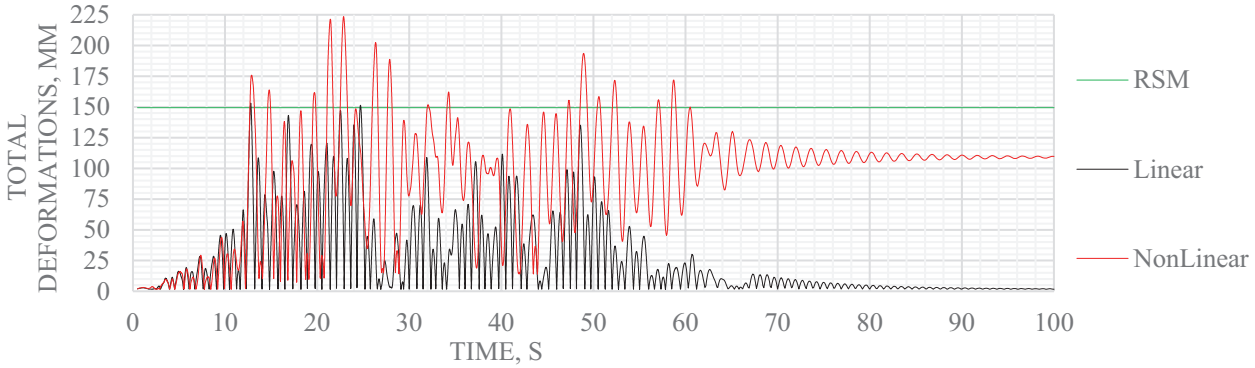


Figure 5. Total deformations single-story frame without modeling the frame moment connection

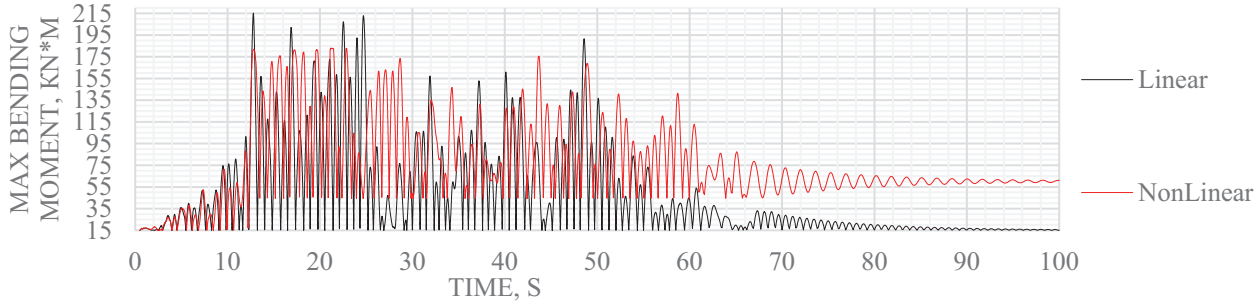


Figure 6. Maximum bending moment in the columns single-story frame without modeling the frame moment connection

Based on the calculation results, the following conclusions can be drawn:

1) Linear calculation in time and RSM have almost identical results with an inaccuracy of about 1–2%. This indicates that the integration step and the Relay damping coefficients are set correctly;

2) In the nonlinear calculation, the base shear decreased by 0.65 times, the maximum bending moment in the columns by 0.85 times, and the total deformation increased by 1.46 times. A decrease in bending moment and base shear indicates that a plastic hinge appeared in the frame, which dissipated seismic energy, and an increase in deformation means that strong residual deformations occurred in the frame and the deformed frame further perceived the seismic impact;

3) In the nonlinear calculation, the maximum stress in the columns is 328 MPa, therefore, the plastic hinge occurs only in the beam.

Step 2. Before modeling solid-state frame moment connection for dynamic calculation, it is worth checking the suitability of their different variants by static calculation.

Common to all considered joints is the connection of the beam to the column via a 25-mm-thick flange using M16 studs with a pretension force of 90 kN. Diaphragm plates are installed internally at the level of the beam's flanges. The results are shown in the table 1.

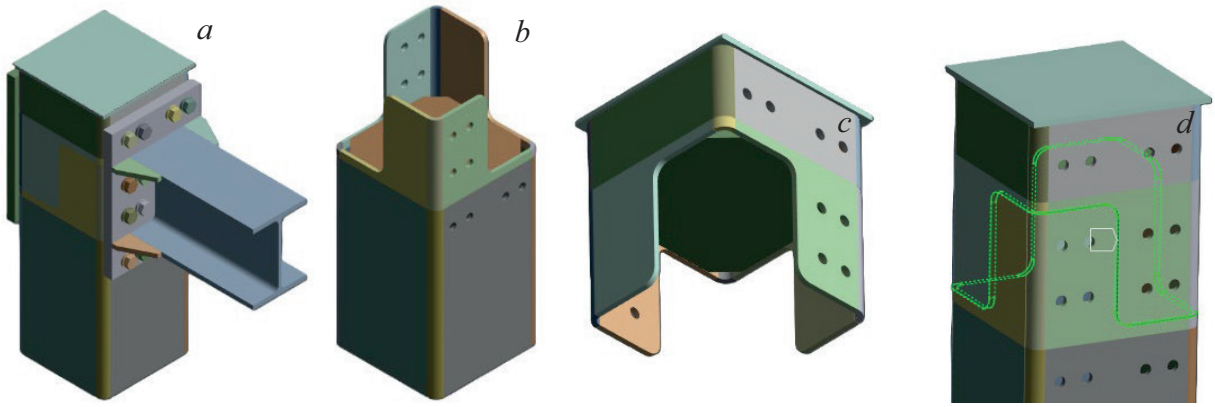


Figure 7. 1 variant. Column with the meander outline: a – assembled butt joint, b-c – jointed parts, d – outline of the cut

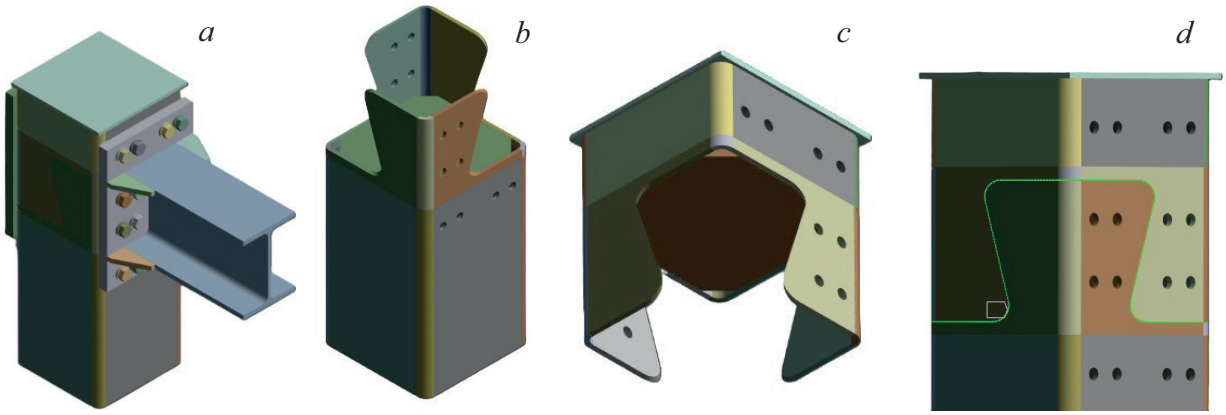


Figure 8. 2 variant. Column with a through-cut along the path: a – assembled butt joint, b-c – jointed parts, d – outline of the cut

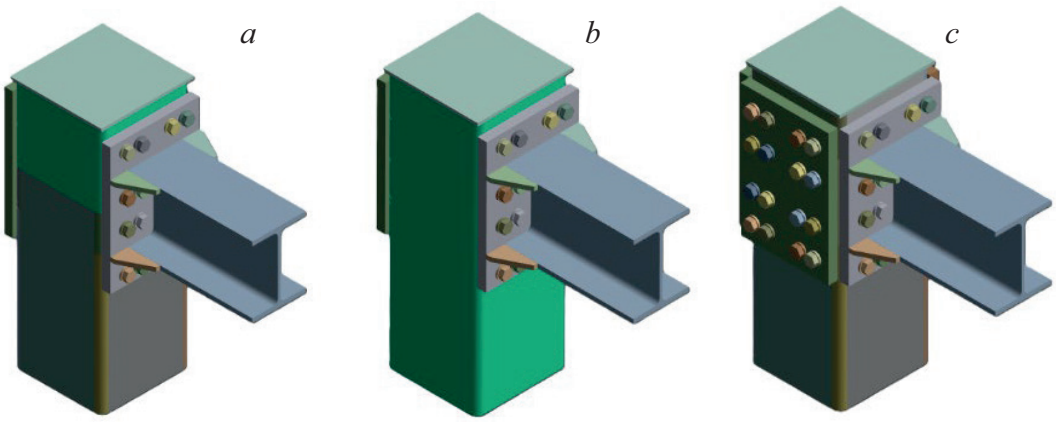


Figure 9. 3-7 variants: a – 3 variant with a cut in the center, b – 4 the uncut variant, c – 5-7 variants (accordingly, 1-3 variants with the addition of side plates, flange thickness)

Table 1. The results of the static calculation of the variants of the head frame moment connection with a load on the beam 135 кN·m.

N	Butt joint Description	Total deformation, mm	Max equivalent plastic strain, mm/mm	Max equivalent stress in studs, MPa
1	Meander outline	27,25	0,198	2412,6
2	Through-cut along the path	35,17*	0,434*	3061,2*
3	Cut in the center	56,78	0,312	4530,3
4	Uncut	8,07	0,018	941,5
5	Meander outline with the addition of side plates	8,36	0,020	1182,5
6	Through-cut along the path with the addition of side plates	8,58	0,027	1359,8
7	Cut in the center with the addition of side plates	9,59	0,053	1043,0

*The * sign means that there is no convergence on 135 кN·m, the values are shown on 121,5 кN·m*

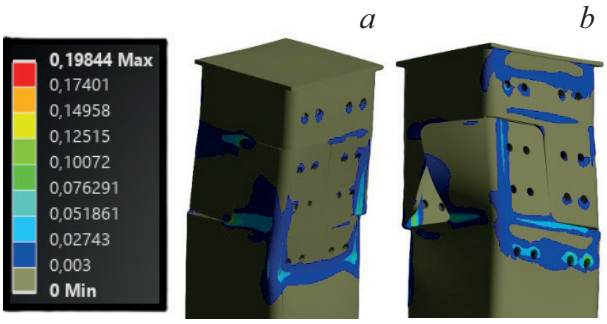


Figure 10. Equivalent plastic strain variant 1: a – front, b – rear

Variants 2-4 clearly demonstrate how different types of cutouts affect the work of joints without side plates. Variant 1 turned out to be the best, since in any direction of the bending moment there will be resistance to bending by one wall of the column.However, even with it, the maximum equivalent plastic strain go beyond the temporary resistance of steel. Variants 5-7, due to the additional plates, are already showing satisfactory performance. In terms of stiffness and strength parameters, variant 5 is closest to variant 4.

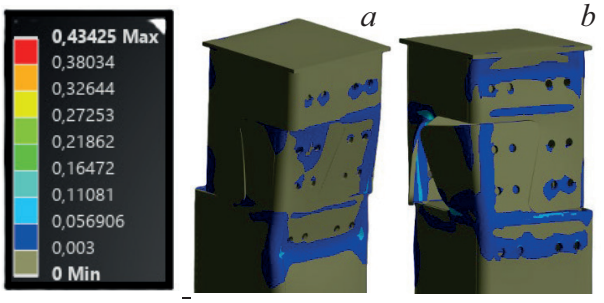


Figure 11. Equivalent plastic strain variant 2: a – front, b – rear

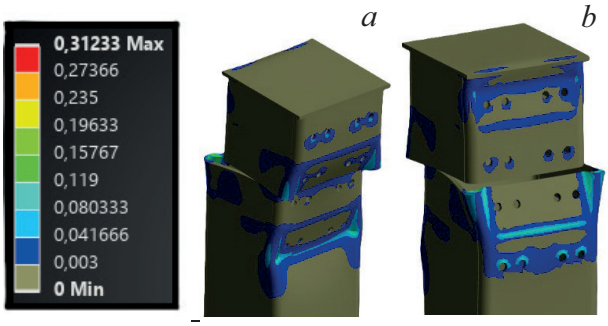


Figure 12. Equivalent plastic strain variant 3: a – front, b – rear

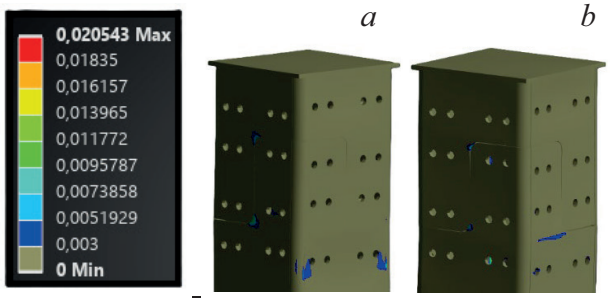


Figure 13. Equivalent plastic strain variant 5: a – front, b – rear

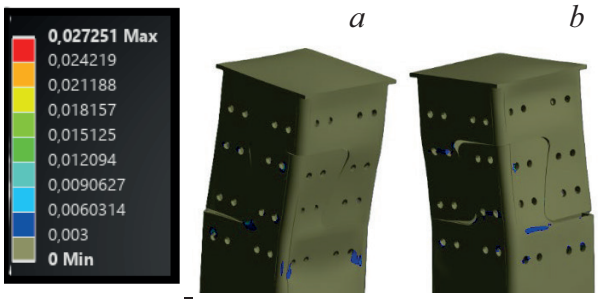


Figure 14. Equivalent plastic strain variant 6: a – front, b – rear

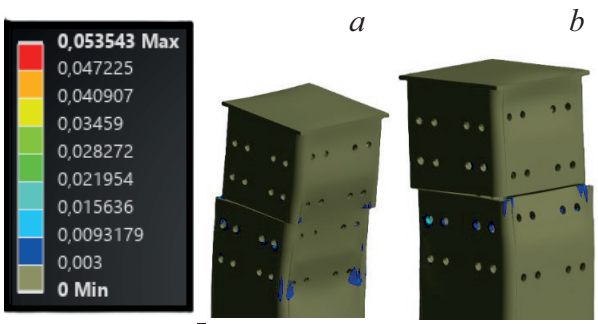


Figure 15. Equivalent plastic strain variant 7: a – front, b – rear

Step 3. In order to make sure whether the difference between options 1 and 5 is significant, it is necessary to perform a dynamic calculation. Let's look at 4 cases of frame moment connection modeling:

1) shell FE uncut;
2) solid FE uncut;
3) solid FE with cut meander outline;
4) solid FE with cut meander outline and non-pretensioned studs.

The results are shown in the figures 16-17.

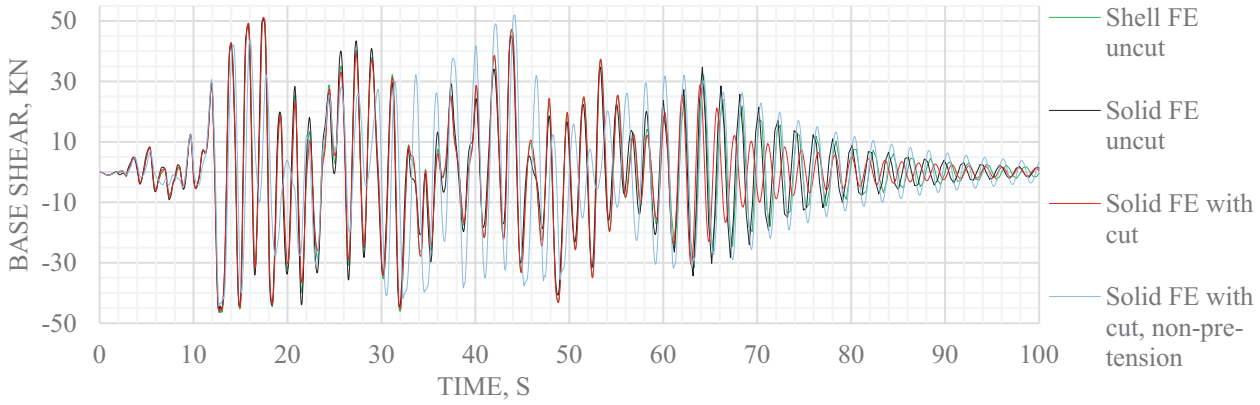


Figure 16. Base shear single-story frame with modeling the frame moment connection

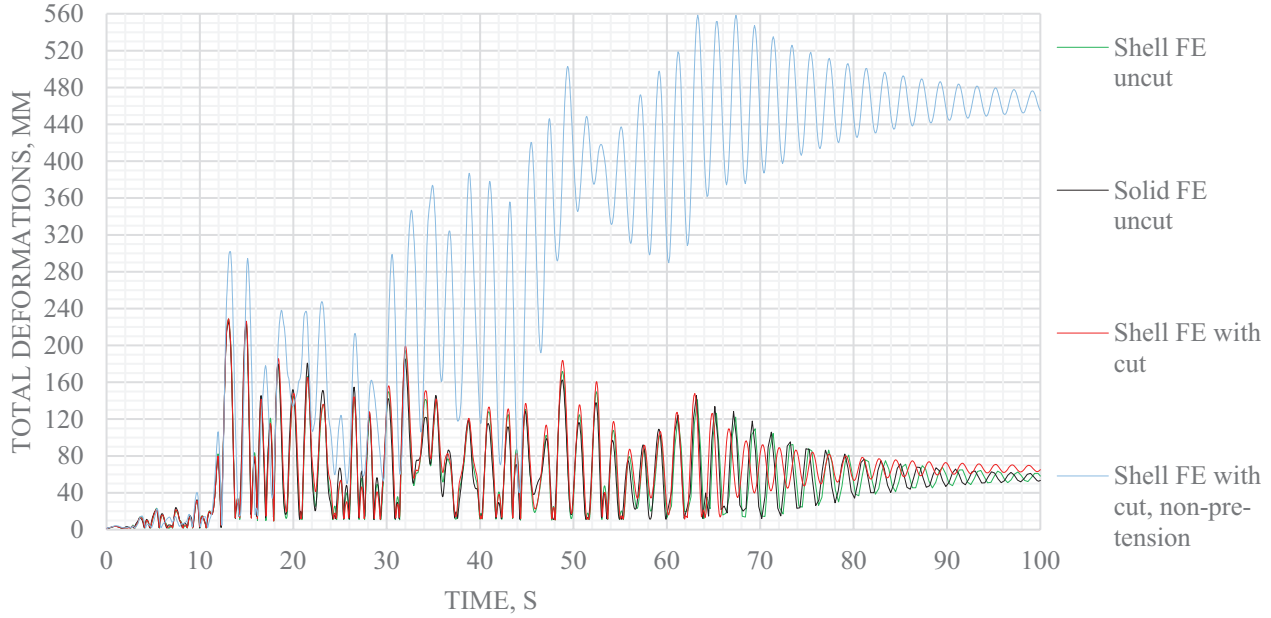


Figure 17. Total deformations single-story frame with modeling the frame moment connection

The graphs show how strongly the pre–tension of the studs affects the stiffness of the connection. The difference in total maximum deformations of 13.07 between solid uncut and with cut is only 1.5%, and, as a result, plastic strain after the earthquake increased by 12%. And with the variant non-pretensioning studs by 13.23 s, the difference is 25.2%, and because of this, the difference in rplastic strain after an earthquake is 793%.

The first example demonstrated that the butt joint with meander outline of hot rolled square pipe with 4 plates, compressed with studs a pre-tention force of 90 kN, allows us to create an equally strong joint of a solid pipe and provides the necessary strength and stiffness for a frame moment connection.

Second example – A 3-story hinged frame with a column pitch of 6m and a floor height of 6.6m. The columns are made from 350x13 rolled square pipe according to Russian State Standard GOST 32931-2015, beams of the 1st floor made of I-beam 30Б1 according to Russian State Standard GOST R 57837-2017, 2nd floor made of I-beam 25Б1, 3rd floor made of I-beam 20Б1. At a distance of 0.5 m from the column, a mono-lithic reinforced concrete floor slab is fixed at-tached to the beam. A plastic hinge is expected in the beam. In addition to its own weight of the structure, a uniformly distributed mass of 350 kg/m^2 is applied to the slab (fig. 18).

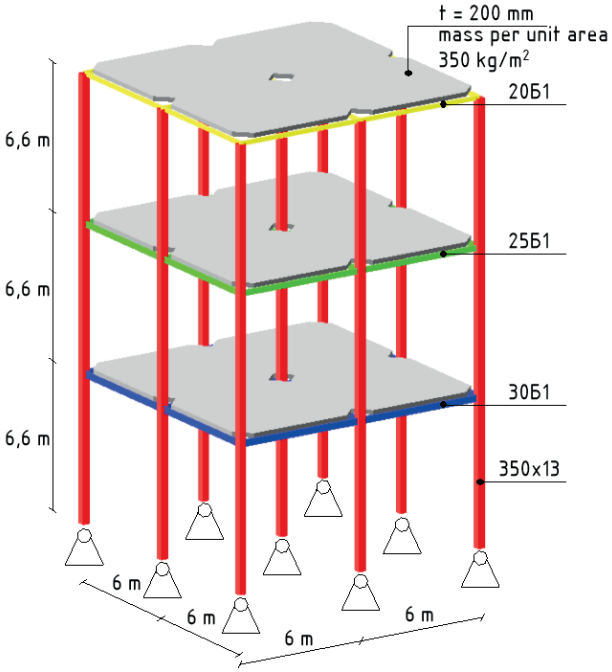


Figure 18. – Scheme of multi-story frame

Step 1. Calculations are performed similarly to the first example, but using a three-component accelerogram of a real earthquake. The results are shown in the figures 19-23.

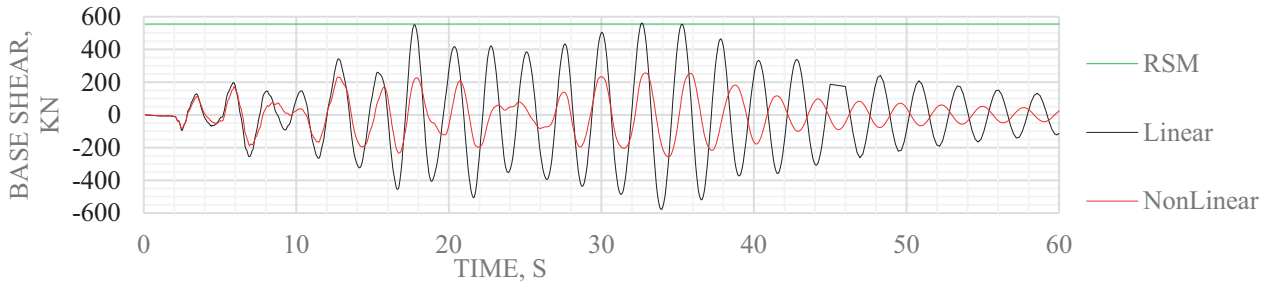


Figure 19. Base shear multi-story frame in longitudinal direction without modeling the frame moment connection

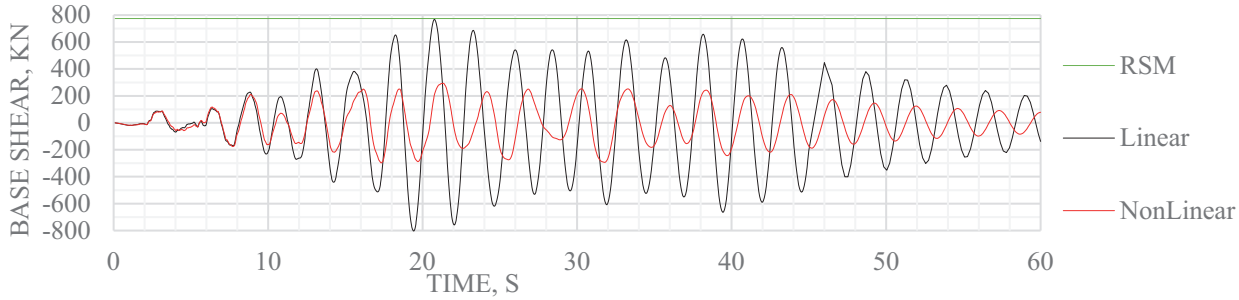


Figure 20. Base shear multi-story frame in transverse direction without modeling the frame moment connection

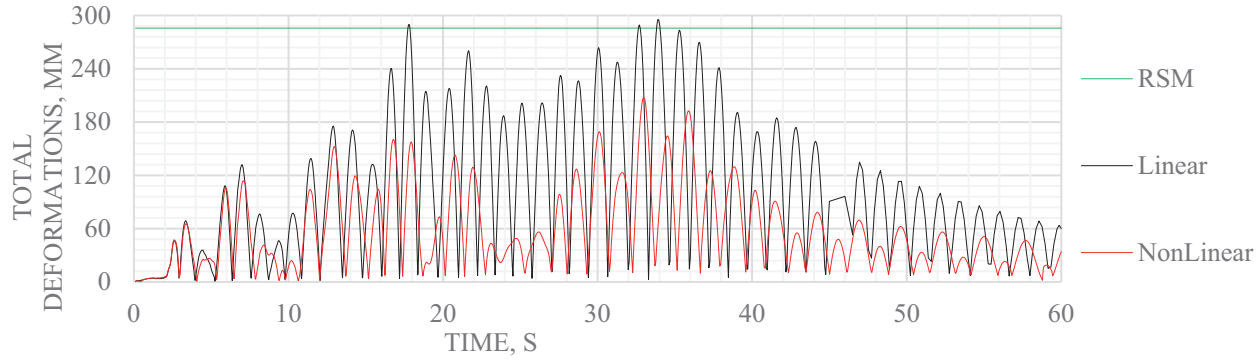


Figure 21. Total deformations multi-story frame in longitudinal direction without modeling the frame moment connection

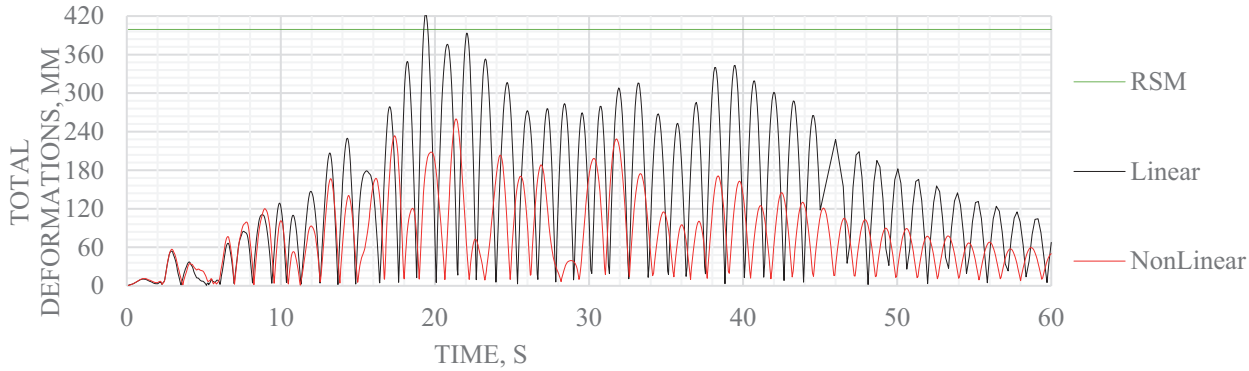


Figure 22. – Total deformations multi-story frame in transverse direction without modeling the frame moment connection

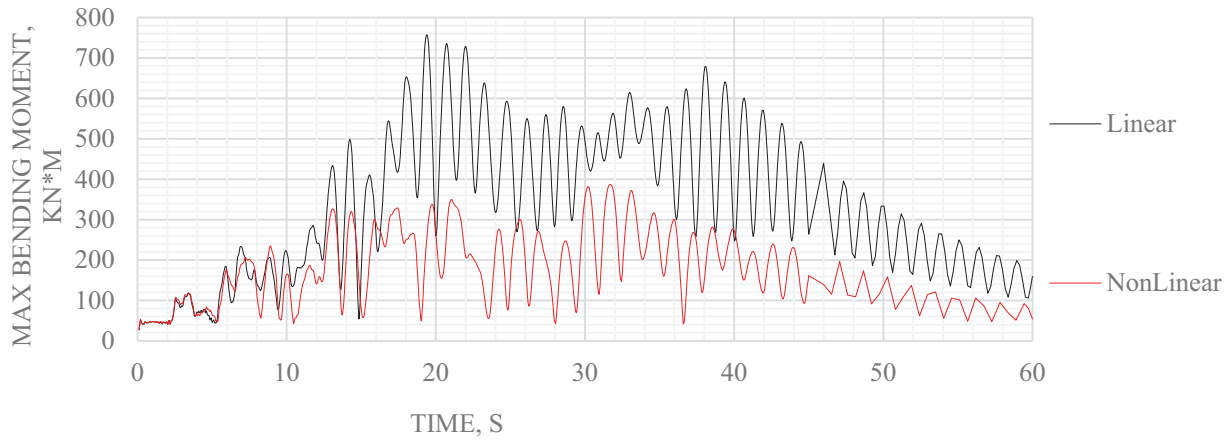


Figure 23. Maximum bending moment in the columns multi-story frame without modeling the frame moment connection

Based on the calculation results, we obtain a situation comparable to the previous example, with the exception of:

1) A plastic hinge did not appear in the beam 3rd floor;

2) In the nonlinear solution, base shear decreased by 0.44 times in the longitudinal and 0.36 times in the transverse directions, the maximum bending moment in the columns by 0.51 times, and total deformation of the scheme decreased by 0.53 times.

Step 2. Next, we form solid frame moment connections models and perform their comparison by static calculation in ANSYS Static Structural. Common to all considered joints is the connection of the beam 30Б1to the column via a 30-mm-thick flange using M20 studs with a pretension force of 90 kN. Diaphragm plates are installed internally at the level of the beam's flanges. Two variants are being considered: with one beam and with 4 (fig. 24). The results are shown in the table 2.

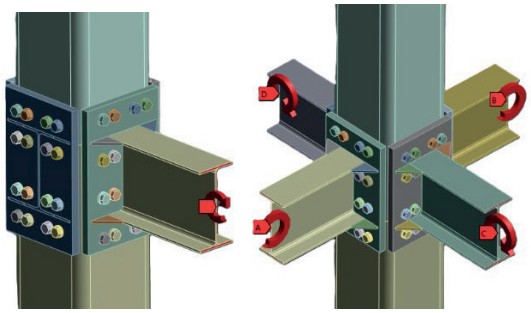


Figure 24. 2 variants solid model frame moment connection

Table 2. The results of the static calculation of the variants of the floor-to -floor frame moment connection with a load on the beam 220 кН ·м

N	Butt joint Description	Total deformation, mm	Max equivalent plastic strain, mm/mm	Max equivalent stress in studs, MPa
1	Uncut, 1 beam	99,86	0,002	704,9
2	Uncut, 4 beams	101,45	0,016	928,6
3	Meander outline, 1 beam	99,25	0,002	718,9
4	Meander outline, 4 beams	102,68	0,033	1533,7
5	Through-cut along the path, 1 beam	99,22	0,004	924,8
6	Through-cut along the path, 4 beams	103,06	0,048	1610,3

Table 2. Continued

7	Cut in the center, 1 beam	99,76	0,003	970,2
8	Cut in the center, 4 beams	103,08	0,044	1650,5

The results show that in the floor-to-floor butt joint, the results are generally comparable with each other, but variant with a Meander outline is closer to the not cut variant.

Step 3. Calculate the entire frame using a solid model with a meander outline.

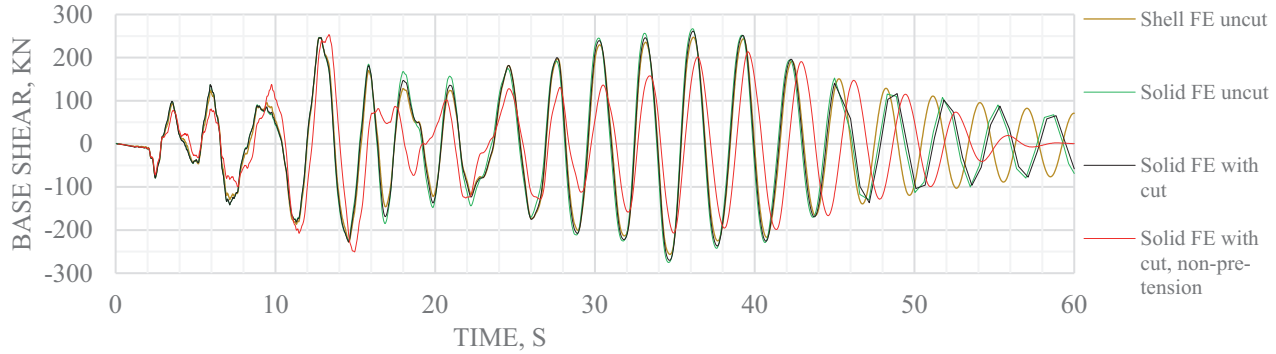


Figure 25. Base shear multi-story frame in longitudinal direction with modeling the frame moment connection

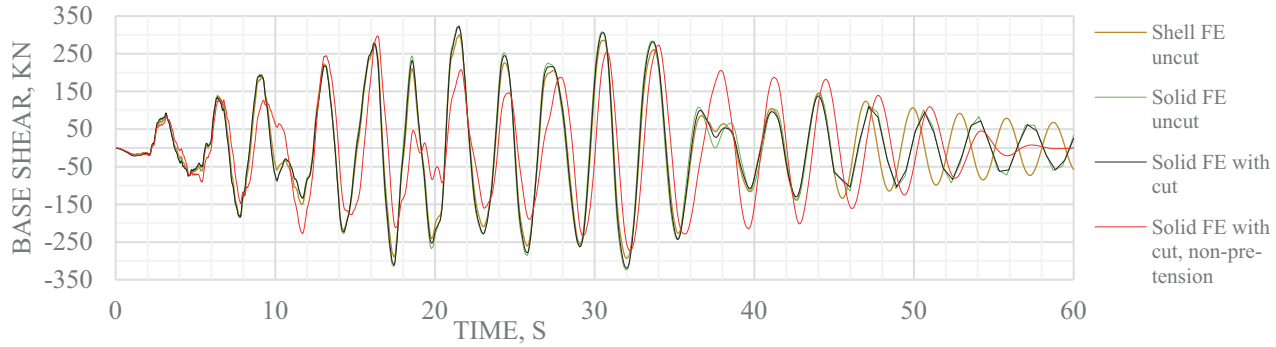


Figure 26. Base shear multi-story frame in transverse direction with modeling the frame moment connection

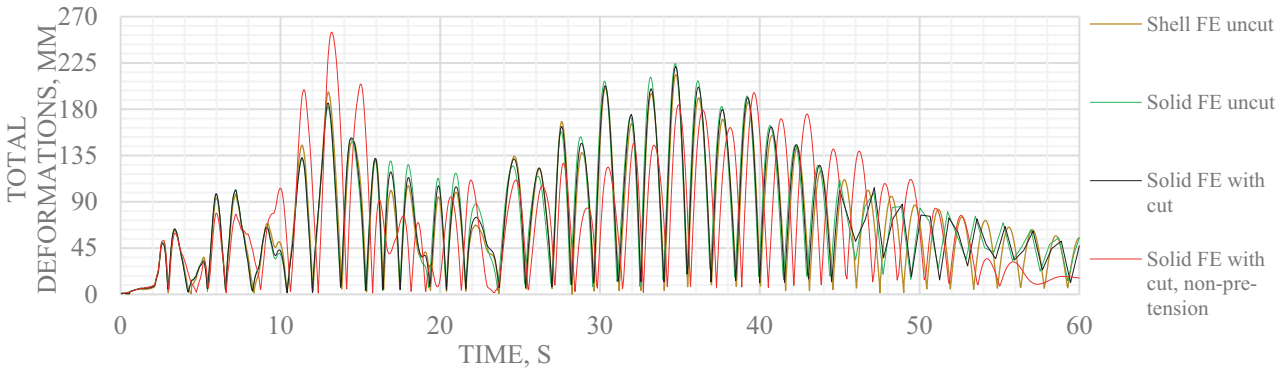


Figure 27. Total deformations multi-story frame in longitudinal direction with modeling the frame moment connection узла

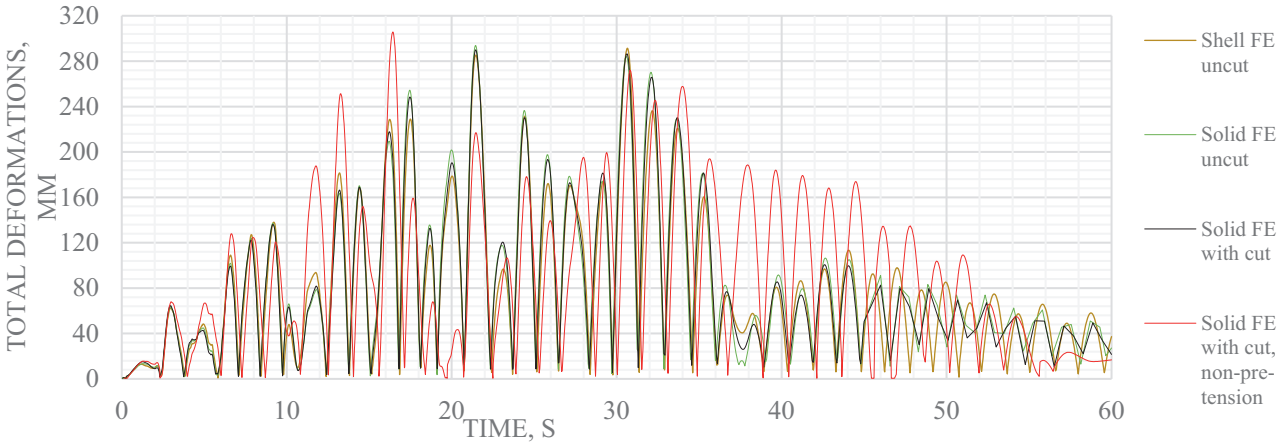


Figure 28. Total deformations multi-story frame in transverse direction with modeling the frame moment connection

The results show that the variants cut and uncut are identical, but without pretension, the frame works differently and its total deformations are higher.

CONCLUSION

It has been found that a butt joint with the outline like a meander is equivalent to a solid column without cutout with 4 plates, compressed with studs a pretention force of 90 kN (fig.1), allowing calculations of entire design model without detailed modeling of the frame moment connection, simply by applying fixed joint of column and beam. Additionally, one advantage of this type of butt joint is its ability to solve the issue of installing diaphragm plates in the box-section column body.

It should be noted that the next stage of the study involves direct testing of the entire frame moment connection on the stand and further consideration of its individual factors and elements to determine their qualitative impact on its bearing capacity, namely the influence of:

1) friction coefficient between steel plates;
2) bolt or studs pretension values;
3) the size of the amplitude and the rounding of the meander;
4) the size of the gaps (tolerances) between the columns to be joined;
5) the vertical distance between the intersecting bolts or studs

REFERENCES

1. **Polyakov V.S., Kilimnik L.S., Cherkashin A.V**. Modern methods of seismic protection of buildings = Sovremennye metody sejsmozashchity zdanij. M.: Stroyizdat; 1989. (In Russ)
2. **Vyscrebentseva M.A., Vu Le.Q.** Methods of seismic and seismic isolation using special devices. Ingineering journal of Don = Inzhenernyj vestnik Dona. 2019;1(52):148. EDN NKHMJV. (In Russ)
3. **Belash T.A**. The use of the "flexible floor" effect in buildings of rigid structural systems. Earthquake-resistant construction. Safety of structures = Sejsmostojkoe stroitel'stvo. Bezopasnost' sooruzhenij. 2023;2:45-53. EDN EQNFVM. (In Russ)
4. **Ujwal M.S., Kumar G.S., Sathvik S., Ramaraju H.K.** Effect of soft story conditions on the seismic performance of tall concrete structures. Asian journal of civil engineering. 2024:1-9. https://doi.org/10.1007/s42107-023-00968-9.
5. **Kuznetsov V.V.** (eds). Metal structures: in 3 t. T. 2. Steel structures of buildings and structures. The designer's handbook = Steel structures of buildings and structures. The designer's handbook. M.: ASV; 1999. (In Russ)
6. **Ostrikov U.M.** Steel earthquake-resistant frames of multistorey buildings = Steel earthquake-resistant frames of multistorey

buildings. Alma-Ata: Kazakhstan; 1985. (In Russ)
7. **Yoshio F., Mikio M., Shokichi G., Hideo O., Yasuhiko T., Koichi S.** et al. Japan, Patent No. JPH09328817A. 1997. Available at: https://worldwide.espacenet.com/patent/search/family/015478447/publication/JPH09328817A?q=pn%3DJPH09328817A
8. **Seizaburo A.** Japan, Patent No. JP2003227172A. Manufacturing method of box-shaped cross section steel column material with built-in diaphragm, and building iron frame column and beam joint part using the box-shaped cross section steel column material with the built-in diaphragm manufactured by the manufacturing method. 2003. Available at: https://worldwide.espacenet.com/patent/search/family/027749152/publication/JP2003227172A?q=pn%3DJP2003227172A
9. **Qiang X.** China, Patent No. CN217782366U. Steel structure beam-column joint adopting integral H-shaped steel connecting piece. 2022. Available at: https://worldwide.espacenet.com/patent/search/family/083905726/publication/CN217782366U?q=pn%3DCN217782366U
10. **Shahabeddin T., Rasoul M., Farhad K**. Moment-connection between I-beam and built-up square column by a diagonal through plate. Journal of constructional steel research. 2012;70:385-401. https://doi.org/10.1016/j.jcsr.2011.10.017
11. **Peykari K., Najafgholipour M.A.** Behavior of steel beam to built-up box column moment connections with vertically stiffened panel zone. Journal of building pathology. 2023;8:6. https://doi.org/10.1007/s41024-022-00253-3
12. **Gerzon M.I., Koval G.F., Kovtun-Gorbacheva T.A., Kilievich A.G.** Russia. Patent No. 1030507. Frame frame assembly = Ustalost' svarnyh soedinenij. 1983. Available at: https://yandex.ru/patents/doc/SU1030507A1_19830723/ (In Russ)
13. **Atsuhide Y., Tatsuo Y., Masahiko U., Ryoichi T., Isao S.** Japan, Patent No. JP2002188208A. Steel-framed beam-column connecting section structure of box-shaped section column. 2002. Available at: https://worldwide.espacenet.com/patent/search/family/018851133/publication/JP2002188208A?q=pn%3DJP2002188208A
14. **Tsutomu A., Yoshihiro F., Katsuhisa N. Japan,** Patent No. JPH11117389A. Beam-column joint method of steel frame construction. 1999. Available at: https://worldwide.espacenet.com/patent/search/family/017632120/publication/JPH11117389A?q=pn%3DJPH11117389A
15. **Chuanxin Z., Hui L., Yuhui D., Yanyong S., Mojun G.** China, Patent No. CN215106097U. Novel steel structure beam column rigid connection joint. 2021. Available at: https://worldwide.espacenet.com/patent/search/family/079307897/publication/CN215106097U?q=pn%3DCN215106097U.
16. **Haijun Z.** China, Patent No. CN217379243U. Joint for steel frame box section column bolt welding and flange connection. 2022. Available at: https://worldwide.espacenet.com/patent/search/family/083089140/publication/CN217379243U?q=CN217379243U
17. **Haoxiang Z.** China, Patent No. CN206220248U. Steel frame joint structure. 2017. Available at: https://worldwide.espacenet.com/patent/search/family/058790862/publication/CN206220248U?q=pn%3DCN206220248U
18. ANSI/AISC 358-22. Prequalified connections for special and intermediate steel moment frames for seismic applications. URL: https://www.aisc.org/publications/steel-standards/ansiaisc-358/.
19. **Akira F., Susumu N., Yasuo W.** Japan, Patent No. JP2821095B2. Column-beam connective structure and method therefor. 1999. Available at: https://worldwide.espacenet.com/patent/search/family/027284153/publication/JP2821095B2?q=pn%3DJP2821095B2
20. **Shoei I., Kazufumi H.** Japan, Patent No. JP3116023B2. Joint device for steel column

and steel beam. 2000. Available at: https://worldwide.espacenet.com/patent/search/family/026496821/publication/JP3116023B2?q=pn%3DJP3116023B2

21. **Kuniaki S., Shoei I., Eiji M.** Japan, Patent No. JPH11148174A. Connecting structure of closed type sectional column and beam. 1999. Available at: https://worldwide.espacenet.com/patent/search/family/018084223/publication/JPH11148174A?q=pn%3DJPH11148174A.
22. **Trufyakova V.I.** (eds.) The strength of welded joints under variable loads = Prochnost' svarnyh soedinenij pri peremennyh nagruzkah. Kiev: Naukova dumka; 1990. (In Russ)
23. **Miller D.K.** Lessons learned from the Northridge earthquake // Engineering structures. 1998. Vol. 20, Is. 4-6. P. 249-260. https://doi.org/10.1016/S0141-0296(97)00031-X.
24. **Jian W., Guang T.W.** Experimental seismic behavior of RHS column-to-i beam connection with additional plates. Iranian journal of science and technology transactions of civil engineering. 2022. Vol. 46. P. 2053-2065. https://doi.org/10.1007/s40996-021-00770-0
25. **Chen C.-C., Lin C.-C., Tsai C.-L.** Evaluation of reinforced connections between steel beams and box col-umns. Engineering structures. 2004; 26(13):1889-1904. https://doi.org/10.1016/j.engstruct.2004.06.017.
26. **Chen C.H., Lin K.C., Jhuang S.J., Chang H.-Y.** Seismic performance evaluation of steel box-column connec-tions with ESW stiffeners. International journal of steel structures. 2020; 20:766-776. https://doi.org/10.1007/s13296-020-00321-9.
27. **Tsai C.-Y., Tsai K.-C., Li C.-H., Wu C.-C., Lin K.-C., Jhuang S.-J.** Seismic fracture evaluation of diaphragm joints in welded beam-to-box column moment connections. Earthquake engineering and structural dynamics. 2020;49:1344-1362. https://doi.org/10.1002/eqe.3293.
28. **Trufyakova V.I.** (eds.) Fatigue of welded joints = Fatigue of welded joints. Kiev: Naukova dumka; 1973. (In Russ).

СПИСОК ЛИТЕРАТУРЫ

1. **Поляков В.С., Килимник Л.Ш., Черкашин А.В.** Современные методы сейсмозащиты зданий. М.: Стройиздат, 1988. 320 с.
2. **Выскребенцева М.А., Ву Ле.К.** Методы сейсмогашения и сейсмоизоляции с применением специальных устройств // Инженерный вестник Дона. 2019. № 1 (52). С. 1–20. EDN: NKHMJV
3. **Белаш Т.А.** Использование эффекта «гибкого этажа» в зданиях жестких конструктивных систем // Сейсмостойкое строительство. Безопасность сооружений. 2023. № 2. С. 45–53. https://doi.org/10.37153/2618-9283-2023-2-45-53. EDN: EQNFVM.
4. **Ujwal M.S., Kumar G.S., Sathvik S., Ramaraju H.K.** Effect of Soft Story Conditions On the Seismic Performance of Tall Concrete Structures // Asian Journal of Civil Engineering. 2024. Vol. 25. P. 3141–3149. https://doi.org/10.1007/s42107-023-00968-9
5. Металлические конструкции: в 3 т. Т. 2. Стальные конструкции зданий и сооружений. Справочник проектировщика / под общ. ред. В.В. Кузнецова. М.: АСВ, 1999. 512 с.
6. **Остриков Г.М.** Стальные сейсмостойкие каркасы многоэтажных зданий. Алма-Ата: Казахстан, 1985. 120 с.
7. Pat. JPH09328817A Japan, IPC B23K9/00, E04B1/24, E04C3/32. Reinforcing construction of joint section and manufacturing of pipe-like body used therefor / Yoshio F., Mikio M., Shokichi G., Hideo O., Yasuhiko T., Koichi S., Kenji S.; applicant and the patent holder Ohbayashi Corp, Nittetsu Column KK. № JP14958696A; appl. 11.06.1996; publ. 22.12.1997. 8 p. URL: https://worldwide.espacenet.com/patent/sea

rch/family/015478447/publication/JPH09328817A?q=pn%3DJPH09328817A.

8. Pat. JP2003227172A Japan, IPC B23K25/00, B23K9/00. Manufacturing method of box-shaped cross section steel column material with built-in diaphragm, and building iron frame column and beam joint part using the box-shaped cross section steel column material with the built-in diaphragm manufactured by the manufactur-ing method / Seizaburo A.; applicant and the patent holder Nippon Steel Corp. № JP2002027726A; appl. 05.02.2002; publ. 15.08.2003. 6 p. URL: https://worldwide.espacenet.com/patent/search/family/027749152/publication/JP2003227172A?q=pn%3DJP2003227172A.
9. Pat. CN217782366U China, IPC E04B1/24, E04B1/58, E04C3/04, E04C3/32. Steel structure beam-column joint adopting integral H-shaped steel connecting piece / Qiang X.; applicant and the patent holder Hang-zhou Jiurong Arch Design Studio. № CN202222146872U; appl. 15.08.2022; publ.11.11.2022. 9 p. URL: https://worldwide.espacenet.com/patent/search/family/083905726/publication/CN217782366U?q=pn%3DCN217782366U.
10. **Shahabeddin T., Rasoul M., Farhad K.** Moment-connection between I-beam and built-up square column by a diagonal through plate. Journal of constructional steel research. 2012;70:385-401. https://doi.org/10.1016/j.jcsr.2011.10.017.
11. **Peykari K., Najafgholipour M.A.** Behavior of steel beam to built-up box column moment connections with vertically stiffened panel zone. Journal of building pathology. 2023;8:6. https://doi.org/10.1007/s41024-022-00253-3.
12. Пат. 1030507 Российская Федерация, МПК E04B 1/24(2006.01), E04B 1/58(2006.01). Узел рамного карка-са / Герзон М.И., Коваль Г.Ф., Ковтун-Горбачева Т.А., Килиевич А.Г.; заявитель и патентооблада-тель Государственный проектный институт Днепрпроектсталь-конструкция. № 3413935; заявл. 29.03.1982; опубл. 23.07.1983. 3 с. URL: https://yandex.ru/patents/doc/SU1030507A1_19830723.
13. Pat. JP2002188208A Japan, IPC E04B1/24, E04B1/58. Steel-framed beam-column connecting section struc-ture of box-shaped section column / Atsuhide Y., Tatsuo Y., Masahiko U., Ryoichi T., Isao S.; applicant and the patent holder H. Atsuhide, Tomoe Corp. № JP2000383483A; appl. 18.12.2000; publ. 05.07.2002. 10 p. URL: https://worldwide.espacenet.com/patent/search/family/018851133/publication/JP2002188208A?q=pn%3DJP2002188208A.
14. Pat. JPH11117389A Japan, IPC E04B1/24. Beam-column joint method of steel frame construction / Tsutomu A., Yoshihiro F., Katsuhisa N.; applicant and the patent holder OHBAYASHI CORP. № JP28094697A; appl. 14.10.1997; publ. 27.04.1999. 12 p. URL: https://worldwide.espacenet.com/patent/search/family/017632120/publication/JPH11117389A?q=pn%3DJPH11117389A.
15. Pat. CN215106097U China, IPC E04B1/24, E04B1/58. Novel steel structure beam column rigid connection joint / Chuanxin Z., Hui L., Yuhui D., Yanyong S., Mojun G.; applicant and the patent holder China IPPR INT Engineering CO LTD. № CN202023017425U; appl. 14.12.2020; publ. 10.12.2021. 7 p. URL: https://worldwide.espacenet.com/patent/search/family/079307897/publication/CN215106097U?q=pn%3DCN215106097U.
16. Pat. CN217379243U China, IPC E04B1/24, E04B1/58. Joint for steel frame box section column bolt welding and flange connection / Haijun Z.; applicant and the patent holder Z. Haijun. № CN202221314657U; appl. 27.05.2022; publ. 06.09.2022. 11 p. URL: https://worldwide.espacenet.com/patent/search/family/083089140/publication/CN217379243U?q=CN217379243U.
17. Pat. CN206220248U China, IPC E04B1/24; E04B1/58. Steel frame joint structure / Haoxiang Z.; applicant and the patent holder Shenzhen A+E Design CO LTD. №

CN201621251360U; appl. 22.11.2016; publ. 06.06.2017. 7 p. URL: https://worldwide.espacenet.com/patent/search/family/058790862/publication/CN206220248U?q=pn%3DCN206220248U.
18. ANSI/AISC 358-22. Prequalified connections for special and intermediate steel moment frames for seismic applications. URL: https://www.aisc.org/publications/steel-standards/ansiaisc-358/.
19. Pat. JP2821095B2 Japan, IPC E04B1/24. Column-beam connective structure and method therefor / Akira F., Susumu N., Yasuo W.; applicant and the patent holder Daiwa House Ind, Dai Ichi High Frequency CO LTD. № JP33619694A; appl. 22.12.1994; publ. 05.11.1998. 16 p. URL: https://worldwide.espacenet.com/patent/search/family/027284153/publication/JP2821095B2?q=pn%3DJP2821095B2
20. Pat. JP3116023B2 Japan, IPC E04B1/24, E04B1/58. Joint device for steel column and steel beam / Shoei I., Kazufumi H.; applicant and the patent holder ITO Shoei; H. Kazufumi. № JP21334197A; appl. 07.08.1997; publ. 11.12.2000. 6 p. URL: https://worldwide.espacenet.com/patent/search/family/026496821/publication/JP3116023B2?q=pn%3DJP3116023B2
21. Pat. JPH11148174A Japan, IPC E04B1/24, E04B1/58. Connecting structure of closed type sectional column and beam / Kuniaki S., Shoei I., Eiji M.; applicant and the patent holder Arutesu KK. № JP31708197A; appl. 18.11.1997; publ. 02.06.1999. 6 p. URL: https://worldwide.espacenet.com/patent/search/family/018084223/publication/JPH11148174A?q=pn%3DJPH11148174A
22. Прочность сварных соединений при переменных нагрузках / под ред. В.И. Труфякова. Киев: Наукова думка, 1990. 256 с.
23. **Miller D.K.** Lessons learned from the Northridge earthquake // Engineering structures. 1998. Vol. 20, Is. 4-6. P. 249-260. https://doi.org/10.1016/S0141-0296(97)00031-X.
24. **Jian W., Guang T.W.** Experimental seismic behavior of RHS column-to-i beam connection with additional plates. Iranian journal of science and technology transactions of civil engineering. 2022. Vol. 46. P. 2053-2065. https://doi.org/10.1007/s40996-021-00770-0
25. **Chen C.-C., Lin C.-C., Tsai C.-L.** Evaluation of reinforced connections between steel beams and box col-umns. Engineering structures. 2004;26(13):1889-1904. https://doi.org/10.1016/j.engstruct.2004.06.017.
26. **Chen C.H., Lin K.C., Jhuang S.J., Chang H.-Y.** Seismic performance evaluation of steel box-column connec-tions with ESW stiffeners. International journal of steel structures. 2020; 20:766-776. https://doi.org/10.1007/s13296-020-00321-9.
27. **Tsai C.-Y., Tsai K.-C., Li C.-H., Wu C.-C., Lin K.-C., Jhuang S.-J.** Seismic fracture evaluation of diaphragm joints in welded beam-to-box column moment connections. Earthquake engineering and structural dynamics. 2020;49:1344-1362. https://doi.org/10.1002/eqe.3293.
28. Усталость сварных соединений / под ред. В.И. Труфякова. Киев: Наукова думка, 1973. 216 с.

Kost Yurii Sergeevich, Graduate student, Department of Energy Transport and Construction, North-Eastern State University, 13 Portovaya St., Magadan, 685000, Russia, e-mail: kost.svgu@mail.ru

Dmitrieva Tatiana Lvovna, Doctor Science of Engineering, Associate professor r, Department of Mechanics and Strength of Materials, Irkutsk National Research Technical University, Lermontov street, 83, Irkutsk, 664074, e-mail: dmitrievat@list.ru

Кость Юрий Сергеевич, аспирант, кафедра энергетики транспорта и строительства , ФГБОУ ВО Северо-Восточный государственный университет; 685000, Россия, Магаданская область, г. Магадан, ул. Портовая, д. 13; e-mail: kost.svgu@mail.ru

Дмитриева Татьяна Львовна, доктор технических наук, доцент, кафедра механики и сопротивления материалов, Иркутский Национальный Исследовательский Технический Университет; 664074, Россия, г. Иркутск, ул. Лермонтова, 83; e-mail: dmitrievat@list.ru

DOI:10.22337/2587-9618-2025-21-2-99-115

STRUCTURAL BEHAVIOR OF GFRP-CONCRETE COMPOSITE COLUMNS UNDER AXIAL LOAD

Mohammed A.M. Khalil, Mohammed M. Salem, Ata El-Kariem Shoeib, Alaa Gamal Sherif

Civil Department, Faculty of Engineering, Mataria, Helwan University, EGYPT

Abstract: Glass Fiber Reinforced Polymer (GFRP) is emerging as an effective alternative to traditional steel in construction due to its superior ability to withstand high loads, light weight, corrosion resistance and low maintenance costs. Optimizing the design of GFRP I-section can lead to significant savings construction costs. The main objective of this study is to understand the effect of introducing GFRP I-section internally on the load bearing capacity of Reinforced Concrete (RC) columns with and without fire. Four RC-column specimens were tested with a square cross-section of 160 mm side dimension and 1540 mm height. I-shaped GFRP section with 5.5 mm thickness for web and flanges, 80 mm flange width, and 100 mm total height is fixed in the center of section of column specimens .The specimens are divided into two groups. The first group has two conventional RC tested column specimens which one exposed to the fire 500°C for 90 minutes and the other without fire. The second group has two RC columns specimens reinforced with GFRP I-section which one exposed to the fire 500°C for 90 minutes and the other without fire. This study has shown that GFRP I-section composite columns exhibit excellent strength and high resistance to axial load than the conventional reinforced concrete columns. The maximum bearing capacity for the composite columns with (GFRP) I-section increased 17% more than the conventional RC columns. The maximum bearing capacity for the composite columns with (GFRP) I-section under the fire decreased 39% more than the composite (GFRP) columns without the fire, and decreased 14% more than the conventional RC columns. By different codes the theoretical axial load is calculated for tested specimens. The Finite element analysis was used to verify experimental results for studying additional parameters are the effect of concrete compressive strength, the steel yield strength, the reinforcement ratio, and the GFRP plate and I-section ratio of RC composite columns.

Keywords: GFRP I-Section, Composite columns, Reinforced concrete columns, Fire, Analysis, Experimental results, theoretical study, Finite element modelling

НЕСУЩАЯ СПОСОБНОСТЬ ЖЕЛЕЗОБЕТОННЫХ КОЛОНН, АРМИРОВАННЫХ GFRP-ПРОФИЛЕМ, ПРИ ДЕЙСТВИИ ПРОДОЛЬНОЙ СИЛЫ И ОГНЕВОМ ВОЗДЕЙСТВИИ

Мохаммед А.М. Халил, Мохаммед М. Салем, Ата Эль-Карим Шойиб, Алаа Гамаль Шериф

Кафедра гражданского строительства, инженерный факультет, Матария, Университет Хелуан, ЕГИПЕТ

Аннотация: Полимер, армированный стекловолокном (GFRP), является эффективной альтернативой традиционной стали в строительстве благодаря своей способности выдерживать высокие нагрузки при небольшом собственном весе, коррозионной стойкости и низких расходах на эксплуатацию. Оптимизация конструкции двутаврового сечения из GFRP может привести к значительной экономии затрат на строительство. Основной целью данного исследования являлось изучение влияния жесткой арматуры в виде двутавоа, выполненного из GFRP, на несущую способность железобетонных колонн при высокотемпературном воздействии от пожара и без него. Были испытаны четыре образца железобетонных колонн квадратного сечения со стороной 160 мм и высотой 1540 мм. В середине сечения образцов колонн были помещены двутавры из GFRP с толщиной полки и стенки 5,5 мм, шириной полки 80 мм и общей высотой 100 мм. Образцы были разделены на две группы. Первая группа состояла из двух обычных образцов железобетонных колонн, один из которых подвергался огневому

воздействию при температуре 500°C в течение 90 минут, а другой не подвергался высокотемпературному воздействию. Вторая группа состояла из двух образцов колонн, армированных двутаврами из GFRP, один из которых подвергался воздействию огня при температуре 500°C в течение 90 минут, а другой не подвергался высокотемпературному воздействию. Данное исследование показало, что колонны, армированные двутаврами из GFRP композита, обладают более высокой прочностью и высокой устойчивостью при сжатии по сравнению с обычными железобетонными колоннами. Максимальная несущая способность колонн, армированных двутаврами из GFRP, увеличилась на 17% по сравнению с обычными железобетонными колоннами. Максимальная несущая способность колонн, армированных композитными двутаврами из GFRP, при воздействии пожара снизилась на 39% по сравнению с аналогичными образцами, не подверженными огневым воздействиям, и оказалась на 14% меньше, чем для обычных железобетонных колонн. В соответствии с различными нормами проектирования выполнен расчет несущей способности испытанных образцов. Для исследования влияния прочности бетона на сжатие, предела текучести стали, процента армирования стальной и GFRP арматурой на несущую способность колонн было дополнительно выполнено моделирование методом конечных элементов.

Keywords: Двутавр из GFRP, композитные колонны, железобетонные колонны, пожар, анализ, экспериментальные результаты, теоретическое исследование, метод конечных элементов

Notation:

A_{ft} Total cross-sectional area of GFRP I-section
Ag Gross area of the concrete column
A_{st} Total cross-sectional area of longitudinal reinforcement
E_s Modulus of elasticity of steel
f Stress at any strain ε
f_c' Ultimate cylinder compressive strength for concrete
f_{cu} Compressive strength of concrete
f_s Stress in steel bars when the concrete reaches the maximum strength
f_f Ultimate compressive strength of GFRP I-section
f_u Ultimate tensile strength of steel
f_y Yield strength of steel
P_n Axial load at the maximum
α_1 Ratio of average stress in rectangular compression block to the specified concrete strength
ε_c Strain in the concrete at reaching the maximum strength
η Reduction factor for the high strength concrete for the rectangular stress distribution
ϕ_c Resistance factor for concrete and equal to 1.0 for laboratory conditions
ϕ_s Resistance factor for steel and equal to 1.0 for laboratory conditions
ε_o Strain at the ultimate cylinder compressive strength f_c'

1. INTRODUCTION

The Study of structural behavior of GFRP composite columns under axial load is important in civil engineering due to the recent increase in the use of composite materials in construction. Glass Fiber Reinforced Polymer (GFRP) columns offer advantages such as high strength-to-weight ratio, corrosion resistance, and durability. When combined with concrete, these columns can provide increased load- bearing capacity and ductility compared to traditional RC columns. Research has presented that the behavior of GFRP-concrete composite columns is influenced by factors such as the type and ratio of GFRP, the bond between GFRP and concrete and the GFRP confinement provided in the structure members. Understanding the performance of these composite columns is essential for designing safe and efficient structures that meet modern engineering standards. Further research is needed to optimize design guidelines and improve our understanding of how these innovative materials behave under different loading conditions. Therefore, optimization of the design of composite sections incorporating GFRP can lead to substantial saving in the construction cost. There are many previous studies that have been conducted on the behavior of composite columns reinforced with

GFRP I-profile and steel bars under axial load. Muhammad et al. [1], studied the performance of the behavior of the composite columns reinforced with the GFRP I-section and C-section under axial land eccentric load. The experiments were conducted using an axial compression test and an eccentric compression test with varying eccentricities. The experimental results show that the specimens reinforced with GFRP I-profiles achieved a higher ultimate load but lower ductility in comparison with the reference columns reinforced with steel bars as well as the composite columns reinforced with C-sections. Jing C [2] conducted an experimental and numerical study of reinforced concrete-filled square GFRP tubular columns under axial compression. Muhammad et al. [3], conducted an experimental study on the axial compressive behavior of GFRP tube reinforced concrete columns. The results of the experiments show that the use of GFRP tubes increases the ductility and strength of concrete columns. Tomblin and Barbero [4] investigated the local buckling behavior of on short columns made of GFRP I-sections and reported that they were dominated by local buckling, while Zureick and Scott [5] concluded that global buckling is the failure mechanism for long columns. Zouheir A. Hashem [6] conducted an analytical and experimental studied the behavior of short and long GFRP composite columns. Lei X [7] conducted a representative experimental investigation on the performance of slender (GFRP) square hollow columns subjected to both axial and eccentric loading. Srinath T [8] conducted an experimental and numerical investigation on the bonding and buckling behavior of GFRP circular column under axial compression. Yujun Qi [9] studied the behavior of pultruded glass fiber reinforced polymer GFRP-wood composite columns under axial compression. Aydin [10] conducted an experimental study to evaluate the tensile and compressive strength of the GFRP profiles at 13 different temperatures. The tensile and compressive strengths decreased by 28% and 75%, respectively at 100°C, compared to 25°C. When the temperature reached 200°C, the GFRP profiles had lost about 50% of their tensile strength and all of their compressive strength. This is mainly due to the degradation and softening of the polymer matrix within the GFRP components at high temperatures, resulting in reduced load carrying capacity. In addition, exposure to fire causes thermal expansion mismatches between the GFRP and concrete layers, inducing cracking and delamination effects that further weaken the overall performance of these composite columns. In general, GFRP profiles are very sensitive to high temperatures and relatively stable at low temperatures. Therefore, more attention should be paid to fire performance when GRP profiles are used in a high-temperature environment. In this study, the behavior of composite columns reinforced with GFRP I-section and exposed to fire at a temperature of 500 degrees for 90 minutes is investigated. The results of experimental, theoretical, and numerical models by using finite element analysis study concerning the axial load behavior of GFRP-concrete composite columns are presented. In addition, a practical guideline of composite columns reinforced with GFRP I-section leading to the most economical design is established and presented. All column specimens were tested under axial loading. Based on the experimental and numerical results, the load-strain curves and the failure modes are analyzed.

2. EXPERIMENTAL PROGRAM

The experimental study of this research is based on testing the behavior of GFRP-concrete composite columns under axial load. The column samples are shown schematically in Fig. 1, and they consist of the following:

2.1 Test parameters and specimen details

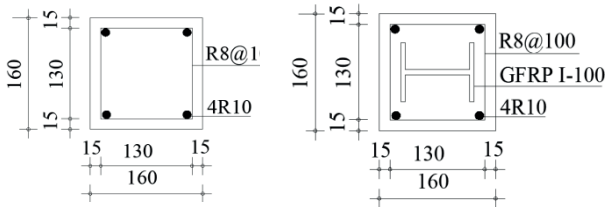
Two main parameters are considered, namely the effect of GFRP I-section on the behavior of RC composite columns and the effect of fire. The concrete dimensions and reinforcement

details of the tested columns are given in Table 1 and Fig. 1. A total of four specimens were fabricated and tested in this experimental study. All tested columns had an overall height of 1540 mm and a cross section of 160 mm x160 mm. All tested columns were reinforced with longitudinal four steel bars of 10 mm diameter and the steel transverse stirrups of 8 mm diameter at 100 mm spacing. The GFRP I-section is 100 mm total height, 80 mm flange width and 5.5mm thickness of web and flanges for the central placement within the RC composite columns. All of the specimens had the same concrete cover of 15 mm.

Table 1. Designations of tested columns

Specimens	Dim. (mm)		Steel		Fire	GFRP I-sec	Notes
	h	b	Longitudinal	Stirrups			
RCC	1540	160	4R10	R8@100	----	----	Reference for (RCCGI-C & RCC-F)
RCCGI-C	1540	160	4R10	R8@100	----	In center	As comparison for (RCC) The Reference for (RCCGI-C-F)
RCC-F	1540	160	4R10	R8@100	Fire	----	As comparison for (RCC)
RCCGI-C-F	1540	160	4R10	R8@100	Fire	In center	As comparison for (RCCGI-C)

Note that:
RCC: The tested conventional reinforced concrete column,
GI : The GRPR I-section
C : Center position
F : Fire



(a) RCC and RCC-F *(b) RCCGI-C and RCCGI-C-F*

Figure 1. Specimens details of tested column

2.2 Material properties

The concrete used was made of Cement (Sina Cement Company), natural siliceous sand, crushed dolomite coarse aggregate with a maximum size of 12.5 mm and superplasticizer (2% of the cement weight). The characteristic compressive strength of the standard concrete cubes after 28 days was 46 MPa. The yield strength and ultimate strength of 8 mm steel bars were 316 MPa and 431 MPa respectively. The yield strength and ultimate strength of 10 mm steel bars were 482 MPa and 652 MPa respectively. According to manufacturing, the tensile strength of GFRP I-section was 336 MPa, and the tensile modulus was 35.3 GPa [11].

2.3 Test Setup and Instrumentation

The test frame shown in Fig. 2 was fixed to the strong solid floor of the RC laboratory at the Faculty of Engineering of Helwan University. The supporting setup consisted of a horizontal frame made of four steel I-beams. It was supported by four vertical steel I-beam legs installed on the strong solid floor and the tested columns were rested on the frame. Loading was achieved by using a 1250 kN capacity cell that transferred the axial load to a steel plate with high rigidity/stiffness at the top of the columns, set up as shown in the side part of Fig. 2.

The load was measured by a load cell with 1250 kN capacity which was connected to a digital display unit. The horizontal sway and vertical displacement at the points shown in Fig. 3a were measured using two linear variable differential transducers (LVDTs) and two dial gauges (DGs) with accuracy of 0.01mm. The (LVDTs) and (DGs) were placed on the side and top surface of the columns as shown in Fig. 3b. Four electrical strain gauges were used to measure the strain in the steel bars and GFRP I-section at the maximum tensile point of the steel bars and GFRP I-section as shown in Fig. 4. This location was maintained for all tested columns.

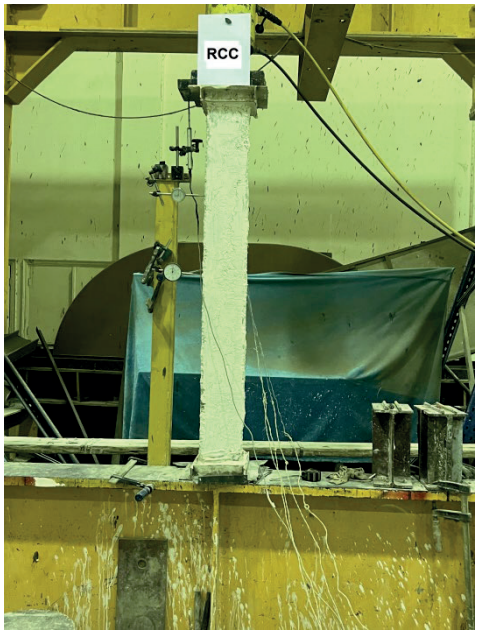
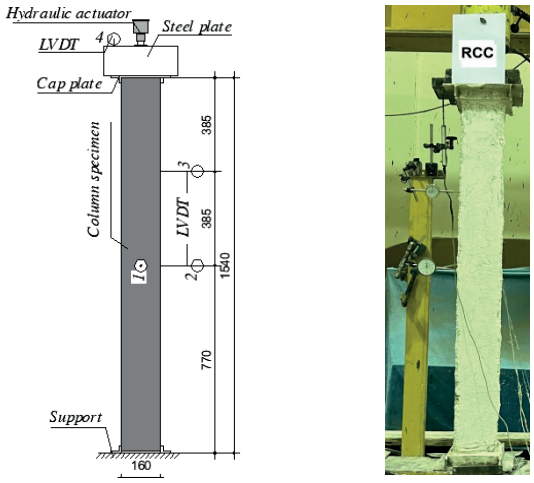
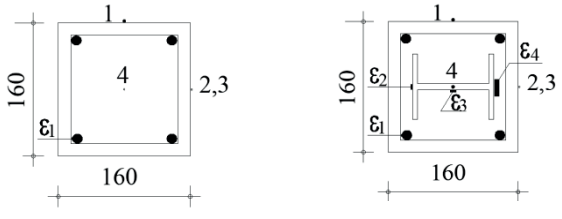


Figure 2. Axial load that transfer from load cell to columns



(a) Position *(b) Arrangement*

Figure 3. Dial gauges and LVDTs



(a) Conventional column *(b) Composite columns*

Figure 4. Test setup LVDT, DG and strain gauges of columns

2.4 Procedure for Firing

The RC column specimens were placed in a circular steel frame with side holes through which the fire was ignited and the specimens were exposed to a fire of 500°C for 90-minutes as shown in Fig. 5. Then the RC columns were left at room temperature for more than 4 hours before loading to failure.



(a) During the fire *(b) After the fire*

Figure 5. Fire of column specimens

3. RESULTS AND DISCUSSION

3.1 Failure modes of columns

The failure modes of the columns of all tested specimens are clearly shown in Fig. 6. All the tested specimens failed happened of the concrete in compression failure under axial load and splitting in the reinforcing steel bars, which occurred after the concrete reached its ultimate stress value. In addition, collapse occurred in GFRP I-section flanges for tested RC composite column as shown in Fig. 6b. The failure happened of the concrete at the mid height of the column as there was deterioration in the polymers when exposed to fire because the organic resin matrix used in GFRP I-section compounds is flammable for tested RC composite column with firing as shown in Fig. 6d.

Cracking of the columns started at loads reached more than 83%, and 94% of the maximum load for the reinforced concrete columns without firing and with firing respectively.



(a) RCC



(b) RCCGI-C



(c) RCC-F



(d) RCCGI-C-F

Figure 6. Failure modes of tested columns

3.2 Cracking and maximum load

The cracking and maximum loads are summarized in Table 2. The results show that the composite RC columns achieved 117% of the axial load bearing capacity of the conventional RC columns. The conventional RC columns exposed to firing achieved 86% of the capacity compared to the RC columns without firing. While, the RC composite columns exposed to firing achieved 61% of the capacity comparing RC composite columns without firing due to the organic resin matrix used in GFRP compounds is flammable. The results shown in Fig. 7 indicate that the maximum bearing capacity was achieved in RC composite column. The maximum reduction in column bearing capacity was due to firing at the composite GFRP I-profile column.

Table 2. The experimental results

Specimens	Cra. Load (kN)	Max. Load (kN)	P_{cr}/P_u	P_u/P_{uCtrl}	Notes
RCC	996.24	1052.90	94.62	1.00	Reference for (RCCGI-C & RCC-F)
RCCGI-C	1165.46	1234.30	94.42	1.17	As comparison for (RCC) Reference for (RCCGI-C-F)
RCC-F	766.30	900.71	85.08	0.86	As comparison for (RCC)
RCCGI-C-F	621.73	746.99	83.23	0.61	As comparison for (RCCGI-C)

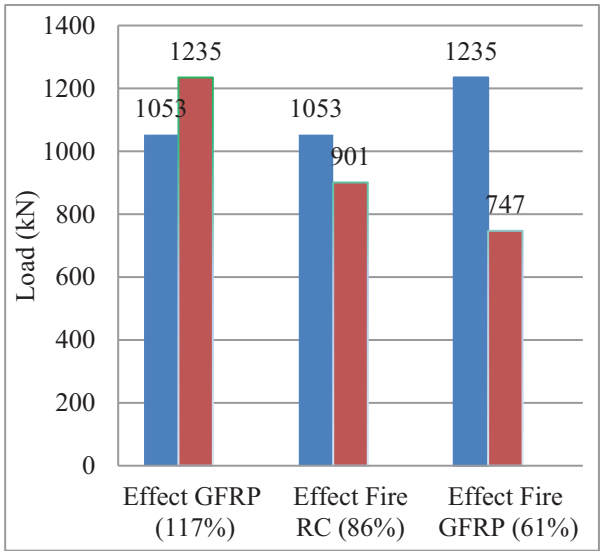


Figure 7. The maximum load and comparison between of tested columns

Comparing the maximum loads of the tested columns, it can be noted that the maximum load of the RC composite columns without firing was higher than that of the conventional RC columns. In RC composite columns, the maximum load increased to 117% compared to conventional RC columns.

3.3 Load–displacement curves

The load–vertical displacement relationships for the tested conventional and RC composite columns are shown in Fig. 8. The displacement values are those measured at the top height point of the RC columns.

The axial stiffness of the tested columns is the resistance of the columns to deflection or deformation under axial load. Stiffness is defined as the ratio of ultimate load to ultimate deflection [12]. The axial stiffness of conventional RC columns without firing was higher than that of RC composite columns and equal to 131.61 kN/mm and 85.94 kN/mm respectively. The axial stiffness of the tested columns without firing was higher than RC columns with firing, the axial stiffness equal to 131.61 kN/mm and 80.27 kN/mm of conventional RC columns without and with firing respectively, while the axial stiffness equal to 85.94 kN/mm and 59.52 kN/mm of RC composite columns without and with firing respectively because of the large deformation.

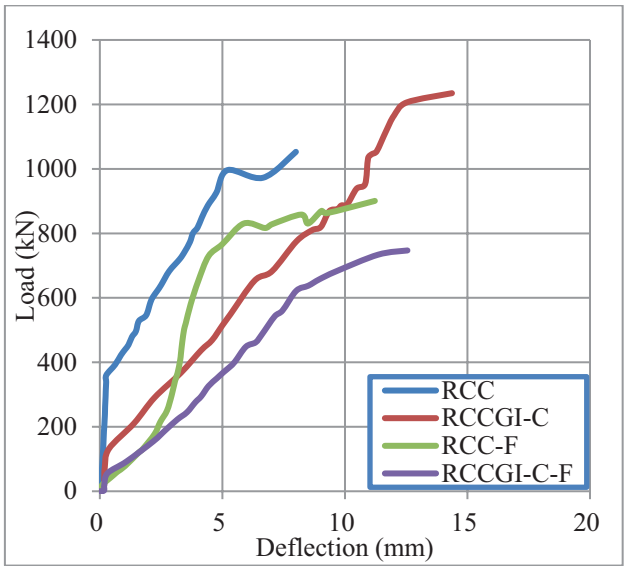
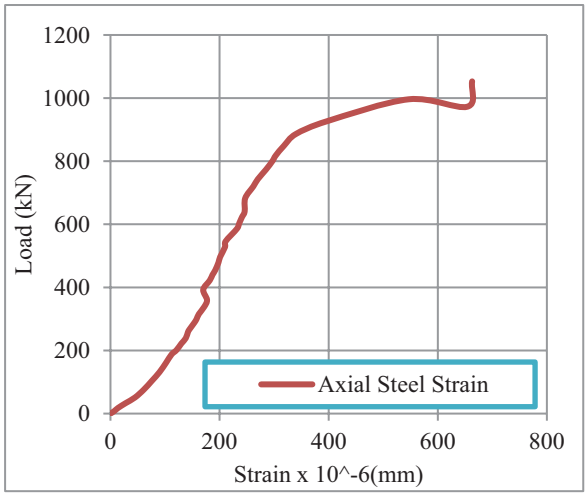


Figure 8. Load vertical displacement curves of tested columns

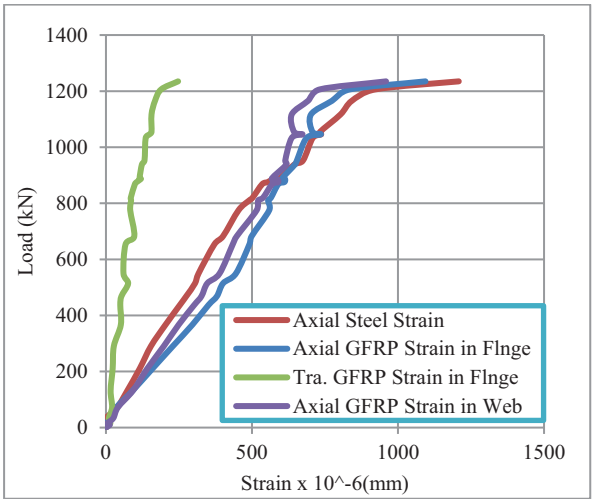
The comparison between the conventional RC columns and the RC composite columns without firing shows that the RC composite columns are more ductile than the conventional RC columns.

3.4 Stress strain curves

The measured stress-strain curves of the tested RC composite column without firing are shown in Fig. 9. The axial strain in steel bars and GFRP I-section has similar behavior at the same load level and recorded low strains of the tested column without firing, while the transverse strain in GFRP I-section is a small value compared to the axial strain. In general, the maximum strain in the steel bars and GFRP I-section not reached half the yielding strain of steel bars. Fig. 9 of RC composite column shows that the strain compatibility in deflection both internal steel and GFRP materials within the columns experience similar strains and deformations when subjected to axial load.



(a) Conventional column



(b) Composite column

Figure 9. The stress-strain curves of conventional and composite columns without firing

4. THEORETICAL ANALYSIS

The ability of common structural analysis tools to predict the performance of the tested RC composite columns was investigated in order to provide practicing engineers with information on their respective reliability according to the different codes was considered.

The ultimate strength of the conventional RC columns is calculated at point failure, the theoretical ultimate strength or nominal strength of a short axially loaded column is determined quite accurately by the Egyptian Code of Practice (ECP-203) [13] and British Standard BS 8110-97 [14], the theoretical maximum load can be calculated by both the concrete and reinforcement contribute in bearing the axial load as the following;

$$P_n = 0.67 f_{cu}(A_g - A_{st}) + f_y A_{st} \qquad (1)$$

According to ACI 318-11 [15], the theoretical maximum load can be calculated as the contribution of both the concrete and the reinforcement in carrying the axial load;

$$P_n = 0.85 f'_c (A_g - A_{st}) + f_y A_{st} \qquad (2)$$

The maximum nominal axial load on a column is calculated from the following equation according to Eurocode [16];

$$P_n = \eta f'_c (A_g - A_{st}) + f_s A_{st} \qquad (3)$$

Where; $\eta = 1.0$ for $f'_c \leq 50$ MPa (4)

$\eta = 1.0 - (f'_c - 50)/200$ for $50 < f'_c \leq 90$ MPa (5)

$$f_s = \varepsilon_c E_s \qquad (6)$$

$\varepsilon_c = 2\%$ for $f'_c < 50$ MPa (7)

$\varepsilon_c(\%) = 2 + 0.085(f'_c - 50)^{0.53}$ for $f'_c \geq 50$ MPa (8)

The maximum nominal axial load on the column is calculated by the following equation according CSA A23.3-04 [17];

$$P_n = \alpha_1 \phi_c f'_c (A_g - A_{st}) + \phi_s f_y A_{st} \qquad (9)$$

$\alpha_1 = 0.85 - 0.0015 f'_c$ but not less than 0.67 (10)

By comparing between the experimental results and values calculated by the theoretical equation of the different codes, find that, the experimental and theoretical results calculated by Egyptian Code of Practice (ECP-203) [13], British Standard BS 8110-97 [14], and ACI 318-11 [15] is scientific research converge very closely for the axial load , indicating the

strength and reliability of the findings obtained and showed similar results as observed by the experiment and no significant differences in axial loads were found as shown in Table 3. Therefore, the proposed equation to calculate the axial load of RC composite columns based on the Egyptian Code of Practice, and different Standard codes as following;

ECP-203 & BS $$P_n = 0.67 f_{cu}(A_g - A_{st}) + f_y A_{st} + 0.65 f_f A_f \quad (11)$$

ACI $$P_n = 0.85 f'_c (A_g - A_{st}) + f_y A_{st} + 0.65 f_f A_f \quad (12)$$

Eurocode $$P_n = \eta f'_c (A_g - A_{st}) + f_s A_{st} + 0.65 f_f A_f \quad (13)$$

CSA $$P_n = \alpha_1 \phi_c f'_c (A_g - A_{st}) + \phi_s f_y A_{st} + 0.65 f_f A_f \quad (14)$$

The reinforced concrete columns exposed to fire at 500 degrees, according to Eurocode 1991-1-2, section 3 [16], for the conventional reinforced concrete columns the reduction factor *kc,θ,* and *ky,θ*, to be applied to the compressive strength of concrete and the yield strength of steel and equal to 0.74 and 0.78 respectively. And it can be applied to composite columns, in addition to neglecting the resistance of GFRP due to the organic resin matrix used in GFRP compounds is melts at high temperature.

Table 3. Comparison between experimental and theoretical results of composite columns

Specimen Code	Maximum load (kN)					$P_{Exp.}$ / $P_{Theo.}$			
	$P_{exp.}$	$P_{ECP\&BS}$	$P_{ACI.}$	$P_{EUR.}$	$P_{CSA.}$	ECP& BS	ACI	EUR	CSA
RCC	1052.90	1043.04	1055.55	1129.69	1,005.50	1.01	1.00	0.93	1.05
RCCGI-C	1234.30	1232.74	1243.74	1299.72	1199.75	1.00	0.99	0.95	1.03
RCC-F	900.71	-------	-------	841.12	-------	-------	-------	1.07	------
RCCGI-C-F	746.99	--------	--------	751.54	--------	--------	--------	0.99	------

The theoretical calculations and the accuracy of the proposed equation according to different codes were able to accurately predict the load capacity of composite columns under vertical load.

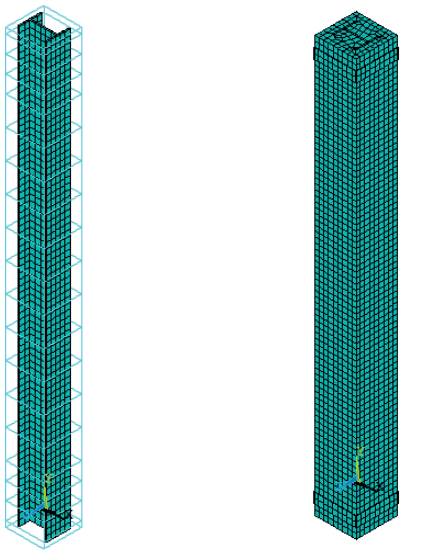
5. NUMERICAL ANALYSIS.

The non-linear finite element analysis method, as well as, the finite element analysis by using ANSYS (R19) program considered. The columns behaved nonlinearly mainly as its component materials have nonlinearity due to elastic plastic steel reinforcement bars and the linear pseudo plastic and brittle behavior of the concrete. This analysis method is currently considered as the state of the art for analysing reinforced concrete structures. However, the use of this sophisticated tool is complicated by the need to select several control parameters, which are usually chosen based on previous experience in correlating the results of the finite element analysis to real experimental results similar to the ones to be analyzed.

In addition to reproducing the behavior of the tested columns without firing, the nonlinear analyses were performed in order to study, the effect of the concrete compressive strength, the effect of the steel compressive strength of steel, the effect of reinforcement ratio, and the effect of percentage of GFRP ratio of the composite columns. The analysis was performed using the finite element package ANSYS [18].

5.1 Modeling

The solid element, SOLID65, was used to model the concrete, the 3D spar Link180 element was used to model the steel bars and the solid element, Solid185, was used to model the GFRP I-section and steel plates at the supports for the columns. The model of the verification column is shown in Fig. 10.



(a) Link elements for steel bars and GFRP I-section *(b) Solid elements for concrete & steel plates*

Figure 10. The model of the column used in the nonlinear analysis

5.2 Material properties

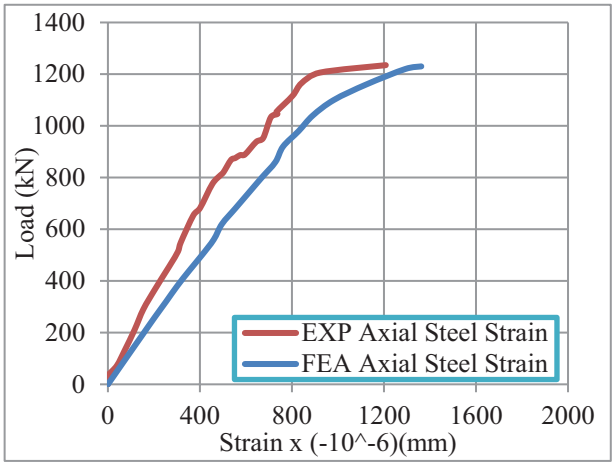
Equation (1), proposed by MacGregor [19], is used to represent the uniaxial compressive stress-strain relationship for concrete.

$$f = \frac{E_c \varepsilon}{1 + (\frac{\varepsilon}{\varepsilon_\circ})^2} \qquad (15)$$

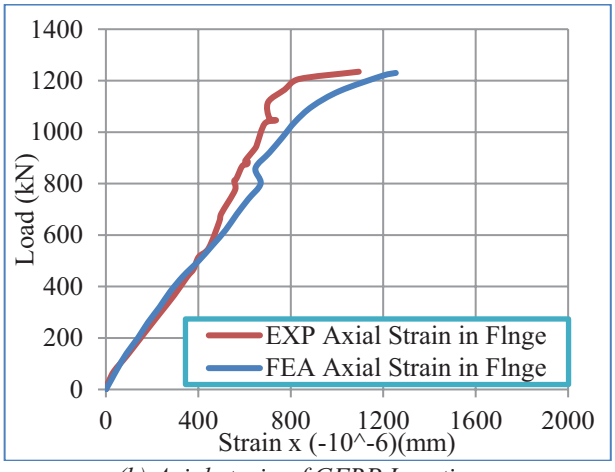
This equation has been used to plot the multi-linear isotropic stress-strain curve for concrete from 0.3fc' to the ultimate compressive strength, *0.3fc'*.the Elastic modulus is defined as 0.3fc', and calculated in the linear region. While elastic plastic uniaxial stress- strain model is used to model reinforcing steel. In addition, the modulus of elasticity and the tensile strength of concrete are calculated using the same specifications. The stress-strain curves of steel bars were presented according to ECP 203 Code of Practice [13]. GFRP was assumed to be linear, elastic and orthotropic material, and the material properties based on provided by the manufacturer were input to the model. The elastic plastic uniaxial stress -strain model given in ECP 203 Code of Practice [13] was used to model steel.

5.3 Validation of the numerical nonlinear model

For the validation of the ANSYS model for the RC composite columns, the determination of the parameters controlling the details of the concrete material model of SOLID65, such as the tensile stiffening and the shear retention across cracks of the reinforced concrete, were determined empirically by finding the values achieving the best fit of the calculated stress - strain curve of the RC composite column with the experimental one. The best numerical curve and the experimental curve are given in Fig. 11. It can be seen that, in general, the numerical curve is matching with the experimental one. However, it is relatively less stiff than the experimental curve.



(a) Axial strain of steel bars



(b) Axial strain of GFRP I-section

Figure 11. The experimental and numerical stress-strain curves of verification column

5.4 Parametric study

After verification of the finite element model, four parameters were further investigated for the conventional RC columns and the RC composite columns: -

(i) Effect of the compressive strength of concrete,
(ii) Effect of the yield strength of steel,
(iii) Effect of reinforcement ratio, and
(iv) Effect of percentage of GFRP I-section ratio of the RC composite columns.

Through it, the proposed equation for calculating the axial load of RC composite columns can be verified.

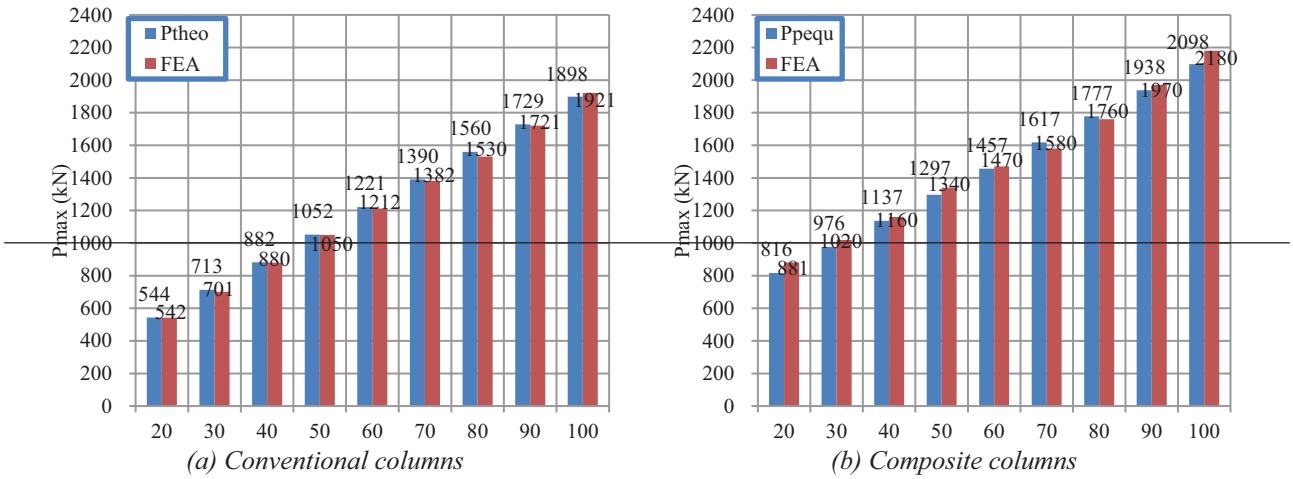
5.4.1 Effect of concrete compressive strength

To investigate the influence of the normal and high compressive strength of concrete on the bearing capacity of columns, nine analyses were performed for concrete strengths ranging from 20 MPa to 100 MPa to account for this parameter in this study for conventional RC columns and RC composite columns.

The theoretical calculated maximum axial loads by the Egyptian Code of Practice (ECP-203) [13] and British Standard BS 8110-97 [14] and the numerical calculated maximum axial loads by finite element analysis are given in Table 4 and Fig. 12. It is noted that the calculated maximum axial loads closely agree with the numerical values and doesn't exceed 2% and 4% for conventional RC columns and RC composite columns respectively, except when the compressive strength of concrete is equal to 20 MPa, the maximum axial loads calculated by finite element analysis is 8% increase about the calculated maximum axial loads by the proposed equation for RC composite columns.

Table 4. Effect of concrete compressive strength on theoretical and numerical maximum axial loads

No.	Concrete compressive strength (F_{cu}) (MPa)	Conventional columns			Composite columns		
		$P_{Theo.}$ (kN)	P_{FEM} (kN)	$P_{FEM}/P_{Theo.}$	$P_{Pequ.}$ (kN)	P_{FEM} (kN)	$P_{FEM}/P_{Pequ.}$
CSC1	20	543.52	542.00	1.00	816.25	881.00	1.08
CSC2	30	712.88	701.00	0.98	976.44	1020.00	1.04
CSC3	40	882.24	880.00	1.00	1136.63	1160.00	1.02
CSC4	50	1051.61	1050.00	1.00	1296.81	1340.00	1.03
CSC5	60	1220.97	1212.00	0.99	1457.00	1470.00	1.01
CSC6	70	1390.33	1382.00	0.99	1617.19	1580.00	0.98
CSC7	80	1559.69	1530.00	0.98	1777.38	1760.00	0.99
CSC8	90	1729.06	1721.00	1.00	1937.56	1970.00	1.02
CSC9	100	1898.42	1921.00	1.01	2097.75	2180.00	1.04



(a) Conventional columns *(b) Composite columns*

Figure 12. Effect of concrete compressive strength on theoretical and numerical maximum axial loads

Fig. 13 shows that the relationship between compressive strength of concrete and axial load of the conventional RC columns and RC composite columns. It can be seen that, the axial load increases linearly proportionally with the increase of compressive strength of concrete.

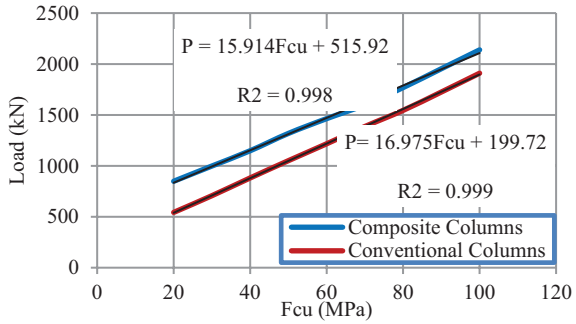


Figure 13. Relationship between concrete compressive strength and axial load

5.4.2 Effect of yield strength of steel

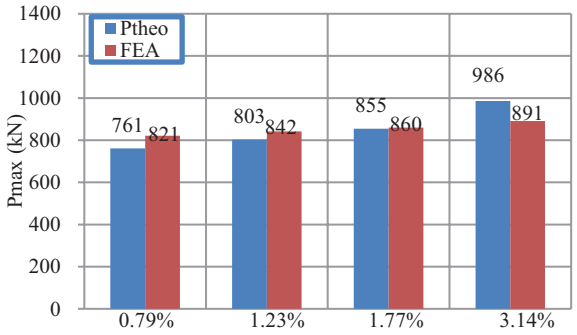
The yield strength of steel does not significantly affect the axial load capacity of conventional RC columns as shown in Table 5 and doesn't apply to RC composite columns; all stresses in the longitudinal reinforcement have been monitored to theoretical specimens by finite element analysis of the previous parameters. It is noted that the maximum stress in steel bars are less than 300 MPa for compressive strength of concrete up to 50 MPa and the stress in steel bars equal to 525.33 MPa of for high compressive strength of concrete at 100 MPa respectively. Therefore, the Eurocode [16] takes the stress value in the longitudinal steel is equal to the young's modulus of steel multiplied by the strain of concrete when reaching the maximum strength.

Table 5. Effect of stress in steel bars at the different compressive strength of concrete

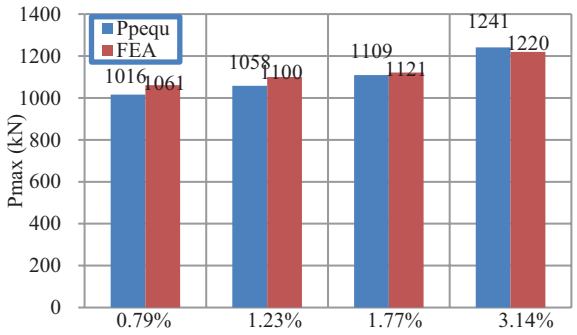
No.	Compressive strength (F_{cu}) (MPa)	Conventional columns	
		P_{FEM} (kN)	Stress in steel (MPa)
CSS1	20	542.00	194.67
CSS2	30	701.00	226.91
CSS3	40	880.00	263.17
CSS4	50	1050.00	288.16
CSS5	60	1212.00	333.95
CSS6	70	1382.00	392.95
CSS7	80	1530.00	428.55
CSS8	90	1721.00	473.61
CSS9	100	1921.00	525.33

5.4.3 Effect of reinforcement ratio

To study the influence of the longitudinal reinforcement ratio (ρ) on the behavior of conventional RC columns and RC composite columns, the analyses were performed for four different values 0.79%, 1.23%, 1.77%, and 3.14% by using diameters of 8 mm, 10 mm, 12 mm, and 16 mm respectively, with concrete compressive strength equal to 40 MPa and steel compressive strength equal to 400 MPa.



(a) Conventional columns



(b) Composite columns

Figure 14. Effect of the reinforcement ratio on theoretical and numerical maximum axial loads

The theoretical calculated maximum axial loads and the numerical maximum axial loads are shown Fig. 14 and given Table 6. It is noted that the calculated maximum axial loads are close the numerical values and don't exceed 4.48% for RC composite columns. While, the theoretical

calculated maximum axial loads increase when the reinforcement ratio is less than 1.25% and decrease when the reinforcement ratio is greater than 2.00%. Therefore, it is possible to reconsider the calculation of the value of axial load resulting from the compressive stress in the reinforcing steel.

Table 6. Effect of reinforcement ratio on theoretical and numerical maximum axial loads

No.	RFT. Ratio (%)	Conventional columns			Composite columns		
		$P_{Theo.}$ (kN)	P_{FEM} (kN)	$P_{FEM}/P_{Theo.}$	$P_{pequ.}$ (kN)	P_{FEM} (kN)	$P_{FEM}/P_{Pequ.}$
RS1	0.79	761.15	821.00	1.08	1015.53	1061.00	1.04
RS2	1.23	803.37	842.00	1.05	1057.76	1100.00	1.04
RS3	1.77	854.98	860.00	1.01	1109.36	1121.00	1.01
RS4	3.14	986.35	891.00	0.90	1240.73	1220.00	0.98

Fig. 15 shows that the relationship between reinforcement ratio and axial load of the conventional RC columns and RC composite columns. It can be seen that, the numerical maximum axial load increases linearly proportionally with the increase of reinforcement ratio up to approximately 3% and then decreases for conventional RC columns, while the rate of increase is linear for RC composite columns.

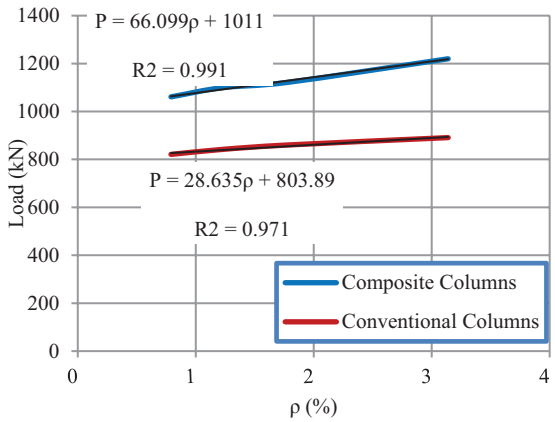


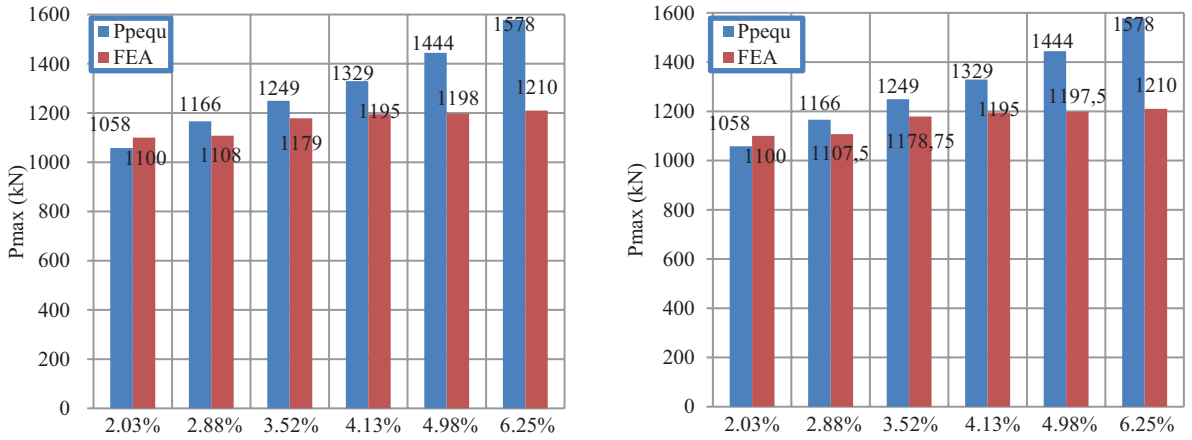
Figure 15. Relationship between reinforcement ratio and axial load

5.4.4 Effect of GFRP ratio

In order to investigate the influence of the GFRP ratio on the behavior of RC composite columns, the analyses were performed for twelve different values ranging from 2.03% to 17.18% by using two different shapes of GFRP sections, GFRP sections were shaped as flat plates, and I-shape respectively, concrete compressive strength was equal to 40 MPa and steel compressive strength was equal to 400 MPa. The theoretical calculated maximum axial loads and the numerical maximum axial loads are given in Table 7 and Fig. 16. It can be seen that the calculated maximum axial loads are close to the numerical values for RC composite columns with GFRP ratio up to 4% and 8% for flat plates and I-shape respectively. While, the numerical maximum axial loads are almost constant at GFRP ratio more than 4% and 8% for flat plates and I-shape respectively. Therefore, the proposed equation for calculating of the axial load of RC composite columns is satisfactory at GFRP ratios less than 4% and 8% for flat plates and I-shape respectively.

Table 7. Effect of GFRP ratio on theoretical and numerical maximum axial loads

No.	GFRP section	GFRP dimensions (mm)	GFRP I-section ratio (%)	P_{Equ} (kN)	P_{FEM} (kN)	P_{FEM} / P_{PEqu}	Stress in steel (Mpa)	Stress in GFRP (MPa)
RGFRP-P1	Flat Plate	89x5.5	2.03	899.91	935.00	1.04	349.05	181.41
RGFRP-P2		84x8	2.88	940.08	998.75	1.06	400.00	212.00
RGFRP-P3		80x10	3.52	970.55	1040.00	1.07	400.00	213.09
RGFRP-P4		76x12	4.13	999.52	995.00	1.00	362.04	166.67
RGFRP-P5		70x15	4.98	1040.20	980.00	0.94	359.82	140.53
RGFRP-P6		60x20	6.25	1058.35	980.00	0.93	301.61	116.70
RGFRP-I1	I-section	100x80x5.5	5.35	1057.76	1100.00	1.04	400.00	292.43
RGFRP-I2		100x80x8	7.63	1165.96	1107.50	0.95	400.00	199.97
RGFRP-I3		100x80x10	9.38	1249.17	1178.75	0.94	400.00	321.55
RGFRP-I4		100x80x12	11.06	1329.42	1195.00	0.90	400.00	205.90
RGFRP-I5		100x80x15	13.48	1444.21	1197.50	0.83	400.00	257.64
RGFRP-I6		100x80x20	17.18	1578.45	1210	0.77	338.93	147.14



(a) Flat Plate shape *(b) I-Shape*

Figure 16. Effect of the GFRP ratio on the theoretical and numerical maximum axial loads

The resistance of the RC composite columns is increases as the surface area of the GFRP increases and the homogeneity inside the concrete section.

6. CONCLUSIONS

From the experimental, theoretical and numerical results on the axial load behavior of the proposed composite columns reinforced with Glass Fibre Reinforced Polymer (GFRP) profiles and longitudinal steel bars, the following conclusions can be drawn:

1. Glass Fiber Reinforced Polymer (GFRP) I-profile concrete composite columns have proven to be structurally efficient elements with high axial load capacity.
2. Compared to the conventional RC columns, the RC composite columns with internal (GFRP) I-profile showed 17% higher ultimate capacity, and less displacement at the same loading levels.
3. The axial load is reduced by about 14% and 39% for conventional RC column and RC composite column respectively exposed to fire at a temperature of 500 C^o to one and half hour.
4. The proposed theoretical equation accurately predicts the axial load calculation of RC composite columns and should take the reduction factor of the compressive strength of GFRP I-section equal to 0.65.

5. The numerical model predictions were close to the experimental results. In a wide range of load -bearing capacity values investigated, less than 1.5% error was observed between the compressive strength predicted by the finite element analysis and the experimental results.
6. The Results indicated that the finite element model used in this study was able to predict the axial load of RC composite columns with reasonable accuracy.
7. The numerical results indicated that the axial load capacity of the RC composite columns increased with increasing GFRP ratio up to 4 % and 8% for flat plate and I-shape respectively.
8. The axial load increases with an increase of the compressive strength of concrete, longitudinal reinforcement ratio for conventional RC columns and RC composite columns.
9. The axial load doesn't increase proportionally with the increasing stress of the rebar, where the effective stress of the rebar doesn't exceed 300 MPa, and 525 MPa for compressive strength of concrete up to 50 MPa and high compressive strength of concrete up to 100 MPa respectively for conventional RC columns.

REFERENCES

1. **Hadi M., Youssef J.** Experimental Investigation of GFRP-Reinforced and GFRP-Encased Square Concrete Specimens under Axial and Eccentric Load, and Four-Point Bending Test // Journal of Composites for Construction, 2016.
2. **Jing C., Zhao L., Wu T., Li.** Experimental and Numerical Simulation of Reinforced Concrete-Filled Square GFRP Tubular Columns under Axial Compression // Materials 17, 2024, 2595.
3. **Hadi M., Wang W., Sheikh M.** Axial compressive behavior of GFRP tube reinforced concrete columns // Construction and Building Materials 81, 2015, 198-207.
4. **Tomblin J., Barbero E.** Local buckling experiments on FRP columns // Thin Walled Sruct. 18(2), 1994, 97-116.
5. **Harvey J.** A reinforced plastic footbridge, Aberfeldy, UK // Structural Engineering International, 4/93, 2018, 229-232.
6. **Robert L., Zouheir A., Short vs.** Long column behavior of pultruted glass-fiber reinforced polymer composites // Construction and Building Materials 15, 2001, 369-378.
7. **Lei X., Yu B., Yujun Q., Hao W.** Pultruded GFRP Square Hollow Columns with Bolted Sleeve Joints under Eccentric Compression //https://www.elsevier.com/userlicense/1.0/, 2018.
8. **Srinath T.** Buckling and Bonding Behavior of Glass Fiber Reinforced Epoxy Resin Composite Column // International Journal of Electrical Engineering and Technology (IJEET), Vol. 11, 2020, 219-224.
9. **Yunjun Q., Lei X., Yu B., Weiqing Liu., Hao W.** Axial Compression Behaviors of Pultruted GFRP-Wood Composite Columns // www.mdpi.com, journal/sensors, 2019.
10. **Aydin F.** Effects of various temperatures on the mechanical strength of GFRP box profiles // Construction and Building Materials 127, 2016, 843-849.
11. **OPCT**. Fiberglass Products Company, 398 Kaiyuan Road, Jizhou District, Hengshui City, Hebei Province, China // www.Chopct.com.
12. **Hassooni A., Zaidee S.** Behavior and Strength of Composite Columns under the Impact of Uniaxial Compression Loading // Engineering Technology and Applied Science Research, Vol. 12, No. 4, 2022, 8843-8849.
13. **Egyptian code** for design and construction of reinforced concrete structures, Housing and Building National Research Center.

Ministry of Housing, Utilities and Urban Planning, Giza, Egypt, ECP 203-2020.
14. **British Standards Institution.** Structural use of concrete, Part 1: code of practice for design and construction. British Standards Institution, London, BS811O - 1997.
15. **ACI Committee.** American Concrete Institute, & International Organization for Standardization, Building code requirements for structural concrete and commentary. American Concrete Institute (ACI 318-11).
16. **European Standard**. Design of concrete structures – part 1-1: General rules and rules for buildings. CEN, Brüssel, EN 1992-1-1, 2011.
17. **CSA Code Canadian** Standards Association for Design of Concrete Structures, Consolidated Mailing, Canada CSA. A23.3-04, 2004.
18. **ANSYS.** "ANSYS Help", Release 19, Copyright 2012.
19. **MacGregor G.** Reinforced Concrete Mechanics and Design", Prentice-Hall, Inc., Englewood Cliffs, NJ, 1992.

СПИСОК ЛИТЕРАТУРЫ

1. **Hadi M., Youssef J.** Experimental Investigation of GFRP-Reinforced and GFRP-Encased Square Concrete Specimens under Axial and Eccentric Load, and Four-Point Bending Test // Journal of Composites for Construction, 2016.
2. **Jing C., Zhao L., Wu T., Li.** Experimental and Numerical Simulation of Reinforced Concrete-Filled Square GFRP Tubular Columns under Axial Compression // Materials 17, 2024, 2595.
3. **Hadi M., Wang W., Sheikh M.** Axial compressive behavior of GFRP tube reinforced concrete columns // Construction and Building Materials 81, 2015, 198-207.
4. **Tomblin J., Barbero E.** Local buckling experiments on FRP columns // Thin Walled Sruct. 18(2), 1994, 97-116.
5. **Harvey J.** A reinforced plastic footbridge, Aberfeldy, UK // Structural Engineering International, 4/93, 2018, 229-232.
6. **Robert L., Zouheir A., Short vs.** Long column behavior of pultruted glass-fiber reinforced polymer composites // Construction and Building Materials 15, 2001, 369-378.
7. **Lei X., Yu B., Yujun Q., Hao W.** Pultruded GFRP Square Hollow Columns with Bolted Sleeve Joints under Eccentric Compression //https://www.elsevier.com/userlicense/1.0/, 2018.
8. **Srinath T.** Buckling and Bonding Behavior of Glass Fiber Reinforced Epoxy Resin Composite Column // International Journal of Electrical Engineering and Technology (IJEET), Vol. 11, 2020, 219-224.
9. **Yunjun Q., Lei X., Yu B., Weiqing Liu., Hao W.** Axial Compression Behaviors of Pultruted GFRP-Wood Composite Columns // www.mdpi.com, journal/sensors, 2019.
10. **Aydin F.** Effects of various temperatures on the mechanical strength of GFRP box profiles // Construction and Building Materials 127, 2016, 843-849.
11. **OPCT**. Fiberglass Products Company, 398 Kaiyuan Road, Jizhou District, Hengshui City, Hebei Province, China // www.Chopct.com.
12. **Hassooni A., Zaidee S.** Behavior and Strength of Composite Columns under the Impact of Uniaxial Compression Loading // Engineering Technology and Applied Science Research, Vol. 12, No. 4, 2022, 8843-8849.
13. **Egyptian code** for design and construction of reinforced concrete structures, Housing and Building National Research Center. Ministry of Housing, Utilities and Urban Planning, Giza, Egypt, ECP 203-2020.
14. **British Standards Institution.** Structural use of concrete, Part 1: code of practice for design and construction. British Standards Institution, London, BS811O - 1997.

15. **ACI Committee.** American Concrete Institute, & International Organization for Standardization, Building code requirements for structural concrete and commentary. American Concrete Institute (ACI 318-11).
16. **European Standard**. Design of concrete structures – part 1-1: General rules and rules for buildings. CEN, Brüssel, EN 1992-1-1, 2011.
17. **CSA Code Canadian** Standards Association for Design of Concrete Structures, Consolidated Mailing, Canada CSA. A23.3-04, 2004.
18. **ANSYS.** "ANSYS Help", Release 19, Copyright 2012.
19. **MacGregor G.** Reinforced Concrete Mechanics and Design", Prentice-Hall, Inc., Englewood Cliffs, NJ, 1992.

Mohammed Abdel-Rahman M. Khalil M.Sc, Faculty of Engineering, Helwan University, Egypt. E-mail: mamkhalil@m-eng.helwan.edu.eg

Mohammed M. Salem, Assistant Professor of Structure Engineering, Faculty of Engineering, Mataria, Helwan University, Egypt. E-mail: Mohamedsalem@m-eng.helwan.edu.eg

Ata El-Kariem Shoeib Soliman, Professor of Reinforced Concrete Structures, Faculty of Engineering, Mataria, Helwan University, Egypt. E-mail: atta_alsayed@m-eng.helwan.edu.eg.

Alaa Gamal Sheriff, Professor of Reinforced Concrete Structures, Faculty of Engineering, Mataria, Helwan University, Egypt. E-mail: agbsherif@gmail.com

Мохаммед Абдель-Рахман М. Халил, магистр технических наук, инженерный факультет, Университет Хелуан, Египет. E-mail: mamkhalil@m-eng.helwan.edu.eg

Мохаммед М. Салем, доцент кафедры инженерных конструкций, инженерный факультет, Матария, Хелуанский университет, Египет. E-mail: Mohamedsalem@m-eng.helwan.edu.eg

Ата Эль-Карим Шоиб Солиман, профессор кафедры железобетонных конструкций, инженерный факультет, Матария, Хелуанский университет, Египет. E-mail: atta_alsayed@m-eng.helwan.edu.eg

Алаа Гамаль Шериф, профессор кафедры железобетонных конструкций, инженерный факультет, Матария, Хелуанский университет, Египет. E-mail: agbsherif@gmail.com

International Journal for Computational Civil and Structural Engineering, 21(2) 116–128 (2025)

DOI:10.22337/2587-9618-2025-21-2-116-128

NUMERICAL ASSESSMENT OF PERMAFROST DEGRADATION AND RECOVERY AND ITS IMPACT ON SOIL MASS STABILITY

Nikolay A. Aniskin, Stanislav A. Sergeev, Andrey V. Stupivtsev, Ilia A. Bokov

National Research Moscow State University of Civil Engineering, Moscow, RUSSIA

Abstract. The paper presents solutions of the unsteady temperature problem and the problem of determining the stress-strain state of the soil massif, which is a bulk construction of stacks used for gold extraction from ore by heap cyanide leaching. In the process of irrigation of the stacks with heated cyanide solution occurs, heating of the soil mass and base, which leads to the formation of a zone of thawed permafrost or the so-called talik. As a result of numerical solution of the non-stationary temperature problem taking into account the step-by-step erection of the soil massif, the impact of air temperature and irrigation solution, the temperature distribution in the massif and the base for the period from the beginning of the massif erection to the 50-year period after the end of construction was obtained. For the most dangerous moment of the end of construction, when the zone of ground thawing is maximum, the stability of the slope together with the base is evaluated using their stress-strain state. The problems were solved by numerical finite element method using PLAXIS software package.

Keywords: soil massif, temperature problem, frozen ground, thawed ground, ground thawing, numerical solution, finite element method, slope stability

ЧИСЛЕННАЯ ОЦЕНКА ДЕГРАДАЦИИ И ВОССТАНОВЛЕНИЯ ВЕЧНОЙ МЕРЗЛОТЫ И ЕЕ ВЛИЯНИЕ НА УСТОЙЧИВОСТЬ ГРУНТОВОГО МАССИВА

Н.А. Анискин, С.А. Сергеев, А.В. Ступивцев, И.А. Боков

Национальный исследовательский Московский государственный строительный университет, г. Москва, РОССИЯ

Аннотация. В статье представлены решения нестационарной температурной задачи и задачи по определению напряженно-деформированного состояния грунтового массива, представляющего собой насыпное сооружение из штабелей, использующихся для добычи золота из руды путем кучного цианидного выщелачивания. В процессе орошения штабелей подогретым раствором цианида происходит, разогрев массива грунта и основания, что приводит к образованию зоны оттаявшей мерзлоты или так называемого талика. В результате численного решения нестационарной температурной задачи с учетом поэтапного возведения грунтового массива, воздействия температуры воздуха и орошающего раствора получено распределение температуры в массиве и основании на период с начала возведения массива до 50-летнего периода после окончания строительства. Для наиболее опасного момента окончания возведения, когда зона оттаивания грунта максимальна, дана оценка устойчивости откоса совместно с основанием с использованием их напряженно-деформированного состояния. Задачи решены численным методом конечных элементов с использование программного комплекса PLAXIS.

Ключевые слова: грунтовый массив, температурная задача, мерзлый грунт, талый грунт, протаивание грунта, численное решение, метод конечных элементов, устойчивость откоса

INTRODUCTION

Most of the territory of the Russian Federation, approximately (65-70) % according to different estimates, is located in permafrost areas. It is most widespread in Eastern Siberia. These regions play a crucial role in the development of the country's economy. This territory is home to a large number of mining enterprises that use various technologies to enrich ore and obtain

metals, including precious metals. One of such methods is heap leaching, a technology that is quite simple and effective [1-7]. It includes several stages (Fig.1):

1. Ore preparation, including its crushing and grinding.
2. Preparation of the base for stacking stacks of crushed ore. Formation of a watertight screen on the sloping surface of the base for the stacks of crushed ore. As a rule, clay soils and polyethylene film are used for the screen device [8]. A drainage layer and reservoir beds for collecting enriched solutions are laid on the screen.
3. Stacking of enriched ore in the stack on the prepared impermeable base.
4. Irrigation of the stacked ore stack with a reagent (cyanide solution) [9-12]. When the solution penetrates through the thickness of crushed ore, gold is leached and carried by the filtering solution, which flows down the inclined reservoir beds and through the prepared chute into the settling pond.
5. Metal precipitation in the settling pond and its extraction [13].

The processed ore array is erected in stages in time with stack dumping. Ore stacks are irrigated, as a rule, year-round. In cold periods of the year the mortar is heated to positive temperatures. The movement of the heated solution down the dumped massif causes its heating, as a result of which a complex temperature regime of both the dumped ore massif and the adjacent base is formed in time. In the process of array construction and its irrigation there is a gradual penetration of heat flow into the base, causing an increase in the temperature of the base soil. In the case where frozen rocks are embedded in the subgrade, thawing occurs. This process gradually penetrates deep into the subgrade. This process causes phase transitions in the soils of the ore massif and the base: transition of water from the solid state - ice to liquid and from liquid to gaseous. These changes cause changes in the properties of soils: thermophysical, filtration, strength, which affects the ongoing processes. Thawing of ice contained in the pores of frozen ground increases its permeability, decreases its thermal conductivity and strength properties. Thus, in time there is a complex change of mutually influencing processes: filtration and temperature processes, formation of stress-strain state.

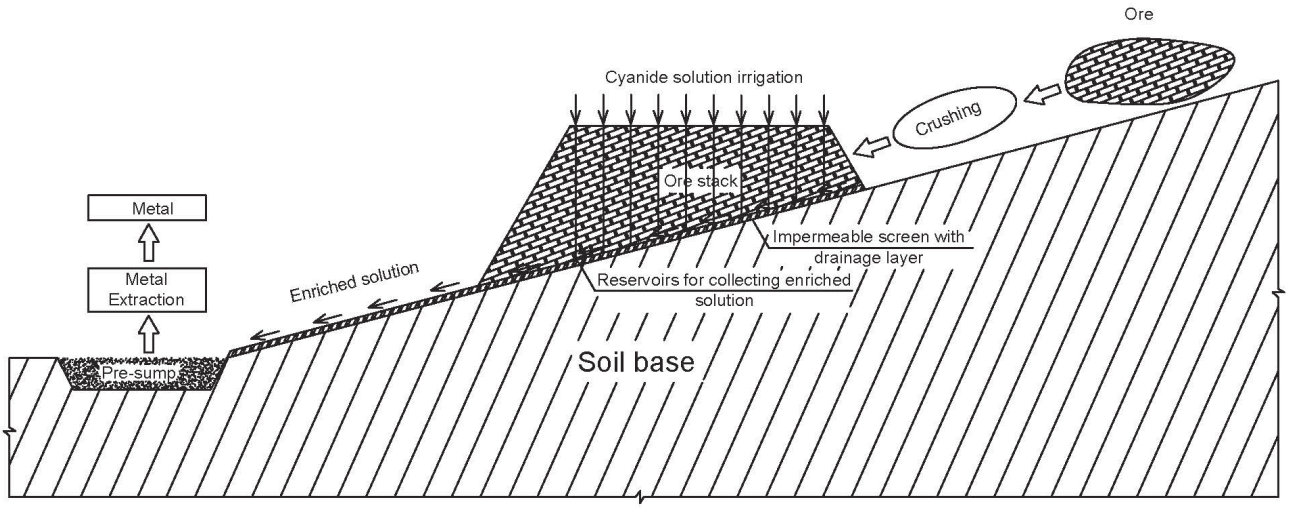


Figure 1. Schematic diagram of gold ore beneficiation process by heap leaching method

In order to assess the behavior of the system "enriched ore massif - base" it is necessary to forecast its formed temperature regime and stress-strain state. The solution of such a problem, taking into account the changes

occurring in the system “ore dressing massif - base” is a rather difficult task.

The solution of non-stationary temperature problems is widespread in the field of hydraulic engineering, since the temperature regime of structures of this type has a significant impact on their operational characteristics. A considerable amount of research in the field of hydraulic engineering is devoted to studies of temperature field distribution, including filtration [14-18].

However, there are no studies of the temperature effects of the heap leach stack massif using the finite element method.

This paper presents some results on solving such a problem numerically using the finite element method. The solution is obtained using PLAXIS 2D software package. The solution allowed obtaining a detailed picture of the change in the temperature regime of the soil massif with an assessment of the degree of degradation of the permafrost base and the time of its recovery. The stability of the slope of the ore massif and the base for the most unfavorable case at the time of maximum thawing of the base was also assessed.

METHODS

The process of heat transfer in the soil massif of stacks of ore to be processed and base is considered. The soil, as it is known, is a porous medium, which consists of solid particles and pores, which can contain water in one of the possible forms: in solid, liquid or gaseous state. The process of heat transfer in a soil mass implies the accumulation of energy in all soil constituents.

Quantitative assessment of the behavior of the soil mass in terms of temperature distribution can be carried out by distinguishing a number of simple processes such as: heat conduction, convection, radiation.

The main mode of heat transfer in the soil mass is heat conduction. The thermal conductivity of a soil mass is the rate at which heat energy passes a unit area of soil due to a unit temperature gradient.

The specific heat flux due to heat conduction is expressed by Fourier's law [19,20]:

$$H = -\lambda_s \frac{\mathrm{dT}}{\mathrm{dz}} \tag{1}$$

where λ_s is the thermal conductivity of a solid material; $\frac{\mathrm{dT}}{\mathrm{dz}}$ is the temperature gradient.

The solution of the temperature problem is reduced to the solution of the known equation of heat flow continuity in the design domain [19,20]:

$$\rho_s c_s \frac{\partial T}{\partial t} = -\frac{\partial G}{\partial z} \tag{2}$$

where ρ_s is the density of the solid material, c_s is the specific heat capacity of the solid material, G is the heat flux density in the soil.

The left side of equation (2) represents the rate of heat accumulation in the soil layer, and the right side represents the heat flux flow rate, or the rate of change in heat flux density with depth.

Taking into account equations (1,2), we obtain:

$$\rho_s c_s \frac{\partial T}{\partial t} = -\frac{\partial}{\partial z}\left(\lambda_s \frac{\mathrm{dT}}{\mathrm{dz}}\right) \tag{3}$$

The energy balance equation for a porous medium in a general form can be written as follows:

$$\frac{\partial T}{\partial t}\left(nS\rho_w e_w + n(1-S)\rho_v \rho_v + (1-n)\rho_s e_s\right) = -\nabla(J_{\mathrm{A}w} + J_c) + Q_T \tag{4}$$

where e_w, e_v, e_s are the internal energy in the water, vapor, and solid phases, respectively, Q_T is the heat source (i.e., the rate of heat generation per unit volume).

In the program complex PLAXIS 2D, the input parameters are parameters for the solid part of the soil mass - for soil particles. And since the parameters determined by

geotechnical engineers are determined for the soil as a whole [21] - it is important to move from general values to private parameters for soil particles [22].

The following dependences are used for the thermal conductivity of soil in different states:

Non-porous material:

$$\lambda_{soil} = \lambda_s \quad (5)$$

Dry material:

$$\lambda_{soil} = (1-n)\lambda_s \quad (6)$$

Phase transition case:

$$\lambda_{soil} = (1-n)\lambda_s + nS[(1-w_u)\lambda_i + w_u\lambda_w] + n(1-S)\lambda_V \quad (7)$$

In other cases:

$$\lambda_{soil} = (1-n)\lambda_s + nS\lambda_w + n(1-S)\lambda_V \quad (8)$$

Where n is the porosity coefficient, S is the degree of water saturation, w_u is the unfrozen water content. Values with index i - ice properties, w - water properties, V - vapor properties.

The heat stored in the ground can be expressed as follows:

Non-porous material:

$$(\rho c)_{soil} = (\rho c)_s \quad (9)$$

Dry material:

$$(\rho c)_{soil} = (1-n)(\rho c)_s \quad (10)$$

Phase transition case:

$$(\rho c)_{soil} = (1-n)(\rho c)_s + nS[(1-w_u)(\rho c)_i + w_u(\rho c)_w] + n(1-S)(\rho c)_V \quad (11)$$

In other cases:

$$\lambda_{soil} = (1-n)(\rho c)_s + nS(\rho c)_w + n(1-S)(\rho c) \quad (12)$$

In addition to heat conduction inside the area under consideration, it is necessary to take into account temperature conditions at its boundaries. At the boundary of the design area with the atmosphere, surface heat transfer occurs, and the ground is heated to some temperature value not exceeding the air temperature. The heat transfer between the air and the ground is determined by the heat transfer coefficient, which is determined in accordance with paragraph D.3 of SP 121.13330.2019 [23] depending on the wind speed:

α_q=2,4v_a+2,3 when $v_a \leq$4,6м/с;
α_q=3,4(v_a-1) when $v_a >$4,6м/с,

where v_a - is the monthly average wind speed, m/s.

При средней скорости ветра 1,5 м/с коэффициент теплообмена составляет 5,9 Вт/(м2·°С).

Using the results of the temperature problem solution, the slope stability coefficient of the design area was calculated using the method of lowering the strength characteristics (angle of internal friction, cohesion and shear strength) until failure was reached [24]. The position of the possible shear surface and the value of the stability coefficient were obtained.

RESEARCH OBJECT

The object of research in this article is the temperature regime and stress-strain state of the ground massif formed during the process of erection and operation, which consists of heap

leach stacks of the gold extraction plant and the base. The facility is located in the permafrost zone. Climatic characteristics of the erection area are presented in Table 1.

Table 1. Mean monthly and mean annual air and cyanide solution temperatures

Month of the year,	1	2	3	4	5	6	7	8	9	10	11	12	Avg. year
Average monthly temperature, °C	-20,8	-18,7	-12,6	-4,4	2,0	7,7	12,5	13,5	8,6	-1,7	-13,7	-19,3	-3,9
Temperature solution °C	19,0	18,9	19,1	18,9	16,5	14,1	14,8	14,6	14,7	15,4	15,4	18,0	16,3

Ore irrigation is performed in the process of ore dumping into the stack, after formation of conventional sections. In cold periods of the year, the solutions are heated to positive temperatures before being fed for processing. Irrigation of the stack is assumed to be year-round. The temperature of the irrigation solution depends on the time of year and is presented in Table 1. The profile of the investigated structure with the stages of stack backfilling and base soils is presented in Figure 2.

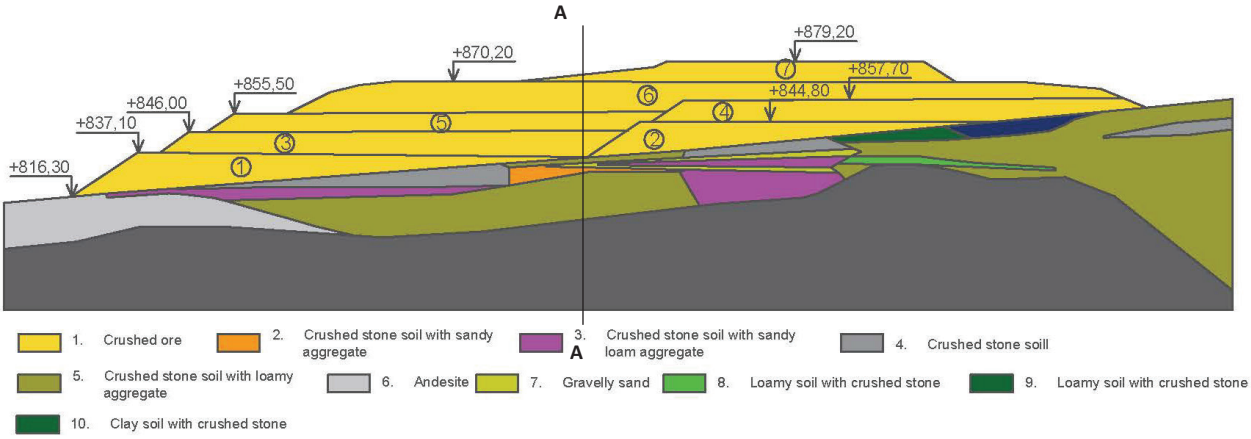


Figure 2. Profile of the investigated structure. Figures show the stage of stack placement

As part of the calculation it is accepted: the erection of the stage lasts from March to October, stacks are erected every year. Construction lasts for 7 years. The schedule of the heap leach stack construction phasing is shown in Figure 3.

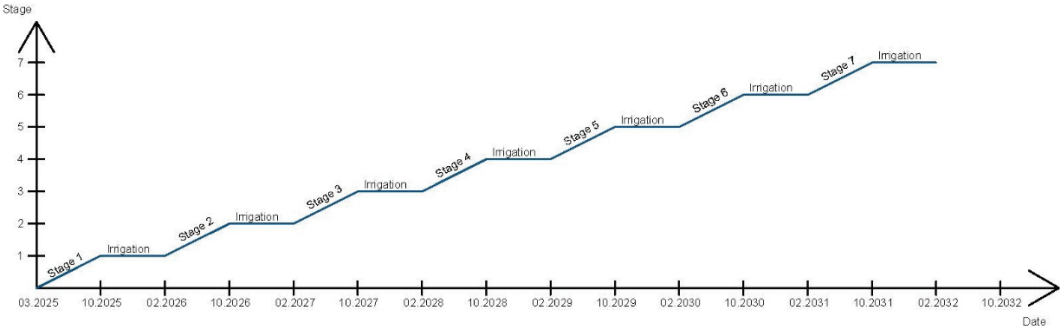


Figure 3. Heap leach stack erection schedule

Since the structures influencing the temperature regime of the ground massif in the permafrost zone require controlling the VAT taking into account the thawing zones, the results of the temperature pattern calculation are used to estimate the thawing zone in order to assess the VAT and slope stability of the heap leach stack. The forecast was performed for the period of massif erection and a period of 50 years from the end of the last stage of erection.

RESULTS

Some of the results of the studies are presented in Figs. 4-6. Fig. 4-5 show isopole patterns of the temperature of the soil massif of heap leach stacks and the base at the time corresponding to the end of backfilling and irrigation of the stacks in the middle of October (Fig. 4) and at the time corresponding to 50 years after the end of backfilling in the middle of December.

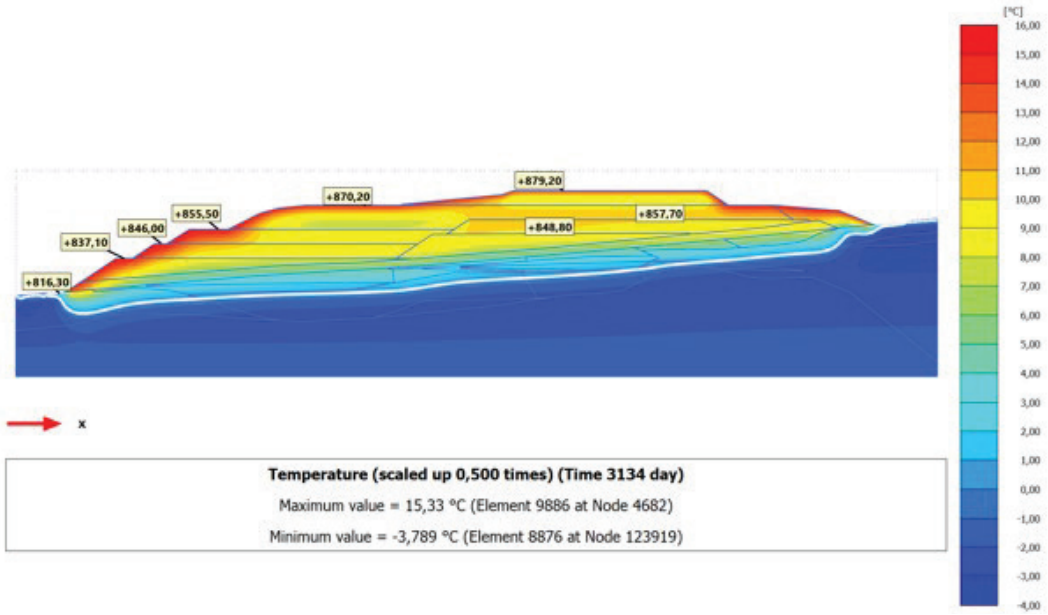


Figure 4. Isopoles of temperature distribution in the soil mass at the time of construction completion - year 7 (October)

Fig. 6 are plots of the temperature change of the considered massif along the vertical section A-A (the position of the section is shown in Fig. 2) at the moments of time 5, 10, 15, 20, 30, 40 and 50 years after the end of construction in the middle of December

The moment of the end of erection is characterized as follows (Fig. 4). Due to the irrigation of the stack array with heated mortar (in October, the mortar temperature is 15.4°C, Table 1), the surface layer of the stacks is warmed, the maximum temperature is the value of 15.3°C. At depth, the entire stack massif is heated, the temperature varies from 15°C in the upper layers to 4.0°C at the base. The base is warmed up to positive temperatures to a depth of 15.2 m. Below this depth, a frozen zone with a minimum temperature of -3.8 °C is preserved.

After the end of the irrigation process in October of the 7th year after the start of the array construction, the base and the stack array gradually cool down (Fig.6). In the stack massif, positive temperatures in its depth are maintained for 40 years after the end of the heap leaching process. By this time, a 34.0 m deep talik with a maximum temperature of 0.8 °C is preserved in the basement.

In 50 years after the end of the facility operation the zone of melted ground in the whole massif completely disappears (Fig. 5, 6). The maximum temperature of the base soil at a depth of 24.0 m is -0.4 °C.

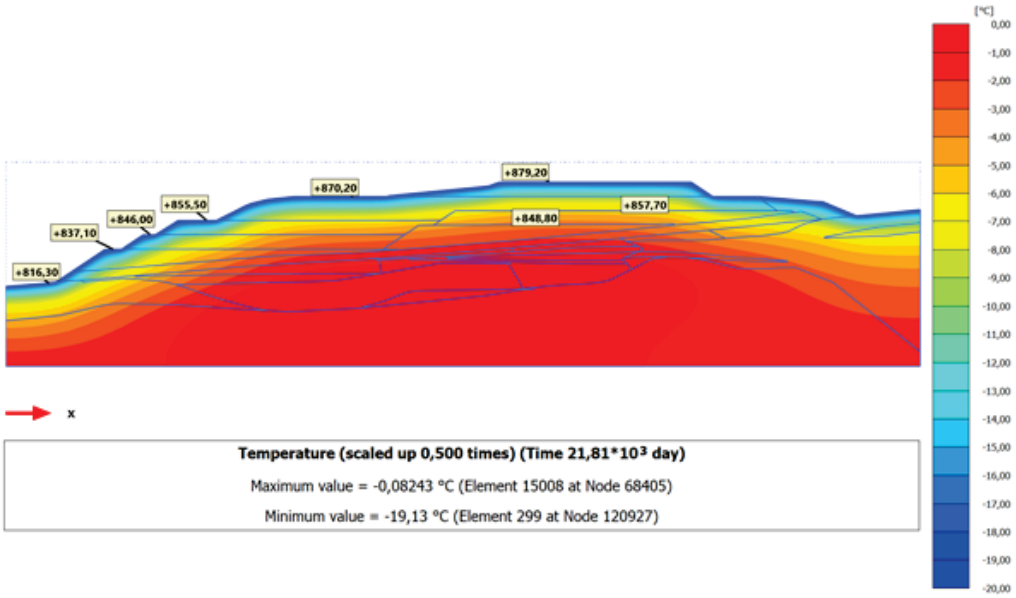


Figure 5. Isopoles of temperature distribution in the soil mass 50 years after construction (December)

According to the results of the temperature regime calculation, the most dangerous moment from the VAT point of view is the moment when the largest part of the soil massif is in the melted state - the moment of stack erection and irrigation works completion. The VAT calculation was performed for the case of the end of construction - the greatest depth of thawing of the stack base at this moment is 15.2 m.

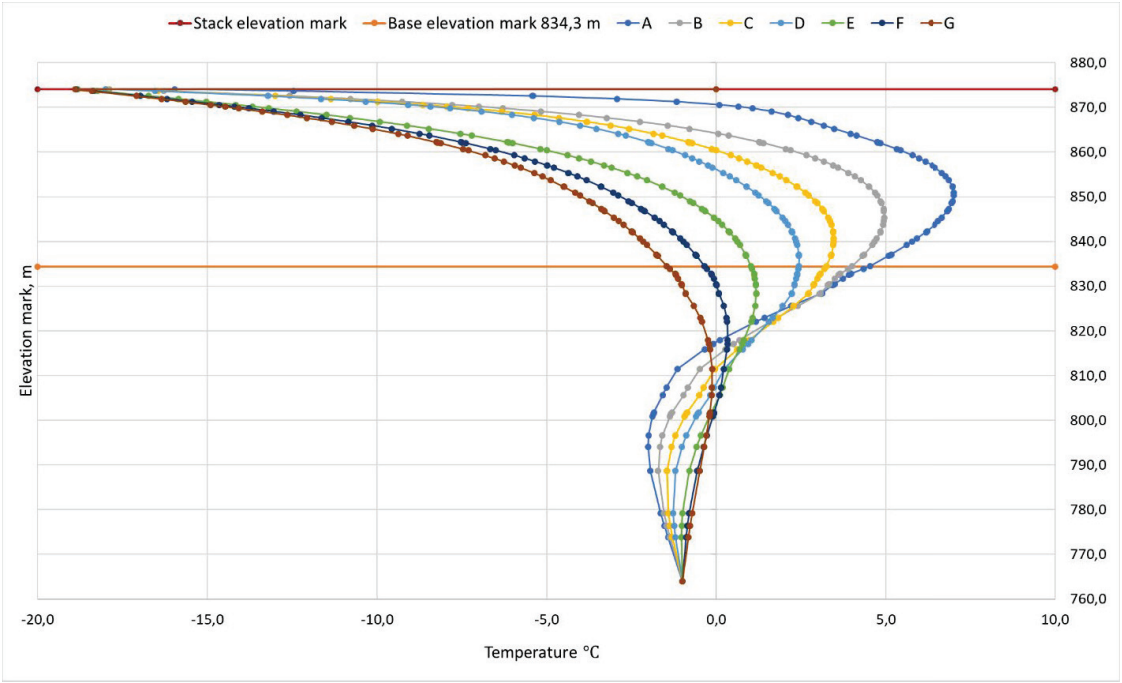


Figure 6. Temperature distribution in the soil massif of stacks along cross-section A-A: after A) 5 years, B) 10 years, C) 15 years, D) 20 years, E) 30 years, F) 40, G) 50 years after the end of construction

To assess the stability of the designed structures in the PLAXIS 2D PC, the Safety calculation [24] was used, in which the strength characteristics of the soils (angle of internal friction, cohesion and shear strength) are successively reduced until failure occurs. The results of the stability calculation are the determination of the potential shear surface, i.e. the most weakened surface along which failure may occur, and the calculated stability coefficient. The tangential shear stresses acting on this surface are maximum. The design stability factor is defined as the ratio of the actual strength to the fracture strength.

The normative criterion of slope stability is compliance with the condition of clause 5.2.2 of SP 116.13330.2012 [25]:

$$\Psi F \leq \frac{\gamma_d}{\gamma_n} R, \qquad (13)$$

where F - design value of the generalized force impact on the structure or its structural elements (force, moment, stress), deformations (displacements) or other parameters for which the limit state is assessed; Ψ - load combination coefficient, γn - reliability coefficient for the responsibility of the structure, taken in calculations for the first group of limit states: for structures of responsibility level KS-2 - 1.20. The value of the normative stability coefficient k_{st} of slopes is calculated as the ratio of forces F and R:

$$k_{st}^n = \frac{R}{F} \geq \frac{\gamma_n \Psi}{\gamma_d}, \qquad (14)$$

To ensure stability, the calculated stability factor should exceed the normative one, determined in accordance with clause 5.2.3 of SP 116.13330.2012 [25].

For structures of responsibility level KS-2 we have:

$$k_{st}^n = \frac{1{,}20 \cdot 1{,}00}{1{,}0} = 1{,}20$$

The result of stability assessment is presented in Fig. 7. The obtained value of the stability coefficient k_{st}=1.589 indicates a large stability reserve of the slope of the soil massif.

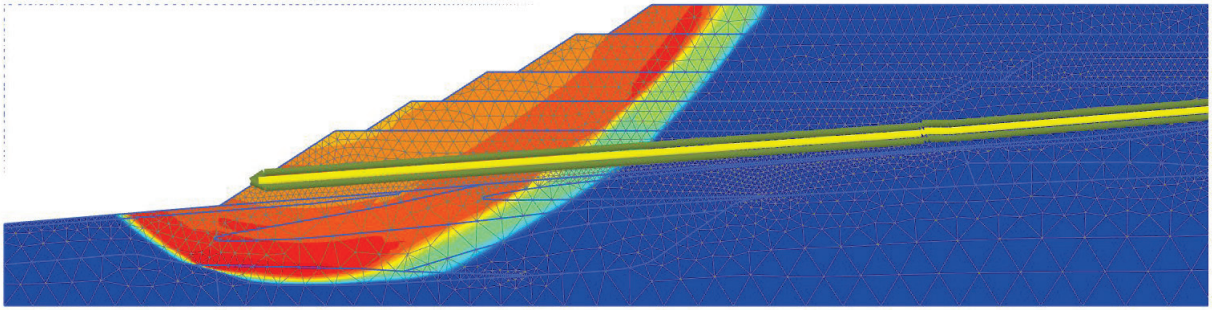


Figure 7. Sliding surface of the stack slope at the moment of erection completion with k_{st}=1.589

CONCLUSIONS

Within the framework of this work the problem of non-stationary temperature flow distribution for the heap cyanide leaching stack structure was set and solved. The solution of this problem allowed to establish thawing zones in order to correctly determine the VAT of the structure and to make a forecast for the service life of the structure.

When solving the problem, such factors as: external air temperature, temperature characteristics of the ground mass, heat transfer from cyanide solution to the stacks, heat transfer coefficient at the air-soil interface are taken into account.

Heap leach stacks are irrigated with cyanide solutions with a temperature of more than 14 °C. This factor forms a thick layer of melted soil in the body of the structure, which in the

process of operation transfers heat to the underlying layers of the soil massif, thus creating a talik.

The thickness of the talik in the soil massif of the stacks and base at the time of completion of backfilling of the structure and irrigation is 50.8 meters. During the operation of the structure, the talik degrades and decreases in size. The time of full dispersion of the melted soil zone is 50 years from the end of construction.

The most dangerous situation in terms of the stability of the slopes of the structure occurs at the moment when the largest part of the soil massif is in the melted state. This situation occurs at the moment when the construction of the structure is completed. According to the results of stability calculations in the PC Plxais 2d the value of the calculated stability coefficient was obtained, which amounted to 1.589, thus the value of the stability coefficient of the stack massif does not contradict the requirements of the normative documentation.

FUNDING

This research was funded by the National Research University Moscow State. University of Civil Engineering (grant for fundamental and applied scientific research, Project No. 29-392/130).

REFERENSES

1. **Ghorbani, Y., Franzidis, J.P., Petersen, J.,** 2016. Heap leaching technology - Current State, innovations, and future directions: A review. Mineral Processing and Extractive Metallurgy Review 37, 73–119. doi:10.1080/08827508.2015.1115990
2. **Thenepalli, T., Chilakala, R.,Tuan, L., Kim, C.S.,** 2019. A brief note on the heap leaching technologies for the recovery of valuable metals. Sustainability (Switzerland). doi:10.3390/su10023347
3. **Petersen, J.,** 2016. Heap leaching as a key technology for recovery of values from low-grade ores – A brief overview. Hydrometallurgy 165, 206–212. doi:10.1016/j.hydromet.2015.09.001
4. **Donato, D.B., Madden-Hallett, D.M., Gursansky, W.,** 2017. Heap leach cyanide irrigation and risk to wildlife: Ramifications for the international cyanide management code. Ecotoxicology and Environmental Safety 140, 271–278. doi:10.1016/j.ecoenv.2017.02.033
5. **Shumilova, L.V., Khatkova, A.N., Myazin, V.P.** et al. Year-Round Heap Leaching of Gold in Cryolithozone. Metallurgist 64, 1046–1056 (2021). https://doi.org/10.1007/s11015-021-01086-0
6. **Rubtsov, Yu. I.** Speed cyanide leaching of gold-containing gravi-concentrates / Yu. I. Rubtsov // Non-ferrous metals. – 2007. – № 10. – C. 60-63. – EDN KUAMWF.
7. Investigation of the possibility of cyanide leaching of gold from unoxidized ores of the Pogromnoye deposit / Yu. I. Rubtsov, E. E. Kosarev, S.D. Soronkhorova, O.V. Fokina // Kulagin Readings: technique and technology of production processes : XIV International Scientific and Practical Conference: in 3 parts, Chita, November 26-28, 2014 / Transbaikal State University. Volume Part 1. - Chita: Transbaikal State University, 2014. - C. 256-260. - EDN SBAHMV.
8. **Fady B.** Abdelaal and R. Kerry Rowe. 2023. Physical and mechanical performance of an HDPE geomembrane in 10 mining solutions with different pHs. Canadian Geotechnical Journal. 60(7): 978-993. https://doi.org/10.1139/cgj-2022-0419
9. **Zelyakh, J.D**. Method of improving the process of noble metal extraction from cyanide solutions / J.D. Zelyakh, K.D. Naumov, V.G. Lobanov // Engineering research and design : Proceedings of the International Conference of graduate students of the engineering school of new

industry of UrFU, Yekaterinburg, May 07, 2018. - Yekaterinburg: Edytus Limited Liability Company, 2019. - C. 35-39. - EDN RWZVKP.

10. **Neudachin, A.P.** Technogenic processes in cyanide leaching of gold / A. P. Neudachin, Y.V. Volovnikova // Geological evolution of water interaction with rocks : Proceedings of the Second All-Russian Conference with international participation, Vladivostok, September 06-11, 2015. - Vladivostok: Federal State Unitary Enterprise "Publishing House Dalnauka", 2015. - C. 496-498. - EDN WESTNN.
11. **C.N. Mpinga, S.M. Bradshaw, G. Akdogan, C.A. Snyders, J.J. Eksteen,** Evaluation of the Merrill–Crowe process for the simultaneous removal of platinum, palladium and gold from cyanide leach solutions, Hydrometallurgy, Volume 142, 2014, Pages 36-46, ISSN 0304-386X, https://doi.org/10.1016/j.hydromet.2013.11.004.
12. **Rondo-Jalca K. D.Santos-Gonzales A.N. Portilla-Rodríguez H.R.** Main gold mining companies using cyanidation leaching processes in Peru DOI: https://doi.org/10.18687/LACCEI2023.1.1.250
13. **Naumov, K.D.** Features of gold cementation by electrolytic zinc powders in the percolation mode / K.D. Naumov, V.G. Lobanov // Izvestiya vysshee uchebnykh uchebnykh obucheniya. Non-Ferrous Metallurgy. - 2020. - № 1. - C. 19-26. - DOI 10.17073/0021-3438-2020-1-19-26. - EDN KMGQHC. Main gold mining companies using cyanidation leaching processes in Peru. Proceedings of the LACCEI international Multi-conference for Engineering, Education and Technology (2023). doi: 10.18687/laccei2023.1.1.25014. Zhang R.V. Hydrosystems in the Arctic zone of Russia. Cryosphere of the Earth. 2016;20(4): 79-92
15. **Zhang R.V.** Geocryological principles of groundwater dams in the cryolithozone under changing climate conditions// Fundamental Research. - 2014. - № 9-2. - P. 288-296; URL: http://www.fundamental-research.ru/ru/article/view?id=34841 (date of reference: 19.10.2016).
16. **Zhang R.V.** Temperature regime and stability of low-pressure hydraulic structures and groundwater channels in cryolithozone. Yakutsk: IMZ SB RAS, 2002. - 207 c.
17. **Aniskin, N., Sergeev, S., & Bokov, I.** (2024). FILTRATION AND TEMPERATURE REGIME OF A FROZEN-TYPE SOIL DAM IN THE CRYOLITHOZONE. International Journal for Computational Civil and Structural Engineering, 20(1), 143-153. https://doi.org/10.22337/2587-9618-2024-20-1-143-153
18. **Trapeznikov A.G., Bekker A.T., Isaeva E.S., Tsimbelman N.Ya., Chernova T.I.** Numerical modeling of the temperature regime of the ground frozen-type dam of the Anadyr hydroelectric complex // Bulletin of the Engineering School of the Far Eastern Federal University. 2022. № 1(50). C. 81-93. https://doi.org/10.24866/2227-6858/2022-1/81-93
19. Heat Flow in the Soil. An Introduction to Environmental Biophysics, 1998 ISBN : 978-0-387-94937-6 Gaylon S. Campbell, John M. Norman
20. **Sultashova, Oralkhan & Khudaybergenov, Yakhshimurad.** (2016). MODELING OF SOIL TEMPERATURE REGIME. 5. 30-34.
21. Text of GOST R 71038-2023 Soils. Methods of laboratory determination of thermophysical characteristics
22. Assignment of thermophysical parameters of soils for temperature calculations in PLAXIS. URL: https://www.notion.so/PLAXIS-d3620d35108443bda23b3334cc7eacf5 – 18.07.2024.
23. State standart 121.13330.2019 Aerodromes
24. PLAXIS 2D 2022. Tutorial Manual. https://communities.bentley.com/cfs-

file/__key/communityserver-wikis-components-files/00-00-00-05
25. State standart 116.13330 Engineering Protection of Territories, Buildings and Structures from Dangerous Geological Processes. The Main Provisions

СПИСОК ЛИТЕРАТУРЫ

1. **Ghorbani, Y., Franzidis, J.P., Petersen, J.,** 2016. Heap leaching technology - Current State, innovations, and future directions: A review. Mineral Processing and Extractive Metallurgy Review 37, 73–119. doi:10.1080/08827508.2015.1115990
2. **Thenepalli, T., Chilakala, R.,Tuan, L., Kim, C.S.,** 2019. A brief note on the heap leaching technologies for the recovery of valuable metals. Sustainability (Switzerland). doi:10.3390/su10023347
3. **Petersen, J.,** 2016. Heap leaching as a key technology for recovery of values from low-grade ores – A brief overview. Hydrometallurgy 165, 206–212. doi:10.1016/j.hydromet.2015.09.001
4. **Donato, D.B., Madden-Hallett, D.M., Gursansky, W.**, 2017. Heap leach cyanide irrigation and risk to wildlife: Ramifications for the international cyanide management code. Ecotoxicology and Environmental Safety 140, 271–278. doi:10.1016/j.ecoenv.2017.02.033
5. **Shumilova, L.V., Khatkova, A.N., Myazin, V.P.** et al. Year-Round Heap Leaching of Gold in Cryolithozone. Metallurgist 64, 1046–1056 (2021). https://doi.org/10.1007/s11015-021-01086-0
6. **Рубцов, Ю.И.** Скоростное цианидное выщелачивание золотосодержащих гравиоконцентратов / Ю. И. Рубцов // Цветные металлы. – 2007. – № 10. – С. 60-63. – EDN KUAMWF.
7. Исследование возможности цианидного выщелачивания золота из неокисленных руд месторождения Погромное / Ю. И. Рубцов, Е. Е. Косарев, С. Д. Соронхорова, О. В. Фокина // Кулагинские чтения: техника и технологии производственных процессов : XIV Международная научно-практическая конференция: в 3-частях, Чита, 26–28 ноября 2014 года / Забайкальский государственный университет. Том Часть 1. – Чита: Забайкальский государственный университет, 2014. – С. 256-260. – EDN SBAHMV.
8. **Fady B. Abdelaal and R. Kerry Rowe.** 2023. Physical and mechanical performance of an HDPE geomembrane in 10 mining solutions with different pHs. Canadian Geotechnical Journal. 60(7): 978-993. https://doi.org/10.1139/cgj-2022-0419
9. **Зелях, Я.Д.** Способ совершенствования процесса извлечения благородных металлов из цианистых растворов / Я.Д. Зелях, К.Д. Наумов, В.Г. Лобанов // Инженерные исследования и проектирование : Материалы Международной конференции магистрантов инженерной школы новой индустрии УрФУ, Екатеринбург, 07 мая 2018 года. – Екатеринбург: Общество с ограниченной ответственностью "Эдитус", 2019. – С. 35-39. – EDN RWZVKP.
10. **Неудачин, А.П.** Техногенные процессы при цианидном выщелачивании золота / А.П. Неудачин, Ю.В. Воловникова // Геологическая эволюция взаимодействия воды с горными породами : Материалы Второй Всероссийской конференции с международным участием, Владивосток, 06–11 сентября 2015 года. – Владивосток: Федеральное государственное унитарное предприятие "Издательство Дальнаука", 2015. – С. 496-498. – EDN WESTNN.
11. **C.N. Mpinga, S.M. Bradshaw, G. Akdogan, C.A. Snyders, J.J. Eksteen,** Evaluation of the Merrill–Crowe process for the simultaneous removal of platinum, palladium and gold from cyanide leach

solutions, Hydrometallurgy, Volume 142, 2014, Pages 36-46, ISSN 0304-386X, https://doi.org/10.1016/j.hydromet.2013.11.004.

12. **Rondo-Jalca K.D. Santos-Gonzales A.N. Portilla-Rodríguez H.R.** Main gold mining companies using cyanidation leaching processes in Peru DOI: https://doi.org/10.18687/LACCEI2023.1.1.250
13. **Наумов, К.Д.** Особенности цементации золота электролизными цинковыми порошками в режиме перколяции / К.Д. Наумов, В.Г. Лобанов // Известия высших учебных заведений. Цветная металлургия. – 2020. – № 1. – С. 19-26. – DOI 10.17073/0021-3438-2020-1-19-26. – EDN KMGQHC. Main gold mining companies using cyanidation leaching processes in Peru. Proceedings of the LACCEI international Multi-conference for Engineering, Education and Technology (2023). doi: 10.18687/laccei2023.1.1.250
14. **Zhang R.V.** Hydrosystems in the Arctic zone of Russia. Cryosphere of the Earth. 2016;20(4): 79-92
15. **Чжан Р.В.** Геокриологические принципы работы грунтовых плотин в криолитозоне в условиях меняющегося климата// Фундаментальные исследования. – 2014. – № 9-2. – С. 288-296; URL: http://www.fundamental-research.ru/ru/article/view?id=34841 (дата обращения: 19.10.2016).
16. **Чжан Р.В.** Температурный режим и устойчивость низконапорных гидроузлов и грунтовых каналов в криолитозоне. Якутск: ИМЗ СО РАН, 2002. – 207 с.
17. **Aniskin, N., Sergeev, S., & Bokov, I.** (2024). FILTRATION AND TEMPERATURE REGIME OF A FROZEN-TYPE SOIL DAM IN THE CRYOLITHOZONE. International Journal for Computational Civil and Structural Engineering, 20(1), 143-153. https://doi.org/10.22337/2587-9618-2024-20-1-143-153
18. **Трапезников А.Г., Беккер А.Т., Исаева Е.С., Цимбельман Н.Я., Чернова Т.И.** Численное моделирование температурного режима грунтовой плотины мерзлого типа Анадырского гидроузла // Вестник Инженерной школы Дальневосточного федерального университета. 2022. № 1(50). С. 81–93. https://doi.org/10.24866/2227-6858/2022-1/81-93
19. Heat Flow in the Soil. An Introduction to Environmental Biophysics, 1998 ISBN : 978-0-387-94937-6 Gaylon S. Campbell, John M. Norman
20. **Sultashova, Oralkhan & Khudaybergenov, Yakhshimurad.** (2016). МОДЕЛИРОВАНИЕ ТЕМПЕРАТУРНОГО РЕЖИМА ПОЧВЫ. 5. 30-34.
21. Text of GOST R 71038-2023 Soils. Methods of laboratory determination of thermophysical characteristics
22. Assignment of thermophysical parameters of soils for temperature calculations in PLAXIS. URL: https://www.notion.so/PLAXIS-d3620d35108443bda23b3334cc7eacf5 – 18.07.2024.
23. State standart 121.13330.2019 Aerodromes
24. PLAXIS 2D 2022. Tutorial Manual. https://communities.bentley.com/cfs-file/__key/communityserver-wikis-components-files/00-00-00-05
25. State standart 116.13330 Engineering Protection of Territories, Buildings and Structures from Dangerous Geological Processes. The Main Provisions

Aniskin Nikolay Alexeyevich, Professor, DSc, Acting Director of the Institute of Hydrotechnical and Power Engineering (IGES) of the National Research Moscow State University of Civil Engineering (NRU MGSU), 129337, Russia, Moscow, Yaroslavskoe shosse, 26, e-mail: Aniskin@mgsu.ru

Sergeev Stanislav Alexeyevich, PhD, Associate Professor of the Department of Hydraulics and Hydraulic Engineering, Researcher at the Scientific and Educational Center "Geotechnics" of the National Research Moscow State University of Civil Engineering (NRU MGSU), 129337, Russia, Moscow, Yaroslavskoe shosse, 26, e-mail: SergeevSA@mgsu.ru

Stupivtsev Andrey Vladimirovich, postgraduate student of the «Hydraulics and hydraulic engineering» department of the Institute of Hydrotechnical and Power Engineering (IGES) of the National Research Moscow State University of Civil Engineering (NRU MGSU), 129337, Russia, Moscow, Yaroslavskoe shosse, 26, e-mail: StupivtsevAV@gmail.com

Bokov Ilia Alexeyevich, postgraduate student of the «Hydraulics and hydraulic engineering» department of the Institute of Hydrotechnical and Power Engineering (IGES) of the National Research Moscow State University of Civil Engineering (NRU MGSU), 129337, Russia, Moscow, Yaroslavskoe shosse, 26, e-mail: ibokov111111@gmail.com

Анискин Николай Алексеевич, профессор, доктор технических наук, исполняющий обязанности директора Института гидротехнического и энергетического строительства (ИГЭС) Национального исследовательского Московского государственного строительного университета (НИУ МГСУ), 129337, г. Москва, Ярославское ш., д. 26, e-mail: Aniskin@mgsu.ru

Сергеев Станислав Алексеевич, кандидат технических наук, доцент кафедры «Гидравлики и гидротехнического строительства», научный сотрудник Научно-образовательного центра «Геотехника» Национального исследовательского Московского государственного строительного университета (НИУ МГСУ) 129337, г. Москва, Ярославское ш., д. 26, e-mail: SergeevSA@mgsu.ru

Ступивцев Андрей Владимирович, аспирант кафедры «Гидравлики и гидротехнического строительства» Национального исследовательского Московского государственного строительного университета (НИУ МГСУ) 129337, г. Москва, Ярославское ш., д. 26, e-mail: StupivtsevAV@gmail.com

Боков Илья Алексеевич, аспирант кафедры «Гидравлики и гидротехнического строительства» Института гидротехнического и энергетического строительства (ИГЭС) Национального исследовательского Московского государственного строительного университета (НИУ МГСУ), 129337, г. Москва, Ярославское ш., д. 26, e-mail: ibokov111111@gmail.com

International Journal for Computational Civil and Structural Engineering, 21(2) 129–137 (2025)

DOI:10.22337/2587-9618-2025-21-2-129-137

EXPERIMENTAL DETERMINATION OF THE TOTAL SHRINKAGE STRAIN OF REINFORCED CONCRETE

Valeryia A. Rzhevutskaya, Yuliya G. Maskalkova

Belarusian-Russian University, Mogilev, BELARUS

Abstract: The article proposes a method for measuring the total shrinkage strain of a reinforced concrete prism in such a way that it is possible to measure the total shrinkage strain on an open surface of the prism no later than three hours after concreting. Furthermore, a monitoring of the strain increase on remaining surfaces of the prism after removing a formwork for concreting is followed. The object of this study is the shrinkage strain of expanded clay concrete and the strain of longitudinal reinforcement. Based on results of the conducted research, a new method for experimentally determining the total shrinkage strain of reinforced concrete was proposed. The suggested method makes it possible to ensure that the shrinkage strain of concrete begin to be recorded from the first day of concreting and the possibility of implementing the proposed method was experimentally confirmed. Prospects for further research are presented in the article.

Keywords: shrinkage, shrinkage strain, reinforced concrete, lightweight concrete, expanded clay concrete, expanded clay steel-reinforced concrete

ЭКСПЕРИМЕНТАЛЬНОЕ ОПРЕДЕЛЕНИЕ ПОЛНЫХ ДЕФОРМАЦИЙ УСАДКИ ЖЕЛЕЗОБЕТОНА

В.А. Ржевуцкая, Ю.Г. Москалькова

Белорусско-Российский университет, Могилев, БЕЛАРУСЬ

Аннотация: В статье предложен способ фиксирования полных деформаций усадки железобетонной призмы таким образом, чтобы было обеспечено измерение полных деформаций усадки на открытой грани не позднее, чем через три часа после бетонирования, с последующим контролем прироста деформаций по остальным граням призмы после ее распалубки. Объектом настоящего исследования являются усадочные деформации керамзитобетона и деформации продольной арматуры. По результатам проведенных исследований предложен новый способ экспериментального определения полных деформаций усадки железобетона, позволяющий обеспечить начало фиксирования деформаций усадки бетона, начиная с первых суток, и экспериментально подтверждена возможность реализации предложенного способа. Представлены перспективы дальнейших исследований.

Ключевые слова: усадка, деформации усадки, железобетон, легкий бетон, керамзитобетон, керамзитожелезобетон

INTRODUCTION

The complex hardening process of cement stone, the structure of concrete, capillary phenomena, and many other related factors causes the development of concrete shrinkage [1–4].

The shrinkage strain of concrete reinforced with bar reinforcement are lower than the strain of unreinforced concrete with the same components of concrete mixture, as noted in the studies [5, 6]. This is due to the fact that the reinforcement acts as an internal connection in the composite and ‘restrains’ the development of unrestrained shrinkage strain of the concrete since the elastic modulus of the reinforcement is significantly higher than the elastic modulus of concrete. As a result of a long shrinkage

process, tensile forces arise in the cement stone, and compressive forces arise in the reinforcing bars. Consequently, the reinforcing bars become a source of additional stresses in the concrete [1].

According to GOST 24544-81, the measurements of concrete shrinkage strain are carried out the next day after concreting, then on the 3rd, 7th, 14th day, and then once every 2 weeks until the end of the investigation. However, it is well known that shrinkage strain develops most intensively in the first day of concrete hardening [7–10]; therefore, using the method based on GOST 24544, a significant part of concrete shrinkage strain will not be recorded. A review of many works, published by researchers from different countries, revealed a lack of proposals for the experimental strain determination in reinforcement bars caused by shrinkage.

Thus, it seems promising to develop such a method for experimentally determining the total shrinkage strain of reinforced concrete, which will make it possible to begin recording concrete shrinkage strain and reinforcement strain (caused by concrete shrinkage) from the first day of concrete hardening.

In the future, the presence of such a method will allow, on the one hand, to verify design models applicable for concrete with cement CEM Class N and, on the other hand, to use the proposed method for an empirically based assessment of the influence of other types of reinforcement (for instance, dispersed) on shrinkage strain development.

Based on the above, the object of the study is the shrinkage strain of expanded clay concrete and the strain of longitudinal reinforcement. The subject of the study is an expanded clay-reinforced concrete sample in the form of a prism with dimensions of 150 × 150 × 600 mm.

The purpose of this study is to implement such a method for measuring the total shrinkage strain of a reinforced concrete prism, which will make it possible to measure the total shrinkage strain on an open surface no later than three hours after concreting. In addition, a subsequent monitoring of the increase in strain along remaining surfaces of the prism after it's removing out of a formwork for concreting should be proposed.

METHODS

The following composition of the expanded clay concrete mixture was chosen for the manufacture of specimens according to [11, 12]: $C : S : G = 1 : 1{,}84 : 0{,}79$ and $W/C = 0.52$. Thus, C is Portland cement with activity of 42.5 MPa produced by Belarusian Cement Plant OJSC. S is river sand with a bulk density of 1670 kg/m^3 and fineness modulus of 2.13. G is expanded clay gravel with particle size of 4–10 mm and compressive cylinder strength of 1.03 MPa produced by Plant of expanded clay gravel in Novolukoml OJSC. W/C is water-cement ratio.

The shrinkage strain of the expanded clay steel-reinforced concrete was recorded on experimental samples (prisms) with dimensions of 150 × 150 × 600 mm. The duration of testing of each specimen was 120 days. During this time, normal temperature and humidity conditions had been maintained in the laboratory in accordance with GOST 24544-81: an average relative air humidity was 55 % and an average temperature was 22 ºC.

The measurement of the total shrinkage strain of the expanded clay steel-reinforced concrete (the samples in shape of prisms) was carried out in the following sequence.

1. Spatial reinforcement cages consisting of longitudinal and transverse reinforcement were manufactured [13].

Reinforcing bars with a diameter of 16 mm with the yield strength of 500 MPa (the longitudinal reinforcement; the percentage of the longitudinal bar reinforcement was $\rho_s = 3.57$ %) and with a diameter of 6 mm with the yield strength of 240 MPa (the transverse reinforcement) were used for manufacture of the reinforcement cages (Figure 1).



Figure 1. Spatial reinforcement cage for manufacture of specimens

2. Perforating holes were made at the ends on both sides in each longitudinal reinforcement bar, and through the holes steel adapter fittings were installed (Figure 2).

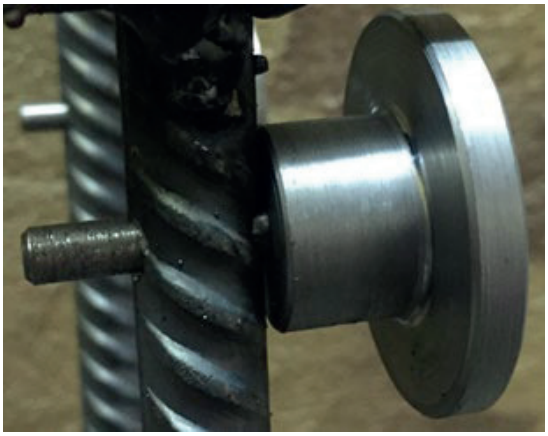


Figure 2. Steel adapter fitting in the longitudinal reinforcement bar

3. The reinforcement cage with the installed steel adapter fittings in it was inserted into a concreting formwork in such a way that the steel adapter fittings were flush with the concreting formwork along the entire surface area of the base of the steel adapter fittings (Figure 3).

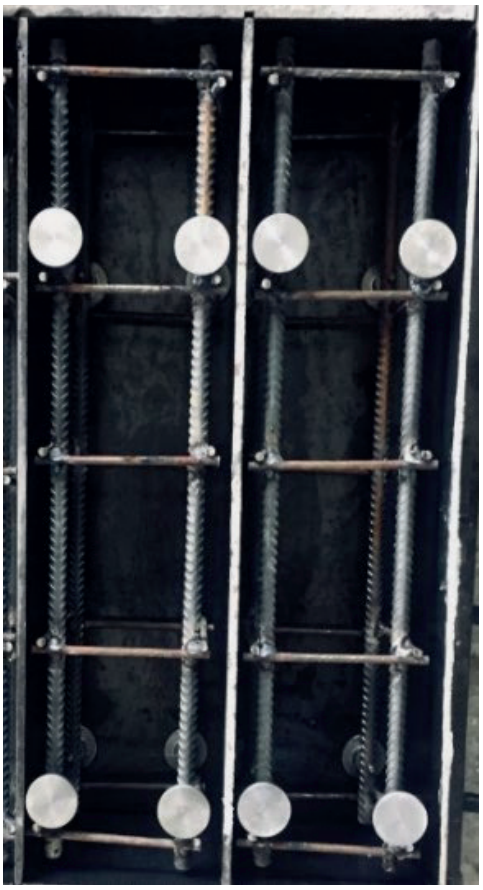


Figure 3. Reinforcement cage inserted in concreting formwork

4. The specimens were concreted in such a way that on the open surface of the horizontally oriented prism the base of the steel adapter fitting was flush with the surface of the laid concrete.
5. The bases of the steel adapter fittings on the open surface of the prism were cleared of concrete sagging and cement laitance after concreting.
6. Steel adapter points were attached to the bases of the steel adapter fittings on the open surface of the prism forty-five minutes after concreting. The steel adapter points were also immersed into the concrete mixture between the steel adapter fittings to a depth not less than the maximum aggregate size.

7. Two hours after installing the steel adapter points, they were connected in pairs to each other by steel rods, which were the base for measuring.
8. Dial-type indicators were installed into the steel adapter points. Thus, the strain in the longitudinal reinforcement bars and in the concrete between the longitudinal reinforcement bars were recorded.
9. The steel rods and the dial-type indicators were installed in a designed position with screws.
10. After removing the experimental prisms out of the formwork, steel adapter points were attached to the bases of the steel adapter fittings on an opposite surface of the prism to record strains in the reinforcement bars. The steel adapter points were also attached to the concrete surface on three surfaces of the prism except for the open surface during the concreting process. The steel adapter points were connected in pairs with steel rods, and then indicators were installed. The steel rods and the dial-type indicators were installed in a designed position with screws (Figure 4).



Figure 4. Dial-type indicators installed into steel adapter points to record shrinkage strain of expanded clay concrete and stain of longitudinal reinforcement

RESULTS AND DISCUSSION

During the investigation, three Series of twin specimens were sequentially tested (three twin samples in each Series). As a result of the research, experimental data had been obtained on the development of the total shrinkage strain of the expanded clay steel-reinforced concrete during 120 days. The experimental data are presented in Table 1 and Figure 5.

Table 1. Mean values of relative strain of the total shrinkage of experimental expanded clay steel-reinforced concrete specimens in form of prisms

Measured parameter in experimental specimens	Series No.	Mean values of relative strain of the total shrinkage						
		1st day	7th day	10th day	28th day	62nd day	91st day	120th day
Strain of expanded clay concrete $\varepsilon_{lcs,s} \times 10^5$	2	-0.61	0.38	0.95	9.27	10.08	12.85	13.85
	3	-0.40	0.36	0.93	9.28	10.51	13.11	14.33
	4	-0.41	0.38	0.94	9.14	11.19	13.41	14.61
Strain of longitudinal reinforcement $\varepsilon_{ss} \times 10^5$	2	0.02	0.48	2.29	5.69	12.78	15.03	15.93
	3	0.03	0.46	2.05	5.73	12.73	15.33	15.98
	4	0.03	0.48	2.27	6.39	12.52	15.01	15.90

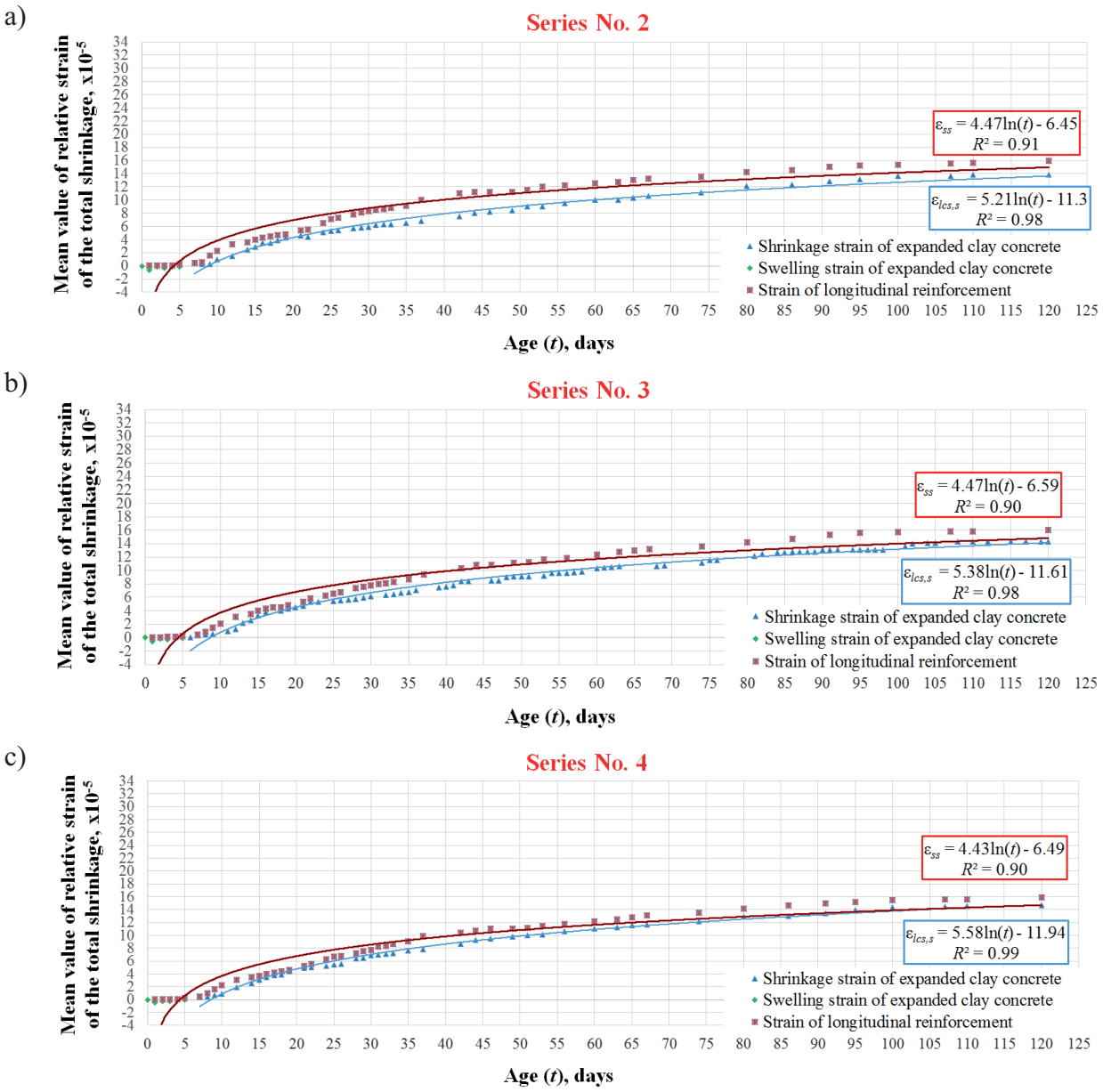


Figure 5. Development of relative strain of the total shrinkage of expanded clay steel-reinforced concrete (a – Series No. 2, b – Series No. 3, c – Series No. 4)

The results of the empirical study, as shown in Figure 5 and Table 1, confirm that the proposed implementation of the method provides measurements of the concrete shrinkage strain between longitudinal reinforcement bars and the strain of longitudinal reinforcement bars, starting from the first day of concreting.

In addition, some researchers [14–20] note a decrease in shrinkage deformation as a result of the addition of fibers to the expanded clay mixture. Nevertheless, the authors do not focus on a factor that affects an absolute value of the total shrinkage strain of fiber-reinforced concrete.

The application of the proposed method made it possible to prove experimentally that low-modulus polypropylene fibers act as an internal bond at an early hardening stage. As a result, there is a stress redistribution in the 'hydrated cement – polypropylene fiber' system, thereby it

makes a significant effect on reducing the shrinkage stresses inside the composite [21].

CONCLUSIONS

Based on the results of the study, the new method has been proposed for experimentally measuring the total shrinkage strain of reinforced concrete. The method makes possible to ensure that shrinkage strain begin to be observed starting from the first day of concreting.

This implementation of the method for shrinkage strain measuring of expanded clay steel-reinforced concrete allows recording the total shrinkage strain of an experimental prism on an open surface no later than three hours after concreting, followed by monitoring an increase in strain along remaining surfaces of the prism (after it's removing out of a formwork for concreting).

REFERENCES

1. **Lazouski D.N., Tur V.V., Gluhov D.O., Lazouski Y.D.** (2021) Uchet polzuchesti i usadki betona po SP 5.03.01-2020 pri raschete zhelezobetonnyh konstrukcij na osnove deformacionnoj raschetnoj modeli [Creep and shrinking of concrete accounting according to SP 5.03.01-2020 when analysis of reinforced concrete structures based on deformational analytical model]. *Vestnik Brestskogo gosudarstvennogo tekhnicheskogo universiteta* [*Vestnik of the Brest State Technical University*], vol. 2(125), pp. 7–12. doi:10.36773/1818-1212-2021-125-2-7-12. (In Russian)
2. **Bazant Z.P.** (2001) Prediction of concrete creep and shrinkage: past, present and future. *Nu clear Engineering and Design*, vol. 203, iss. 1, pp. 27–38. doi:10.1016/S0029-5493(00)00299-5.
3. **Rzhevutskaya V.A.** (2020) Shrinkage of expanded clay concrete: A review. *AlfaBuild*, vol. 15, iss. 3, 6 p. doi:10.34910/ALF.15.1.
4. **Krivitskiy P., Shelest H., Nevdakh A., Sedlyr T.** (2024) Fiziko-mekhanicheskie harakteristiki konstrukcionnogo keramzitobetona v praktike sovremennogo stroitel'stve [Physical and mechanical characteristics of structural expanded direction concrete in the practice of modern construction]. *Vesnik Hrodzenskaha Dziarzhaunaha Universiteta Imia Ianki Kupaly. Seryia 6. Tekhnika* [*Bulletin of the Yanka Kupala Grodno State University. Series 6, Engineering*], vol. 14, iss. 2, pp. 33–35. Available at: https://vesnik.grsu.by/?p=s6&lang=ru. (In Russian)
5. **Bondarenko V.M., Suvorkin D.G.** (1987) Reinforced concrete and stone structures. *Vysshaya shkola* [*Higher education*], 386 p. (In Russ.). Available at: https://gbk.kgasu.ru/images/stories/metodmat/BondarenkoSuvorkinGbiKamKonstr_1987.pdf.
6. **Babich E.M.** (1988) Konstrukcii iz legkih betonov na poristyh zapolnitelyah [Structures made of light concrete on porous aggregates]. *Vysshaya shkola* [*Higher education*], 207 p. Available at: https://knizhen-pazar.net/products/books/746359-konstruktsii-iz-legkih-betonov-na-porist-h-zapolnitelyah. (In Russian)
7. **Bentur A., Igarashi Sh., Kovler K.** (2001) Prevention of autogenous shrinkage in high-strength concrete by internal curing using wet lightweight aggregates. *Cement and Concrete Research*, vol. 31, pp. 1587–1591. Available at: doi:10.1016/S0008-8846(01)00608-1.
8. **Zhuang Y., Zheng D., Zhen Ng., Ji T., Chen X.** (2016) Effect of lightweight aggregate type on early-age autogenous shrinkage of concrete. *Construction and*

Building Materials, vol. 120, pp. 373–381. doi:10.1016/j.conbuildmat.2016.05.105.

9. **Clarke J.L.** (2005) *Structural lightweight aggregate concrete*. Glasgow: Blackie Academic & Professional, an imprint of Chapman & Hall, 161 p.
10. **Wendling A., Sadhasivam K., Floyd R.W.** (2018) Creep and shrinkage of lightweight self-consolidating concrete for prestressed members. *Construction Building Materials*, vol. 167, pp. 205–215. doi:10.1016/j.conbuildmat.2018.02.017.
11. **Maskalkova Y.G., Rzhevutskaya V.A.** (2022) Compressive cylinder strength and deformability of expanded clay fiber-reinforced concrete with polypropylene fiber. *International Journal for Computational Civil and Structural Engineering*, vol. 18, iss. 2, pp. 31–42. doi:10.22337/2587-9618-2022-18-2-31-42.
12. **Maskalkova Yu.G., Rzhevutskaya V.A.** (2022) Size effect of cube specimen on strength of expanded clay fiber-reinforced concrete. *Magazine of Civil Engineering*, vol. 116, iss. 8, 18 p. doi:10.34910/MCE.116.12.
13. **Semenyuk S., Maskalkova Yu., Rzhevutskaya V.** (2020) Osobennosti opredeleniya stesnennoj usadki keramzitozhelezobetona [Features of determining restricted shrinkage of reinforced claydite-concrete]. *Vestnik Polockogo gosudarstvennogo universiteta* [*Vestnik of the Polotsk State University*], vol. 8, pp. 58–65. Available at: https://elib.psu.by/handle/123456789/25843. (In Russian)
14. **Kuryatnikov Yu.Yu., Kochetkov R.S.** Razrabotka matematicheskih modelej fiziko-mekhanicheskih svojstv modificirovannogo keramzitobetona [Development of mathematical models of physico-mechanical properties of modified expanded clay concrete]. *Innovacii i modelirovanie v stroitel'nom materialovedenii* [*Innovations and modeling in building materials science*], pp. 64–69. Available at: https://elib.tstu.tver.ru/MegaPro/Download/MObject/30794/001-000135274-000000000-0000-0000-01.pdf. (In Russian)
15. **Suvorov I.O.** (2016) Dispersnoe poliarmirovanie kak sposob snizheniya usadki fibropenobetona [Dispersed polyarming as a way to reduce shrinkage of fibropenocrete]. (PhD Thesis). S.-Petersburg: St. Petersburg State University of Architecture and Civil Engineering, 137 p. Available at: https://www.dissercat.com/content/dispersnoe-poliarmirovanie-kak-sposob-snizheniya-usadki-fibropenobetona/read. (In Russian)
16. **Costa H., Júlio E., Lourenço J.** (2012) New approach for shrinkage prediction of high-strength lightweight aggregate concrete. *Constructions and Buildings materials*, vol. 35, pp. 84–91. doi:10.1016/j.conbuildmat.2012.02.052.
17. **Zhao H., Ma Y., Zhang J., Hu Zh., Li H., Wang Y., Liu J., Wang K.** (2022) Effect of clay content on shrinkage of cementitious materials. *Construction and Building Materials*, vol. 157, 12 p. doi:10.1016/j.conbuildmat.2021.125959.
18. **Zhao S., Li Ch., Zhao M., Zhang X.** (2016) Experimental study on autogenous and drying shrinkage of steel fiber reinforced lightweight-aggregate concrete. Advances in Materials Science and Engineering, vol. 2016, 9 p. doi:10.1155/2016/2589383.
19. **Gong J, Zeng W., Zhang W.** (2018) Influence of shrinkage-reducing agent and polypropylene fiber on shrinkage of ceramsite concrete. *Construction and Building Materials*, vol. 159, pp. 155–163. doi:10.1016/j.conbuildmat.2017.10.064.
20. **Hussein Z.M., Khalil W.I., Ahmed H.K.** (2020) Shrinkage and impact strength of fibre-reinforced artificial lightweight aggregate concrete. Materials Science and Engineering, vol. 671, iss. 1, pp. 1–11. doi:10.1088/1757-899X/671/1/012118.

21. **Rzhevutskaya V.A., Moskal'kova Yu.G.** (2024) Polypropylene fiber as a factor of reduction the total shrinkage strain of expanded clay concrete. *Russian Journal of Building Construction and Architecture*, vol. 64, pp. 6–15. doi:10.36622/2542-0526.2024.64.4.001.

СПИСОК ЛИТЕРАТУРЫ

1. **Лазовский Д.Н., Тур В.В., Глухов Д.О., Лазовский Е.Д.** Учет ползучести и усадки бетона по СП 5.03.01-2020 при расчете железобетонных конструкций на основе деформационной расчетной модели // Вестник Брестского государственного технического университета, 2021, № 2 (125). С. 7–12. doi:10.36773/1818-1212-2021-125-2-7-12.
2. **Bazant Z.P.** Prediction of concrete creep and shrinkage: past, present and future // Nuclear Engineering and Design, 2001, No. 203, pp. 27–38. doi:10.1016/S0029-5493(00)00299-5.
3. **Rzhevutskaya V.A.** Shrinkage of expanded clay concrete: A review // AlfaBuild, 2020, No. 15(3), 6 p. doi:10.34910/ALF.15.1.
4. **Кривицкий П.В., Шелест Е.В., Невдах А.А., Седляр Т.Н.** Физико-механические характеристики конструкционного керамзитобетона в практике современного строительстве // Вестник Гродненского государственного университета имени Янки Купалы. Серия 6, Техника, 2024, Том 14, № 1. С. 35-43. Режим доступа: https://vesnik.grsu.by/?p=s6&lang=ru.
5. **Бондаренко В.М., Суворкин Д.Г.** Железобетонные и каменные конструкции // Высшая школа, 1987. 386 с. Режим доступа: https://gbk.kgasu.ru/images/stories/metodmat/BondarenkoSuvorkinGbiKamKonstr_1987.pdf.
6. **Бабич Е.М.** Конструкции из легких бетонов на пористых заполнителях // Киев : Вища Школа, 1988. 207 с. Режим доступа: https://knizhen-pazar.net/products/books/746359-konstruktsii-iz-legkih-betonov-na-porist-h-zapolnitelyah.
7. **Bentur A., Igarashi Sh., Kovler K.** Prevention of autogenous shrinkage in high-strength concrete by internal curing using wet lightweight aggregates // Cement and Concrete Research. 2001б No. 31, pp. 1587–1591. doi:10.1016/S0008-8846(01)00608-1.
8. **Zhuang Y., Zheng D., Zhen Ng., Ji T., Chen X.** Effect of lightweight aggregate type on early-age autogenous shrinkage of concrete // Construction and Building Materials, 2016, No. 120, pp. 373–381. doi:10.1016/j.conbuildmat.2016.05.105.
9. **Clarke J.L.** Structural lightweight aggregate concrete. Glasgow: Blackie Academic & Professional, an imprint of Chapman & Hall, 2005, 161 pages.
10. **Wendling A., Sadhasivam K., Floyd R.W.** Creep and shrinkage of lightweight self-consolidating concrete for prestressed members // Construction Building Materials, 2018, No. 167, pp. 205–215. doi:10.1016/j.conbuildmat.2018.02.017.
11. **Maskalkova Y.G., Rzhevutskaya V.A.** Compressive cylinder strength and deformability of expanded clay fiber-reinforced concrete with polypropylene fiber // International Journal for Computational Civil and Structural Engineering, 2022, No. 18, pp. 31–42. doi:10.22337/2587-9618-2022-18-2-31-42.
12. **Maskalkova Yu.G., Rzhevutskaya V.A.** Size effect of cube specimen on strength of expanded clay fiber-reinforced concrete // Magazine of Civil Engineering, 2022, No. 116(8), 18 pages. doi:10.34910/MCE.116.12.
13. **Семенюк С.Д., Москалькова Ю.Г., Ржевуцкая В.А.** Особенности определения стесненной усадки керамзитожелезобетона // Вестник Полоцкого гос. ун-та. Серия F.

Строительство. Прикладные науки. Новополоцк, 2020, № 8. С. 58–65. Режим доступа: https://elib.psu.by/handle/123456789/25843.

14. **Курятников Ю.Ю., Кочетков Р.С.** Разработка математических моделей физико-механических свойств модифицированного керамзитобетона // Инновации и моделирование в строительном материаловедении, 2019. С. 64–69. Режим доступа: https://elib.tstu.tver.ru/MegaPro/Download/MObject/30794/001-000135274-000000000-0000-0000-01.pdf.
15. **Суворов И.О.** Дисперсное полиармирование как способ снижения усадки фибропенобетона : дис. … канд. техн. наук : 05.23.05. Санкт-Петербург, 2015. 137 с. Режим доступа: https://www.dissercat.com/content/dispersnoe-poliarmirovanie-kak-sposob-snizheniya-usadki-fibropenobetona/read.
16. **Costa H., Júlio E., Lourenço J.** New approach for shrinkage prediction of high-strength lightweight aggregate concrete // Constructions and Buildings materials, 2012, No. 35, pp. 84–91. doi:10.1016/j.conbuildmat.2012.02.052.
17. **Zhao H., Ma Y., Zhang J., Hu Zh., Li H., Wang Y., Liu J., Wang K.** Effect of clay content on shrinkage of cementitious materials // Construction and Building Materials, 2022, No. 157, 12 pages. doi:10.1016/j.conbuildmat.2021.125959.
18. **Zhao S., Li Ch., Zhao M., Zhang X.** Experimental study on autogenous and drying shrinkage of steel fiber reinforced lightweight-aggregate concrete // Advances in Materials Science and Engineering, 2016, No. 2016. 9 pages. doi:10.1155/2016/2589383.
19. **Gong J, Zeng W., Zhang W.** Influence of shrinkage-reducing agent and polypropylene fiber on shrinkage of ceramsite concrete. Construction and Building Materials, 2018, No. 159, pp. 155–163. doi:10.1016/j.conbuildmat.2017.10.064.
20. **Hussein Z.M., Khalil W.I., Ahmed H.K.** Shrinkage and impact strength of fibre-reinforced artificial lightweight aggregate concrete // Materials Science and Engineering, 2020, No. 671(1), pp. 1–11. doi:10.1088/1757-899X/671/1/012118.
21. **Rzhevutskaya V.A., Moskal'kova Yu.G.** Polypropylene fiber as a factor of reduction the total shrinkage strain of expanded clay concrete // Russian Journal of Building Construction and Architecture, 2024, No. 64, pp. 6–15. doi:10.36622/2542-0526.2024.64.4.001.

Yuliya G. Maskalkova. PhD. in Engineering, Associate Professor, Associate Professor at the Department of Industrial and Civil Construction, Belarusian-Russian University, Mira Ave, 43, Mogilev, 212000, Belarus, e-mail: julia43@tut.by; ORCID ID: 0000-0002-4107-2452

Valeryia A. Rzhevutskaya. Senior lecturer at the Department of Industrial and Civil Construction, Belarusian-Russian University, Mira Ave, 43, Mogilev, 212000, Belarus, e-mail: valeriarzhevuckaya@gmail.com; ORCID ID: 0000-0001-8854-5408

Москалькова Ю. Г. К.т.н, доцент, доцент кафедры «Промышленное и гражданское строительство», Белорусско-Российский университет, пр. Мира, 43, Могилев, 212000, Беларусь, e-mail: julia43@tut.by; ORCID ID: 0000-0002-4107-2452

Ржевуцкая В. А. Ст. преподаватель кафедры «Промышленное и гражданское строительство», Белорусско-Российский университет, пр. Мира, 43, Могилев, 212000, Беларусь, e-mail: valeriarzhevuckaya@gmail.com; ORCID ID: 0000-0001-8854-5408

International Journal for Computational Civil and Structural Engineering, 21(2) 138–148 (2025)

DOI:10.22337/2587-9618-2025-21-2-138-148

ADAPTIVE NEURO-FUZZY SYSTEM FOR ESTIMATION OF BIOPOSITIVITY OF BUILT ENVIRONMENT

Valeriy I. Telichenko [1], Nikita S. Rud [2]

[1] Moscow State University of Civil Engineering (National Research University), Moscow, RUSSIA
[2] Nhood Russia, Moscow, RUSSIA

Abstract: Negative environmental impact (NEI) is the result of human economic activity, including construction. At first sight, reducing the negative environmental impact and creating a comfortable living environment (LE) seem to be mutually exclusive concepts. Within the framework of research in this area, it is advisable to us e a complex concept of biopositivity of construction objects. This concept will help to determine the balance between reducing NEI and ensuring the comfort, health and well-being of consumers. The literature review did not indicate any researches in which fuzzy logic methods, including fuzzy logic inference models, were utilized to assess the biopositivity of the living environment of residential buildings. Moreover, the existing methods of "post occupancy evaluation" (POE) do not assume the integration of quantitative and qualitative user assessments to manage the quality of the building environment. The paper presents a methodology for assessing the integral index of biopositivity of civil buildings and iterative determination of the values of the LE parameters, at which the comfort of the individual consumer will be ensured. The simulation procedure of adaptive neuro-fuzzy inference system was implemented in MATLAB software using Neuro-Fuzzy Designer. The model was trained on a data set of 843 strings. Instrumentally measured values of LE parameters were used as predictors, and the response was a qualitative user assessment of the LE. The proposed model of the process of forming a comfortable and biopositive LE provides an opportunity to take into account a set of main factors that form the LE, to fix an integral indicator of the biopositivity of a building facility and make a decision on its advanced improvement.

Keywords: sustainable development, environmental safety, living environment, biopositivity, design criteria, comfort, health saving

ОЦЕНКА БИОПОЗИТИВНОСТИ СРЕДЫ ЖИЗНЕДЕЯТЕЛЬНОСТИ ГРАЖДАНСКИХ ЗДАНИЙ НА ОСНОВЕ АДАПТИВНОЙ НЕЙРО-НЕЧЕТКОЙ СИСТЕМЫ ВЫВОДА

В.И. Теличенко[1], Н.С. Рудь[2]

[1] Национальный исследовательский Московский государственный строительный университет, г. Москва, РОССИЯ
[2] ООО «Нью иммо сервисиз», г. Москва, РОССИЯ

Аннотация: Негативное влияние на окружающую среду (НВОС) обусловлено хозяйственной деятельностью человека, в том числе строительной. На первый взгляд снижение НВОС и создание комфортной среды жизнедеятельности (СЖ) видятся взаимоисключающими концепциями. В рамках исследований по данному направлению целесообразно использование комплексного понятия биопозитивности строительных объектов, которое при их оценке позволит определить баланс между снижением НВОС и обеспечением комфортности, здоровья и благополучия пользователей. Проведенный анализ литературных источников не выявил работ, в которых для оценки биопозитивности среды жизнедеятельности гражданских зданий использовались методы нечеткой логики, в то числе модели нечеткого логического вывода. Более того существующие методики «оценки зданий после заселения» (post occupancy evaluation или POE) не предполагают интеграции количественных и качественных пользовательских оценок для управления качеством СЖ. В статье представлена методика оценки интегрального показателя биопозитивности гражданских зданий и итерационного определения значений параметров СЖ, при которых будет обеспечен комфорт конечного пользователя. Процедура моделирования адаптивной нейро-нечеткой системы выво-

да реализована в среде MATLAB с использованием Neuro-Fuzzy Designer. Модель обучалась на выборе из 843 строк. В качестве предикторов использованы инструментально измеренные значения параметров СЖ, а отклик – качественная пользовательская оценка СЖ здания. Предложенная модель процесса формирования комфортной и биопозитивной СЖ предоставляет возможность учитывать совокупность главных факторов, формирующих СЖ, фиксировать интегральный показатель биопозитивности строительного объекта и принимать решение о его опережающем повышении.

Ключевые слова: устойчивое развитие, экологическая безопасность, среда жизнедеятельности, биопозитивность, критерии проектирования, комфорт, здоровьесбережение

INTRODUCTION

Within the context of the modern pace of life, the development of communications and information technologies, growing urbanization leading to overpopulation of megalopolises, the achievements of post-industrial society, together with the increased mobility of the population of large cities, the change of ideas about the quality of living environment (LE) is inevitable.

In Russia, the creation of a comfortable living environment is one of the priority tasks of the national projects “Housing” and “Ensuring Sustainable Reduction of Uninhabitable Housing Stock”. However, the lack of a clear definition of the concept of “comfort” and methods of its objective assessment significantly complicates the development of effective design solutions [1].

Methods of evaluation of completed construction projects traditionally rely on expert assessments based on technical criteria. However, they often do not take into account an end-user's satisfaction. As response to this challenge, the Post Occupancy Evaluation (POE) methodology, aimed at analyzing user evaluations of buildings after occupancy, began to develop in the 1960s in Western countries [2-5]. Currently, one of the most common POE methodologies is the system developed by the Center for Built Environment (CBE) at the University of California, Berkeley. This methodology suggests the use of Likert scales to assess user satisfaction with various aspects of SL and allows benchmarking buildings to identify problem areas and suggestions for improvement [7].

However, within the framework of the abovementioned methods, quantitative assessment of the LE parameters and qualitative user assessment of L factors are considered separately. Integration of qualitative and quantitative assessments supported by modern mathematical and system-technical methods will allow us to create a refined model of forming a comfortable environment for successful management of its characteristics.

One of the most complex concepts in the field of ecological safety of construction is biopositivity. According to A.N. Tetior's definition, the biopositivity of buildings and structures implies their ability to integrate organically into ecosystems, minimize negative environmental impact (NEI), contribute to the restoration of nature and provide a high quality of life for users [7, 8]. However, the concepts of reducing the negative environmental impact and creating a comfortable environment are often viewed as mutually exclusive.

The introduction of biopositivity as an integral indicator of LE allows us to consider the problem in a comprehensive way, seeking to determine the balance between environmental safety and user comfort.

The objective of this study is to integrate the qualitative user assessment of the biopositivity of LE with instrumentally measured values of LE parameters through the development of an adaptive neuro-fuzzy inference system (ANFIS). This approach will allow to fix the integral index of biopositivity of a construction object and plan its advanced improvement.

MATERIALS AND METHODS

The authors have formed a system of 36 factors of biopositivity of LE of residual buildings. The factors are subdivided into 10 groups:

1. Factors determining the parameters of climatic conditions of the territories adjacent to the building;
2. Factors determining the spatial comfort of the internal environment of the building;
3. Factors determining the ergonomics of space;
4. Factors determining satisfaction with the quality of finishing materials;
5. Factors determining visual comfort;
6. Factors determining acoustic comfort;
7. Factors determining thermal comfort;
8. Factors determining air quality;
9. Factors determining water quality;
10. Factors determining the operation of the building as a whole.

Based on the formed system of factors [9] of biopositivity LE for administrative buildings, a survey has been developed to collect initial data for the subsequent mathematical modeling.

To obtain a sample, 843 respondents - users of 11 administrative buildings in Moscow were interviewed. The respondents were practicing specialists in the field of design and construction of buildings and structures. Within the framework of the survey the respondents were offered 36 questions. Each of them corresponds to the factors of biopositivity of LE [10], as well as 1 generalizing question, within the framework of which it was necessary to assess the overall comfort of the building in which they are located.

Each of the 37 questions required selecting 1 of 7 verbal judgments that characterize the degree of comfort of the environment for each factor. The following verbal judgments were used:

- Absolutely discomforting;
- Discomfortable;
- Relatively uncomfortable;
- Neutral;
- Relatively comfortable;
- Comfortable;
- Absolutely comfortable.

In general, these judgments correspond to a 7-point Likert rating scale. The results of user ratings were coded on a scale of -3 to 3, where 0 is neutral, for further statistical analysis.

Next, a regression model was developed where the qualitative biopositivity scores of each environmental factor are the predictors and the building biopositivity score is the response. The purpose of this step is to identify the most significant environmental factors for modeling fuzzy inference systems. The slide shows the results of the analysis of variance. The model explains about 88% of the variability in the response. Significant factors were determined on the basis of P-value, those predictors with P-value less than 95% and multicollinear predictors were eliminated [11].

As a result, 25 significant factors remained. This is a lot for modeling fuzzy inference, for which it is recommended to use 5 input parameters [12]. To determine 5 significant factors for modeling adaptive neuro-fuzzy inference system, the predictors were sorted by the modulus of regression coefficient. Thus, it was determined that the significant factors for modeling ANFIS are: the quality of finishing materials (VOC emission), the level of natural lighting, the level of artificial lighting, the level of penetrating airborne noise, and air temperature.

Simultaneously with the survey, instrumental measurements [13] of the following parameters were carried out in each room or zone (in case of open office layout) for further modeling of the adaptive neuro-fuzzy inference system: VOC concentration; CO2 concentration; concentration of fine particles PM 2.5; CEO measured in a separate zone or office of the object under study; illumination of the working surface; light pulsation; penetrating noise level; air temperature; air humidity.

Measurements of air temperature and humidity, VOC concentration, CO2 concentration, concentration of fine particles, light pulsation, working surface illumination were carried out by the Climate Guard mobile indoor climate measuring station. ClimateGuard is a hardware-software complex that allows collecting, analyzing and transmitting information on indoor climate parameters to external information systems. The Climate Guard station registers the

values of indoor climate parameters using the following sensors:

- Concentration CO2 - mh-z19b;
- Temperature, humidity – bme280;
- VOC - bme680;
- Light pulsation - as7262;
- Illumination of the working surface - bh1750;
- Concentration of fine particles - pms7003;

Air flow velocity was measured with a Testo 425 thermoanemometer. To measure the level of penetrating airborne noise, a noise meter ECOFIZIKA 110A and a microphone VMK-205 were usedConcentration of fine particles.

RESULTS AND DISCUSSION

Neuro-fuzzy network construction will be performed in MATLAB program software, using Neuro-fuzzy designer extension package, the interface "rule viewer" of which allows to iteratively select the values of environmental parameters and immediately see their influence on the overall level of biopositivity of the object.

As part of the objective of developing a methodology for selecting or iteratively selecting a combination of values of environmental parameters, which will ensure the comfort of the end user of LE, it seems necessary to reduce the number of terms of five input linguistic variables. When using 5 input variables with 7 linguistic terms in each, the model will be considered numerically and linguistically complete, but the number of rules will be 16807. The use of such a large rule base is impractical due to limited computing power. When reducing the number of terms of input variables to 5, it is proposed to combine the terms "Absolutely Discomfortable" and "Discomfortable" into a group under the term "Discomfortable", and the terms "Absolutely Comfortable" and 'Comfortable' into a group under the term "Comfortable". When using 5 input parameters with 5 terms in each, the number of product rules will be 3125.

If the number of terms of input linguistic variables is reduced to 3, it is also proposed to combine the terms "Relatively discomforting", 'Neutral' and "Relatively comfortable" into a group under the term "Neutral". If 5 input parameters with 3 terms each are used, the number of production rules will be 243.

Note that if 7 and 5 linguistic terms are used in each input parameter, the response surfaces of the output functions are more detailed relative to the system in which 3 linguistic terms are used in the input parameters. Also, in the case of more detailed response surfaces it is possible to note the presence of clearly limited areas of the surface, reflecting one or another linguistic term of the output variables. However, within the framework of solving the problem of developing a methodology for assessing the biopositivity of construction solutions, taking into account the limited computing power, it will be reasonable to adopt in the development of an adaptive neuro-fuzzy output system 5 input variables with 3 linguistic terms in each.

Moreover, this decision can be justified by the methodology adopted in [14], where the user's assessments of the comfort of SL on a 7-point scale (from -3 to 3) were combined into 3 groups according to the principle similar to that adopted in this paper:

• The group "Discomfortable" combines the therms "Absolutely Discomfortable", "Discomfortably Discomfortable";

• The group "Neutral" combines the terms "Relatively Discomfortable", 'Neutral' and "Relatively Comfortable";

• The group "Comfortable" combines the therms "Absolutely Comfortable", "Comfortable".

Thus the following input variables are defined:

- Quality of finishing materials: VOC emission. Therms: discomforting, comfortable, neutral.
- Level of natural light. Therms: discomforting, neutral, comfortable.
- Level of artificial light. Therms: discomforting, neutral, comfortable.
- Level of penetrating airborne noise. Therms: discomforting, neutral, comfortable.

- Air temperature. Therms: discomfort, neutral, comfortable.

As ANFIS implements Sugeno's fuzzy inference system as a dataframe [15, 16], a data set should be adopted to train the neural network, in which user ratings of the overall biopositivity of the building's SL coded based on a 7-point rating scale will be the response, and instrumentally measured values will be used as predictors:

– VOC concentration (ppm);
– ALF (%);
– Illumination of the working surface (lx);
– Penetrating airborne noise level (dBA);
– Air temperature (°C).

The 843 rows raw data array was divided into train and test samples in the ratio of 360 to 483 rows. The model was trained at 150 epochs [17]. Based on the training results, the model error was 0.0714.

According to the modeling results, the model of user's perception of the values of LE factors. In the Neuro-fuzzy designer extension package, the "rule viewer" interface allows to iteratively select such a combination of values of environmental factors that will allow to achieve a high index of biopositivity of LE and user comfort (Fig. 1).

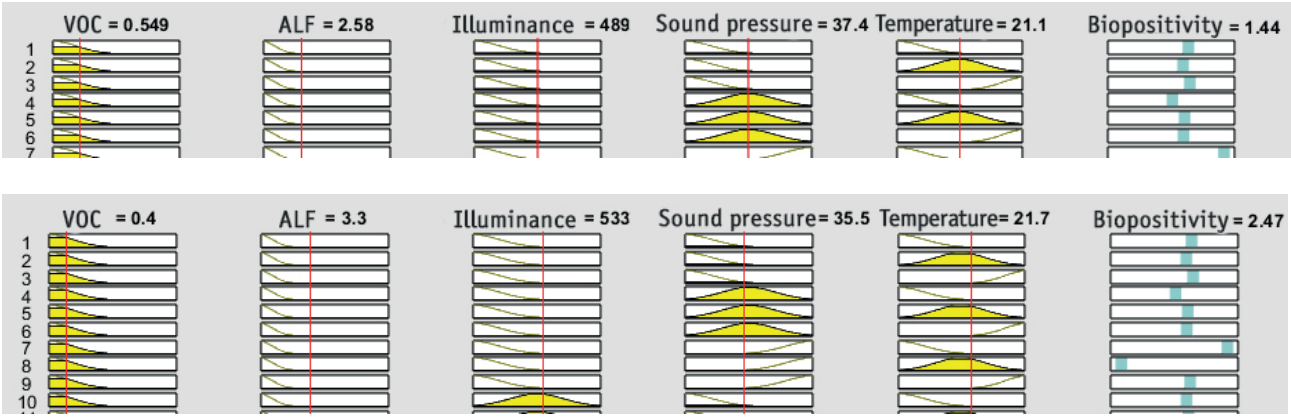


Figure 1. The Rule viewer interface of Matlab software, which allows iterative selection of co-combinations of the values of the biopositivity factors of the LE

As part of the analysis of modeling results it is necessary to investigate the function of integral index of biopositivity of LE (Biopositivity) at different combinations of input parameters.

The function of the integral biopositivity index at input parameters VOC concentration and sound pressure level has the following form (Figure 2).

The diagram shows that the greatest value of the Integral Index of Biopositivity comes at sound pressure values of less than 45 dBA and VOC concentration levels of less than 1 ppm, which are optimal for the human body. If the recommended MPC of VOCs is exceeded and the recommended sound pressure level is exceeded, the Biopositivity value is the lowest.

The function of the Integral index of biopositivity at input variables Temperature of air and Illumination of working surface has the form (Figure 3).

The graph shows that the greatest value of the Integral index of biopositivity is achieved at levels of natural and artificial lighting levels optimum for the human body, which is described in Section 1.2 of the article. At the value of illumination of the working surface in the range of 400-700 lux and the value of air temperature in the range of 21-23 °C the value of the Integral index of biopositivity is the greatest.

The function of the Integral Biopositivity Index with the input variables Quality of finishing materials: VOC emission and Illumination of the working surface has the form (Figure 4).

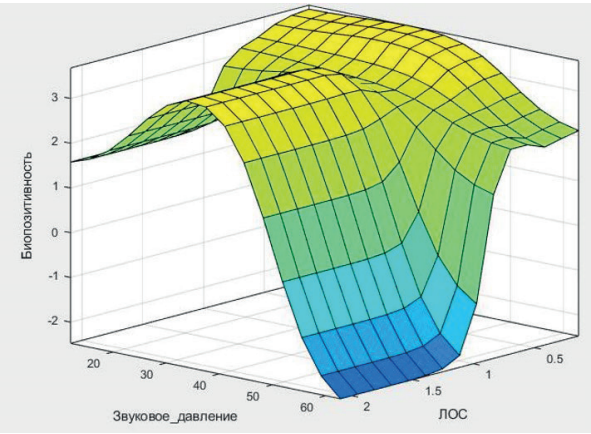


Figure 2. Function Integral biopositivity indicator with input variables VOC concentration and sound pressure level

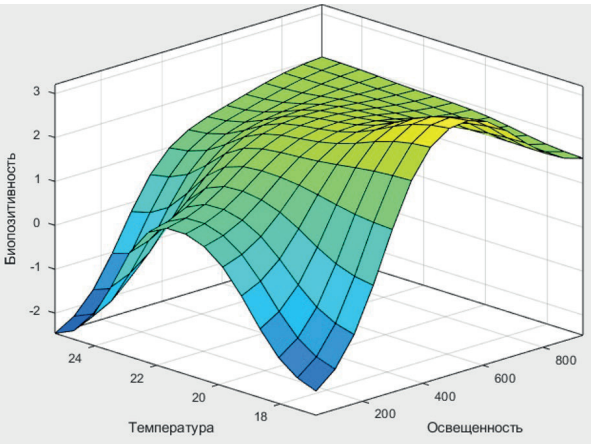


Figure 3. Function Integral indicator of biopositivity with input variables Temperature and Illuminance

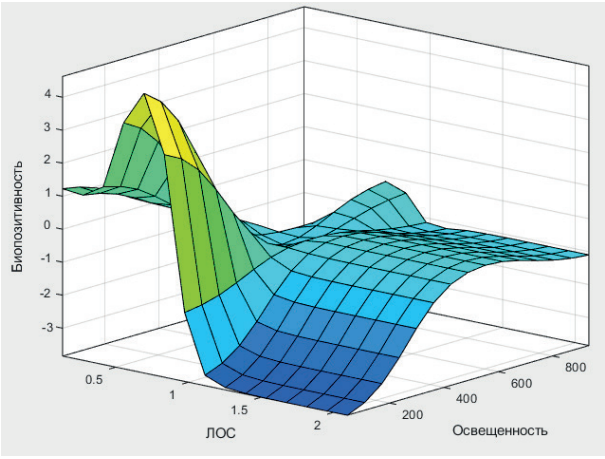


Figure 4. Function Integral biopositivity index with the input variables VOC concentration and Sound pressure level

The diagram demonstrates that the greatest value of the Integral index of biopositivity is achieved at values of VOC concentration up to 1 ppm and values of illumination of the working surface up to 400 lux. The lowest value of the Integral index of biopositivity is achieved at maximum VOC concentration and minimum illumination of the working surface.

Based on the study of adaptive neuro-fuzzy inference system it can be drawn a conclusion that the model to a large extent logically describes the subjective human perception of biopositivity factors of the environment [18]. Thus, the developed model should be used to solve the problem of iterative selection of combinations of environmental parameters that ensure the comfort of the end user of an administrative building.

The assessment of the biopositivity of building objects must account for a significant number of both internal and external environmental factors that are related to both design decisions and operational modes, along with the subjective perception of the biopositivity of environmental factors by building users.

From the point of view of quality management and life cycle management of a building project, especially the longest stage of the life cycle such as operation, assessment as benchmarking is not a sufficient tool to improve the quality of the object. In order to realize the advanced planning of increasing the integral indicator of biopositivity of the object, it is necessary to use the methodology of assessment of biopositivity of the construction object and the subsequent iterative determination of the values of the parameters of LE (diagrammatic interpretation is presented in Figure 5), at which the comfort of the user of the construction object will be ensured, which consists in performing a number of interrelated steps:

1. Analysis of project documentation and management company documentation to examine which of the biopositivity factors are present at the facility.
2. Conduct a user survey. Using the survey form presented in Annex 1 of this study to conduct a survey of regular users of the facility. In

order to achieve a representative sample, it is necessary to survey at least 30% with the number of regular users up to 1000 people, at least 25% with the number of regular users from 1001 to 2000 people, at least 20% with the number of regular users from 2001 to 3500 people, at least 15% with the number of regular users from 3501 to 5000 people, at least 10% with the number of regular users from 5001 to 10000 people [19, 20].

3. Conducting instrumental measurements of environmental parameters: VOC concentration; CO2 concentration; concentration of CEO, concentration of fine particles PM 2.5; CEO measured in a separate zone or office of the object under study; illumination of the working surface; light pulsation; penetrating noise level; air temperature; air humidity.

4. Coding the respondent's answers on a numerical scale from -3 to 3 in increments of 1 to allow for regression analysis of the results.

5. Conducting regression analysis of the coded responses of respondents. Determination of significant factors of biopositivity of LE on the basis of P-values of each environmental factor, which are predictors within the regression model. Determination of significant factors for neuro-fuzzy network modeling by ranking the moduli of the regression coefficients of the predictors. For further modeling of the neuro-fuzzy network, 5 predictors with the highest values of regression coefficient modules are taken as significant modeling factors.

6. Building a refined regression model to assess the significance of the model and verify the absence of multicollinearity.

7. Modeling of adaptive neuro-fuzzy inference system in MATLAB software program.

8. Fixing the integral indicator of biopositivity of the construction facility.

9. Iterative determination of the combination of the values of the parameters of LE, at which the comfort of the user of the construction facility will be ensured in the interface “rule viewer” of the extension package Neuro-fuzzy designer of the Matlab software program.

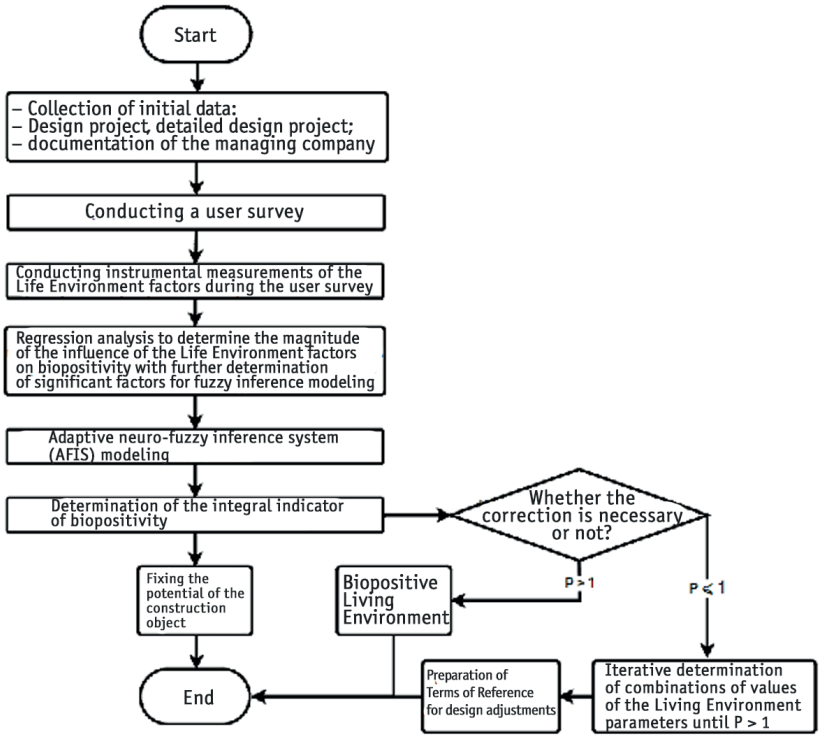


Figure 5. Flow chart of the methodology of biopositivity assessment and subsequent iterative determination of combinations of values of environmental parameters, which ensure the comfort of the user of a facility

CONCLUSIONS

As part of this study, an adaptive neuro-fuzzy model has been developed for iterative determination of combinations of the values of the parameters of the LE, at which the comfort of the users of the administrative building will be ensured. The response function of the output variable Biopositivity at different combinations of input variables has been analyzed. The adaptive neuro-fuzzy network to a large extent correctly describes the subjective human perception of the biopositivity of the factors of LE.

The methodology for assessing the biopositivity of a construction facility (on the example of an administrative building), which allows to fix the integral indicator of biopositivity of a construction facility and plan its advanced increase. The methodology can be widely applied in the management of construction facilities and used in the formation of technical specifications for the reconstruction and design of various types of residential buildings.

As the sampling of user assessments of the biopositivity factors of LE and instrumentally measured values of environmental factors of different types of civil buildings increases, the retrained adaptive neuro-fuzzy inference systems will be useful in determining the normative values of LE parameters.

REFERENCES

1. **Telichenko, V.I.** Design parameters of comfortable living environment in regulatory documentation [Text] / V.I. Telichenko, A.A. Benuzh, N.S. Rud, O.U. Yeye // Industrial and civil construction. - 2020. - № 5. - C. 51-56. - DOI 10.33622/0869-7019.2020.05.51-56.
2. **Elijah-Barnwell S, Friedow B**. Development and Psychometric Testing of a Post-Occupancy Evaluation. HERD Heal Environ Res Des J. 2014;8(1):115-121. doi:10.1177/193758671 400800109
3. **Riley, M.** A Review of the Evolution of Post-Occupancy Evaluation as a Viable Performance Measurement Tool [Электронный ресурс] /M. Riley, S. Moody, M. Pitt // CiteSeerx, 2009. – URL:http://citeseerx.ist.psu.edu/viewdoc/summary?doi=10.1.1.590.726
4. **Zimring, C**. Facility Performance Evaluation (FPE) [Электронный ресурс]/ C. Zimring, M. Rashid, R. Kampschrorer// Whole Building Design Guide: WDBG. A program of the National Institute of Building Science. 10.27.2014. – URL: http://wbdg.org/resources/fpe.php
5. W.F.E. Preiser, Learning from Our Buildings - A State-Of-The-Pratice Summary of Post-Occupancy Evaluation, 2001.
6. **Likert, Rensis** (1932). "A Technique for the Measurement of Attitudes". Archives of Psychology. 140: 1–55.
7. **Tetior, A.N.** Ecological harmony, beauty, comfort of the city (on the basis of ecological infrastructure): textbook for students of higher educational institutions, studying in the direction of training (specialties) 280402 / A. N. Tetior; A. N. Tetior; Ministry of Agriculture of the Russian Federation, Federal State Educational Institution of Higher Professional Education Moscow State University of Environmental Engineering. - Moscow: MSUP, 2010. - 312 p.
8. **Tetior, A.N.** Urban ecology: a textbook for students studying in the direction 653500 “Construction” / A. N. Tetior; A. N. Tetior. - Moscow: Academia, 2006. - 336 p.
9. **Parkinson, T., Schiavon, S., Kim, J., & Betti, G.** Common sources of occupant dissatisfaction with workspace environments in 600 office buildings // Buildings and Cities. – 2023 - 4(1), 17–35. https://doi.org/10.5334/bc.274
10. **Wargocki P., Schiavon S., Goins J., Arens E., Zhang H.** Satisfaction and self-estimated performance in relation to indoor environmental quality and building features // Building and Environment. 2020. Vol.

169. P. 106568. DOI: 10.1016/j.buildenv.2019.106568.
11. **Imbens G.W**. Statistical Significance, p-Values, and the Reporting of Uncertainty // Journal of Economic Perspectives. 2021. Vol. 35. P. 157–174.
12. **Telichenko, V.I.** Qualitative assessment of the living environment of civil buildings after occupancy [Text] / V.I. Telichenko, M.Y. Slesarev, A.A. Benuzh, N.S. Rud // Industrial and Civil Engineering. - 2022. - № 9. - C. 20-25. - DOI 10.33622/0869-7019.2022.09.20-25.
13. **Candido, C., Kim, J., de Dear, R., Thomas, L.** BOSSA: a multidimensional post-occupancy evaluation tool // Building Research & Information. 2016. Т. 44. № 2. С. 214–228. DOI: 10.1080/09613218.2015.1072298
14. **Graham L.T., Parkinson T., Schiavon S.** Lessons learned from 20 years of CBE's occupant surveys // Buildings and Cities. 2021. Vol. 2. № 1. P. 166–184. DOI: 10.5334/bc.76.
15. **Ebrat, M.; Ghodsi, R**. Risk assessment of construction projects using network based adaptive fuzzy system.Int. J. Acad. Res. 2011, 3, 411–417
16. **Kaur, A.; Kaur, A.** Comparison of Mamdani-type and Sugeno-type fuzzy inference systems for air conditioning system. Int. J. Soft Comput. Eng. 2012, 2, 323–325.
17. **Shoorehdeli, M.A.; Teshnehlab, M.; Sedigh, A.K.; Khanesar, M.A.** Identification using ANFIS with intelligent hybrid stable learning algorithm approaches and stability analysis of training methods. Appl. Soft Comput. J. 2009, 9, 833–850.
18. **Kim J., de Dear R.** Nonlinear relationships between individual IEQ factors and overall workspace satisfaction // Building and Environment. 2018. Vol. 142. P. 502–512. DOI: 10.1016/j.buildenv.2018.06.034.
19. **Altomonte S., Saadouni S., Kent M.G., Schiavon S.** Satisfaction with indoor environmental quality in BREEAM and non-BREEAM certified office buildings // Architectural Science Review. 2017. Vol. 60, No. 4. Pp. 343–355. DOI: https://doi.org/10.1080/00038628.2017.1336983.
20. **Schiavon S., Altomonte S.** Occupant satisfaction in LEED and non-LEED certified buildings // Building and Environment. 2019. Vol. 148. P. 1–9. DOI: 10.1016/j.buildenv.2018.10.034.

СПИСОК ЛИТЕРАТУРЫ

1. **Telichenko, V.I.** Design parameters of comfortable living environment in regulatory documentation [Text] / V.I. Telichenko, A.A. Benuzh, N.S. Rud, O.U. Yeye // Industrial and civil construction. - 2020. - № 5. - C. 51-56. - DOI 10.33622/0869-7019.2020.05.51-56.
2. **Elijah-Barnwell S, Friedow B**. Development and Psychometric Testing of a Post-Occupancy Evaluation. HERD Heal Environ Res Des J. 2014;8(1):115-121. doi:10.1177/193758671 400800109
3. **Riley, M.** A Review of the Evolution of Post-Occupancy Evaluation as a Viable Performance Measurement Tool [Электронный ресурс] /M. Riley, S. Moody, M. Pitt // CiteSeerx, 2009. – URL:http://citeseerx.ist.psu.edu/viewdoc/summary?doi=10.1.1.590.726
4. **Zimring, C**. Facility Performance Evaluation (FPE) [Электронный ресурс]/ C. Zimring, M. Rashid, R. Kampschrorer// Whole Building Design Guide: WDBG. A program of the National Institute of Building Science. 10.27.2014. – URL: http://wbdg.org/resources/fpe.php
5. W.F.E. Preiser, Learning from Our Buildings - A State-Of-The-Pratice Summary of Post-Occupancy Evaluation, 2001.
6. **Likert, Rensis** (1932). "A Technique for the Measurement of Attitudes". Archives of Psychology. 140: 1–55.

7. **Tetior, A.N.** Ecological harmony, beauty, comfort of the city (on the basis of ecological infrastructure): textbook for students of higher educational institutions, studying in the direction of training (specialties) 280402 / A. N. Tetior; A. N. Tetior; Ministry of Agriculture of the Russian Federation, Federal State Educational Institution of Higher Professional Education Moscow State University of Environmental Engineering. - Moscow: MSUP, 2010. - 312 p.
8. **Tetior, A.N.** Urban ecology: a textbook for students studying in the direction 653500 "Construction" / A. N. Tetior; A. N. Tetior. - Moscow: Academia, 2006. - 336 p.
9. **Parkinson, T., Schiavon, S., Kim, J., & Betti, G.** Common sources of occupant dissatisfaction with workspace environments in 600 office buildings // Buildings and Cities.-2023- 4(1), 17–35. https://doi.org/10.5334/bc.274
10. **Wargocki P., Schiavon S., Goins J., Arens E., Zhang H.** Satisfaction and self-estimated performance in relation to indoor environmental quality and building features // Building and Environment. 2020. Vol. 169. P. 106568. DOI: 10.1016/j.buildenv.2019.106568.
11. **Imbens G.W**. Statistical Significance, p-Values, and the Reporting of Uncertainty // Journal of Economic Perspectives. 2021. Vol. 35. P. 157–174.
12. **Telichenko, V.I.** Qualitative assessment of the living environment of civil buildings after occupancy [Text] / V.I. Telichenko, M.Y. Slesarev, A.A. Benuzh, N.S. Rud // Industrial and Civil Engineering. - 2022. - № 9. - C. 20-25. - DOI 10.33622/0869-7019.2022.09.20-25.
13. **Candido, C., Kim, J., de Dear, R., Thomas, L.** BOSSA: a multidimensional post-occupancy evaluation tool // Building Research & Information. 2016. T. 44. № 2. C. 214–228. DOI: 10.1080/09613218.2015.1072298
14. **Graham L.T., Parkinson T., Schiavon S.** Lessons learned from 20 years of CBE's occupant surveys // Buildings and Cities. 2021. Vol. 2. № 1. P. 166–184. DOI: 10.5334/bc.76.
15. **Ebrat, M.; Ghodsi, R**. Risk assessment of construction projects using network based adaptive fuzzy system.Int. J. Acad. Res. 2011, 3, 411–417
16. **Kaur, A.; Kaur, A.** Comparison of Mamdani-type and Sugeno-type fuzzy inference systems for air conditioning system. Int. J. Soft Comput. Eng. 2012, 2, 323–325.
17. **Shoorehdeli, M.A.; Teshnehlab, M.; Sedigh, A.K.; Khanesar, M.A.** Identification using ANFIS with intelligent hybrid stable learning algorithm approaches and stability analysis of training methods. Appl. Soft Comput. J. 2009, 9, 833–850.
18. **Kim J., de Dear R.** Nonlinear relationships between individual IEQ factors and overall workspace satisfaction // Building and Environment. 2018. Vol. 142. P. 502–512. DOI: 10.1016/j.buildenv.2018.06.034.
19. **Altomonte S., Saadouni S., Kent M.G., Schiavon S.** Satisfaction with indoor environmental quality in BREEAM and non-BREEAM certified office buildings // Architectural Science Review. 2017. Vol. 60, No. 4. Pp. 343–355. DOI: https://doi.org/10.1080/00038628.2017.1336983.
20. **Schiavon S., Altomonte S.** Occupant satisfaction in LEED and non-LEED certified buildings // Building and Environment. 2019. Vol. 148. P. 1–9. DOI: 10.1016/j.buildenv.2018.10.034.

Valeriy I. Telichenko, Professor, Doctor of Technical Sciences, Full member of Russian Academy of Architecture and Construction Sciences (RAACS), professor of department of Construction of Thermal and Nuclear Power Facilities of National Research Moscow State University of Civil Engineering,; 26, Yaroslavskoe Shosse, Moscow, 129337, Russia; e-mail: president@mgsu.ru

Nikita S. Rud, Head of environmental engineering, Nhood Russia; Verkhnyaya Krasnoselskaya St, bld. 3 s. 2, Moscow, 107140, Russia; E-mail: RudbNS@gmail.com

Теличенко Валерий Иванович Профессор, доктор технических наук, академик РААСН, профессор кафедры Строительства объектов тепловой и атомной энергетики Национального исследовательского Московского государственного строительного университета,; 129337, Россия, г. Москва, Ярославское шоссе, дом 26; E-mail: president@mgsu.ru

Рудь Никита Сергеевич, Руководитель экологического инжиниринга, ООО «Нью иммо сервисиз»; 107140, город Москва, Верхняя Красносельская ул, д. 3 стр. 2; E-mail: RudbNS@gmail.com

International Journal for Computational Civil and Structural Engineering, 21(2) 149–160 (2025)

DOI:10.22337/2587-9618-2025-21-2-149-160

EARTH CORE ROCKFILL DAM: INTERACTION OF WATER AND SOIL

Mikhail P. Sainov, Aleksandr A. Boldin

Moscow State University of Civil Engineering, Moscow, RUSSIA

Abstract: Accuracy of results of numerical modeling of the structure stress-strain state (SSS) depends on adequacy of design scheme. At elaboration of design scheme of an embankment dam the important aspect is selection of force loads from water. Water medium may create several types of force loads on the dam: hydrostatic pressure, buoyancy and seepage volumetrically distributed forces, as well as arise internal pore pressure in soil.

Selection of design scheme of the earth core rockfill dam depends on permeability of the clayey soil of the seepage-control core and the speed of the seepage regime formation. Analysis of the field observations over the state of constructed dams showed that this process may occur in different ways. In some dams after the reservoir impoundment the seepage regime is installed relatively quickly, in other dams there takes place a durable process of pore pressure dissipation and soil consolidation.

For estimation of the effect of the form and method of loads application, the analysis of the stress-strain state of high earth core rockfill dam for three design schemes was carried out. These are cases with conditionally impermeable, well permeable and scarcely permeable core soil. In the first case the core is subject to hydrostatic pressure, in the second to the force from the steady regime of the seepage flow, in the third, inequality of pore pressure and seepage forces takes place.

For analysis there was used the software package MIDAS, which permits conducting combined analysis of SSS and seepage regime, solving tasks related to consolidation of soils. Coulomb-Mohr model was used for modeling of soil.

Analysis showed that the dam SSS in three design schemes varies greatly. The dam is subject to the highest pressures and deformations in the case of the impermeable core at the action of hydrostatic pressure. The dam SSS at well permeable core, where seepage flow quickly becomes steady, is more favorable. The case of scarcely permeable soil is unfavorable from the point of view of core crack resistance. Due to core pressure, buoyant and seepage forces the stresses in soil skeleton are small. At that, horizontal displacements of the dam by value are closer to displacements in case of water impervious soil. This frequent case may be the most dangerous for the dam safety.

Keywords: earth core rockfill dam, stress-strain state, seepage, pore water pressure, loads, numerical analysis, finite element method

КАМЕННО-ЗЕМЛЯНАЯ ПЛОТИНА: ВЗАИМОДЕЙСТВИЕ ВОДЫ И ГРУНТА

М.П. Саинов, А.А. Болдин

Национальный исследовательский Московский государственный строительный университет, г. Москва, РОССИЯ

Аннотация: Точность результатов численного моделирования напряжённо-деформированного состояния (НДС) сооружения зависит от адекватности его расчётной схемы. При составлении расчётной схемы грунтовой плотины важнейшим аспектом является выбор силовых нагрузок от воды. Водная среда может создавать на плотину несколько видов силовых нагрузок: гидростатическое давление, взвешивающие и фильтрационные объёмно распределённые силы, а также вызывать в грунте внутреннее поровое давление.

Выбор расчётной схемы каменно-земляной плотины зависит от проницаемости глинистого грунта противофильтрационного ядра и скорости формирования его фильтрационного режима. Анализ натурных наблюдений за состоянием построенных плотин показал, что этот процесс может происходить поразному. В одних плотинах после наполнения водохранилища фильтрационный режим устанавливался относительно быстро, а в других происходил длительный процесс рассеивания порового давления и консолидации грунта.

Для оценки влияния формы и способа приложения нагрузок был выполнен расчёт напряжённо-деформированного состояния высокой каменно-земляной плотины для трёх расчётных схем. Это случаи

с условно водонепроницаемым, хорошо проницаемым и маловодопроницаемым грунтом ядра. В первом случае на ядро действует гидростатическое давление, во втором – силы от установившегося фильтрационного потока, в третьем происходит постоянное изменение порового давления и фильтрационных сил.
Для расчётов использовался программный комплекс MIDAS, который позволяет вести совместный расчёт НДС и фильтрационного режима, решать задачи о консолидации грунтов. Для моделирования грунта использовалась модель Кулона-Мора.
Анализ показал, что НДС плотины в трёх расчётных схемах сильно различается. Наибольшие напряжения и деформации плотина испытывает в случае водонепроницаемого ядра, при действии гидростатического давления. НДС плотины в случае хорошо проницаемого ядра, в котором быстро устанавливается фильтрационный поток, является более благоприятным. Случай маловодопроницаемого грунта является неблагоприятным с точки зрения трещиностойкости ядра. Из-за порового давления, взвешивающих и фильтрационных сил напряжения в скелете грунта малы. При этом горизонтальные смещения плотины по величине ближе к смещениям в случае водонепроницаемого грунта. Этот часто встречающийся случай может являться наиболее опасным для безопасности плотины.

Ключевые слова: каменно-земляная плотина с ядром, напряжённо-деформированное состояние, фильтрация, поровое давление, нагрузки, численное моделирование, метод конечных элементов

INTRODUCTION

Analysis of stress-strain state (SSS) is an obligatory element of design validation of embankment dams, which refer to the first and the second category hydraulic structures, such requirement is stated in the code of practice SP 39.13330.2012 «Embankment Dams». These calculations are required for assessment of the dam safety.

Due to complexity, SSS analyses may be carried out only by numerical modeling; it permits solving the most complicated tasks. However, accuracy of numerical modeling depends on adequacy of the structure design scheme: on boundary conditions, construction sequence scheme, etc. One of the important components of the design scheme are combination and character of acting loads; for the dam first of all these are loads from water. Water medium may create several types of loads: hydrostatic pressure, buoyant force (Archimedes force), as well as seepage forces. Hydrostatic pressure is distributed along the surface area and buoyant and seepage forces are distributed in volume. Seepage forces are directed toward the side of going down head.

At conducting analyses, it is necessary to assign loads properly in order to adequately simulate the real conditions of the dam performance. For the dams with a central seepage control element in the form of a clay core (for example, earth core rockfill dam) the issue of the design scheme selection and the types of acting loads is not univocal. The design scheme is determined by the fact whether the clay core is pervious or not.

Like all the soils, the clayey soils are pervious, however, their seepage factor is very small. According to Russian building codes, in seepage control elements there should be used the soils with seepage factor less than 0.1 m/day ($1.2 \cdot 10^{-4}$ cm/s); in real dams it is even less (less than 0.005 m/day).

Evidently due to low permeability of the clayey soil the process of water penetration into the core should be durable, therefore, after the reservoir impoundment the seepage regime is established not at once. In this case the core may be considered as impervious.

By the results of numerical modeling of the non-steady regime conducted in 1, 2], penetration of water from the upstream side into the core should take years. In [2] it is stated that even after dozens of years the most part of the core is still dry. However, this concept is not right because initially the clayey soil is placed into the core at optimal humidity, which corresponds to actually full water saturation. Initial water saturation will contribute to quicker advancement of the seepage area boundary.

However, it does not mean that seepage flow in the core quickly becomes steady. The obstacle will be pore pressure formed in the clayey soil

at its compaction under the action of external loads. With time the soil is consolidated: due to seepage the pore pressure is gradually dissipated to the level corresponding to the seepage flow pressure, however, this process may be durable.

To estimate the duration of the consolidation process we fulfilled analysis of data of field observations over the state of dams, published in different sources. In [3, 4] there described the results of field observations over pore pressure in the dams constructed in the XX-th century. Field measurements show that the rate of consolidation process may be variable. In Aswan dam (Egypt, 1970, H=111 m) and Pachkamar dam (Uzbekistan, 1968, H=71 m) the process of the core soil consolidation was quick, but in the core of Talbingo dam (Australia) the pore pressure reached considerable values and dissipated slowly [3]. In ultra-high Nurek HPP dam (Tajikistan, 1980, H=300 m) by the moment of completion of construction, which lasted about 9 years and was performed in parallel with the reservoir impoundment, the most part of pore pressure was dissipated by the moment of start of operation [4].

Field measurements on the dams constructed in the XXI-st century [5–10] also confirm that there may be two possible cases.

In the first case the soil consolidation is quick and is nearly fully completed during construction period. Such case took place in ultra-high Nuozhadu dam (China, 2012, H=261.5 m) [5, 6]. By the start of operation period the seepage flow stabilized in the core of Eyvashan dam (Iran, 2015, H=71 m) [7, 8]. Such case is possible only when the core soil is sufficiently pervious.

The second case refers to durable soil consolidation, which is not completed during construction period and lasts for a long time during operation period. Such case took place in Karkhe dam (Iran, 2001, H=127 m). In spite of the fact that the reservoir impoundment was in parallel with the dam construction, pore pressure was still high for a long time [9]. Durable high pore pressure is considered to be the cause of increased deformations of Masjed-e-Soleyman dam (Iran, 2002, H=177 m) [10]. This case occurs if the core soil has low water permeability.

The design scheme of loads action corresponds to each of two considered cases. In the first case (permeable soil, quick consolidation) the load from water acts in the form of volumetrically distributed seepage forces.

In the second case (low soil permeability, durable consolidation) the character of loads is more complicated: it varies with time. At first, before the reservoir impoundment, pore pressure appears in the placed soil. After some time, following the appearance of hydraulic connection between the pores there will appear seepage forces in soil corresponding to pore pressure. Then, immediately after the reservoir impoundment the hydrostatic pressure appears on the core upstream face. Then, it will gradually disappear and will be replaced by seepage forces directed inside the core. The seepage regime will gradually change until it becomes steady.

Hydrostatic pressure on the core upstream face may also appear if reservoirs are impounded quickly after completion of the dam construction. Such case took place at construction of Gavshan dam (Iran, 2004, H=123 m) [11], Luding (China, 2016, H=84 m) [12].

As we see, loads from water may not only obtain different forms but may be transformed from one form to another.

At conducting SSS analyses different authors use various schemes of loads application. For example, in calculations [12–16] the core was assumed impervious and was loaded by hydrostatic pressure. In calculations [7, 8] the core was assumed fully permeable. And in calculations [5, 10] the soil was assumed scarcely permeable and SSS analyses were with consideration of PWP.

The aim of this study is revealing real conditions of formation of an earth core rockfill dam SSS and selection of the most adequate design scheme.

Similar study was fulfilled in [17]. At SSS analysis two cases were considered: 1) reservoir is impounded only after the dam is constructed for the full height; 2) reservoir is impounded gradu-

ally with growth of the dam height. Calculations showed that impoundment sequence has small effect on the dam stress state, but its integral displacement in case 1 is more than that in case 2. However, in calculations [17] the cases with permeable and low permeable soils were not taken into account. Calculations were carried out for relatively high seepage factor of the core soil (0.006 m/day), therefore, the effect of appearing increased pore pressure in the core was not revealed.

METHODS

For reaching the targeted aim the results of SSS analyses for several possible design schemes were compared. Three schemes were considered.

Scheme №1. The core is assumed to be fully impervious. In this case the load from water acts in the form of hydrostatic pressure on the core upstream face, and the core clayey soil is assumed to be water saturated (due to placement at optimal humidity). This scheme corresponds to the moment of time after quick reservoir impoundment.

Scheme №2. The core is well permeable and the seepage flow in the core is steady. In this case the load from water is realized in the form of seepage forces distributed in the core body. At that, the core soil is in suspended by water state, the pore pressure in it corresponds to the seepage pressure. This scheme is also possible at soil low permeability after the durable period of the dam operation.

Scheme №3 corresponds to the case when the core soil has low water permeability. In this case the increased pore pressure occurs in soil. As compared to scheme №2 in this design scheme the seepage flow in the core is still not stabilized, seepage forces are always variable in time by value and direction.

Calculations by schemes №2 and №3 pose a more complicated task than those by scheme №1. In scheme №2 consideration of seepage forces requires preliminary analysis of steady seepage regime in the core. In scheme №3 solving the task on the dam SSS should be performed jointly with solving the seepage task. For solving the static-seepage task, a special software is required.

Such possibility is provided by software package MIDAS, which uses the finite element method (FEM).

Analyses were conducted on the example of the ultra-high Earth Core Rockfill Dam (ECRD), whose structural design is similar to that of Nurek HPP dam (fig. 1). The dam is located on rock foundation. The height of fill in the considered section is 292.5 m.

The dam central core is made of sandy loam, it rests on bulk concrete. The shells are made of gravel-pebble soil and are covered by a layer of rock mass.

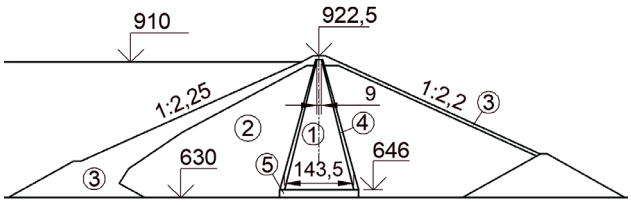


Figure 1. Scheme of rockfill dam structure
1 – core of sandy loam; 2 – shells of gravel-pebble soil; 3 – protection from rockfill; 4 – transition zone; 5 – concrete mass

The dam finite element model consists of 6975 nodes and 6906 finite elements.

During analyses the sequence of dam construction and reservoir impoundment was taken into account; they were realized in parallel. Duration of construction is about 9 years.

Coulomb-Mohr model was used for description of deformation and strength of soils. The following physical and mechanical properties of materials were used during calculations: ρ_d – density in dry state, ρ_{sat} – density in water saturated state; E – modulus of linear deformation; ν – Poisson's ratio, φ – angle of internal friction, c – cohesion. Parameters of shear strength (φ and c) of soils were taken from analogs. They are determined in [18] by processing of experi-

mental results [19, 20]. Cohesion for macro-fragmental soils simulates the effect of gearing.
The adopted in the analysis characteristics of soils are presented below:
For core sandy loam: ρ_d=2.10 t/m^3, ρ_{sat}=2.28 t/m^3, E=40 MPa, ν=0.32, φ=33º, c=100 kPa;
For gravel-pebble soil: ρ_d=2.16 t/m^3, ρ_{sat}=2.35 t/m^3, E=150 MPa, ν=0.27, φ=37.9º, c=112 kPa;
For rock mass: ρ_d=1.96 t/m^3, ρ_{sat}=2.22 t/m^3, E=150 MPa, ν=0.27, φ=39.3º, c=250 kPa;
For soil of transition zones: ρ_d=2.16 t/m^3, ρ_{sat}=2.35 t/m^3, E=55 MPa, ν=0.30, φ=32º, c=60 kPa.
Sandy loam seepage factor was taken equal $8.64 \cdot 10^{-5}$ m/day, macro-fragmental soils were taken more permeable by several orders.

RESULTS AND DISCUSSION

Results of SSS analyses of the considered ECRD are presented for the moment of completion of construction and reservoir impoundment. Fig.2–5 shows distribution of the dam displacements and stresses for three considered design schemes. In the table there indicated the maximum values of horizontal (U_x) and vertical (U_y) displacements of the dam.

Table. Maximum values of displacements

Scheme	1	2	3
U_x [cm]	287	191	264
U_y [cm]	440	366	346

Analysis shows that the dam SSS in schemes 1, 2, 3 principally differs from each other.
SSS in scheme 1 (impervious core) is characterized by maximum by value stresses and deformations. Several specific features may be marked.
The first peculiarity refers to the fact that in the impervious core the soil is not subject to buoyant force of water and consequently, it has large weight. Therefore, the dam has maximum settlements (440 cm, fig.2,a), and high vertical stresses (4.5 MPa, fig.4,a) appear in the core. The settlement comprises 1.5% of the dam height. Distribution of vertical stresses evidences about presence of arch effect, when there occurs deficit of compressive stresses in the core and their surplus in the shells.
The second peculiarity is related to the fact that at the boundary of the core with the upstream shell there appears a jump in value of horizontal stresses. It is caused by hydrostatic pressure on the core upstream face. Concentrated action of water causes increased horizontal displacements of the core near the upstream face (fig.4,a). It is scheme 1 where the dam is subject to maximum by value horizontal displacements (287 cm).
In scheme 2 the core is subject to pore pressure corresponding to the steady seepage regime (fig.6.a). It was determined at each stage by the seepage analysis.
In scheme 2 the dam SSS is characterized by less level of compression in the core as compared to scheme 1. Due to buoyant force of water the vertical stresses in the core do not exceed 3.5 MPa (fig.4,b). the dam maximum settlement amounts to 366 cm (fig.2,b), which is by 17% less, than in scheme 1.
At analysis by scheme 2 the dam has minimal horizontal displacements; they do not exceed 2 m (fig.3,b). They are less by one third that in scheme 1. The characteristic feature of SSS is low level of compression in the core near the upstream face, but toward the downstream face the horizontal compressive stresses gradually increase (fig.4,b).
In scheme 3 SSS is not only of another character than in schemes 1 and 2, but is not within the limits between them. Specific features of SSS refer to appearance of increased pore pressure in the dam core due to external loads.
Maximum dam settlement in scheme 3 amounts to 346 cm, which is even less than in scheme 2 (fig.2,c). This decrease is due to presence of seepage gradient directed upward. The dam maximum horizontal displacement amounts to 264 cm (fig.3,c); by value it is close to the displacement in scheme 1.

Maximum difference of SSS is revealed in the core stress state, because increased pore water pressure (PWP) acts in it. By the results of analysis, the growth of PWP occurs during the whole construction period. By its completion the maximum PWP reaches 3 MPa (fig.6.b). This is relatively small due to long duration of construction and other factors [21].

Due to increased PWP for the dam SSS in scheme 3 the minimum level of compression in the core is a characteristic feature. Horizontal stresses are noticeably low than in scheme 2. The field of low compressive horizontal stresses is located in the core lower part (up to 0.5 MPa, fig.5,c). Considerable decrease of compression also refers to vertical stresses. No tensile stresses are formed in the core, but in the upper part of the core the vertical stresses are small (fig.5,c). The low level of effective compressive stresses creates threat for the core hydraulic break and development of fractures in it.

One might say that out of the three considered design schemes it is scheme 3 that turned to be the most unfavorable. This is confirmed by the experience in operation of Masjed-e-Soleyman dam [10], where the durable process of soil consolidation became a possible cause of the core seal failure.

Besides, attention should be paid to one more characteristic feature of the dam SSS in scheme 3. It refers to increased level of compression in the part of the downstream shell adjoining to the core. Increase of compression is observed both in vertical (fig.4,c), and horizontal (fig.5,c) stresses. It is explained by the fact that due to presence of pore pressure the most part of load is transferred from the core to the downstream shell.

Stress state of the upstream shell in all the schemes is actually the same.

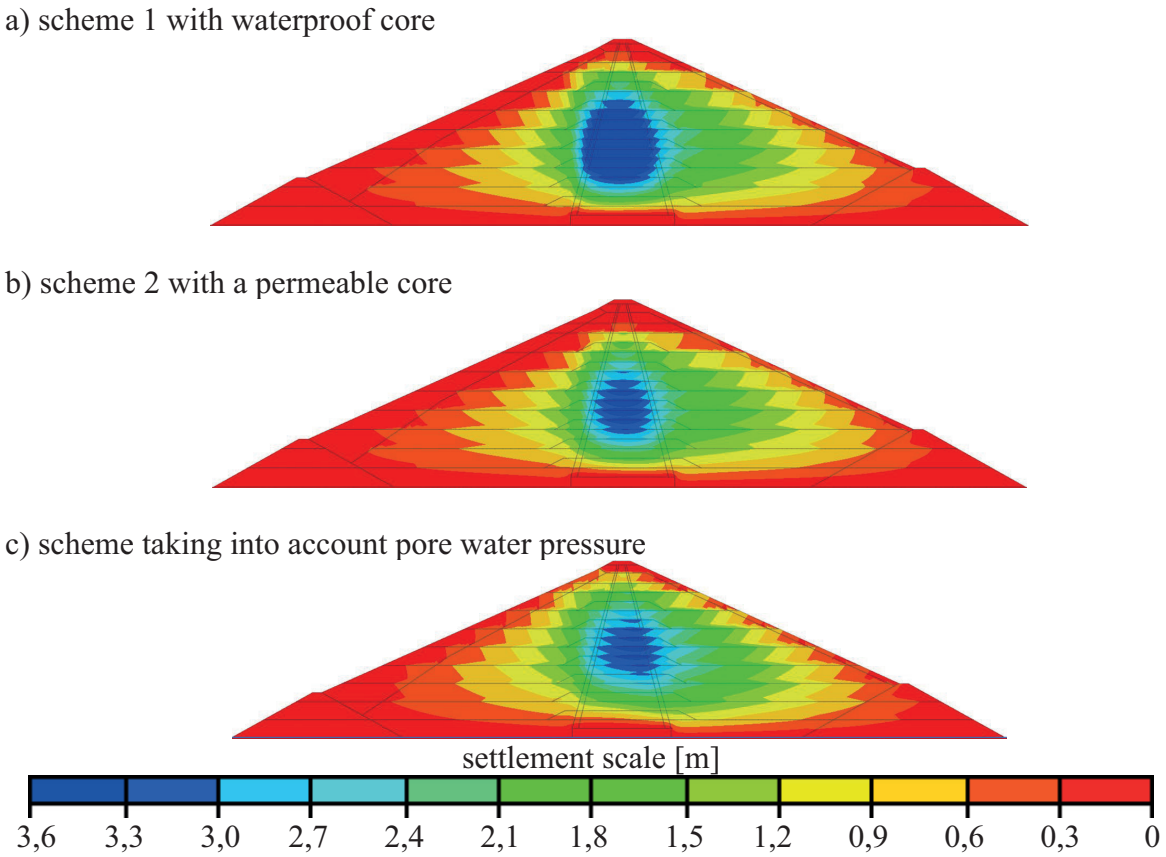
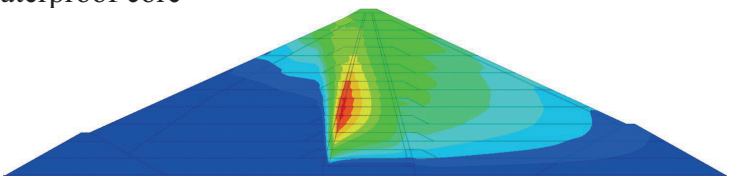
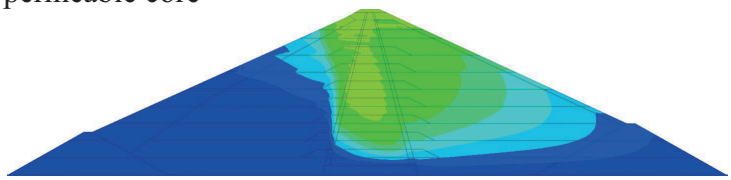


Figure 2. Dam settlements at the end of the construction period

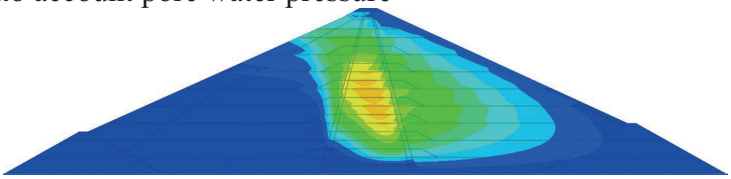
a) scheme 1 with waterproof core



b) scheme 2 with a permeable core



c) scheme taking into account pore water pressure



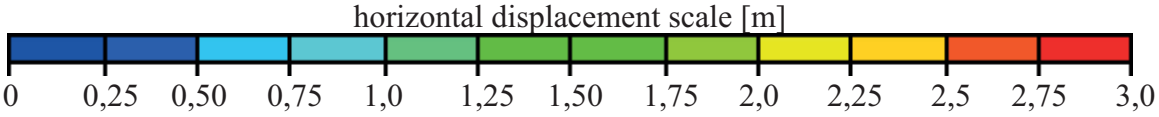
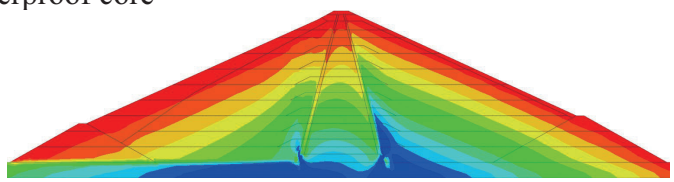
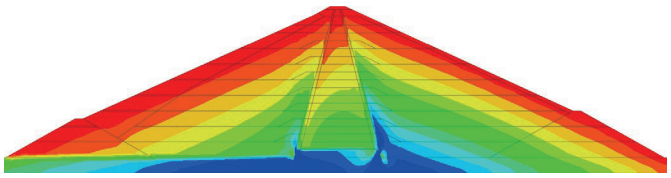


Figure 3. Horizontal displacements of the dam during the construction period

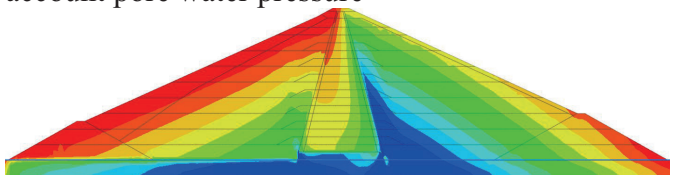
a) scheme 1 with waterproof core



b) scheme 2 with a permeable core



c) scheme taking into account pore water pressure



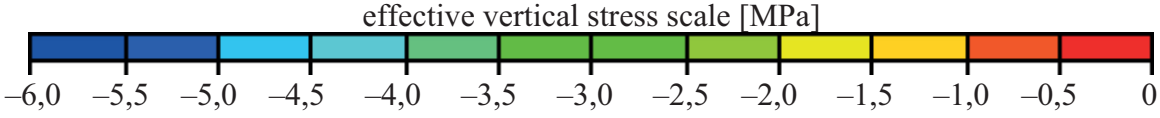
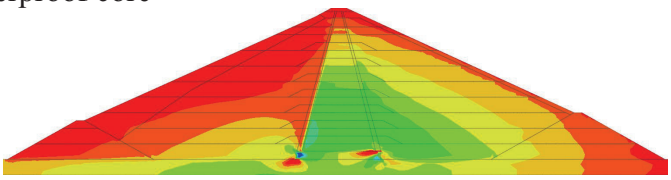
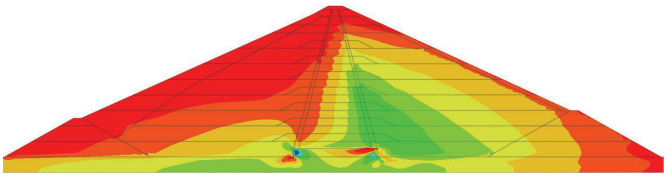


Figure 4. Vertical stresses in the dam soil

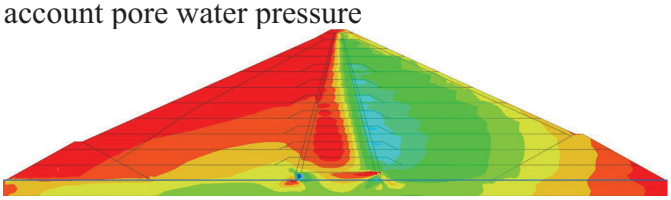
a) scheme 1 with waterproof core



b) scheme 2 with a permeable core



c) scheme taking into account pore water pressure



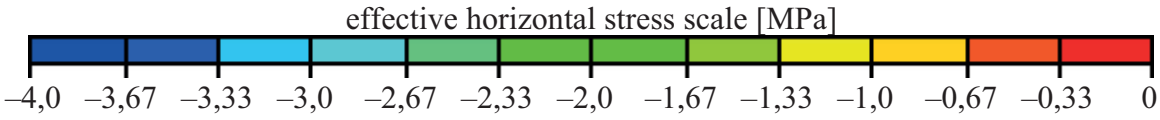
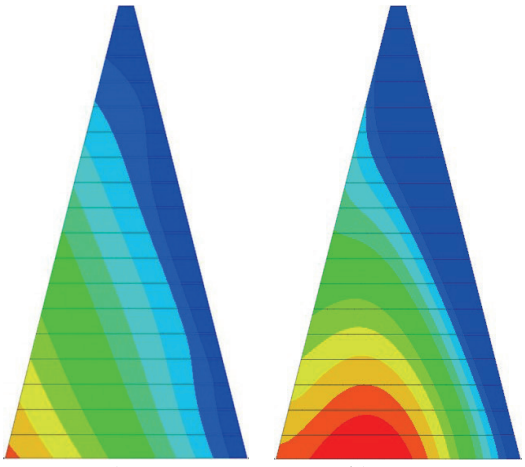


Figure 5. Horizontal stresses in the dam soil



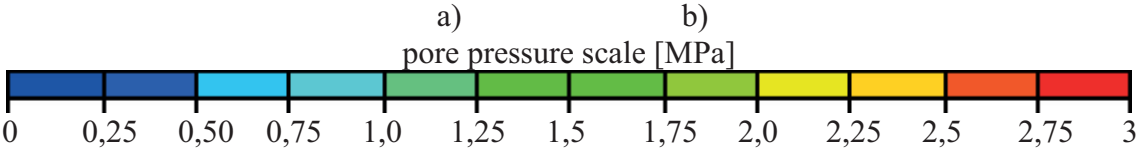


Figure 6. Pore water pressure in the dam core:
a – filtration pore pressure at steady state filtration conditions, b – pore pressure at the time of completion of construction in soil consolidation mode

CONCLUSION

1. The method of application of loads from water greatly affects the displacements of an earth core rockfill dam and stress state of its seepage control core. Therefore, accuracy of numerical modeling of stress-strain state of such dam is greatly dependent on adequacy of its design scheme and, first of all, on the scheme of application of loads from water.
2. Field investigations of stress-strain state of earth core rockfill dams show that different forms of loading by water forces on the structure may take place. They are determined by core soil permeability. The design scheme should be chosen depending on this factor.
3. Stress-strain state of an earth core rockfill dam obtained in each of the considered schemes of loads application is characterized by their own unfavorable effects. At the impervious core the dam is subject to maximum displacements and stresses. At rather permeable core, steady seepage flow, the dam SSS is the most favorable. The case with low permeable soil is characterized by low level of compression in the core due to appearance of pore pressure in soil. The dam SSS in this case may present danger from the point of view of the core crack resistance.
4. The dam seepage regime varies with time, and loads from water transfer from one type to another: from hydrostatic pressure to the forces from steady seepage flow. At that, the dam stress-strain state also transforms. For the considered dam the intermediate state at unsteady seepage regime turned to be dangerous.

REFERENCES

1. **Aniskin N.A., Rasskazov L.N., Yadgorov E.K.** (2017) Filtration, pore pressure, and settling from consolidation of an ultrahigh dam. *Power Technology and Engineering*, vol. 50, no 6, pp. 600–605. doi: 10.1007/s10749-017-0757-4
2. **Aniskin N.A., Sergeev S.A.** (2022) Chislennye resheniya zadach neustanovivshejsya fil'tracii v gidrotekhnike [Numerical solutions to unsteady filtration problems in hydraulic engineering]. *Vestnik MGSU* [Monthly Journal on Construction and Architecture], vol.17, no 11, pp. 1478–1487. doi: 10.22227/1997-0935.2022.11.1478-1487
3. **Rasskazov L.N., Yadgorov E.K., Nikolaev V.B.** (2018) Field Observations of Soil Settlements, Displacements, and Pore Pressure in Dams. *Power Technology and Engineering*, vol. 51, no 6, pp.611–620. doi: 10.1007/s10749-018-0881-9
4. **Rasskazov L.N., Yadgorov E.Kh., Burenkov P.M.** (2016) Pore Pressure Dissipation in the Core of the Nurek Dam. *Power Technology and Engineering*, vol.50, no 1, pp.54–56. doi: 10.1007/s10749-016-0658-y
5. **Wu Y., Zhang B., Yu Y., Zhang Z**. (2016) Consolidation analysis of Nuozhadu high earth-rockfill dam based on the coupling of seepage and stress-deformation physical state. *International Journal of Geomechanics*, vol. 16, no 3, 04015085. doi: 10.1061/(ASCE)GM.1943-5622.0000555
6. **Lv X., Chi S**. (2018) Strain Analysis of the Nuozhadu High Rockfill Dam during Initial Impoundment. *Mathematical Problems in Engineering*, 7291473 doi: 10.1155/2018/7291473
7. **Beiranvand B., Komasi M.** (2019) Monitoring and numerical analysis of pore water pressure changes Eyvashan dam during the first dewatering period. *Journal of Applied Research in Water and Wastewater*, vol.6, no 1, pp.1–7
8. **Komasi M., Beiranvand, B.** (2020) Study of Hydraulic Failure Mechanism in the Core of Eyvashan Earth Dam with the Effect of Pore Water Pressure and Arching. *Journal of Stress Analysis*, vol.4, no 2, pp. 55–67. doi:10.22084/jrstan.2020.20022.1110
9. Mir Mohammad Hosseini S.M., Ahmadi Fard R. (2023) Pore pressure development in the core of earth dams during simultaneous construction and impounding. *Electron-*

ic Journal of Geotechnical Engineering, vol. 8, pp.1–13.
10. **Akhtarpour A., Salari M.** (2020) The deformation mechanism of a high rockfill dam during the construction and first impounding. *Scientia Iranica A*, vol.27, no 2, pp. 566–587. doi: 10.24200/sci.2018.20778
11. **Rashidi M., Mohsen Haeri S**. (2017) Evaluation of the behavior of earth and rockfill dams during construction and first impounding using instrumentation data and numerical modeling. *Journal of Rock Mechanics and Geotechnical Engineering*, vol. 9, pp.709–725. doi: 0.1016/j.jrmge.2016.12.003
12. **Pan L., Wu B., Wang D., Zhou X., Wang L., Zhang Y.** (2024) Study on impoundment deformation characteristics and crack of high core rockfill dam based on inversion parameters, *Water*, vol. 16, 188. doi: 10.3390/w16010188
13. **Javanmard M., Amiria F., Safavi S.M.** (2019) Instrumentation Readings versus Numerical Analysis of Taham Dam. *International Journal of Engineering A: Basics*, vol. 32, no 1, pp.28–35. doi:10.5829/ije.2019.32.01a.04
14. **Sainov M.P.** (2022) Assessment of crack resistance of ultra-high earth core rockfill dam by pore pressure. *Magazine of Civil Engineering*, vol. 114, no. 6. Article No. 11411. doi: 10.34910/MCE.114.11
15. **Topçu S., Seyrek, E.** (2023) Numerical Analysis for Investigation of Hydraulic Fracturing Potential of the Rockfill Dam. *Journal of Scientific Reports-A*, no 55, pp. 173-184. doi: 10.1016/j.cviu.2017.00.000
16. **Juraev D., Matkarimov P.** (2023) Stress-strain state and strength of earth dams under static loads. E3S Web of Conferences 365, 03008. doi: 10.1051/e3sconf/202336503008
17. **Qun C., Yu H.Z., Min T., Chang R.H**. (2014) Modelling the Construction of a High Embankment Dam. KSCE Journal of Civil Engineering, vol. 18, no 1, pp.93–102. doi: 10.1007/s12205-014-0180-4
18. **Sainov M.P., Kotov F.V.** (2024) Parametry modeli uprochnyayushchegosya grunta dlya modelirovaniya vysokih gruntovyh plotin [Parameters of a hardening soil model for modeling high embankment dams]. *Journal of Science and Education of North-West Russia*, vol. 10, no 2, pp. 56–67.
19. **Marsal R.J.** (1967) Large Scale Testing of Rockfill Materials, *Journal of Soil Mechanics and Foundations Division*, vol. 93, no 2, pp. 27–43. doi: 10.1061/JSFEAQ.000095
20. **Jia Y., Xu B., Chi S., Xiang B., Zhou Y.** (2017) Research on the Particle Breakage of Rockfill Materials during Triaxial Tests. *International Journal of Geomechanics*, vol. 17, no 10, 04017085. doi: 10.1061/(ASCE)GM.1943-5622.0000977
21. **Sainov M.P., Boldin A.A.** (2024) Formirovanie porovogo davleniya v yadre kamenno-zemlyanoj plotiny ot sobstvennogo vesa [Formation of pore pressure in the earth-core rockfill dam due to the dead weight]. Hydrotechnika,. no 2, pp. 10–14.

СПИСОК ЛИТЕРАТУРЫ

1. **Aniskin N.A., Rasskazov L.N., Yadgorov E.K.** (2017) Filtration, pore pressure, and settling from consolidation of an ultra-high dam. *Power Technology and Engineering*, vol. 50, no 6, pp. 600–605. doi: 10.1007/s10749-017-0757-4
2. **Aniskin N.A., Sergeev S.A.** (2022) Chislennye resheniya zadach neustanovivshejsya fil'tracii v gidrotekhnike [Numerical solutions to unsteady filtration problems in hydraulic engineering]. *Vestnik MGSU* [Monthly Journal on Construction and Architecture], vol.17, no 11, pp. 1478–1487. doi: 10.22227/1997-0935.2022.11.1478-1487
3. **Rasskazov L.N., Yadgorov E.K., Nikolaev V.B.** (2018) Field Observations of Soil Settlements, Displacements, and Pore Pressure in Dams. *Power Technology and Engineering*, vol. 51, no 6, pp.611–620. doi: 10.1007/s10749-018-0881-9

4. **Rasskazov L.N., Yadgorov E.Kh., Burenkov P.M.** (2016) Pore Pressure Dissipation in the Core of the Nurek Dam. *Power Technology and Engineering*, vol.50, no 1, pp.54–56. doi: 10.1007/s10749-016-0658-y
5. **Wu Y., Zhang B., Yu Y., Zhang Z**. (2016) Consolidation analysis of Nuozhadu high earth-rockfill dam based on the coupling of seepage and stress-deformation physical state. *International Journal of Geomechanics*, vol. 16, no 3, 04015085. doi: 10.1061/(ASCE)GM.1943-5622.0000555
6. **Lv X., Chi S**. (2018) Strain Analysis of the Nuozhadu High Rockfill Dam during Initial Impoundment. *Mathematical Problems in Engineering*, 7291473 doi: 10.1155/2018/7291473
7. **Beiranvand B., Komasi M.** (2019) Monitoring and numerical analysis of pore water pressure changes Eyvashan dam during the first dewatering period. *Journal of Applied Research in Water and Wastewater*, vol.6, no 1, pp.1–7
8. **Komasi M., Beiranvand, B.** (2020) Study of Hydraulic Failure Mechanism in the Core of Eyvashan Earth Dam with the Effect of Pore Water Pressure and Arching. *Journal of Stress Analysis*, vol.4, no 2, pp. 55–67. doi:10.22084/jrstan.2020.20022.1110
9. Mir Mohammad Hosseini S.M., Ahmadi Fard R. (2023) Pore pressure development in the core of earth dams during simultaneous construction and impounding. *Electronic Journal of Geotechnical Engineering*, vol. 8, pp.1–13.
10. **Akhtarpour A., Salari M.** (2020) The deformation mechanism of a high rockfill dam during the construction and first impounding. *Scientia Iranica A*, vol.27, no 2, pp. 566–587. doi: 10.24200/sci.2018.20778
11. **Rashidi M., Mohsen Haeri S**. (2017) Evaluation of the behavior of earth and rockfill dams during construction and first impounding using instrumentation data and numerical modeling. *Journal of Rock Mechanics and Geotechnical Engineering*, vol. 9, pp.709–725. doi: 0.1016/j.jrmge.2016.12.003
12. **Pan L., Wu B., Wang D., Zhou X., Wang L., Zhang Y.** (2024) Study on impoundment deformation characteristics and crack of high core rockfill dam based on inversion parameters, *Water*, vol. 16, 188. doi: 10.3390/w16010188
13. **Javanmard M., Amiria F., Safavi S.M.** (2019) Instrumentation Readings versus Numerical Analysis of Taham Dam. *International Journal of Engineering A: Basics*, vol. 32, no 1, pp.28–35. doi:10.5829/ije.2019.32.01a.04
14. **Sainov M.P.** (2022) Assessment of crack resistance of ultra-high earth core rockfill dam by pore pressure. *Magazine of Civil Engineering*, vol. 114, no. 6. Article No. 11411. doi: 10.34910/MCE.114.11
15. **Topçu S., Seyrek, E.** (2023) Numerical Analysis for Investigation of Hydraulic Fracturing Potential of the Rockfill Dam. *Journal of Scientific Reports-A*, no 55, pp. 173-184. doi: 10.1016/j.cviu.2017.00.000
16. **Juraev D., Matkarimov P.** (2023) Stress-strain state and strength of earth dams under static loads. E3S Web of Conferences 365, 03008. doi: 10.1051/e3sconf/202336503008
17. **Qun C., Yu H.Z., Min T., Chang R.H**. (2014) Modelling the Construction of a High Embankment Dam. KSCE Journal of Civil Engineering, vol. 18, no 1, pp.93–102. doi: 10.1007/s12205-014-0180-4
18. **Sainov M.P., Kotov F.V.** (2024) Parametry modeli uprochnyayushchegosya grunta dlya modelirovaniya vysokih gruntovyh plotin [Parameters of a hardening soil model for modeling high embankment dams]. *Journal of Science and Education of North-West Russia*, vol. 10, no 2, pp. 56–67.
19. **Marsal R.J.** (1967) Large Scale Testing of Rockfill Materials, *Journal of Soil Mechanics and Foundations Division*, vol. 93, no 2, pp. 27–43. doi: 10.1061/JSFEAQ.000095
20. **Jia Y., Xu B., Chi S., Xiang B., Zhou Y.** (2017) Research on the Particle Breakage of Rockfill Materials during Triaxial Tests. *International Journal of Geomechanics*,

vol. 17, no 10, 04017085. doi: 10.1061/(ASCE)GM.1943-5622.0000977

21. **Sainov M.P., Boldin A.A.** (2024) Formirovanie porovogo davleniya v yadre kamenno-zemlyanoj plotiny ot sobstvennogo vesa [Formation of pore pressure in the earth-core rockfill dam due to the dead weight]. Hydrotechnika,. no 2, pp. 10–14.

Mikhail Petrovich Sainov — doctor of technical sciences, assistant professor, professor, department of hydraulic and hydraulic engineering, Federal State Budget Educational Institute of Higher Education «Moscow State University of Civil Engineering (National Research University)» (MGSU), 510, 26, Yaroslavskoe highway, Moscow, Russian Federation), SainovMP@mgsu.ru

Aleksandr Anatolevich Boldin — Postgraduate student, department of hydraulic and hydraulic engineering, Federal State Budget Educational Institute of Higher Education «Moscow State University of Civil Engineering (National Research University)» (MGSU), 510, 26, Yaroslavskoe highway, Moscow, Russian Federation), alex.boldin2012@yandex.ru

Михаил Петрович Саинов — доктор технических наук, доцент, профессор, кафедра гидравлики и гидротехнического строительства, Федеральное государственное образовательное учреждение высшего образования «Национальный исследовательский Московский государственный строительный университет» (НИУ МГСУ), комн. 510, дом 26, Ярославское шоссе, Moscow, 129337, Российская Федерация, SainovMP@mgsu.ru

Александр Анатольевич Болдин — аспирант, кафедра гидравлики и гидротехнического строительства, Федеральное государственное образовательное учреждение высшего образования «Национальный исследовательский Московский государственный строительный университет» (НИУ МГСУ), комн. 510, дом 26, Ярославское шоссе, Moscow, 129337, Российская Федерация, alex.boldin2012@yandex.ru

DOI:10.22337/2587-9618-2025-21-2-161-170

NONLOCAL IN TIME DYNAMIC DEFORMATION MODEL AND ITS CALIBRATION BASED ON THE BEAM VIBRATION EXPERIMENT RESULTS

Vladimir N. Sidorov [1], Elena. S. Badina [1,2], Roman O. Tsarev [1,2]

[1] Moscow State University of Civil Engineering, Moscow, RUSSIA
[2] Institute of Applied Mechanics of Russian Academy of Sciences, Moscow, RUSSIA

Abstract: The article is devoted to the development of a nonlocal in time model of a material dynamic deformation and its calibration on the basis of the beam vibration experiment results. The model is based on the defining relations of nonlocal mechanics. Elastic forces in a system are considered dependent on the entire history of its deformation, and not only on the instantaneous deformed state under consideration. The nonlocal in time model of a dynamic deformation is proposed as an alternative to detailed three-dimensional models when modeling the dynamic behavior of elements and systems made of materials characterized by an inhomogeneous structure or anisotropic properties. The model is incorporated into the FEA algorithm to make it usable for applied engineering problems. As a numerical example, the oscillation of a bending beam is considered. A method for the identification of the governing parameter of a nonlocal in time model based on the least squares method is being implemented based on the results of laboratory tests of bent beams for free vibrations.

Keywords: Nonlocal mechanics, nonlocal damping, numerical simulation, finite element method, beam vibrations

НЕЛОКАЛЬНАЯ ВО ВРЕМЕНИ МОДЕЛЬ ДИНАМИЧЕСКОГО ДЕФОРМИРОВАНИЯ МАТЕРИАЛА И ЕЁ КАЛИБРОВКА ПО РЕЗУЛЬТАТАМ ДИНАМИЧЕСКИХ ИСПЫТАНИЙ ИЗГИБАЕМЫХ БАЛОК

В.Н. Сидоров [1], Е.С. Бадьина [1,2], Р.О. Царёв [1,2]

[1] Национальный исследовательский Московский государственный строительный университет, г. Москва, РОССИЯ
[2] Институт прикладной механики Российской академии наук, г. Москва, РОССИЯ

Аннотация: статья посвящена разработке нелокальной во времени модели динамического деформирования материала и её калибровке по результатам лабораторных испытаний изгибаемых балок. Модель построена на основании определяющих соотношений нелокальной механики. Упругие силы в системе считаются зависящими от всей истории её деформирования, а не только от рассматриваемого мгновенного деформированного состояния. Нелокальная во времени модель динамического деформирования предлагается в качестве альтернативы подробным трёхмерным моделям при моделировании динамического поведения элементов и систем, выполненных из материалов, характеризующихся неоднородной структурой или обладающих анизотропными свойствами. Модель интегрирована в алгоритм метода конечных элементов, чтобы сделать её применимой для решения прикладных инженерных задач. В качестве численного примера рассматривается задача о колебаниях изгибаемой балки. Методика определения управляющего параметра нелокальной во времени модели, основанная на методе наименьших квадратов, реализуется с использованием лабораторных испытаний изгибаемых балок на свободные колебания.

Ключевые слова: Нелокальная механика, нелокальное демпфирование, численное моделирование, метод конечных элементов, колебания балок

INTRODUCTION

Detailed three-dimensional numerical models are often used for the analysis of systems and structures made of composite materials. Such an approach makes it possible to accurately describe material structure and properties. Such models provide high-quality results and are

widely used in the calculations of critical structures. However, they have a significant disadvantage — high computational complexity, which limits their use in multivariate calculations, optimization, and in solving problems that require modeling of large systems or their behavior over the long time intervals.

In this regard, development of the alternative less resource-intensive models that are equivalent to detailed three-dimensional models in terms of the adequacy of describing the dynamic behavior of composite elements becomes urgent.

The reduce of three-dimensional models of composite materials that take into account their internal structure or their anisotropy to lower-dimensional ones is the problem which does not have the unique solution [1]. The criterion for the chosen approach effectiveness can be the correspondence of the obtained results to experimental data in a certain class of problems.

One possible approach to this problem involves constructing lower-dimensional models based on specific hypotheses, particularly nonlocal ones [2].

Among nonlocal models, it is worth mentioning the spatially nonlocal model of the elastic properties of materials proposed by Eringen [3]. These studies were further developed and applied e.g. in [4] to the analysis of Euler–Bernoulli beams made of porous viscoelastic materials. Another nonlocal in space model was described in the book [5] (Kunin chains) and it was noted that this model can be used as an approximate description of a homogeneous three-dimensional medium. Nonlocal in space model of internal damping was proposed by Russel [6]. The model was applied to the problems of dynamics and stability of rods and shells by V.D. Potapov [7,8]. His approach was further studied and expanded in research implemented by the authors [9, 10]. The nonlocal in time model of dynamic deformation of the material presented in [10] shares common features with Boltzmann-Volterra hereditary model [11].

NONLOCAL IN TIME MODEL OF THE MATERIAL DEFORMATION

In the most general case, the nonlocal formulation of the dynamics of solids problem assumes that elastic and damping forces at a certain point of the body depend not only on the local values of strains and strain rates in time and space, respectively, but also on the values of strains and strain rates in a certain area adjacent to the point under consideration throughout the deformation history. The influence of points in space on each other diminishes with increasing distance, and the impact of previous deformation history on the current state of the system decreases over time.

In the classical local formulation, the defining relations for viscoelastic material, as described by the Kelvin-Voigt model, take the following form:

$$\sigma^{ij} = C^{ijkl}\varepsilon_{kl} + X^{ijkl}\frac{\partial \varepsilon_{kl}}{\partial t}, \tag{1}$$

where C^{ijkl} is elastic moduli tensor, $X^{ijkl} = C^{ijkl}t_e$ is viscosity moduli tensor, t_e is the retardation time, σ^{ij} is stress tensor, ε_{kl} is strain tensor.

The Cauchy relation:

$$\varepsilon_{ij} = \frac{1}{2}\left(\nabla_i u_j + \nabla_j u_i\right), \tag{2}$$

Where ∇_i is the differential operator and u_i is the components of displacements.

When transitioning to a nonlocal formulation, relation (1) takes the following form. [2]:

$$\begin{aligned}\sigma^{ij} &= C^{ijkl}\int_{\Omega}\int_{-\infty}^{t} K(\bar{r},\bar{\theta})\,R(t,\tau)\varepsilon_{kl}(\theta,\tau)d\tau d\theta \\ &+ X^{ijkl}\int_{\Omega}\int_{-\infty}^{t} D(\bar{r},\bar{\theta})\,G(t,\tau)\dot{\varepsilon}_{kl}(\theta,\tau)d\tau d\theta\,.\end{aligned} \tag{3}$$

Here, K and D are spatial kernel functions of elasticity and damping operators respectively; R

and G are temporal kernel functions of elasticity and damping operators respectively; $\bar{r}$ and $\bar{\theta}$ are spatial coordinate vectors; t and τ represent time; and Ω denotes the neighborhood of the point under consideration. The kernel functions are considered invariant with respect to shifts in time and space, thus:

$$\sigma^{ij} = C^{ijkl}\int_{\Omega}\int_{-\infty}^{t} K\left(\left|\bar{r}-\bar{\theta}\right|\right) R(t-\tau)\varepsilon_{kl}(\theta,\tau)d\tau d\theta + X^{ijkl}\int_{\Omega}\int_{-\infty}^{t} D\left(\left|\bar{r}-\bar{\theta}\right|\right) G(t-\tau)\dot{\varepsilon}_{kl}(\theta,\tau)d\tau d\theta. \quad (4)$$

In (4), the kernel functions are considered isotropic, meaning that the influence of different points in time and space on each other decreases at the same rate in all directions. In the most general case, the kernels can be considered anisotropic, i.e. they have different rates of influence decay in different directions. Taking into account all four types of nonlocality simultaneously when solving dynamic problems makes sense only if it reflects the real features of the material's dynamic behavior. To construct a phenomenological description of the dynamics of elements made of composite materials, various special cases of expression (4) are used, which allows to achieve sufficient computational accuracy, but do not overload the model.

By using the Dirac δ-functions as kernels, specific cases of nonlocal models can be obtained from the most general nonlocal stress-strain relationship (4).

In case of representing all four kernels as the δ-functions, we obtain:

$$\sigma^{ij} = C^{ijkl}\int_{\Omega}\int_{-\infty}^{t} \delta\left(\left|\bar{r}-\bar{\theta}\right|\right)\delta(t-\tau)\varepsilon_{kl}(\theta,\tau)d\tau d\theta + X^{ijkl}\int\int^{t} \delta\left(\left|\bar{r}-\bar{\theta}\right|\right)\delta(t-\tau)\dot{\varepsilon}_{kl}(\theta,\tau)d\tau d\theta \quad (5)$$

It is obvious that expression (5) is equivalent to the local classical viscoelastic model (1), which is thus a special case of a nonlocal model.

By various combinations of δ-functions with nonlocal kernels it is possible to derive from (4) various types of non-local models discussed in the literature, such as nonlocal in space model of elasticity (similar to Eringen model [3]), a nonlocal in space damping model [7,8], a nonlocal in time damping model [10].

The model presented in this paper is based on the assumption that elastic forces in a system depend not only on its current deformed state, but also on the previous deformation history. Such a model refers to the fourth type of nonlocality in which the elastic properties of the material are considered to be nonlocal in time:

$$\sigma^{ij} = C^{ijkl}\int_{\Omega}\int_{-\infty}^{t} \delta\left(\left|\bar{r}-\bar{\theta}\right|\right) R(t-\tau)\varepsilon_{kl}(\theta,\tau)d\tau d\theta + X^{ijkl}\int_{\Omega}\int_{-\infty}^{t} \delta\left(\left|\bar{r}-\bar{\theta}\right|\right)\delta(t-\tau)\dot{\varepsilon}_{kl}(\theta,\tau)d\tau d\theta \quad (6)$$

By integrating the δ-functions in (6) and taking into account only the time interval from the beginning of the system`s oscillations [12], we can obtain:

$$\sigma^{ij} = C^{ijkl}\int_{0}^{t} R(t-\tau)\varepsilon_{kl}(\tau)d\tau + X^{ijkl}\dot{\varepsilon}_{kl} \quad (7)$$

For now, the type of kernel function is not correlated with the specific features of the material structure and is mainly selected for computational efficiency reasons. Thus the kernel function in the nonlocal model can take different forms such as exponential function, error function, etc [2]. However, all types of kernels have to meet the normalization requirement:

$$\int^{t} R(t-\tau)\,d\tau = 1 \quad (8)$$

A common property of these functions, taking into account the normalization condition (8), is that, in some cases, the kernel function reduces to the Dirac δ-function, and, consequently, the model transforms to a local classical one.

THE FINITE ELEMENT FORMULATION

In order to make the nonlocal in time dynamic deformation model suitable for practical calculations, it has been integrated into the finite element method algorithm.
The physical interpretation of the finite element dynamic problems can be based on the principle of virtual work [13]:

$$\int_V \rho \ddot{u}_i \delta u_i dV + \int_V \sigma_{ij} \delta \varepsilon_{ij} dV = \int_A q_i \delta u_i dA + \int_V F_i \delta u_i dV. \quad (9)$$

Here ρ is a material density; q_i and F_i are surface and body forces; δu_i is the field of virtual displacements; $\delta \varepsilon_{ij}$ is the field of virtual strains. The two dots denote the second time derivative. Using the defining relation of a nonlocal in time dynamic deformation model (7) and considering the components of elastic moduli tensor constant in time, we can rearrange (9) as:

$$\int_V \rho \ddot{u}_i \delta u_i dV + \int_V C^{ijkl} \int_0^t R_t(t-\tau) \varepsilon_{kl}(\tau) d\tau \, \delta \varepsilon_{ij} dV + \int_V X^{ijkl} \dot{\varepsilon}_{kl} \delta \varepsilon_{ij} dV = \int_A q_i \delta u_i dA + \int_V F_i \delta u_i dV. \quad (10)$$

When employing the finite element approach, the actual strain and displacement fields for an element are replaced by approximate ones [14]:

$$\tilde{u} \approx \boldsymbol{N}\boldsymbol{d}, \quad (11)$$

where $\boldsymbol{N}$ is the shape functions matrix, $\boldsymbol{d}$ is the vector of displacements along the nodal degrees of freedom.
With the matrix operator of Cauchy relations $\boldsymbol{A}$ we can write $\boldsymbol{A}\boldsymbol{N} = \boldsymbol{B}$, then assumed element strain field is:

$$\tilde{\varepsilon} = \boldsymbol{B}\boldsymbol{d}. \quad (12)$$

Considering this and omitting the virtual nodal displacements according to the principle of virtual work [13] we can represent (10) in matrix form:

$$\int_V \rho \boldsymbol{N}^{\boldsymbol{T}} \boldsymbol{N} dV \ddot{\boldsymbol{d}} + \int_V \boldsymbol{B}^{\boldsymbol{T}} \boldsymbol{X} \boldsymbol{B} dV \dot{\boldsymbol{d}} + \int_V \boldsymbol{B}^{\boldsymbol{T}} \boldsymbol{C} \int_0^t R(t-\tau) \boldsymbol{B}\boldsymbol{d}(\tau) d\tau \, dV = \int_A \boldsymbol{N}\boldsymbol{q} dA + \int_V \boldsymbol{N}\boldsymbol{F} dV \quad (13)$$

For beam vibrations, we have only one component of $\boldsymbol{C}$ matrix: Young modulus *E;* and one component of strain:

$$\varepsilon_{11} = -y \frac{d^2 v}{dx^2}. \quad (14)$$

Here x is the longitudinal coordinate of the beam, y is the distance from the neutral layer of the bending beam to the point at which the deformation ε_{11} is calculated, v is the beam deflection function. The assumed solution $\tilde{v} \approx \boldsymbol{N}\boldsymbol{d}$ for each beam element can be written using Hermit interpolation functions:

$$\boldsymbol{N} = \begin{bmatrix} \frac{2s^3}{l^3} - \frac{3s^2}{l^2} + 1 \\ \frac{s^3}{l^2} - \frac{2s^2}{l} + s \\ \frac{3s^2}{l^2} - \frac{2s^3}{l^3} \\ \frac{s^3}{l^2} - \frac{s^2}{l} \end{bmatrix}, \quad (15)$$

where l is an element length, $s \in [0, l]$ is an element longitudinal coordinate.
Using $\frac{d^2}{ds^2}$ as $\boldsymbol{A}$ we have:

$$\boldsymbol{B} = \frac{d^2\boldsymbol{N}}{ds^2} = \begin{bmatrix} \frac{12s}{l^3} - \frac{6}{l^2} \\ \frac{6s}{l^2} - \frac{4}{l} \\ \frac{6}{l^2} - \frac{12s}{l^3} \\ \frac{6s}{l^2} - \frac{2s}{l} \end{bmatrix}. \quad (16)$$

Since all elements of $\boldsymbol{B}$ matrix are time independent we can take it out of the integral over time in (13). Then taking into account that cross-sectional moment of inertia is $I_z = \int_A y^2 dA$ we obtain:

$$\int_l \rho A \boldsymbol{N}^T \boldsymbol{N} ds \ddot{\boldsymbol{d}} + \int_l \boldsymbol{B}^T \chi I_z \boldsymbol{B} ds \dot{\boldsymbol{d}} + \int_l E I_z \boldsymbol{B}^T \boldsymbol{B} \int_0^t R(t-\tau)\boldsymbol{d}(\tau) d\tau \, ds = \boldsymbol{F}. \quad (17)$$

Here $\boldsymbol{M_i} = \int_l \rho A \boldsymbol{N}^T \boldsymbol{N} ds$ is the beam element mass matrix, $\boldsymbol{D_i} = \int_l \boldsymbol{B}^T \chi I_z \boldsymbol{B} ds$ is the element damping matrix, $\boldsymbol{K_i} = \int_l E I_z \boldsymbol{B}^T \boldsymbol{B} ds$ is the element stiffness matrix, $\boldsymbol{F}$ – is the load vector.
In (17) the damping matrix is proportional to the stiffness matrix. The same result was obtained in [10], where the damping matrix was derived using the stationary condition of the system's total energy during vibration.
After assembling $\boldsymbol{M_i}$, $\boldsymbol{D_i}$, $\boldsymbol{K_i}$ to a global mass matrix $\boldsymbol{M}$, damping matrix $\boldsymbol{D}$ and stiffness matrix $\boldsymbol{K}$ of the beam, we can write the finite element formulation of equation of motion:

$$\boldsymbol{M}\ddot{\boldsymbol{d}} + \boldsymbol{D}\dot{\boldsymbol{d}} + \boldsymbol{K}\int_0^t R(t-\tau)\boldsymbol{d}(\tau)d\tau = \boldsymbol{F}. \quad (18)$$

For the material with constant in time Young modulus in equation (18) the kernel function convolute only with the nodal displacement vector, and stiffness matrix of the beam $\boldsymbol{K}$ remains outside of the integral.
In this research error function was used as the kernel function:

$$R(t-\tau) = \frac{2\eta}{\sqrt{\pi}} \cdot e^{-\eta^2(t-\tau)^2}. \quad (19)$$

Here η is the parameter that characterizes the rate at which the kernel function decreases. It determines how much of the deformation history significantly impacts the current state of the system. The smaller the value of the scale parameter η, the more nonlocal the model becomes. Conversely, the larger the η, the closer is the model to the local classical one. Figure 1 illustrates how this parameter influences the shape of the kernel.

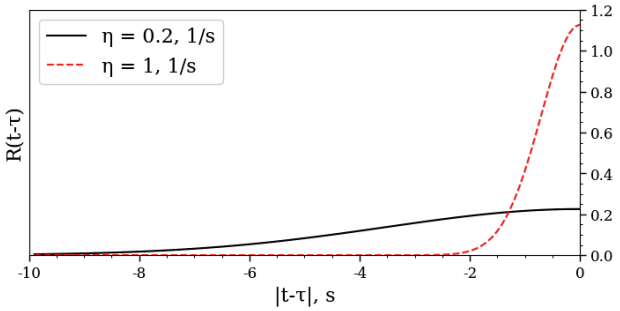


Figure 1 Error kernel functions for different values of η

Since the solution of the dynamic problem using the finite element method is discretized in time, the kernel function (19) was replaced by its discrete equivalent:

$$R = \sum_{j=1}^{i} \frac{2\eta}{\sqrt{\pi}} e^{-\eta^2\left(t_i - \left(\tau_j - \frac{\Delta t}{2}\right)\right)^2} \Delta t, \quad (20)$$

where i and j are numbers of time steps, Δt is the time increment.

BEAM VIBRATIONS MODELLING CONSIDERING THE ELASTIC PROPERTIES OF THE MATERIAL NONLOCAL IN TIME

To solve the equation of motion in matrix form, an implicit scheme [15] was employed. In this case, the nodal velocities and accelerations are represented as:

$$\dot{\boldsymbol{d}}_{i+1} = \frac{\boldsymbol{d}_{i+1} - \boldsymbol{d}_i}{\Delta t}; \qquad \ddot{\boldsymbol{d}}_{i+1} = \frac{2}{\Delta t^2}\left(\boldsymbol{d}_{i+1} - \boldsymbol{d}_i - \dot{\boldsymbol{d}}_\iota \cdot \Delta t\right) - \ddot{\boldsymbol{d}}_\iota \tag{21}$$

Since, in the case of employing an implicit scheme, the memory function is applied over the entire deformation process, ending at time t_{i+1}, the discrete integral kernel (20) has been divided into two parts [16]: α - the weighting coefficient associated with $\boldsymbol{d}_{i+1}$, β - the sum of all other weights (fig. 2):

$$\alpha = \frac{2\eta}{\sqrt{\pi}} \cdot e^{-\eta^2 (t_{i+1} - t_i)^2} \cdot \Delta t; \qquad \beta = \Delta t \sum_{j=1}^{i} \frac{2\eta}{\sqrt{\pi}} \cdot e^{-\eta^2 (t_i - t_{j-1})^2} \tag{22}$$

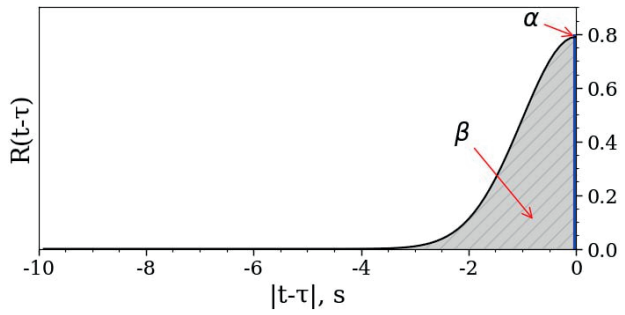


Figure 2. Kernel function divided into two parts

Then the computational scheme for solving the equation of motion by the Newmark method is as follows:

$$\boldsymbol{Q}\boldsymbol{d}_{i+1} = \boldsymbol{F}_{i+1} + \mathbf{M}\ddot{\boldsymbol{d}}_i + \boldsymbol{Q}_1\dot{\boldsymbol{d}}_i + \boldsymbol{Q}_2\boldsymbol{d}_i - \boldsymbol{K}\beta, \tag{23}$$

where:

$$\boldsymbol{Q} = \frac{2}{\Delta t^2}\boldsymbol{M} + \frac{1}{\Delta t}\boldsymbol{D} + \boldsymbol{K}\alpha, \qquad \boldsymbol{Q}_1 = \frac{2}{\Delta t}\boldsymbol{M}, \qquad \boldsymbol{Q}_2 = \frac{2}{\Delta t^2}\boldsymbol{M} + \frac{1}{\Delta t}\boldsymbol{D}, \tag{24}$$

To assess the effect of changes in the scale parameter η on the results of mathematical modeling, the vibrations of a 12-meter fixed-end beam (Fig. 3) made of thermoactive vinyl ester glassfiber-reinforced plastic were considered as a numerical example. The beam was loaded with an instantaneously applied and evenly distributed load with an intensity of -10 kN/m.

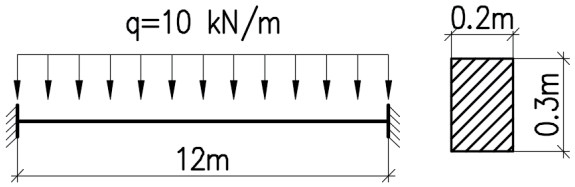


Figure 3. The calculation scheme of the considered beam

The characteristics of the material are given in Table 1.

Table 1. Characteristics of thermoactive vinyl ester glass-reinforced plastic

Young's Modulus (longitudinal), E_{lw}	17.2 GPa
Poisson's Ratio (longitudinal), μ_{lw}	0.32
Density, ρ	1900 kg/m^3
Damping coefficient, ξ	0.042

A software module written in Python was developed to solve the equation of motion and compute the nodal displacements, velocities, and accelerations of the beam accounting for nonlocal in time dynamic deformation. The results of the computer simulation are presented on fig. 4.

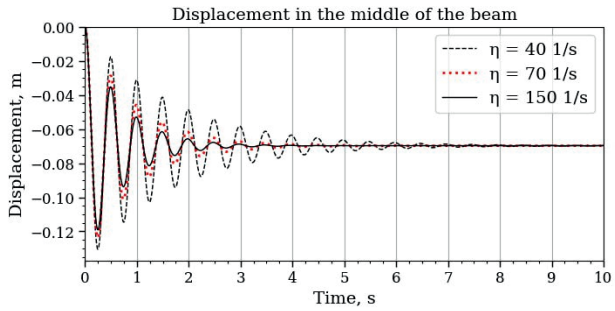


Figure 4. Vertical displacements history of the central node of the beam, obtained for three different scale parameters

Analyzing the presented graphs, it can be observed that as the parameter η decreases (indicating a higher degree of non-locality), the amplitude of oscillations increases.

IDENTIFICATION OF THE SCALE PARAMETER OF THE NONLOCAL MODEL BASED ON THE BEAM VIBRATION EXPERIMENT

One of the key challenges when using nonlocal models in applied problems is the necessity of determining the scale parameter η. In this study, a method for identifying the scale parameter through model calibration based on experimental data is proposed. The approach is based on the least squares method and involves minimizing the standard deviation between the results of numerical simulations and experimental measurements. To find the optimal value of the scale parameter that provides the best match between the model and the experimental data, the golden ratio method [17] was employed.

The proposed methodology was implemented based on the results of laboratory tests conducted on beams made of lightweight concrete filled with ceramic microspheres. The experiment was carried out with the support of the Scientific Research Center "Nanomaterials and Nanotechnologies" and the Research Institute of Experimental Mechanics of the Moscow State University of Civil Engineering. The characteristics of the material are presented in Table 2. The properties are isotropic, but the material has a heterogeneous structure.

Table 2. Properties of the lightweight concrete filled with the ceramic microspheres

Young's Modulus (longitudinal), E_{lw}	78.5 GPa
Density, ρ	1700 kg/m^3
Damping coefficient, ξ	0.0765

Identification of the model parameters was carried out based on the accelerations history of the free vibrations of a fixed-end beam initiated by a test hammer strike. To register the accelerations of the structure in the middle of the beam, a single-axis accelerometer was used (fig 5).

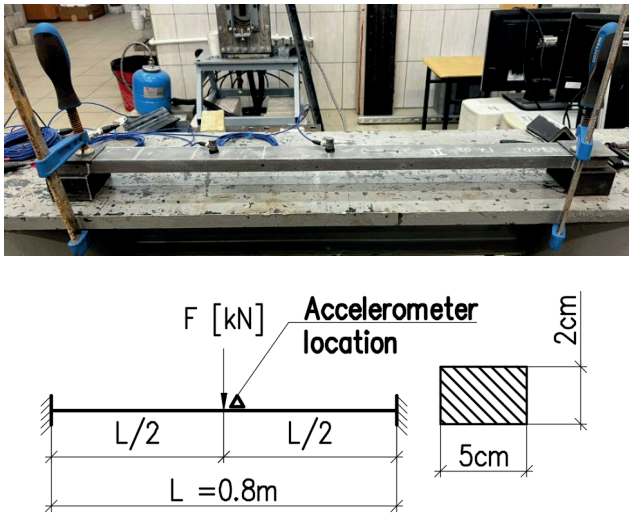


Figure 5. lightweight concrete beam used in the experiment

The received signal was synchronized and recorded using the National Instruments PXIe-1082 multichannel measuring system, which provides a sampling frequency of up to 12 kHz. This accuracy of registration made it possible to record in detail the accelerogram of the oscillatory process.

The acceleration time history at the mid-cross-section of the beam was used as a reference against which the results of one-dimensional modeling, based on local and non-local dynamic deformation models, were compared.

On figure 6 the comparison of the results obtained by local mathematical model with the experimental acceleration history is shown.

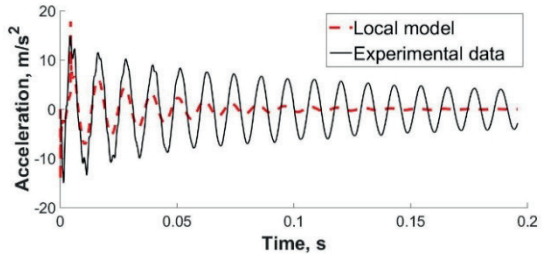


Figure 6. comparison of the reference accelerations with the results obtained by local classical model

Nonlocal in time dynamic deformation model of the beam vibration was calibrated by the experimental data. The comparison of those results with the experimental accelerations is presented on figure 7.

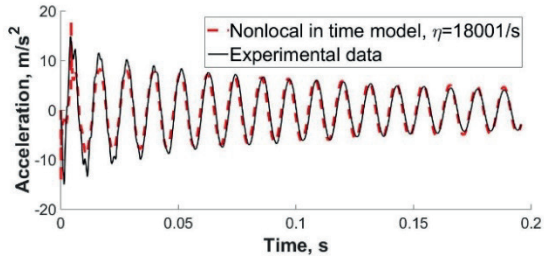


Figure 7. comparison of the results obtained by the nonlocal in time dynamic deformation model with the experimental accelerations

It is evident that the nonlocal in time model provides a better correspondence with the experimental data compared to the classical local model of beam vibration, which does not account for the inhomogeneous structure of the material. Although the nonlocal in time model also does not explicitly consider this inhomogeneity, it remains sufficiently flexible to accurately describe the dynamic behavior of beams made of such materials.

CONCLUSION

Nonlocal in time models of dynamic deformation of the material can serve as an effective alternative to detailed three-dimensional models when describing the dynamic behavior of materials with complex internal structure. The developed model has been integrated into the finite element method algorithm, enabling its application to practical problems. The method for determining the scale parameter of a nonlocal in time model was implemented based on the results of a laboratory experiment. It is shown that in comparison with the local classical model, the developed model makes it possible to achieve a better match with the experimental results.

ACKNOWLEDGEMENT

This research is supported by Russian Science Foundation (Project No 25-11-00140).

REFERENCES

1. **Kilchievsky N.A.** Foundations of Analytical Mechanics of Shells: In 2 Parts. Part 1. Kiev: Publishing House of the Academy of Sciences of the Ukrainian SSR, 1963. 354 pp. (In Russian)
2. **Lei Y., Friswell M.I., Adhikari S.** A Galerkin Method for Distributed Systems with Non-local Damping. International Journal of Solids and Structures, 2006, Vol. 43, pp. 3381–3400.
3. **Eringen A.C., Edelen D.G.B.** Nonlocal Elasticity. International Journal of Engineering Science, 1972, Vol. 10(3), pp. 233–248.
4. **Barretta R., Marotti de Sciarra F., Pinnola F.P.** On the Nonlocal Bending Problem with Fractional Hereditariness. Meccanica, 2022.
5. **Kunin I.A.** Theory of Elastic Media with Microstructure. Nonlocal Theory of Elasticity. Moscow: Main Edition of Physico-Mathematical Literature of the "Nauka" Publishing House, 1975. 416 p. (In Russian)
6. **Russell D.L.** On Mathematical Models for the Elastic Beam with Frequency-Proportional Damping. Control and

Estimation in Distributed Parameter Systems. SIAM, Philadelphia, PA, 1992, pp. 125–169.
7. **Potapov V.D.** On the Stability of Columns under Stochastic Loading Taking into Account Nonlocal Damping. Journal of Machinery Manufacture and Reliability, 2012, Vol. 41, No. 4, pp. 284–290.
8. **Potapov V.D.** Stability of a Flat Arch Subjected to Deterministic and Stochastic Loads Taking into Account Nonlocal Damping. Journal of Machinery Manufacture and Reliability, 2013, Vol. 42, No. 6, pp. 450–456.
9. **Fyodorov V.S., Sidorov V.N., Shepitko E.S.** Consideration of Nonlocal Damping for Computer Modelling of Vibrations in Linear and Nonlinear Systems under Stochastic Loads. IOP Conference Series: Materials Science and Engineering, 2018, Vol. 456(1).
10. **Sidorov V.N., Badina E.S., Detina E.P.** Nonlocal-in-Time Model of Material Damping in Dynamic Analysis of Composite Structural Elements. International Journal for Computational Civil and Structural Engineering, 2021, Vol. 17(4), pp. 14–21.
11. **Volterra V.** Lessons on Function Theory. Paris, Cauthier Villard, 1913. (In French)
12. **Rabotnov Yu.N**. Elements of Hereditary Mechanics of Rigid Bodies. Main Edition of Physico-Mathematical Literature of the "Nauka" Publishing House, 1977. 384 p. (In Russian)
13. **Khechumov R.A., Keppler H., Prokopyev V.I.** Application of the Finite Element Method to Structural Calculations. Publishing House of the Association of Construction Universities, 1994. 350 p. (In Russian)
14. **Bhatti M.A.** Fundamental Finite Element Analysis and Applications: with Mathematica and Matlab Computations. Wiley, 2005. 700 p.
15. **Sidorov V.N., Badina E.S.** Finite Element Method in Stability and Vibration Problems of Rod Structures. AVS Publishing, Moscow, 2021. 172 p. (In Russian)
16. **Sidorov V.N., Badina E.S., Tsarev R.O.** Calibration of the Nonlocal Dynamic Deformation Model of a Flexural Beam Based on Numerical Experiment Results. International Journal for Computational Civil and Structural Engineering, 2024, Vol. 20(2), pp. 132–140.
17. **Abbasov M.E.** Optimization Methods. Saint Petersburg: VVM Publishing House, 2014. 64 p. (In Russian)

СПИСОК ЛИТЕРАТУРЫ

1. **Кильчевский Н.А.** Основы аналитической механики оболочек: в 2 ч. Часть 1. Киев: Изд-во Акад. наук УССР. 1963. 354 с.
2. **Lei Y., Friswell M.I., Adhikari S**. A Galerkin Method for Distributed Systems with Non-local Damping. International Journal of Solids and Structures, 2006, V. 43, pp. 3381–3400.
3. **Eringen A.C., Edelen D.G.B.** Nonlocal elasticity. International Journal of Engineering Science, 1972, 10(3), pp. 233–48.
4. **Barretta R., Marotti de Sciarra F., Pinnola F.P.** On the nonlocal bending problem with fractional Hereditariness. Meccanica, 2022.
5. **Кунин И.А.** Теория упругих сред с микроструктурой. Нелокальная теория упругости. М.: Главная редакция физико-математической литературы издательства «Наука»,1975, 416 с.
6. **Russell D.L.** On mathematical models for the elastic beam with frequency-proportional damping. Control and Estimation in Distributed Parameter Systems. SIAM, Philadelphia, PA, 1992, pp. 125–169.
7. **Potapov V.D.** On the Stability of Columns under Stochastic Loading Taking into Account Nonlocal Damping. Journal of Machinery Manufacture and Reliability, 2012, Vol. 41, No. 4, pp. 284–290.
8. **Potapov V.D.** Stability of a Flat Arch Subjected to Deterministic and Stochastic Loads Taking into Account Nonlocal

Damping. Journal of Machinery Manufacture and Reliability, 2013, Vol. 42, No. 6, pp. 450–456.
9. **Fyodorov V.S., Sidorov V.N., Shepitko E.S.** Nonlocal damping consideration for the computer modelling of linear and nonlinear systems vibrations under the stochastic loads. IOP Conference Series: Materials Science and Engineering, 2018, V. 456(1).
10. **Sidorov V.N., Badina E.S., Detina E.P.** Nonlocal in Time Model of Material Damping in Composite Structural Elements Dynamic Analysis. International Journal for Computational Civil and Structural Engineering, 2021, 17(4), pp. 14–21.
11. **Volterra V.** Leçons sur les functions de lignes. Paris, Cauthier Villard, 1913.
12. **Работнов Ю.Н.** Элементы наследственной механики твёрдых тел. Главная редакция физико-математической литературы издательства «Наука», 1977, 384 с.
13. **Хечумов Р.А., Кепплер Х., Прокопьев В.И.** Применение метода конечных элементов к расчету конструкций. Изд-во Ассоц. строит. вузов, 1994, 350 с.
14. **Bhatti M.A.** Fundamental Finite Element Analysis and Applications: with Mathematica and Matlab Computations. Wiley, 2005, 700 p.
15. **Сидоров В.Н., Бадьина Е.С.** Метод конечных элементов в задачах устойчивости и колебаний стержневых конструкций. Издательство АСВ, М. 2021. 172 с.
16. **Sidorov V.N., Badina E.S., Tsarev R.O.** Calibration of the Nonlocal Dynamic Deformation Model of a Flexural Beam Based on Numerical Experiment Results. International Journal for Computational Civil and Structural Engineering, 2024, 20(2), pp. 132–140.
17. **Аббасов М.Э.** Методы оптимизации. СПб.: Издательство “ВВМ”, 2014, 64 с.

Vladimir N. Sidorov, Academician of Russian Academy of Architecture and Construction Science, Professor, Dr.Sc, Rectorate Counselor, Head of the Department of Computer Science and Applied Mathematics, National Research University Moscow State University of Civil Engineering, 129337, Russia, Moscow, Yaroslavskoe Highway, 26, e-mail: sidorov.vladimir@gmail.com.

Elena S. Badina, Associate Professor, Ph.D, Associate Professor of the Department of Computer Science and Applied Mathematics, National Research University Moscow State University of Civil Engineering, Senior Researcher at the Department of Mechanics of Structured and Heterogeneous Environment of the Institute of Applied Mechanics of the Russian Academy of Sciences; 129337, Russia, Moscow, Yaroslavskoe Highway, 26, e-mail: shepitko-es@mail.ru.

Roman O. Tsarev, Research Engineer, Department of Analytical Fundamental Scientific Research on the Dynamics of Building Structures, Scientific and Educational Center for Computer Modeling of Unique Buildings, Structures and Complexes, Moscow State University of Civil Engineering, PhD student of the Department of Mechanics of Structured and Heterogeneous Environment of the Institute of Applied Mechanics of the Russian Academy of Sciences; 125040, Russia, Moscow Leningradsky Ave., 7, p. 1, e-mail: tsarev.r.o@yandex.ru

Сидоров Владимир Николаевич, академик РААСН, профессор, доктор технических наук, советник при ректорате, заведующий кафедрой информатики и прикладной математики Национального исследовательского Московского государственного строительного университета, 129337, г. Москва, Ярославское шоссе, д. 26, e-mail: sidorov.vladimir@gmail.com.

Бадьина Елена Сергеевна, доцент, кандидат технических наук, доцент кафедры информатики и прикладной математики Национального исследовательского Московского государственного строительного университета, старший научный сотрудник Отдела механики структурированной и гетерогенной среды Института прикладной механики Российской академии наук, 129337, г. Москва, Ярославское шоссе, д. 26, e-mail: shepitko-es@mail.ru.

Царев Роман Олегович, инженер-исследователь отдела аналитических фундаментальных научных исследований по динамике строительных конструкций Научно-образовательного центра компьютерного моделирования уникальных зданий, сооружений и комплексов (НОЦ КМ) Московского государственного строительного университета (НИУ МГСУ), аспирант отдела механики структурированной и гетерогенной среды Института прикладной механики Российской академии наук; 125040, Россия, г. Москва Ленинградский просп., 7, стр. 1, e-mail: tsarev.r.o@yandex.ru

International Journal for Computational Civil and Structural Engineering, 21(2) 171–176 (2025)

DOI:10.22337/2587-9618-2025-21-2-171-176

ASSESSMENT OF THE DISTRIBUTION OF THE SOIL DEFORMATION MODULUS BASED ON CPT DATA

Nune Tigabu Abera [1,2], Ludmila V. Kirianova [2]

[1] Wachemo University, Hosanna, ETHIOPIA

[2] National Research Moscow State University of Civil Engineering, Moscow, RUSSIA

Abstract: Consideration of soil deformation characteristics is a crucial factor in the design and construction of infrastructure facilities, as they can have a significant impact on the stability and serviceability of structures. Changes in the soil deformation modulus with depth reflect changes in soil density, layering, and stress levels. Accurate assessment of the soil deformation variability is important to ensure the safety and reliability of building foundations. This paper focuses on testing the statistical hypothesis about the type of the soil deformation modulus probability distribution when analyzing cone penetration testing (CPT) data. The soil deformation modulus probability distribution is assumed to be normal and this fact is not checked before modelling. In this paper it is shown that Weibull, Lognormal and Gamma distributions are more suitable than normal for CPT data taken from an open internet source.

Keywords: Cone penetration test (CPT), studies of soil deformation properties, statistical hypothesis testing, distribution type hypothesis

ОЦЕНКА РАСПРЕДЕЛЕНИЯ МОДУЛЯ ДЕФОРМАЦИИ ГРУНТА НА ОСНОВЕ ДАННЫХ CPT

Нуне Тигабу Абера [1,2], Л.В. Кирьянова [2]

[1] Университет Вачемо, г. Осанна, ЭФИОПИЯ

[2] Национальный исследовательский Московский государственный строительный университет (НИУ МГСУ), г. Москва, РОССИЯ

Аннотация: Учет деформационных характеристик грунта является решающим фактором при проектировании и строительстве объектов инфраструктуры, поскольку они может оказать существенное влияние на устойчивость и работоспособность сооружений. Изменения модуля деформации с глубиной отражают изменения плотности почвы, ее слоистости и уровней напряжения. Точная оценка изменчивости деформаций грунта имеет важное значение для обеспечения безопасности и надежности основания зданий. В работе особое внимание уделяется проверке статистической гипотезы о виде вероятностного распределения модуля деформации грунта при анализе данных статистического зондирования (CPT). Принято считать, что вероятностное распределение модуля деформации грунта является нормальным и этот факт не проверяют перед проведением моделирования. В работе показано, что распределения Вейбулла, Логнормальное и Гамма подходят больше, чем нормальное для данных статического зондирования грунта, взятых из открытого интернет – источника. Приведены примеры моделирования гауссовского и логнормального двумерных случайных полей модуля деформации грунта на фиксированной глубине (в плане).

Ключевые слова: Статическое зондирование, исследования деформационных свойств грунта, проверка статистических гипотез, гипотеза о виде распределения

INTRODUCTION

It is known that one of the main factors influencing the buildings settlements value and structures, as well as the possible settlements unevenness, is the soil deformation modulus values and its statistical heterogeneity. Cone penetration testing (CPT) data provide the most complete picture of the strain modulus values at various points in the soil mass [1 - 4]. The strain modulus distribution models could be

useful in solving problems on systematization of static sensing results given in [5 - 10] to ensure safety and reliability. The probability distribution density of the soil deformation modulus plays an important role in building adequate models. According to [11], this distribution is assumed to be normal. Let us check this statement with the example data from [12]. These data represent the results of widely used field surveys that provide a continuous profile of soil physical properties through tip resistance, sleeve friction and pore water pressure during cone penetration. An initial statistical analysis of the data from [12] has already been performed by the authors in [13]. The purpose of such measurements is to assess the strength, stiffness and compressibility of the soil, which are key parameters for determining its deformation behavior [14]. The proper selection of the type of probability distribution can make the model of ground deformation behavior more accurate. We can consider the realization of the random field as a model of the distribution of the soil deformation modulus. The correct estimation of the variation of cone resistance q_c with depth is crucial in geotechnical engineering as it provides insight into the strength and stiffness of the soil. Hypothesis testing offers a statistical basis for assessing whether there is a statistically significant relationship between q_c and depth, indicating the presence of heterogeneity in the soil profile [15 - 16].

METHODS

There are several methods for testing the hypothesis about the type of distribution in mathematical statistics. Pearson's method χ^2 is the universal and most commonly used method. The maximum likelihood method is also widely adopted. It should be noted that the validity of the hypothesis about the type of probability distribution itself cannot be proved, only its admissibility is concluded [17]. Visualizing the data in different ways helps to make a correct hypothesis about the type of distribution. All calculations and graphs were performed in the MATLAB software environment.

The statistical heterogeneity of soil deformation modulus can be interpreted as a trajectory of a random process. For correct transition from the static sounding data to the construction of the ground deformation modulus model, it is possible, using the methods of the theory of random processes, to construct a continuous model using the available discrete statistical material. During construction of the model, the utilization of interpolation methods is not correct due to the peculiarities of the distribution of soil properties in space [16] and the influence of this distribution on the magnitude of non-uniform settlements.

Further we will use the model proposed in [18], when considering the statistical heterogeneity of the ground deformation modulus in plan view:

$$q_c(x, y) = m + \zeta\,(x, y),$$

where $q_c(x, y)$ is the realisation of a two-dimensional random process, $\zeta\,(x, y)$ is the realization of a two-dimensional stationary process with zero mean, and m is an average value of the ground deformation modulus at the considered depth.

Modelling of the Gaussian random field realizations is carried out by the method of canonical decompositions as a partial sum of Fourier series with random uncorrelated coefficients:

$$\zeta(x, y) = \sum_{k=-K}^{K} \sum_{n=-N}^{N} \psi_{k,n}\ exp\left\{\pi\left(\frac{k}{X_{max}}x + \frac{n}{Y_{max}}y\right)i\right\},$$

where X_{max} is the maximum value of the variable x, Y_{max} is the maximum value of the variable y, and $\psi_{k,n}$ are normal random variables with zero mean and variance defined through the covariance function.

The relationship between the lognormal and normal distribution was used to model the realization of a lognormal random field.

RESULTS AND DISCUSSION

Statistical analyses have been performed to quantify the variability of soil deformation parameters within each depth segment. Figures 1 - 4 show the histograms (purple color) of the soil deformation modulus with some theoretical probability densities, namely: Normal (red color), Weibull (blue color), Lognormal (brown color) and Gamma (grey color).

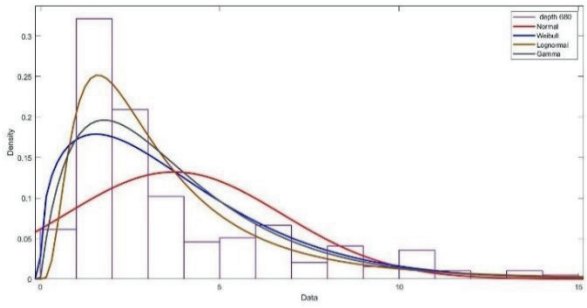


Figure 1. Histogram of the soil deformation modulus with some theoretical probability densities on 680 mm depth

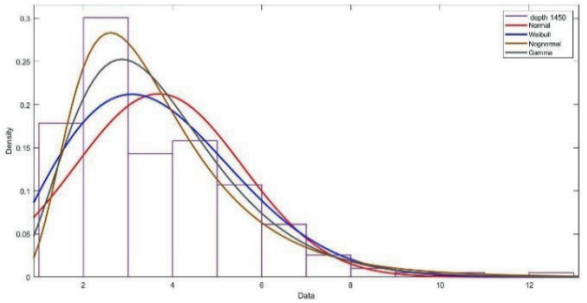


Figure 2. Histogram of the soil deformation modulus with some theoretical probability densities on 1450 mm depth

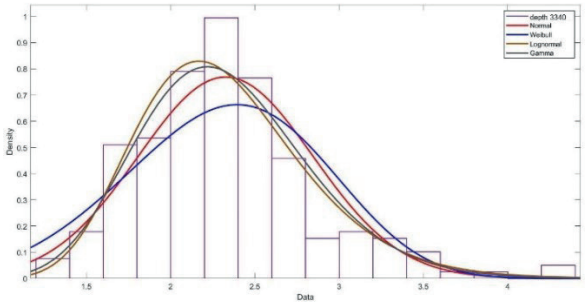


Figure 3. Histogram of the soil deformation modulus with some theoretical probability densities on 3340 mm depth

Table 1 summarizes the values of the logarithm of the likelihood function for the designated depths (mm). Note that the logarithm of the likelihood function is always negative. The greater its value, the more plausible the sample is, assuming that the hypothesis about the type of distribution is true. The lognormal or gamma distribution proved to be the most appropriate.

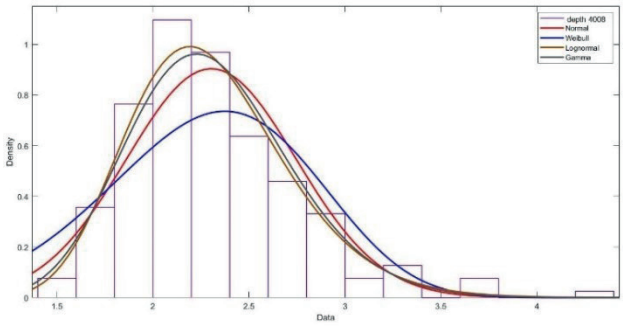


Figure 4. Histogram of the soil deformation modulus with some theoretical probability densities on 4005 mm depth

Table 1 The values of the logarithm of the likelihood function

	Log likelihood			
depth	Normal	Weibull	lognormal	Gamma
680	-494	-439	-422	-434
1450	-401	-383	-367	-372
1700	-363	-351	-336	-340
2300	-316	-306	-270	-280
2905	-235	-236	-212	-217
3340	-149	-160	-139	-140
3875	-125	-141	-109	-113
4005	-117	-136	-102	-106

Table 2 contains the probabilities for the designated depths (mm) for observing the test statistic χ^2 if the main hypothesis about the distribution type is true. Usually, the main hypothesis is rejected if this probability is less than 0.01. Here, too, the lognormal or gamma distribution proved to be the most appropriate.
Figures 5 - 8 show two different realizations each of Gaussian and lognormal random fields with the same numerical characteristics: mean and variance.

Table 2 The probabilities of the test statistic χ^2

depth	Normal	Weibull	lognormal	Gamma
680	8.6e-11	0.0008	0.0120	1.3e-04
1450	0.0026	0.0306	0.0023	0.0043
1700	7.9e-05	0.0056	0.2457	0.1410
2300	0.0225	0.0312	0.7060	0.3372
2905	3.5e-08	1.2e-08	0.0269	0.0012
3340	0.0071	1.8e-05	0.4525	0.1670
3877	0.0153	2.3e-05	0.3997	0.2031
4005	0.0119	5.3e-07	0.4558	0.2385

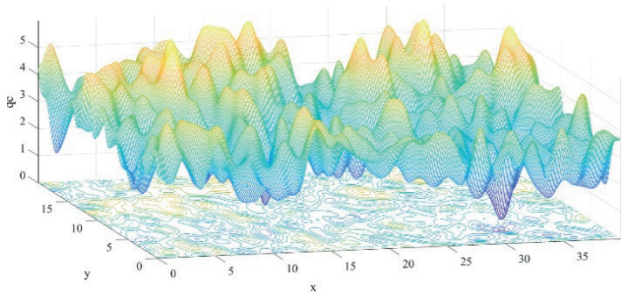


Figure 5. First realizations of the Gaussian random field on 1450 mm depth

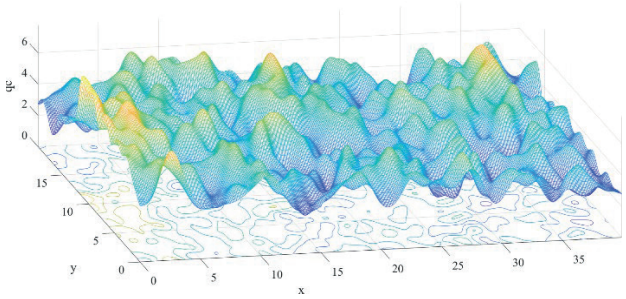


Figure 6. Second realizations of the Gaussian random field on 1450 mm depth

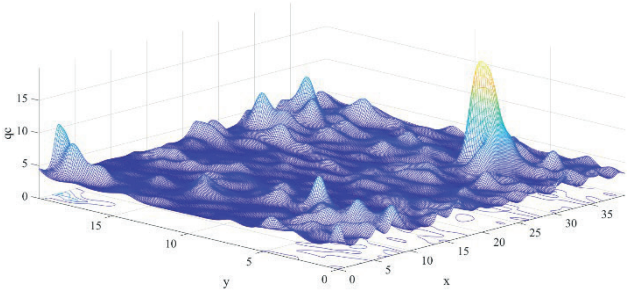


Figure 7. First realizations of the lognormal random field on 1450 mm depth

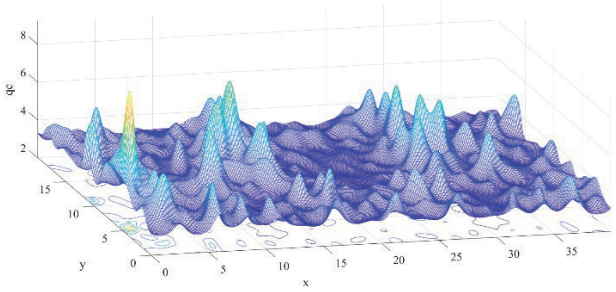


Figure 8. Second realizations of the lognormal random field on 1450 mm depth

It is noticeable that these fields have different distributions, which extends the possibility of using random field realizations in modeling the variability of the soil deformation modulus.

CONCLUSION

It is known (for example [19]) that the design of engineering geological objects that require ensuring the necessary reliability requires a deep understanding of the nature of soil variability, which could be modeled as a random field characterized by a probability density function with its basic statistical characteristics. When building random field models, the correct choice of the probability density function plays a crucial role. The studies carried out in this research have shown that it is incorrect to use only the normal distribution when modeling the behavior of the soil deformation modulus. Calculations show that in some cases the Lognormal distribution or the Gamma distribution are more appropriate than the Normal one. Therefore, before constructing a model of soil deformation modulus variability, it is necessary to test the hypothesis about the type of distribution of the studied quantity. The application of different types of random field distributions can improve the models used in the design of construction projects.

ACKNOWLEDGEMENTS

The authors cordially thank Prof. Marina V. Shitikova for her attention to the research and helpful comments that improved the article.

REFERENCES

1. **Zakharov M.S**. Static sounding in engineering surveys. SPb: SPbGASU, 2007, 71 p.
2. **Ziangirova R.S., Kashirskiy V.I.** Static sounding in engineering-geological surveys // Engineering Geology, 2006, pp. 13-20.
3. **Ryzhkov I.B., Isaev O.N.** Static sounding of soils. MOSCOW: ASV, 2010. 496 p.
4. **Sanglera G.** Research of soils by probing method (with the use of penetrometers). Moscow: Stroyizdat, 2012, 234 p.
5. **Belyaev V.P.** Pile foundations in the conditions of construction and reconstruction of Samara. Samara: SISU, 2005, 141 p.
6. **Dzagov A.M.** To the estimation of pile resistance in subsidence soils based on the results of static probing // Foundations, foundations and soil mechanics. 2007, № 5, pp. 28-30.
7. **Ignatova O.I.** Deformation characteristics of Jurassic clayey soils of Moscow // Foundations, Foundations and Soil Mechanics. 2009, № 5. C. 24-28.
8. **Minkin M.A.** Methods and techniques of engineering-geocryological surveys. Ukhta: Institute of Management, Information and Business, 2005, 252 p.
9. **Ukhov S.B., Semyonov V.V., Znamenskiy V.V.** Mechanics of soils, bases and foundations. Moscow: Higher School, 2007, 566 p.
10. **Lunne T., Robertson P.K., Powell J.J.** Cone penetration testing in geotechnical practice. Spon Press: London, 2004, 312 p.
11. **Zakharov M.S.** Engineering-geological and engineering-geotechnical surveys. SPb: ONTI, 2014, 103 p.
12. Database. [Electronic resource] URL: http://140.112.12.21/issmge/tc304.htm
13. **Abera N.T., Kiryanova L.** Assessing the distribution of statistical heterogeneity of the soil deformation modulus based on static soil sensing // E3S Web of Conferences, 2023, Vol. 410, Paper ID 03006, DOI: 10.1051/e3sconf/ 202341003006 EID: 2-s2.0-85170277695
14. **Zhang J., Litton R.L.** Geostatistical analysis of spatial variability of soil properties // Canadian Journal of Geotechnical Engineering, 2003, 40(3), pp. 517–531.
15. **Fenton G.A., Griffiths D.W.** Probabilistic methods of geotechnical design. New York: Taylor and Francis, 2007, DOI:10.1007/978-3-211-73366-0
16. **Baecher G., Christian J.** Reliability and statistics in geotechnical engineering. London: John Wiley & Sons, 2003, 210 p.
17. **Kobzar A.I.** Applied mathematical statistics: for engineers and scientific workers. Moscow: Fizmatlit, 2006, 813 p.
18. **Abera N.T.** Methodology for estimating the distribution of statistical non-homogeneity of soil deformation modulus based on the static sounding // Scientific and Technical Bulletin of the Volga Region, 2024, № 4, pp 61-64.
19. **Fung K. K., Huang S**. A critical review of reliability analysis of geotechnical engineering problems // Computers and Geotechnical Engineering, 2008, 35(6), 828-848

СПИСОК ЛИТЕРАТУРЫ

1. **Захаров М.С**. Статическое зондирование в инженерных изысканиях. СПб: СПбГАСУ, 2007, 71 с.
2. **Зиангирова Р.С., Каширский В.И.** Статическое зондирование в инженерно-геологических изысканиях // Инженерная геология, 2006, С. 13-20.
3. **Рыжков И.Б., Исаев О.Н.** Статическое зондирование грунтов. М.: АСВ, 2010, 496 с.

4. **Санглера Г.** Исследование грунтов методом зондирования (с применением пенетрометров). М.: Стройиздат, 2012, 234 с.
5. **Беляев В.П.** Свайные фундаменты в условиях строительства и реконструкции г. Самары. Самара: СИСУ, 2005, 141 с.
6. **Дзагов А.М.** К оценке сопротивления сваи в просадочных грунтах по результатам статического зондирования // Основания, фундаменты и механика грунтов. 2007, № 5. С. 28-30.
7. **Игнатова О.И.** Деформационные характеристики юрских глинистых грунтов Москвы // Основания, фундаменты и механика грунтов. 2009, № 5. С. 24-28.
8. **Минкин М.А.** Методика и методы инженерно-геокриологических изысканий. Ухта: Институт управления, информации и бизнеса, 2005, 252 с.
9. **Ухов С.Б., Семенов В.В., Знаменский В.В.** Механика грунтов, основания и фундаменты. М: Высшая школа, 2007, 566 с.
10. **Lunne T., Robertson P.K., Powell J.J.** Cone penetration testing in geotechnical practice. Spon Press: London, 2004, 312 p.
11. **Захаров М.С.** Инженерно-геологические и инженерно-геотехнические изыскания. СПб: ОНТИ, 2014, 103 с.
12. База данных. [Электронный ресурс] URL: http://140.112.12.21/issmge/tc304.htm
13. **Abera N.T., Kiryanova L.** Assessing the distribution of statistical heterogeneity of the soil deformation modulus based on static soil sensing // E3S Web of Conferences, 2023, Vol. 410, Paper ID 03006, DOI: 10.1051/e3sconf/202341003006 EID: 2-s2.0-85170277695
14. **Zhang, J. and Litton, R.L.** Geostatistical analysis of spatial variability of soil properties // Canadian Journal of Geotechnical Engineering, 2003, 40(3), pp. 517–531.
15. **Fenton G.A., Griffiths, D.W.** Probabilistic methods of geotechnical design. New York: Taylor and Francis, 2007, DOI:10.1007/978-3-211-73366-0
16. **Baecher G., Christian J.** Reliability and statistics in geotechnical engineering. London: John Wiley & Sons, 2003, 210 p.
17. **Кобзарь А.И.** Прикладная математическая статистика: для инженеров и науч. работников. Москва: Физматлит, 2006, 813 с.
18. **Абера Н.Т.** Методика оценки распределения статистической неоднородности модуля деформации грунтов на основе статического зондирования // Научно-технический вестник Поволжья, 2024, №4, С. 61-64.
19. **Fung K. K., Huang S**. A critical review of reliability analysis of geotechnical engineering problems // Computers and Geotechnical Engineering, 2008, 35(6), 828-848

Nune Tigabu Abera — Master of Science, Department of Mathematics, College of Natural and Computing Sciences, Wachemo University, PO Box-667, Hosanna, Ethiopia; PhD student; Russia, National Research Moscow State University of Civil Engineering, Russia, 129337, Moscow, 26 Yaroslavskoe Shosse; E-mail: tigabera2004@gmail.com

Нуне Тигабу Абера — магистр, Факультет математики, Колледж естественных и вычислительных наук, Университет Вачемо, почтовый ящик-667, Осанна, Эфиопия; аспирант, Федеральное государственное бюджетное образовательное учреждение высшего образования «Национальный исследовательский Московский государственный строительный университет» (НИУ МГСУ), Россия, 129337, Москва, Ярославское шоссе, 26; E-mail: tigabera2004@gmail.com.

Kirianova Ludmila V. — Associate Professor, PhD in physics and mathematics; Russia, National Research Moscow State University of Civil Engineering, Russia, 129337, Moscow, 26 Yaroslavskoe Shosse; E-mail: KiryanovaLV@mgsu.ru. ORCID: 0000-0003-4087-037X

Кирьянова Людмила Владимировна — доцент, кандидат физико-математических наук, Федеральное государственное бюджетное образовательное учреждение высшего образования «Национальный исследовательский Московский государственный строительный университет» (НИУ МГСУ) , Россия, 129337, Москва, Ярославское шоссе, 26; E-mail: KiryanovaLV@mgsu.ru. ORCID: 0000-0003-4087-037X

International Journal for Computational Civil and Structural Engineering, 21(2) 177–186 (2025)

DOI:10.22337/2587-9618-2025-21-2-177-186

DEEP BEAM ANALYSIS WITH THE USE OF DISCRETE-CONTINUAL FINITE ELEMENT METHOD IN THE PRESENCE OF A VERTICAL CRACK

Marina L. Mozgaleva, Pavel A. Akimov

National Research Moscow State University of Civil Engineering, Moscow, RUSSIA

Abstract: Deep beam analysis with the use of discrete-continual finite element method in the presence of vertical crack is under consideration in the distinctive paper. The operational formulation within discrete-continual approach is given, examples of analysis are presented. Cases of different lengths of the corresponding vertical crack are analyzed. The presented examples demonstrate the advantages of the discrete-continual finite element method used in comparison with the conventional finite element method (the use of the latter is associated with a significant increase in the number of nodes in the grid domain and, consequently, with an increase in the order of the resolving system of equations).

Keywords: discrete-continual finite element method, numerical solution, deep beam, structural analysis, crack, finite element method

РАСЧЕТ БАЛКИ-СТЕНКИ С ИСПОЛЬЗОВАНИЕМ ДИСКРЕТНО-КОНТИНУАЛЬНОГО МЕТОДА КОНЕЧНЫХ ЭЛЕМЕНТОВ ПРИ НАЛИЧИИ ВЕРТИКАЛЬНОЙ ЩЕЛИ

М.Л. Мозгалева, П.А. Акимов

Национальный исследовательский Московский государственный строительный университет, г. Москва, РОССИЯ

Аннотация: В настоящей статье рассматривается расчет балки-стенки с использованием дискретно-континуального метода конечных элементов при наличии вертикальной щели. Приведены операторная постановка задачи в рамках дискретно-континуального подхода, примеры расчета. Анализируются случаи различной длины соответствующей вертикальной щели. Представленные примеры демонстрируют преимущества используемого дискретно-континуального метода конечных элементов по сравнению с традиционным методом конечных элементов (использование последнего связано со значительным увеличением количества узлов сеточной области и, следовательно, с увеличением порядка разрешающей системы уравнений).

Ключевые слова: дискретно-континуальный метод конечных элементов, численное решение, балка-стенка, расчеты конструкций, щель, метод конечных элементов

INTRODUCTION

Deep beam analysis with the use of discrete-continual finite element method (DCFEM) has been already considered in [1-9, 13]. Corresponding systematic literature review has been presented in [1-9, 13] as well. In this regard, let us immediately move on to the main material of the distinctive paper in case of presence of a vertical crack.

1. FORMULATIONS OF THE PROBLEM

Let the constancy of the parameters of the problem be in the direction corresponding to x_2 (main direction). The operational formulation of the problem with the use of so-called method of extended domain [2], taking into account the selection of the main direction, is determined by the equation [3]:

$$\overline{z}' = \tilde{L}\overline{z} + \overline{\overline{F}},$$
$$0 \le x_1 \le \ell_1, \quad -\ell_2/2 \le x_2 \le \ell_2/2, \quad (1.1)$$

where we have

$$\tilde{L} = \left[\begin{array}{c|c} 0 & E \\ \hline L_{vv}^{-1}L_{uu} & L_{vv}^{-1}L_{uv} \end{array}\right]; \quad (1.2)$$

$$L_{uu} = \partial_1^* D_1^T C D_1 \partial_1; \quad (1.3)$$

$$L_{uv} = \partial_1^* D_1^T C D_2 - D_2^T C D_1 \partial_1; \quad (1.4)$$

$$L_{vv} = D_2^T C D_2; \quad (1.5)$$

$$E = \begin{bmatrix} 1 & \\ & 1 \end{bmatrix}; \quad (1.6)$$

$$D_1 = \begin{bmatrix} 1 & 0 \\ 0 & 0 \\ 0 & 1 \end{bmatrix}; \quad D_2 = \begin{bmatrix} 0 & 0 \\ 0 & 1 \\ 1 & 0 \end{bmatrix}; \quad (1.7)$$

$$C = \begin{bmatrix} 2\mu+\lambda & \lambda & 0 \\ \lambda & 2\mu+\lambda & 0 \\ 0 & 0 & \mu \end{bmatrix}; \quad (1.8)$$

$$\partial_k = \frac{\partial}{\partial x_k}, \quad \partial_k^* = -\partial_k, \quad k = 1,2; \quad (1.9)$$

$$\overline{\overline{F}} = \left[\begin{array}{c} 0 \\ \hline -L_{vv}^{-1}\overline{\overline{F}} \end{array}\right]; \quad \overline{z} = \begin{bmatrix} \overline{u} \\ \overline{v} \end{bmatrix}; \quad (1.10)$$

$$\overline{u} = \begin{bmatrix} u_1 \\ u_2 \end{bmatrix}; \quad \overline{v} = \partial_2 \overline{u} = \begin{bmatrix} v_1 \\ v_2 \end{bmatrix}; \quad (1.11)$$

ℓ_1, ℓ_2 are corresponding dimensions of extended domain (linear dimensions of considering structure) [2]; $x = (x_1, x_2)$; x_1, x_2 are Cartesian coordinates; μ and λ are Lame parameters [14, 15]; Ω is the domain, occupied by structure;

$$\Omega = \{ (x_1, x_2): \quad 0 < x_1 < \ell_1; \quad -\ell_2/2 < x_2 < \ell_2/2 \}; \quad (1.12)$$

$\theta(x_1, x_2)$ is characteristic function of domain Ω; $\delta_\Gamma = \delta_\Gamma(x_1, x_2)$ is the delta function of boundary $\Gamma = \partial\Omega$; $\overline{n} = [\, n_1 \;\; n_2 \,]^T$ is boundary normal vector; $\overline{F}$ is the load vector in domain Ω; $\bar{f}$ is the corresponding boundary load vector; $\overline{u}$ is the vector of displacements (unknown vector function),

The system of equations (1.1) is supplemented by boundary conditions, which are set in sections with coordinates

$$x_2^1 = -\ell_2/2; \quad x_2^2 = \ell_2/2.$$

The discrete component of the numerical solution is represented by direction along the axe x_1.

2. EXAMPLES OF ANALYSIS

2.1. The first example.

Let us consider the analysis of a deep beam, fixed along the lateral faces in both directions, under the action of an external load concentrated at a point $x_2 = 0$, directed along an axis parallel to x_1 (Figure 1).

Let us consider the following geometrical parameters of structure:

$$\ell_1 = 1\,\text{m}, \quad \ell_2 = 10\,\text{m}.$$

Let us consider the following parameters of the material of the structure:

$$E = 2650 \cdot 10^4 \text{ kN/m2}$$

is the elasticity coefficient;

$$\nu = 0.15$$

is the Poisson's ratio.

Let us consider the following external load

$$P = 100\,\text{kN}.$$

Let's consider the dependence of the results of analysis on the gap length.

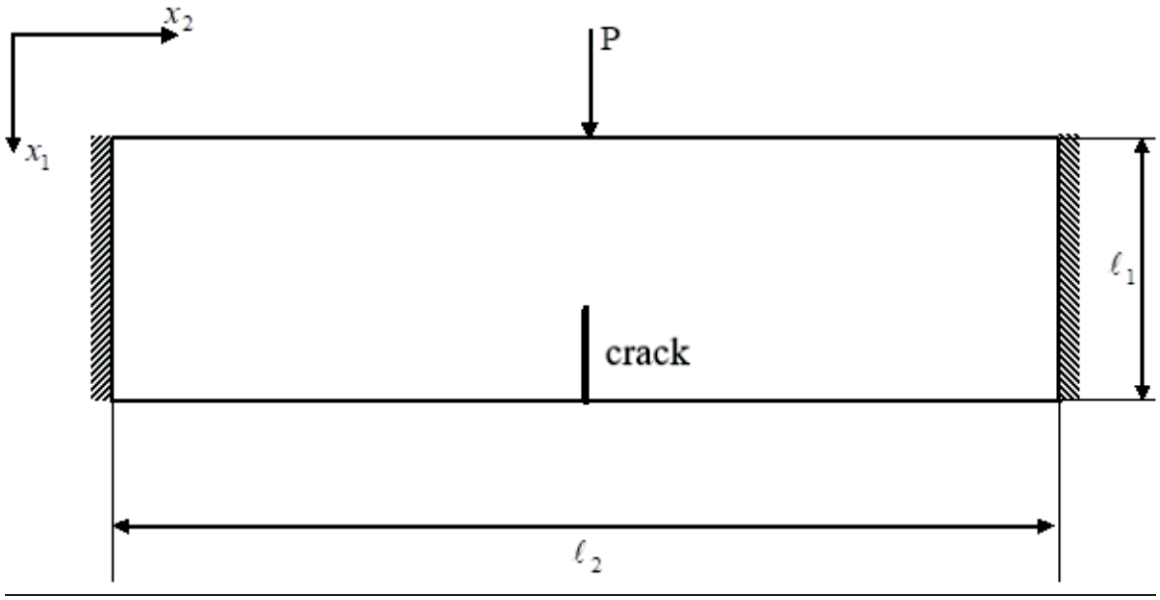


Figure 1. Example of analysis

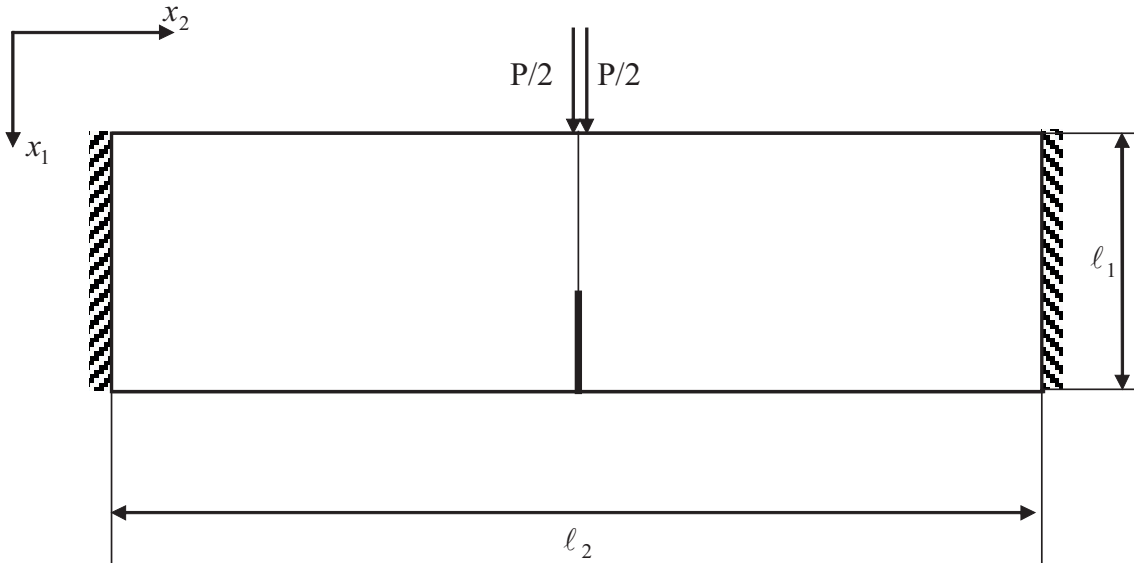


Figure 2. Design model

Let us consider the original problem in the form of a combination of two boundary problems (Figure 2).

The interface passes along the axis of the load action. In this case, the interface boundary equations at the nodes outside the gap line represent the conditions of ideal contact. The equations at the nodes in the gap zone represent the free edge conditions. The load is specified on both sides of the interface at a distance of $2 \cdot 10^{-7}$ m. The discrete component includes $n = 33$ nodes (32 finite elements).

A graphical comparison of the numerical solution at the interface nodes for different values of the gap length dl ($dl = 0$ (no gap), $dl = \ell_1 / 8$, $dl = \ell_1 / 4$, $dl = \ell_1 / 2$). Besides, we consider the case when we have $L1 = \ell_1$ and $L2 = \ell_2$.

As can be seen, as the length of the gap increases, its opening increases (Figure 4), and the expansion stresses in the immediate vicinity of its beginning also increase (Figures 5, 6).

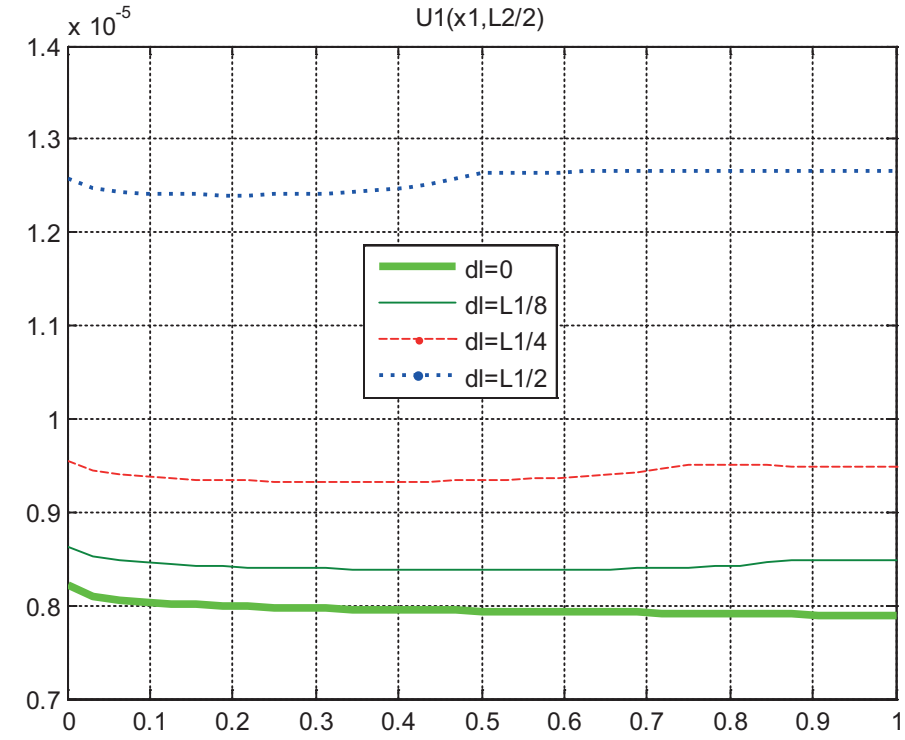


Figure 3. Displacements U1

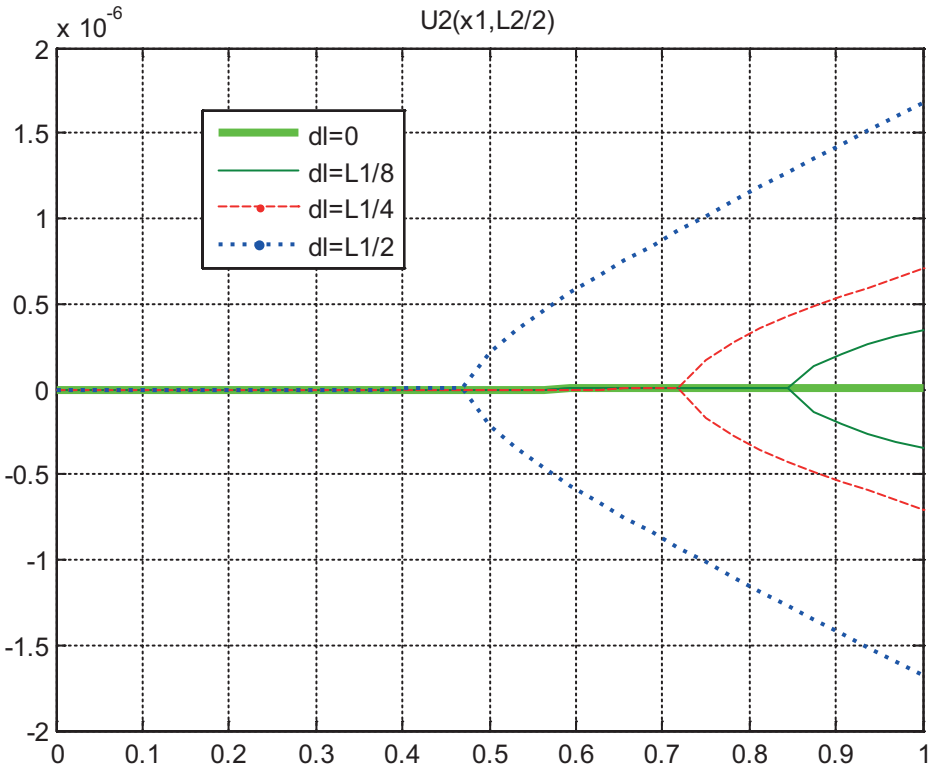


Figure 3. Displacements U2

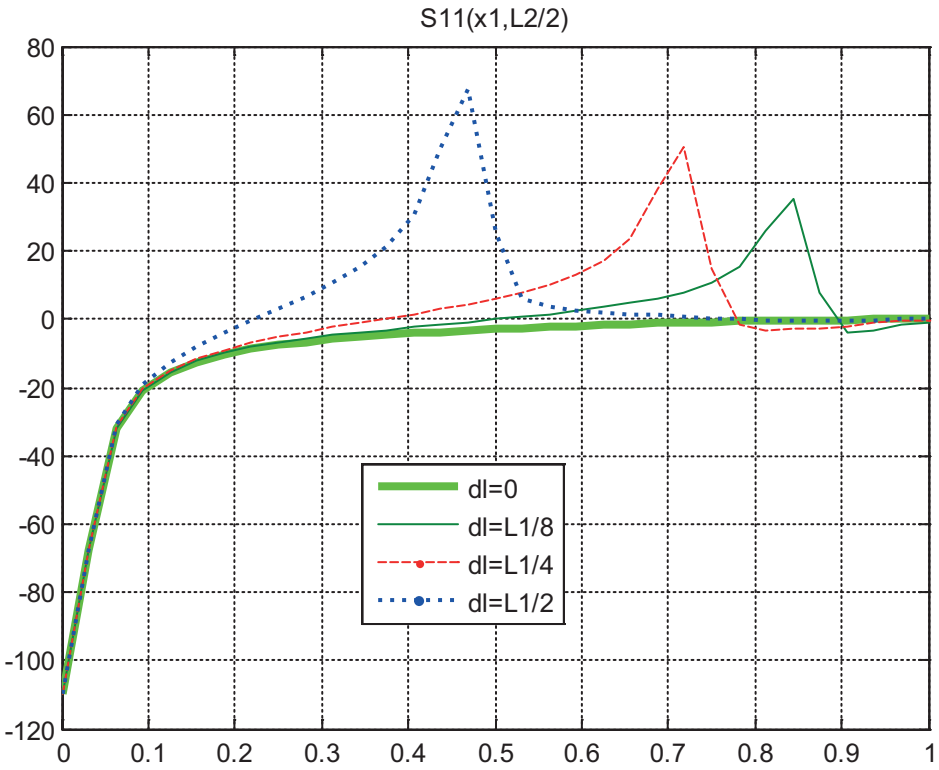


Figure 5. Stresses $\sigma 11$

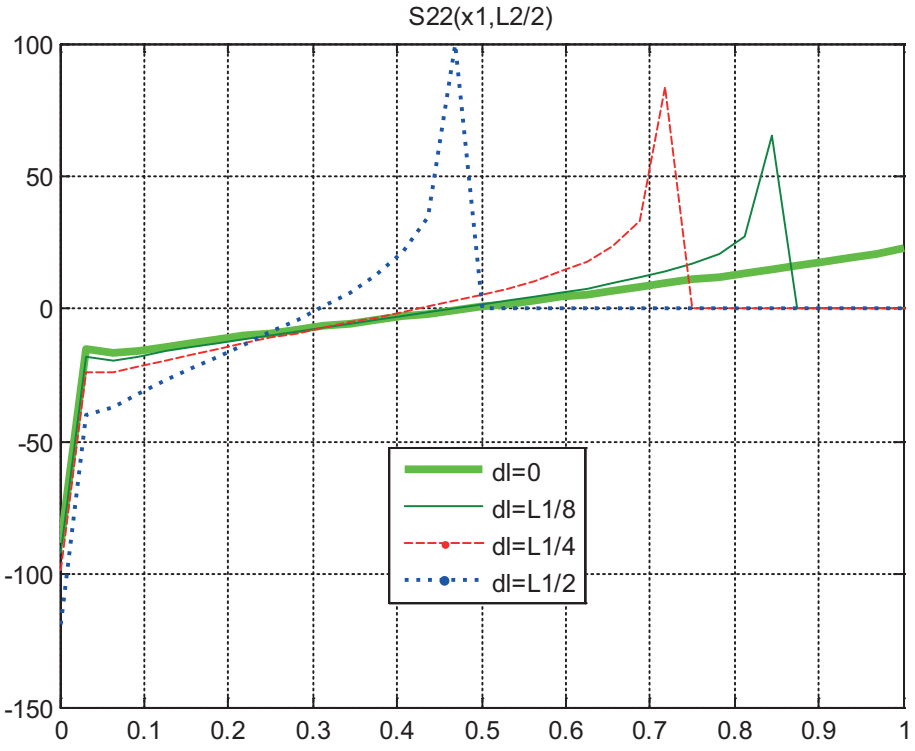


Figure 6. Stresses $\sigma 22$

2.2. The second example.

Let us consider the analysis of a deep beam (Figure 7), fixed along the lateral faces in both directions, under the action of equal external loads concentrated symmetrically relative to the point $x_2 = 0$, directed along the axis parallel to x_1. The loads are concentrated at points with coordinates $(0, x_2 f(1))$ and $(0, x_2 f(2))$ respectively.

Let us consider the following geometrical parameters of structure:

$$\ell_1 = 1\,\text{m}, \quad \ell_2 = 10\,\text{m}.$$

Let us consider $dl = \ell_1 / 2$ is the crack length.

Let us consider the following parameters of the material of the structure:

$$E = 2650 \cdot 10^4 \text{ kN/m2}$$

is the elasticity coefficient;

$$\nu = 0.15$$

is the Poisson's ratio.

Let us consider the following external load

$$P = 100\,\text{kN}.$$

Let us consider the dependence of the results of analysis on the distance between the points of application of loads ($x_2 f(2) - x_2 f(1)$).

Let us consider the initial problem in the form of joining two boundary problems (Figure 8).

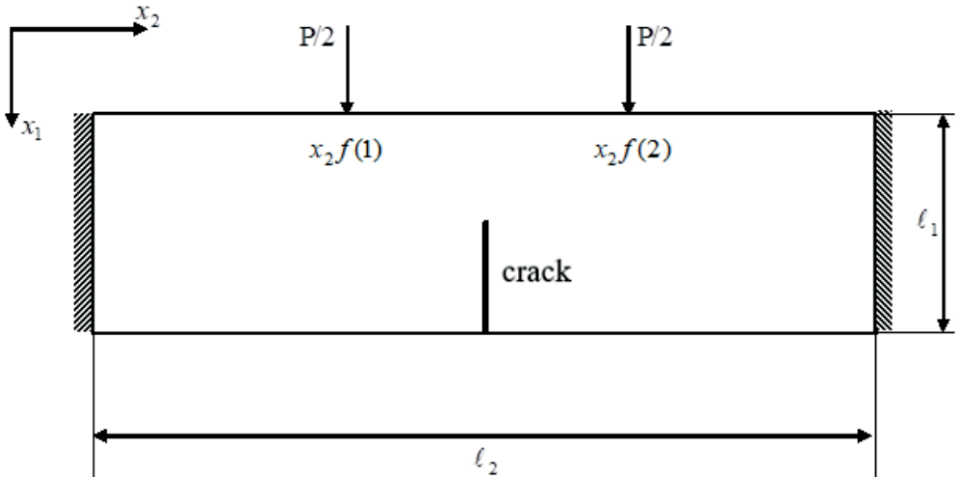


Figure 7. Example of analysis

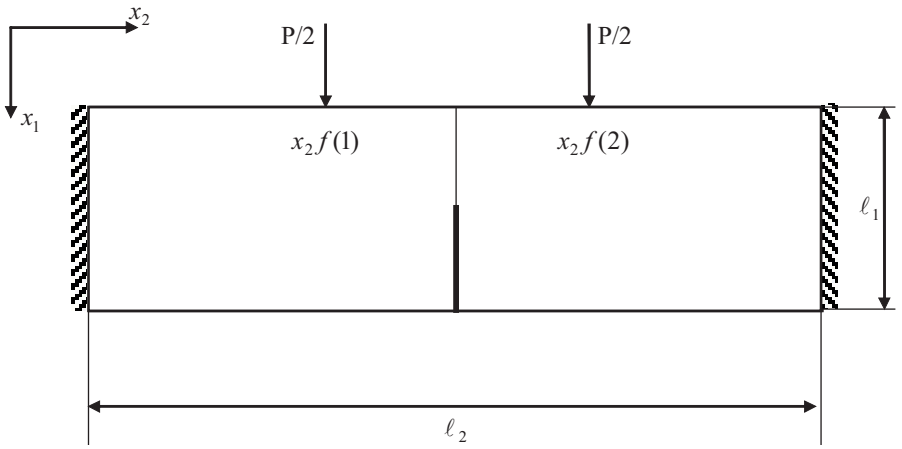


Figure 8. Design model

The joining boundary line passes along the axis $x_2 = 0$ (divides the structure in half). In this case, the joining boundary equations at the nodes outside the gap line represent the conditions of ideal contact. The equations at the nodes that fall within the gap zone represent the free edge conditions. The discrete component includes $n = 33$ nodes (32 finite elements).

A graphical comparison of the numerical solution at the joint nodes for different values of the distance $x_2 f(2) - x_2 f(1)$ between the points of application of loads is presented below.

In this case we have

$$x_2 f = (-3.75, 3.75), \quad x_2 f = (-2.5, 2.5),$$
$$x_2 f = (-1.25, 1.25), \quad x_2 f = (-2 \cdot 10^{-7}, 2 \cdot 10^{-7}).$$

From the graphical comparison it follows that the smaller the distance between the points of application of loads, the greater the gap opening (Figure 10), and the expansion stresses in the immediate vicinity of its beginning also increase (Figures 11, 12).

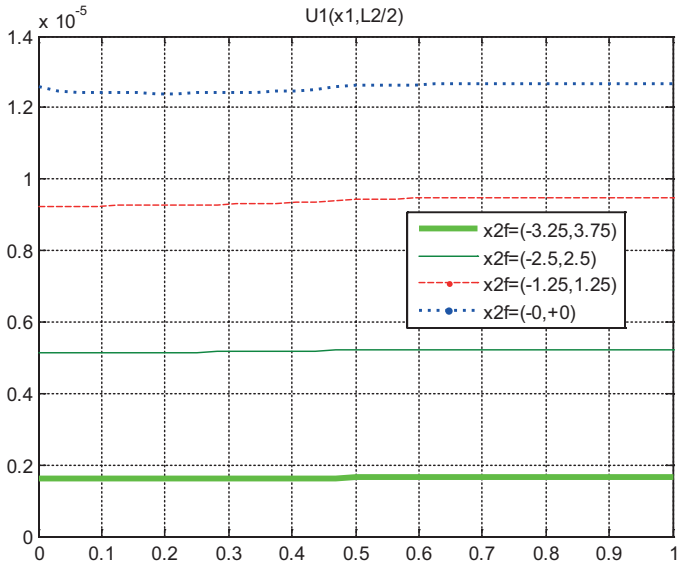


Figure 9. Displacements U1

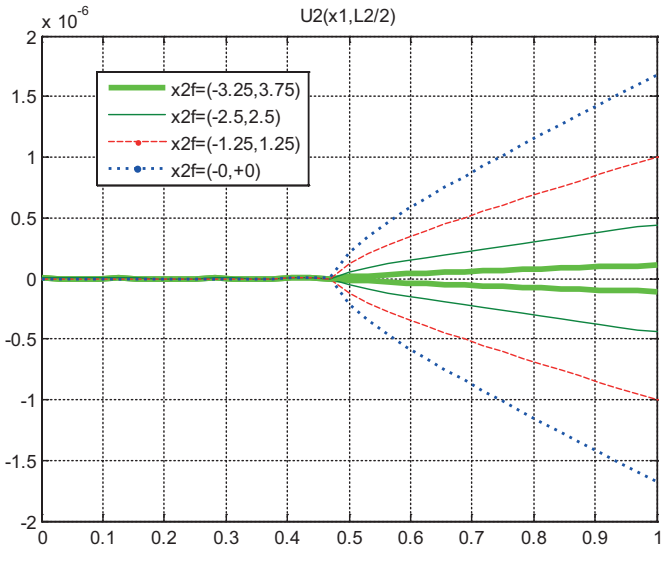


Figure 10. Displacements U2

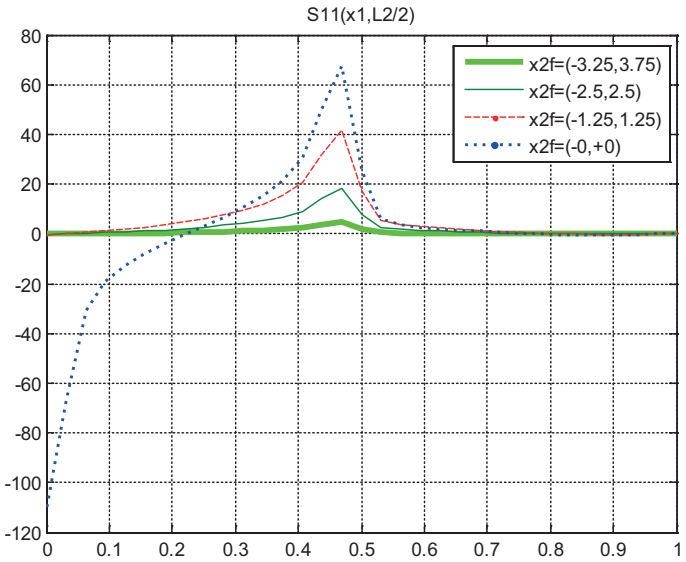


Figure 11. Stresses $\sigma 11$.

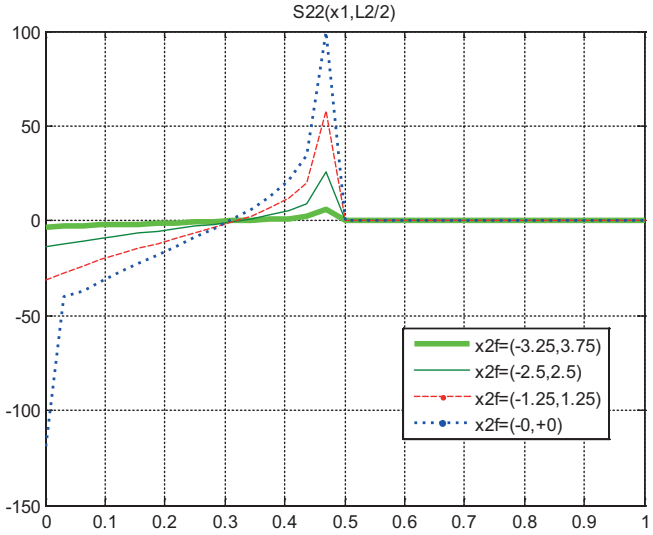


Figure 12. Stresses $\sigma 22$.

CONCLUSION

In the presented examples of analysis, there is a significant excess of the size of the structure along the axis x_2 compared to the size along the axis x_1. In this case, the numerical solution of the problem with the use of discrete-continual finite element method is the most effective, since the traditional finite element method would lead to a significant increase in the nodes of the mesh domain and, consequently, to an increase in the order of the resolving system of equations.

REFERENCES

1. **Akimov P.A.** Correct Direct Discrete-Continual Boundary Element Method of Structural Analysis. // Applied Mechanics and Materials Vols. 395-396 (2013), pp. 529-532.
2. **Akimov P.A., Mozgaleva M.L.** Method of Extended Domain and General Principles of Mesh Approximation for Boundary Problems of Structural Analysis. // Applied Mechanics and Materials, 2014, Vols. 580-583, pp. 2898-2902.

3. **Akimov P.A., Mozgaleva M.L.** Wavelet-based Multilevel Discrete-Continual Finite Element Method for Local Deep Beam Analysis. // Applied Mechanics and Materials Vols. 405-408 (2013), pp. 3165-3168.
4. **Akimov P.A., Mozgaleva M.L., Mojtaba Aslami, Negrozov O.A.** About Verification of Discrete-Continual Finite Element Method of Structural Analysis. Part 1: Two-Dimensional Problems // Procedia Engineering, Vol. 91 (2014), pp. 2-7.
5. **Akimov P.A., Mozgaleva M.L., Mojtaba Aslami, Negrozov O.A.** Wavelet-Based Discrete-Continual Finite Element Method of Local Structural Analysis for Two-Dimensional Problems // Procedia Engineering, Vol. 91 (2014), pp.8-13.
6. **Akimov P.A., Mozgaleva M.L., Negrozov O.A.** About Verification of Discrete-Continual Finite Element Method for Two-Dimensional Problems of Structural Analysis. Part 1: Deep Beam with Constant Physical and Geometrical Parameters Along Basic Direction. // Advanced Materials Research, Vols. 1025-1026 (2014), pp. 89-94.
7. **Akimov P.A., Mozgaleva M.L., Negrozov O.A.** About Verification of Discrete-Continual Finite Element Methodfor Two-Dimensional Problems of Structural Analysis. Part 2: Deep Beam with Piecewise Constant Physical and Geometrical Parameters Along Basic Direction. // Advanced Materials Research, Vols. 1025-1026 (2014), pp. 95-103.
8. **Akimov P.A., Sidorov V.N.** Correct Method of Analytical Solution of Multipoint Boundary Problems of Structural Analysis for Systems of Ordinary Differential Equations with Piecewise Constant Coefficients. // Advanced Materials Research Vols. 250-253, 2011, pp. 3652-3655.
9. **Mozgaleva M.L., Akimov P.A.** Solution of the Problem of Two-Dimensional Theory of Elasticity with the Use of Discrete-Continual Finite Element Method in the Presence of a Crack. // International Journal for Computational Civil and Structural Engineering, 2024, Volume 20, Issue 2, pp. 192-198.
10. **Zienkiewicz O.C., Morgan K.** Finite Elements and Approximation. Dover Publications, 2006, 352 pages.
11. **Zienkiewicz O.C., Taylor R.L., Zhu J.Z.** The Finite Element Method: Its Basis and Fundamentals. Butterworth-Heinemann, Sixth edition, 2005, 752 pages.
12. **Zienkiewicz O.C., Taylor R.L.** The Finite Element Method for Solid and Structural Mechanics. Volume 2. Butterworth-Heinemann, Sixth Edition, 2005, 736 pages.
13. **Zolotov A.B., Akimov P.A.** Semianalytical Finite Element Method for Two-dimensional and Three-dimensional Problems of Structural Analysis. // Proceedings of the International Symposium LSCE 2002 organized by Polish Chapter of IASS, Warsaw, Poland, 2002, pp. 431-440.
14. **Lur'e A.I.** Teorija uprugosti [Theory of Elasticity]. Moscow, Nauka, 1970, 939 pages (in Russian).
15. **Parton V.Z., Perlin P.I.** Metody matematicheskoj teorii uprugosti [Methods of Mathematical Theory of Elasticity]. Moscow, Nauka, 1981, 688 pages (in Russian).

СПИСОК ЛИТЕРАТУРЫ

1. **Akimov P.A.** Correct Direct Discrete-Continual Boundary Element Method of Structural Analysis. // Applied Mechanics and Materials Vols. 395-396 (2013), pp. 529-532.
2. **Akimov P.A., Mozgaleva M.L.** Method of Extended Domain and General Principles of Mesh Approximation for Boundary Problems of Structural Analysis. // Applied Mechanics and Materials, 2014, Vols. 580-583, pp. 2898-2902.
3. **Akimov P.A., Mozgaleva M.L.** Wavelet-based Multilevel Discrete-Continual Finite Element Method for Local Deep Beam Analysis. // Applied Mechanics and Materials Vols. 405-408 (2013), pp. 3165-3168.
4. **Akimov P.A., Mozgaleva M.L., Mojtaba Aslami, Negrozov O.A.** About Verification of Discrete-Continual Finite Element

Method of Structural Analysis. Part 1: Two-Dimensional Problems // Procedia Engineering, Vol. 91 (2014), pp. 2-7.
5. **Akimov P.A., Mozgaleva M.L., Mojtaba Aslami, Negrozov O.A.** Wavelet-Based Discrete-Continual Finite Element Method of Local Structural Analysis for Two-Dimensional Problems // Procedia Engineering, Vol. 91 (2014), pp.8-13.
6. **Akimov P.A., Mozgaleva M.L., Negrozov O.A.** About Verification of Discrete-Continual Finite Element Method for Two-Dimensional Problems of Structural Analysis. Part 1: Deep Beam with Constant Physical and Geometrical Parameters Along Basic Direction. // Advanced Materials Research, Vols. 1025-1026 (2014), pp. 89-94.
7. **Akimov P.A., Mozgaleva M.L., Negrozov O.A.** About Verification of Discrete-Continual Finite Element Methodfor Two-Dimensional Problems of Structural Analysis. Part 2: Deep Beam with Piecewise Constant Physical and Geometrical Parameters Along Basic Direction. // Advanced Materials Research, Vols. 1025-1026 (2014), pp. 95-103.
8. **Akimov P.A., Sidorov V.N.** Correct Method of Analytical Solution of Multipoint Boundary Problems of Structural Analysis for Systems of Ordinary Differential Equations with Piecewise Constant Coefficients. // Advanced Materials Research Vols. 250-253, 2011, pp. 3652-3655.
9. **Mozgaleva M.L., Akimov P.A.** Solution of the Problem of Two-Dimensional Theory of Elasticity with the Use of Discrete-Continual Finite Element Method in the Presence of a Crack. // International Journal for Computational Civil and Structural Engineering, 2024, Volume 20, Issue 2, pp. 192-198.
10. **Zienkiewicz O.C., Morgan K.** Finite Elements and Approximation. Dover Publications, 2006, 352 pages.
11. **Zienkiewicz O.C., Taylor R.L., Zhu J.Z.** The Finite Element Method: Its Basis and Fundamentals. Butterworth-Heinemann, Sixth edition, 2005, 752 pages.
12. **Zienkiewicz O.C., Taylor R.L.** The Finite Element Method for Solid and Structural Mechanics. Volume 2. Butterworth-Heinemann, Sixth Edition, 2005, 736 pages.
13. **Zolotov A.B., Akimov P.A.** Semianalytical Finite Element Method for Two-dimensional and Three-dimensional Problems of Structural Analysis. // Proceedings of the International Symposium LSCE 2002 organized by Polish Chapter of IASS, Warsaw, Poland, 2002, pp. 431-440.
14. **Лурье А.И.** Теория упругости. – М.: Наука, 1970. – 939 с.
15. **Партон В.З., Перлин П.И.** Методы математической теории упругости. – М.: Наука, 1981. – 688 с.

Marina L. Mozgaleva, Senior Scientist Researcher, Dr.Sc.; Professor of Department of Applied Mathematics, National Research Moscow State University of Civil Engineering; 26, Yaroslavskoe Shosse, Moscow, 129337, Russia; Email: marina.mozgaleva@gmail.com.

Pavel A. Akimov, Full Member of the Russian Academy of Architecture and Construction Sciences, Professor, Dr.Sc.; Rector of National Research Moscow State University of Civil Engineering; 26, Yaroslavskoe Shosse, Moscow, 129337, Russia; E-mail: AkimovPA@mgsu.ru, rector@mgsu.ru, pavel.akimov@gmail.com.

Мозгалева Марина Леонидовна, старший научный сотрудник, доктор технических наук; профессор кафедры прикладной математики Национального исследовательского Московского государственного строительного университета; 129337, Россия, г. Москва, Ярославское шоссе, дом 26; E-mail: marina.mozgaleva@gmail.com.

Акимов Павел Алексеевич, академик РААСН, профессор, доктор технических наук; ректор Национального исследовательского Московского государственного строительного университета; 129337, Россия, г. Москва, Ярославское шоссе, дом 26; E-mail: AkimovPA@mgsu.ru, rector@mgsu.ru, pavel.akimov@gmail.com.

International Journal for Computational Civil and Structural Engineering, 21(2) 187–199 (2025)

DOI:10.22337/2587-9618-2025-21-2-187-199

NUMERICAL MODELING OF CAST-IN-PLACE REINFORCED CONCRETE BUBBLE DECK FLOOR SLABS UTILIZED IN EARTHQUAKE-PRONE REGIONS

Alexander M. Belostotsky [1,2]***, Alexander I. Nagibovich*** [1,2]***, Sergey V. Scherbina*** [1,2]***, Tatiana N. Vasileva*** [1,2]

[1] National Research Moscow State University of Civil Engineering, Moscow, RUSSIA
[2] Research & Development Centre StaDyO, Moscow, RUSSIA

Abstract: This article presents developed techniques for numerical modelling of lightweight cast-in-place reinforced concrete bubbledeck floor slabs and a comparative analysis of different approaches to numerical modelling of buildings and structures with such lightweight floors, that are constructed in earthquake-prone regions.

Keywords: finite element method, modal analysis, earthquake excitation, mechanical safety, void formers, lightweight cast-in-place reinforced concrete floor slabs

ЧИСЛЕННОЕ МОДЕЛИРОВАНИЕ МОНОЛИТНЫХ ЖЕЛЕЗОБЕТОННЫХ ПЕРЕКРЫТИЙ С ПУСТОТООБРАЗОВАТЕЛЯМИ, ПРИМЕНЯЕМЫХ В СЕЙСМИЧЕСКИ АКТИВНЫХ РАЙОНАХ

А.М. Белостоцкий [1,2]***, А.И. Нагибович*** [1,2]***, С.В. Щербина*** [1,2]***, Т.Н. Васильева*** [1,2]

[1] Национальный исследовательский Московский государственный строительный университет, г. Москва, РОССИЯ
[2] АО «Научно-исследовательский центр СтаДиО», г. Москва, РОССИЯ

Аннотация: В настоящей статье представлены разработанные авторами методики численного моделирования облегченных монолитных железобетонных перекрытий с пустотообразователями и сравнительный анализ различных подходов численного моделирования для зданий и сооружений, строящихся в сейсмически активных районах и имеющих в своём составе подобные облегчённые плиты перекрытий.

Ключевые слова: метод конечных элементов, модальный анализ, сейсмическое воздействие, механическая безопасность, пустотообразователи, облегченные монолитные железобетонные перекрытия

1. INTRODUCTION

Nowadays, a significant part of building constructions is made of cast-in-place reinforced concrete. Concrete high density and, hence, large dead weight of structural components made of it is a significant disadvantage. It leads to higher loads, in particular seismic ones, on vertical structural elements and foundations, increased construction costs and time. Therefore, different ways to decrease dead weight are employed when designing buildings and structures, particularly in earthquake-prone regions.

Utilization of void formers (see Fig. 1) is one of the ways to decrease the dead weight of concrete structures. The void formers to use in reinforced concrete floor slabs may be extractable and unextractable, may be made of different materials and have various shapes, as it is stated in [1]. For some types of void formers, there are proprietary standards [12] [13] and recommendations for calculation of a stress-strain state of voided floor slabs exposed to special combinations of loads [14].

There exists a large amount of researches on a bubbledeck floor slabs response to various exci-

tations (see [2-11]). According to these studies, usage of bubbledeck floor slabs has a small impact onto structural strength, but at the same time reduces structural stiffness, that, evidently, affects an eigenfrequency spectrum of the considered building or structure.

When designing a building or a structure constructed in an earthquake-prone region, a response spectrum analysis is commonly performed with a large number of eigenmodes taken into account. Hence, utilization of a bubbledeck floor slab solution should be explicitly taken into account during the design procedure, in particular when calculating the design stress-strain state.

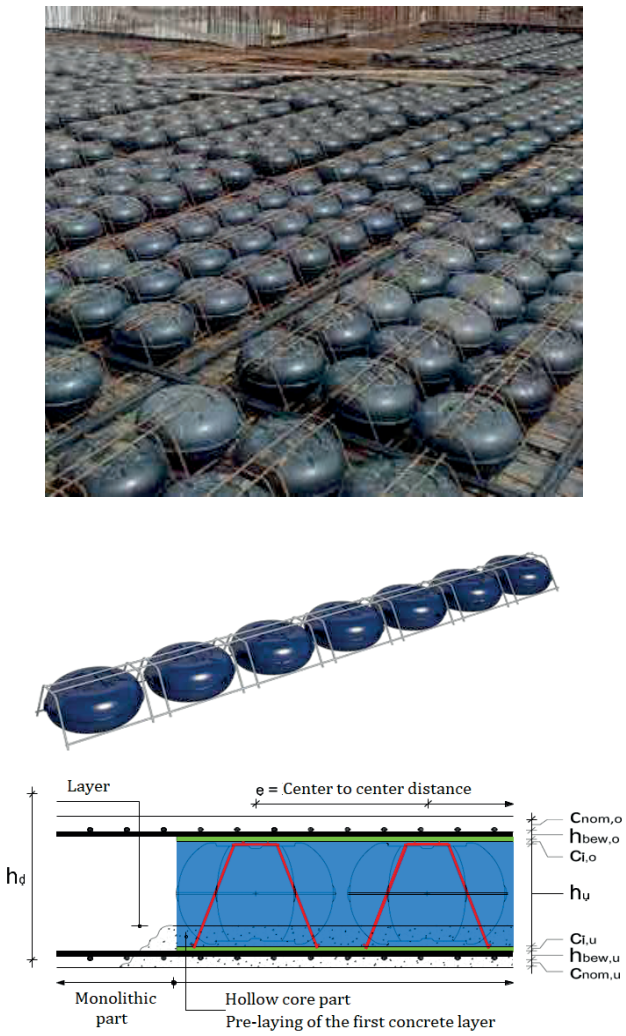


Figure 1. An example of void formers used in reinforced concrete floor slabs, and their geometrical parameters

The finite element method (FEM) is widely used to perform such an analysis. The most accurate way to compute eigenfrequencies, eigenmodes and a stress-strain state of structural elements with a complex shape of the cross-section (for instance, a hollow core structure) is to use solid finite elements for spatial discretization of the problem. Yet, such a technique is computationally ineffective and, thus, used in practice very rarely. A common practice is to use structural finite elements, shell and beam ones, to spatially discretize a structural mechanics problem.

In the present paper considered are different approaches to numerical modelling of lightweight cast-in-place reinforced concrete bubbledeck floor slabs with an aim to correctly simulate floor slab stress-strain state, elastic stiffness and eigenfrequency spectrum, that allows one to utilize such an approach in design practice.

2. PROBLEM FORMULATION

To evaluate an accuracy of different approaches to numerical modelling of lightweight cast-in-place reinforced concrete bubbledeck floor slabs, a single floor cell of a reinforced concrete frame building has been considered (see Fig. 2).

The chosen part of the floor slab has dimensions of 5.6×5.6 meters and comprises 16 void former cells in each direction. The floor slab has the following values of its geometrical parameters: the floor slab thickness h_d = 250mm; the void former height h_u = 140mm; the concrete cover at the upper slab face $c_{nom,o}$ = 20mm; the concrete cover at the lower slab face $c_{nom,u}$ = 20mm; the distance between bubbles centers e = 350mm; the void former diameter d = 315mm. A cross-section of the single void former cell is shown in Fig. 3.

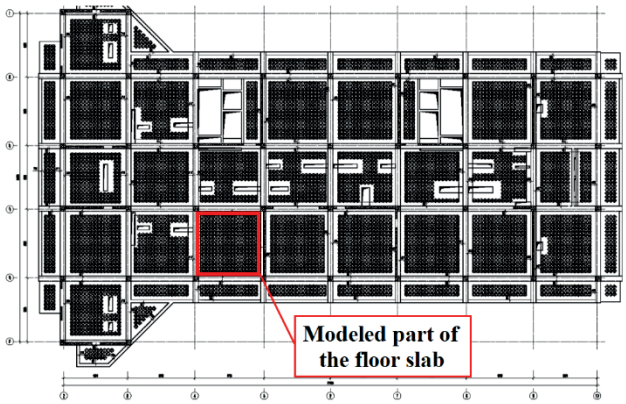


Figure 2. The drawing of a bubbledeck floor slab in the reinforced concrete frame building (a part of the slab chosen for a comparative analysis of various numerical modelling techniques is outlined in red)

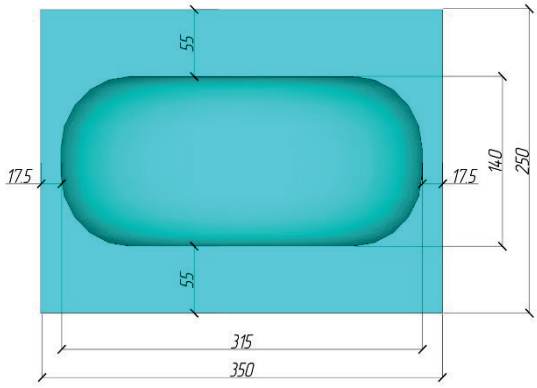


Figure 3. The cross-section of a void former cell used in the considered bubbledeck floor slab

Properties of the considered bubbledeck floor slab material are given in Table 1.

Table 1. Bubbledeck floor slab material properties

Material	Elastic Modulus E, GPa	Poisson's ratio ν	Density ρ, kg/m^3
Concrete B25	30	0.2	2500

The following engineering approaches to numerical modelling of such lightweight structural elements have been considered and compared with the reference and between each other: 1) the void former cell has been considered as a honeycomb structure with top and bottom cover plates which have been all discretized through shell finite elements with effective thickness, density and stiffness; 2) the void former cell has been considered as a homogeneous plate with effective properties, which has been discretized through shell finite elements.

Problem spatial discretization through solid finite elements and the simulation results obtained using such an approach have been taken as a reference. Since only elastic part of the problem has been considered, utilization of the numerical solution as a reference is appropriate, since high accuracy of finite element simulations within the theory of elasticity has been verified multiple times (see, for instance, [1]).

3. FINITE ELEMENT MODELS

The verified ANSYS software [1] has been used for all simulations (a static loading analysis and a modal analysis). In the model assembled for the reference simulations, hexahedral eight node finite elements of the type SOLID185 have been used. In the models, which have been intended to evaluate two different engineering approaches to numerical modelling of bubbledeck floor slabs, quadrilateral four node finite elements of the type SHELL181, in which the Reissner-Mindlin plate theory is implemented, have been utilized.

The whole FE model utilized for the reference simulations and the mesh within the void former cell are illustrated in Fig. 4. The whole model comprises 1 039 247 nodes (three degrees of freedom (DOF) per each node) and 1 056 768 finite elements.

The FE model used to evaluate the first engineering approach to numerical modelling of the bubbledeck floor slab consists of two horizontal layers of plane finite elements connected together through the honeycomb structure also meshed with plane finite elements. A comparison of the void former cell and its approximation through plane structural elements is given in Fig. 5. The whole model and the mesh within the void former cell are illustrated in Fig. 6. The FE model comprises 3 011 nodes (six DOF per each node) and 4 224 finite elements.

The FE model used to evaluate the second engineering approach to numerical modelling of the bubbledeck floor slab is shown in Fig. 7. The model comprises 289 nodes (six DOF per each node) and 256 finite elements. All DOFs (Ux, Uy, Uz, Rotx, Roty, Rotz) of the nodes located at the slab boundaries are restrained. The existence of voids in the floor slab have been simulated through setting effective values of the material density and elastic modulus.

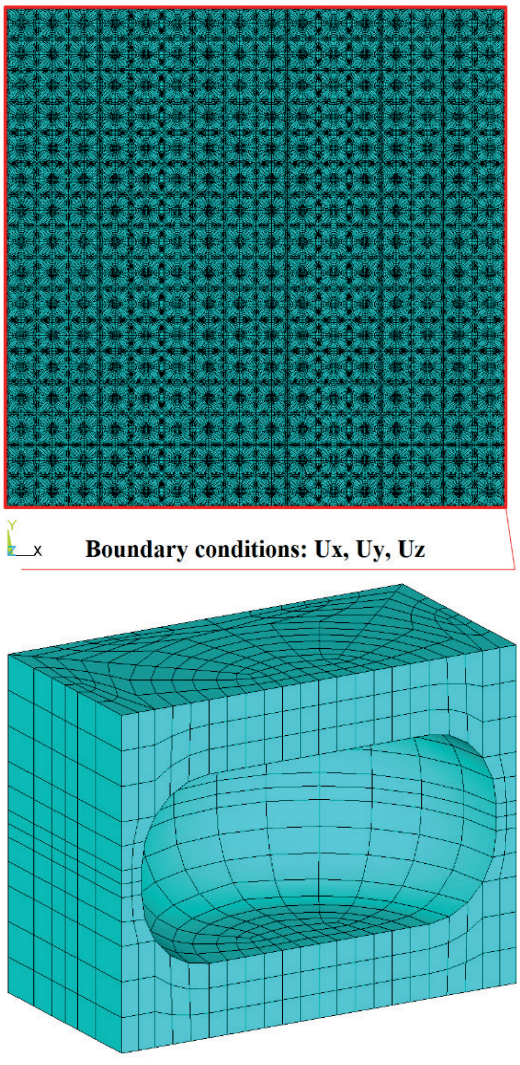


Figure 4. The model of the considered cast-in-place reinforced concrete bubbledeck floor slab meshed with hexahedral finite elements: (a) top view with boundary conditions; (b) mesh within the void former cell

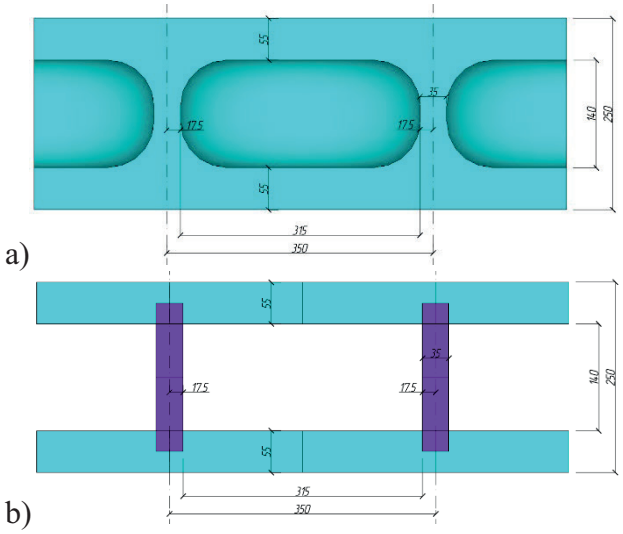


Figure 5. Interrelation between the actual geometry of the bubbledeck floor slab (a) and its approximation through plane structural elements (b) (In the bottom figure different colours correspond to parts with different thicknesses)

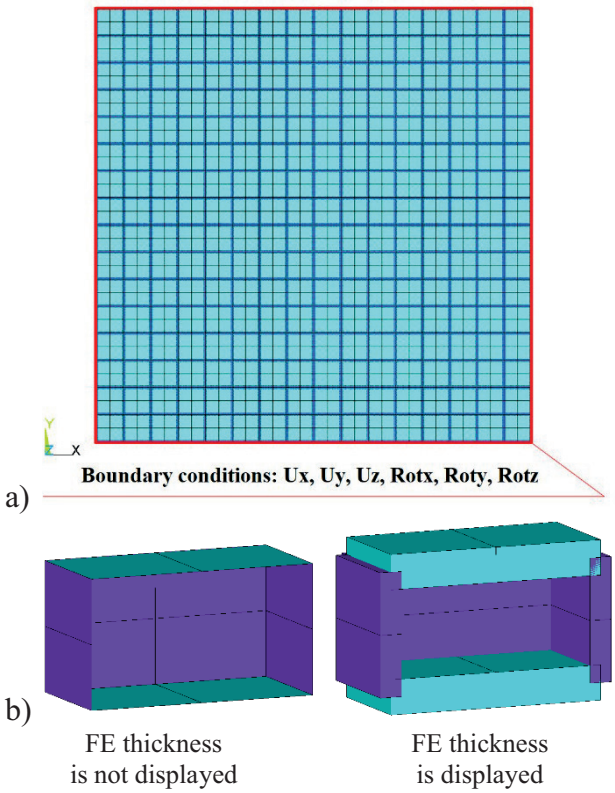


Figure 6. The FE model used to evaluate the first engineering approach to numerical modelling of the bubbledeck floor slab: (a) top view with boundary conditions; (b) mesh within the void former cell

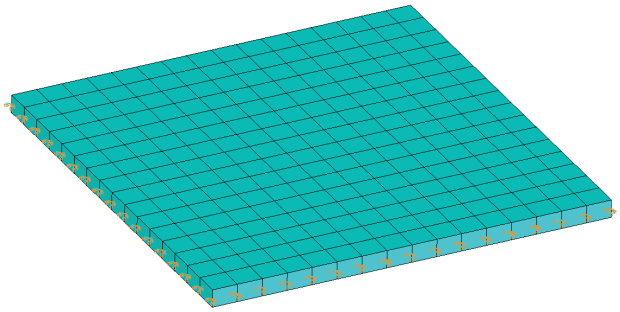
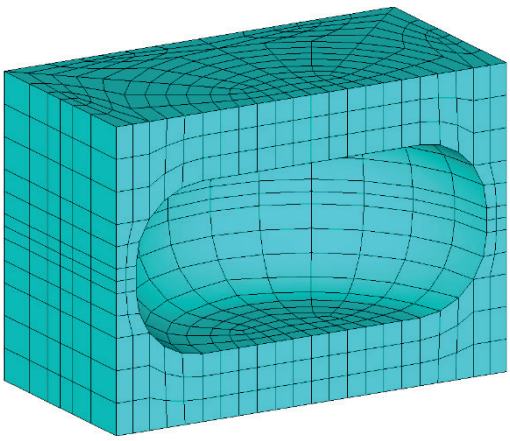


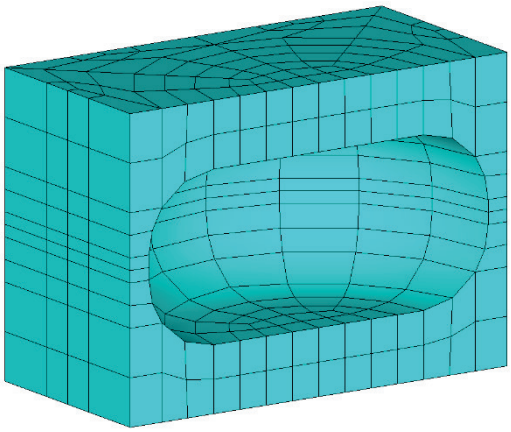
Figure 7. The FE model used to evaluate the second engineering approach to numerical modelling of the bubbledeck floor slab with finite element thickness and boundary conditions displayed

4. MESH SENSITIVITY ANALYSIS

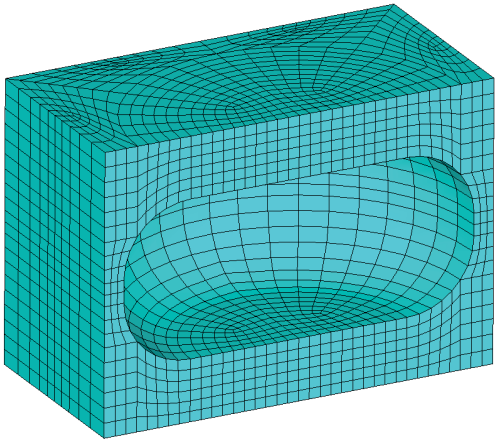
Before conducting simulations with shell finite elements, a mesh sensitivity analysis for the model discretized with solid finite elements had been performed. Three different element sizes had been used to calculate eigenfrequencies and eigenmodes of the considered slab (see Fig. 8). Results of the conducted modal analysis are given in Table 2. As it is seen from Table 2, there is negligible difference between the results obtained using different mesh sizes.



a)



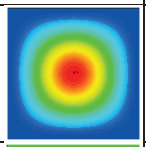
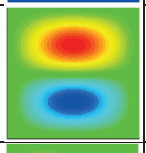
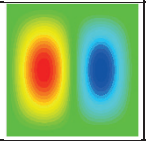
b)

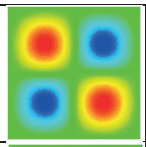
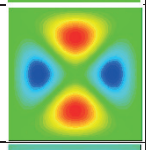
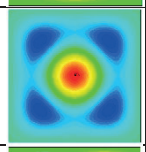
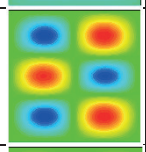
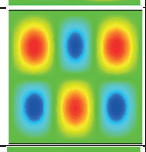
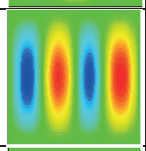
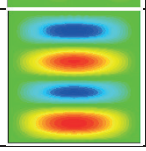


c)

Figure 8. Meshes considered during the mesh sensitivity analysis: (a) reference mesh; (b) coarse mesh (twice as large); (c) fine mesh (1.5 times smaller)

Table 2. Eigenfrequencies and eigenmodes calculated using the reference FE model with different mesh sizes

#	Eigenmode	Reference mesh	Coarse mesh	Fine mesh	Δ, %
		Eigenfrequency, Hz			
1		50.04	50.05	50.03	0.0
2		98.25	98.42	98.2	0.2
3		98.25	98.42	98.2	0.2

4		140.22	140.61	140.05	0.3
5		167.67	168.25	167.53	0.3
6		169.03	169.60	168.89	0.3
7		204.93	205.80	204.61	0.4
8		204.93	205.80	204.61	0.4
9		254.44	255.78	254.08	0.5
10		254.44	255.78	254.09	0.5

5. PARAMETRIC ANALYSIS OF THE ENGINEERING APPROACHES

A parametric analysis of the FE models used to evaluate two engineering approaches to numerical modelling of bubbledeck floor slabs has been performed to determine, which parameters of the problem have a significant influence onto the static and dynamic response of the considered slab and what effective values they should be set to have the static and dynamic response equivalent to that of the reference FE model discretized through solid finite elements.

Three different sets of parameters to variate (denoted as 1A, 1B, and 1C, respectively) have been considered for the first engineering FE model, and one set of parameters to variate (denoted as 2A) has been considered for the second engineering FE model.

The parameters set 1A (see Table 3). The reference density value (see Table 1) of both the horizontal plates and vertical ribs of the first engineering FE model has been increased by a factor of k_ρ = 1.1484 (up to 2871.1 kg/m^3) to equalize the mass of the whole model to that of the reference FE model (which equals 13 634 kg). Then, the elastic modulus of plane vertical elements, which model vertical ribs of the bubbledeck floor slab, have been iteratively changed to the final value of 87 GPa to match the results of the modal analysis obtained with the reference FE model.

Table 3. The parameters set 1A

#	Element	E, GPa	ν	ρ, kg/m^3	t, mm
1	Horizontal plate of the floor slab	30	0.2	2871.1	55
2	Vertical rib of the floor slab	87	0.2	2871.1	35

Note: parameters different from the reference ones are colored in blue

The parameters set 1B (see Table 4). To equalize the mass of the whole engineering model to that of the reference one, the thickness t of the vertical ribs has been increased by a factor of k_t = 1.5421 (up to 54 mm) with the values of all other parameters being kept equal to the reference ones.

Table 4. The parameters set 1B

#	Element	E, GPa	ν	ρ, kg/m^3	t, mm
1	Horizontal plate of the floor slab	30	0.2	2500	55
2	Vertical rib of the floor slab	30	0.2	2500	54

Note: parameters different from the reference ones are colored in blue

The parameters set 1C (see Table 5). To equalize the mass of the whole engineering model to that of the reference one, the thickness t of both the horizontal plates and vertical ribs has been increased by a factor of k_t = 1.1483 (up to 63.2 and 40.2 mm, respectively) with the values of all other parameters being kept equal to the reference ones.

Table 5. The parameters set 1C

#	Element	E, GPa	ν	ρ, kg/m^3	t, mm
1	Horizontal plate of the floor slab	30	0.2	2500	63.2
2	Vertical rib of the floor slab	30	0.2	2500	40.2

Note: parameters different from the reference ones are colored in blue

The parameters set 2A (see Table 6). The reference density value (see Table 1) of the second engineering FE model has been decreased by a factor of k_ρ = 1.4376 (down to 1739.1 kg/m^3) to equalize the mass of the whole model to that of the reference FE model (which equals 13 634 kg). Then, the elastic modulus of the slab has been iteratively changed to the final value of 24 GPa to match the results of the modal analysis obtained with the reference FE model.

Table 6. The parameters set 2A

#	Element	E, GPa	ν	ρ, kg/m^3	t, mm
1	Floor slab	24	0.2	1739.1	250

Note: parameters different from the reference ones are colored in blue

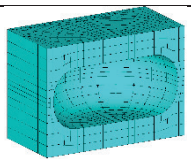
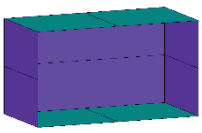
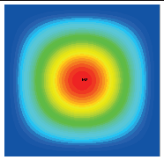
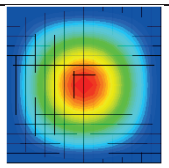
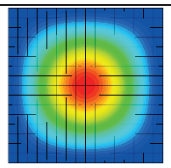
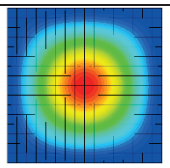
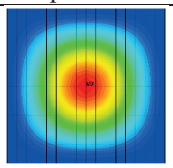
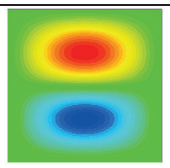
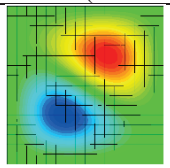
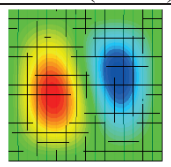
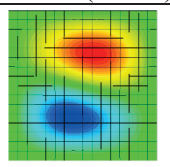
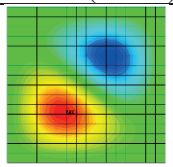
6. SIMULATION RESULTS AND THEIR COMPARISON

Below in Tables 7-9 and Fig. 9, the simulations results obtained using different FE models are presented and compared with each other.

The results of the modal analysis presented in Table 7 reveal that the best agreement with the reference FE model, in which the spatial discretization of the voided floor slab has been carried out through solid finite elements, has been obtained for the model created within the (first) engineering approach, in which the void former cell has been considered as a honeycomb structure with top and bottom cover plates which have been all discretized through shell finite elements with the values of their parameters given in Table 3.

The results of the static loading of the slab by its dead weight given in Tables 8, 9 and Fig. 9 also show that the FE model created within the first engineering approach with the values of the parameters given in Table 3 yields the closest agreement (both for normal stress and displacements) with the results obtained for the reference FE model constructed using solid finite elements.

Table 7. Results of the modal analysis (In brackets given are the discrepancy, in percent, from the results obtained with the reference finite element model)

#	 Reference finite element model	 Finite element model for the 1st engineering approach			 Finite element model for the 2nd engineering approach
		Parameters set 1A	Parameters set 1B	Parameters set 1C	
1	 50.0 Hz	 50.2 Hz (+0.4 %)	 47.9 Hz (-4.4 %)	 49.2 Hz (-1.8 %)	 49.4 Hz (-1.3 %)
2	 98.3 Hz	 98.3 Hz (+0.1 %)	 92.0 Hz (-6.3 %)	 92.9 Hz (-5.5 %)	 100.7 Hz (+2.5 %)

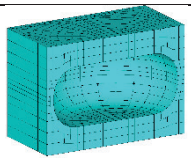
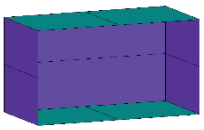
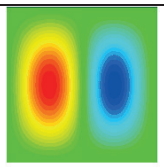
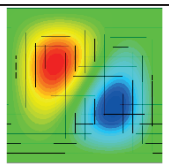
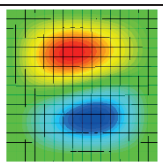
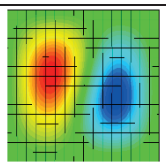
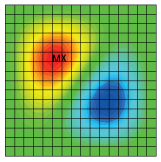
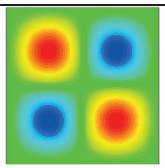
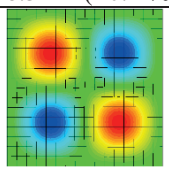
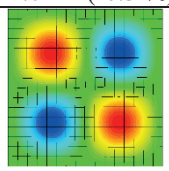
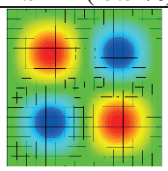
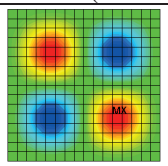
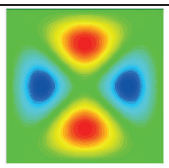
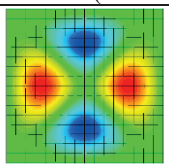
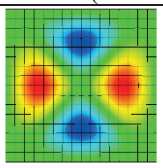
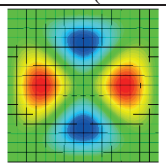
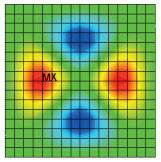
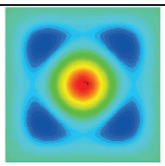
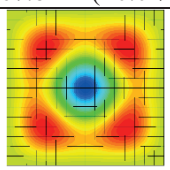
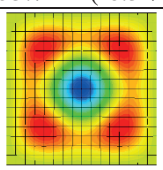
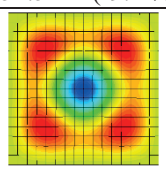
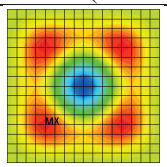
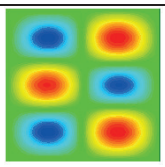
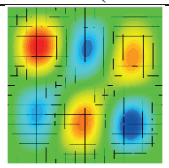
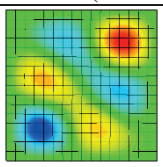
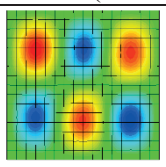
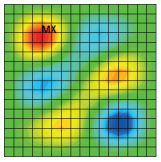
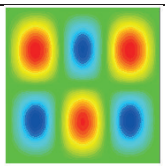
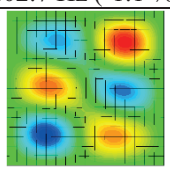
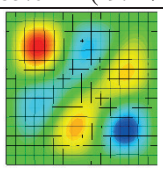
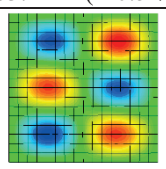
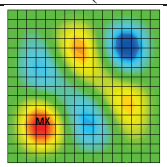
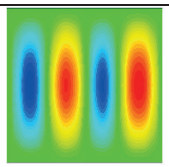
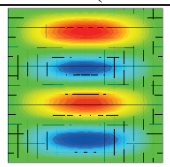
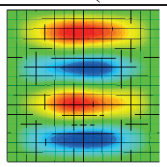
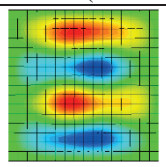
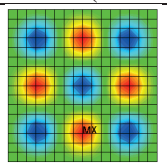
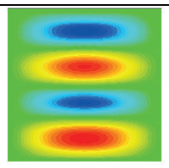
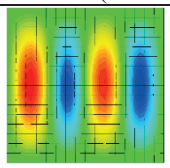
#	 Reference finite element model	 Finite element model for the 1st engineering approach			 Finite element model for the 2nd engineering approach
		Parameters set 1A	Parameters set 1B	Parameters set 1C	
3	 98.3 Hz	 98.3 Hz (+0.1 %)	 92.0 Hz (-6.3 %)	 92.9 Hz (-5.5 %)	 100.7 Hz (+2.5 %)
4	 140.2 Hz	 139.0 Hz (-0.9 %)	 129.2 Hz (-7.9 %)	 129.2 Hz (-7.8 %)	 146.3 Hz (+4.3 %)
5	 167.7 Hz	 167.8 Hz (+0.0 %)	 153.7 Hz (-8.3 %)	 152.5 Hz (-9.1 %)	 181.7 Hz (+8.4 %)
6	 169.0 Hz	 169.0 Hz (0.0 %)	 155.0 Hz (-8.3 %)	 153.8 Hz (-9.0 %)	 182.8 Hz (+8.1 %)
7	 204.9 Hz	 202.7 Hz (-1.1 %)	 185.6 Hz (-9.4 %)	 183.4 Hz (-10.5 %)	 222.6 Hz (+8.6 %)
8	 204.9 Hz	 202.7 Hz (-1.1 %)	 185.6 Hz (-9.4 %)	 183.4 Hz (-10.5 %)	 222.6 Hz (+8.6 %)
9	 254.4 Hz	 254.4 Hz (0.0 %)	 228.9 Hz (-10.1 %)	 223.8 Hz (-12.0 %)	 292.0 Hz (+14.8 %)
10	 254.4 Hz	 254.4 Hz (0.0 %)	228.9 Hz (-10.1 %)	223.8 Hz (-12.0 %)	293.7 Hz (+15.4 %)

Table 8. Comparison of the vertical displacements due to the slab dead weight

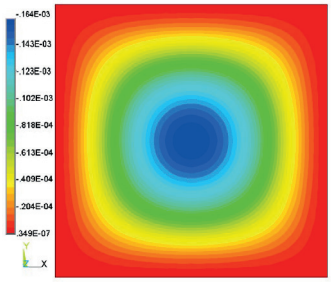
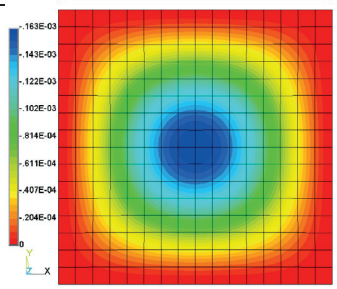
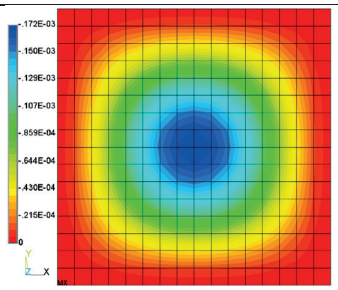
Reference finite element model		Uz_{max} = -0.164 mm
Finite element model for the 1st engineering approach (parameters set 1A)		Uz_{max} = -0.163 mm (-0.6%)
Finite element model for the 2nd engineering approach		Uz_{max} = -0.172 mm (+4.9%)

Table 9. Comparison of the normal stress along X-axis at the top face of the slab in the central cross-section due to the slab dead weight

FE model	Min σ_x, Pa	Δ, %	Max σ_x, Pa	Δ, %
Reference finite element model	-325163	-	904902.1	-
Finite element model for the 1st engineering approach (parameters set 1A)	-306776	-5.7	702694.7	-22.3
Finite element model for the 2nd engineering approach	-275379	-15.3	509014.4	-43.7

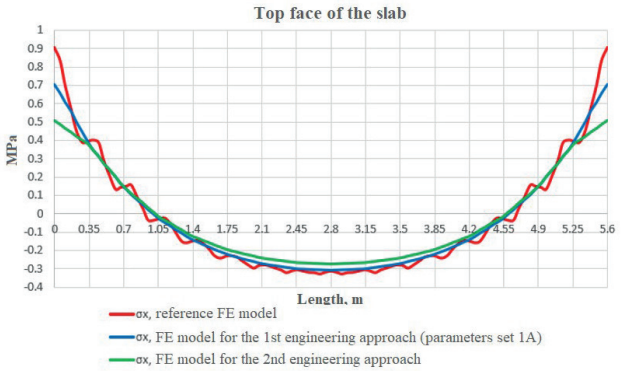


Figure 9. Normal stress along X-axis at the top face of the slab in the central cross-section due to the slab dead weight

CONCLUSION

The following conclusions can be made based on the analysis results and their comparison:

1. As expected, mesh sensitivity of the results obtained for the model meshed with solid finite elements is negligible within the problems of the theory of elasticity, in particular for the modal analysis.
2. The engineering approach to numerical modelling of reinforced concrete bubbledeck floor slabs, within which the void former cell of the slab is modelled as a honeycomb structure with top and bottom cover plates, which are all discretized through shell finite elements with effective density (which has been increased by a factor of 1.1484 relative to the reference one) and stiffness (which has been increased by a factor of 2.9 relative to the reference one for the vertical ribs of the slab), has revealed the best agreement with the results obtained for the slab model meshed with solid finite elements, both for the modal analysis and the static loading analysis. For the first 10 eigenmodes the largest difference in eigenfrequency has been obtained to be 1.1%. The difference in static deflection due to the slab dead weight has been obtained to be 0.6%. The difference in normal stresses at the top face of the slab in the central cross-section has been obtained to be less than 23%.

3. The engineering approach to numerical modelling of reinforced concrete bubbledeck floor slabs, within which the void former cell of the slab is modelled as a homogeneous plate with effective properties, has yielded larger discrepancy with the reference results. For the first 10 eigenmodes the largest difference in eigenfrequency has been obtained to be 15.4%. The difference in static deflection due to the slab dead weight has been obtained to be 4.9%. The difference in normal stresses at the top face of the slab in the central cross-section has been obtained to be less than 44%.

Further research on the subject should be devoted to numerical modelling of bubbledeck floor slabs together with vertical load-bearing structural elements.

REFERENCES

1. **Dzhamuev B.K.** The effect of non-removable void generators on the strength of monolithic reinforced concrete floor slabs clamped along the contour. *Building and Reconstruction*. 2024; (2): 3-15. (In Russ.)
2. **Tiwari N. and Zafar S.** Structural Behavior of Bubble Deck Slabs and Its Application: Main Paper. IJSRD International Journal for Scientific Research & Development. 2016. Vol. 4. Issue 02. Pp: 433-437. ISSN (online): 2321-0613.
3. **Ibrahim A. M., Ali N. K., and Salman W. D.** Flexural Capacities of Reinforced Concrete Two-Way Bubbledeck Slabs of Plastic Spherical Voids. J. Print. Iraq. 2013. Vol. 06. No. 02. Pp: 9-20.
4. **Valivonis J., Skuturna T, Daugeviius M. and Šneideris A.** Punching shear strength of reinforced concrete slabs with plastic void formers. Constr. Build. Mater. 2017. Vol.145. Pp: 518-527.
5. **Saifulla M., Azeem M. A.** Comparative Seismic Performance of a Conventional Slab and Flat Slab over a Bubble Deck Slab. International Journal of Emerging Technology and Advanced Engineering. November 2017. Vol. 7. Issue 11. Pp: 137-143.
6. **Teja P. P., Kumar P. V, Mounika C. R., and Saha P.** Structural Behavior of Bubble Deck Slab. January 2012. Pp: 383-388.
7. **Lakshmikanth L., Poluraju P.** Performance of Structural Behaviour of Bubble Deck Slab. International Journal of Recent Technology and Engineering (IJRTE). April 2019. Vol.7. Issue 6C2. ISSN: 2277-3878.
8. **Varghese J. P, M. George.** Parametric Investigation on the Seismic Response of Voided and Solid Flat Slab Systems. IJISET - International Journal of Innovative Science, Engineering & Technology. March 2018. Vol. 5. Issue 3. Pp: 256-258.
9. **Mahalakshmi S., S. Nanthini S., and Saha A. P. E**xperimental Studies on Comparison of Conventional Slab and Bubble Deck Slab Based on Strength. 2017. Vol. 5. Pp: 580-588.
10. **Orlova M.D., Mnushkin M.A., Evtushenko I.S., Vinogradova K.I., Egarmin K.A.** Analysis of the use of hollow formers from recycled polypropylene in the creation of lightweight monolithic floors. Research of various directions of modern science: Collection of materials of the XXI International Scientific and practical Conference. Part 1. Moscow. 2017. Pp.562-567. (In Russ)
11. **Filimonova E. S**. Analysis of the stress-strain state of a monolithic floor slab with void generators according to the Cobiax system based on various computational models // J. Young Scientist. 2022. No. 20 (415). Pp. 107-109. (In Russ.)
12. STO 35546020.001-2016 «Fixed formwork (voids and couplings) Sibforma ®. General information about the technology, product range. Recommendations for the calculation and design of monolithic girderless floor slabs with non-removable formwork Sibform ® in accordance with Code of Practice 63.13330.2012». (In Russ.)

13. STO 38311046-001-2019 «Monolithic reinforced concrete lightweight slabs with Simkar void formers. Rules of design and construction». (In Russ.)
14. Recommendations for the calculation of monolithic beamless floor slabs with Simkar void-forming slabs (without prestressing)/National Research Moscow State University of Civil Engineering, 2014. -119c.
15. **Белостоцкий А.М., Дубинский С.И., Аул А.А., Нагибович А.И., Афанасьева И.Н., Козырев О.А., Павлов А.С.** Verification report ANSYS Mechanical software (4 volume). – M.: National Research Moscow State University of Civil Engineering, Research & Development Centre StaDyO, 2009, 2024.
16. Code of Practice 63.13330.2018 “Concrete and reinforced concrete structures. General provisions”.
17. Structural Analysis Guide, Documentation for ANSYS, Release 21R2. 2021.
18. **A. Belostotsky, A. Nagibovich, P. Novikov, V. Vershinin.** EARTHQAUKE OF BUILDINGS AND STRUCTURES: REGULATORY «MUST-DO» OR SCIENTIFICALLY SUBSTANTIATED RESULTS // International Journal for Computational Civil and Structural Engineering. – 2024. – Vol. 20, No. 4. – P. 241-252.
19. **D. Dmitriev, P. Novikov, S. Petryashev, A. Nagibovich.** CONSIDERATION OF THE SEISMIC IMPACT’S WAVE NATURE IN THE DESIGN JUSTIFICATION OF HIGH-RISE BUILDINGS SEISMIC RESISTANCE // International Journal for Computational Civil and Structural Engineering. – 2024. – Vol. 20, No. 3. – P. 198-205.
20. **A. Belostotsky, A. Nagibovich, A. Pavlov.** NUMERICAL SIMULATION OF THE STRESS-STRAIN STATE OF A LARGE-SPAN STRUCTURE WITH JOINTS WITH GAP UNDER THE SEISMIC LOADS IN A TRANSIENT DYNAMIC // International Journal for Computational Civil and Structural Engineering. – 2023. – Vol. 19, No. 3. – P. 165-172.
21. **Malahova A.N**. Pustotnye kessonnye plity perekrytij monolitnyh mnogoetazhnyh zdanij [Hollow coffered floor slabs of monolithic multi-storey buildings] // J. Vestnik MGSU. 2016. No. 6. Pp. 15-24. (rus)

СПИСОК ЛИТЕРАТУРЫ

1. **Джамуев Б.К.** Влияния несъемных пустотообразователей на прочность защемленных по контуру монолитных железобетонных плит перекрытия. Строительство и реконструкция. 2024;(2):3-15.
2. **Tiwari N. and Zafar S.** Structural Behavior of Bubble Deck Slabs and Its Application: Main Paper. IJSRD International Journal for Scientific Research & Development. 2016. Vol. 4. Issue 02. Pp: 433-437. ISSN (online): 2321-0613.
3. **Ibrahim A. M., Ali N. K., and Salman W. D.** Flexural Capacities of Reinforced Concrete Two-Way Bubbledeck Slabs of Plastic Spherical Voids. J. Print. Iraq. 2013. Vol. 06. No. 02. Pp: 9-20.
4. **Valivonis J., Skuturna T, Daugeviius M. and Šneideris A.** Punching shear strength of reinforced concrete slabs with plastic void formers. Constr. Build. Mater. 2017. Vol.145. Pp: 518-527.
5. **Saifulla M., Azeem M. A.** Comparative Seismic Performance of a Conventional Slab and Flat Slab over a Bubble Deck Slab. International Journal of Emerging Technology and Advanced Engineering. November 2017. Vol. 7. Issue 11. Pp: 137-143.
6. **Teja P. P., Kumar P. V, Mounika C. R., and Saha P.** Structural Behavior of Bubble Deck Slab. January 2012. Pp: 383-388.
7. **Lakshmikanth L., Poluraju P.** Performance of Structural Behaviour of Bubble Deck Slab. International Journal of Recent Technology and Engineering (IJRTE). April 2019. Vol.7. Issue 6C2. ISSN: 2277-3878.

8. **Varghese J. P, M. George. Parametric** Investigation on the Seismic Response of Voided and Solid Flat Slab Systems. IJISET - International Journal of Innovative Science, Engineering & Technology. March 2018. Vol. 5. Issue 3. Pp: 256-258.
9. **Mahalakshmi S., S. Nanthini S., and Saha A. P.** Experimental Studies on Comparison of Conventional Slab and Bubble Deck Slab Based on Strength. 2017. Vol. 5. Pp: 580-588.
10. **Орлова М.Д., Мнушкин М.А., Евтушенко И.С., Виноградова К.И., Егармин К.А.** Анализ применения пустотообразователей из рециклированного полипропилена при создании облегченных монолитных перекрытий. Исследование различных направлений современной науки: Сборник материалов XXI Международной научнопрактической конференции. Ч.1. Москва. 2017. С.562-567.
11. **Филимонова Е. С.** Анализ напряженно-деформированного состояния монолитной плиты перекрытия с пустотообразователями по системе Cobiax на основании различных расчетных моделей // Молодой ученый. 2022. № 20 (415). С. 107-109.
12. СТО 35546020.001-2016 «Несъемная опалубка (пустотообразователи и соединительные муфты) Сибформа®. Общие сведения о технологии, номенклатура изделий. Рекомендации по расчету и конструированию монолитных безбалочных плит перекрытий с несъемной опалубкой Сибформа® в соответствии с СП 63.13330.2012».
13. СТО 38311046-001-2019 «Монолитные железобетонные облегченные плиты с пустотообразователями Simkar. Правила проектирования и возведения».
14. Рекомендации по расчету монолитных безбалочных плит перекрытий с пустотообразователями «Симкар» (без предварительного напряжения)/ФБГОУ ВПО «МГСУ». -М. МГСУ, 2014. -119с.
15. **Белостоцкий А.М., Дубинский С.И., Аул А.А., Нагибович А.И., Афанасьева И.Н., Козырев О.А., Павлов А.С.** Верификационный отчет по программному комплексу ANSYS Mechanical (4 тома). – М.: ЗАО НИЦ СтаДиО, НОЦ КМ МГСУ, 2009, 2024.
16. СП 63.13330.2018. Бетонные и железобетонные конструкции. М., Минстрой, 2018.
17. Structural Analysis Guide, Documentation for ANSYS, Release 21R2. 2021.
18. **A. Belostotsky, A. Nagibovich, P. Novikov, V. Vershinin.** EARTHQAUKE OF BUILDINGS AND STRUCTURES: REGULATORY «MUST-DO» OR SCIENTIFICALLY SUBSTANTIATED RESULTS // International Journal for Computational Civil and Structural Engineering. – 2024. – Vol. 20, No. 4. – P. 241-252.
19. **D. Dmitriev, P. Novikov, S. Petryashev, A. Nagibovich.** CONSIDERATION OF THE SEISMIC IMPACT'S WAVE NATURE IN THE DESIGN JUSTIFICATION OF HIGH-RISE BUILDINGS SEISMIC RESISTANCE // International Journal for Computational Civil and Structural Engineering. – 2024. – Vol. 20, No. 3. – P. 198-205.
20. **А.М. Белостоцкий, А.С. Павлов, А.Н. Нагибович.** Численное моделирование напряженно-деформированного состояния большепролетного сооружения с люфтами в опорах с учетом сейсмического воздействия в нелинейной динамической постановке // International Journal for Computational Civil and Structural Engineering, 2023, Том 19 № 3, pp. 165-172 https://ijccse.iasv.ru/index.php/ijccse/article/view/705/385
21. **Малахова А.Н.** Пустотные кессонные плиты перекрытий монолитных многоэтажных зданий // Вестник МГСУ. 2016. № 6. С. 15-24

Alexander M. Belostotsky – DSc, Professor, Full Member of the Russian Academy of Architecture and Construction Sciences, Scientific adviser at Zolotov Research and Educational Center for Computational Modelling of the National Research Moscow State University of Civil Engineering; 129337, Russia, Moscow, Yaroslavskoe shosse, 26. E-mail: amb@stadyo.ru

Белостоцкий Александр Михайлович – д.т.н., профессор, академик РААСН, научный руководитель НОЦ КМ им. А.Б. Золотова Национального исследовательского Московского государственного строительного университета; 129337, Россия, г. Москва, Ярославское шоссе, д. 26. E-mail: amb@stadyo.ru

Alexander I. Nagibovich – engineer at Zolotov Research and Educational Center for Computational Modelling of the National Research Moscow State University of Civil Engineering; 129337, Russia, Moscow, Yaroslavskoe shosse, 26. Leading calculation engineer at the Scientific and Research Center StaDyO; 18, The 3rd Yamskogo Polya st., Moscow, 125040, Russia. E-mail: nagibovich@yandew.ru

Нагибович Александр Игоревич – к.т.н., старший научный сотрудник НОЦ КМ им. А.Б. Золотова Национального исследовательского Московского государственного строительного университета; 129337, Россия, г. Москва, Ярославское шоссе, д. 26. Ведущий инженер-расчетчик АО НИЦ СтаДиО; E-mail: nagibovich@yandex.ru

Sergey V. Scherbina – engineer at Zolotov Research and Educational Center for Computational Modelling of the National Research Moscow State University of Civil Engineering; 129337, Russia, Moscow, Yaroslavskoe shosse, 26. Calculation engineer at the Scientific and Research Center StaDyO; 18, The 3rd Yamskogo Polya st., Moscow, 125040, Russia. E-mail: scherbine@mail.ru

Щербина Сергей Викторович – инженер НОЦ КМ им. А.Б. Золотова Национального исследовательского Московского государственного строительного университета; 129337, Россия, г. Москва, Ярославское шоссе, д. 26. Инженер-расчетчик АО НИЦ СтаДиО; E-mail: scherbine@mail.ru

Tatiana N. Vasileva – engineer at Zolotov Research and Educational Center for Computational Modelling of the National Research Moscow State University of Civil Engineering; 129337, Russia, Moscow, Yaroslavskoe shosse, 26. Calculation engineer at the Scientific and Research Center StaDyO; 18, The 3rd Yamskogo Polya st., Moscow, 125040, Russia. E-mail: rabitfew@gmail.com

Васильева Татьяна Николаевна – инженер НОЦ КМ им. А.Б. Золотова Национального исследовательского Московского государственного строительного университета; 129337, Россия, г. Москва, Ярославское шоссе, д. 26. Инженер-расчетчик АО НИЦ СтаДиО; E-mail: rabitfew@gmail.com

DOI:10.22337/2587-9618-2025-21-2-200-219

3D CONCRETE PRINTING: A STUDY OF PRINTED STRUCTURES DURABILITY

Aleksey O. Adamtsevich, Andrey P. Pustovgar, Liubov A. Adamtsevich, Yuriy I. Markov

Moscow State university of Civil Engineering, Jaroslavskoe Shosse 26, Moscow, RUSSIA

Abstract: The article presents the results of an experimental study of the influence of technological parameters of construction 3D concrete printing (3DCP) on the durability of printed elements of building structures during accelerated model aging in a climatic chamber. The aim of the work was to study the patterns of degradation of multilayer concrete samples printed on a construction 3D printer in various ways (with and without layer bonding, as well as with cold joint modeling) under cyclic climatic influences. For the experiments, an industrially produced composition of the material for additive construction production 3D4Art was used, applied by a workshop construction 3D printer of a portal design. The control group consisted of monolithic samples of similar geometry. The study included a comparative analysis of the degradation kinetics and mechanisms of destruction of samples during 100 cycles of combined exposure to freezing thawing with humidification. The results demonstrate that while maintaining the overall structural integrity of all samples, 3D printed elements exhibit an increased tendency to crack formation in the areas of interlayer contacts, which is especially pronounced in the case of technological defects (cold seam). The obtained data emphasizes the need for further research into the influence of technologically conditioned defects on changes in the mechanical properties of structural elements during aging. The results of the work are of practical importance for optimizing the technological modes of construction 3D printing to increase the durability of erected structures.

Keywords: 3D concrete printing, additive construction production, durability, interlayer adhesion

АДДИТИВНОЕ СТРОИТЕЛЬНОЕ ПРОИЗВОДСТВО: ИССЛЕДОВАНИЕ ДОЛГОВЕЧНОСТИ НАПЕЧАТАННЫХ КОНСТРУКЦИЙ

А.О. Адамцевич, А.П. Пустовгар, Л.А. Адамцевич, Ю.И. Марков

Национальный исследовательский Московский государственный строительный университет, г. Москва, РОССИЯ

Аннотация: В статье представлены результаты экспериментального исследования влияния технологических параметров строительной 3D-печати бетоном (3DCP) на долговечность напечатанных элементов строительных конструкций при ускоренном модельном старении в климатической камере. Целью работы являлось изучение закономерностей деградации многослойных бетонных образцов, напечатанных на строительном 3D-принтере различными способами (с перевязкой и без перевязки слоев, а также с моделированием холодного шва), в условиях циклических климатических воздействий. Для экспериментов использовался промышленно производимый состав материала для аддитивного строительного производства 3D4Art, наносимый цеховым строительным 3D-принтером портальной конструкции. Контрольную группу составили монолитные образцы схожей геометрии.

В ходе исследования проведен сравнительный анализ кинетики деградации и механизмов разрушения образцов в течение 100 циклов комбинированного воздействия замораживания-оттаивания с увлажнением. Результаты демонстрируют, что при сохранении общей структурной целостности всех образцов, 3D-печатные элементы проявляют повышенную склонность к трещинообразованию в зонах межслоевых контактов, особенно выраженную в случае наличия технологических дефектов (холодный шов).

Полученные данные подчеркивают необходимость дальнейших исследований влияния технологически обусловленных дефектов на изменение механических свойств конструкционных элементов в процессе старения. Результаты работы имеют практическое значение для оптимизации технологических режимов строительной 3D-печати с целью повышения долговечности возводимых конструкций.

Ключевые слова: 3D печать бетоном, аддитивное строительное производство, долговечность, межслойная адгезия

INTRODUCTION

Recently, more and more attention has been paid to issues of additive construction production, both in Russia and abroad. Thus, for the keyword combination 3D concrete printing in the international Scopus database, 3482 results are available for all time as of June 2025 (sample 1), for the phrase concrete printing - 3916 publications (sample 2). At the same time, not many publications are devoted to durability issues (the complex of words 3D concrete printing + durability was selected to assess the state) (sample 3) - Figure 1.

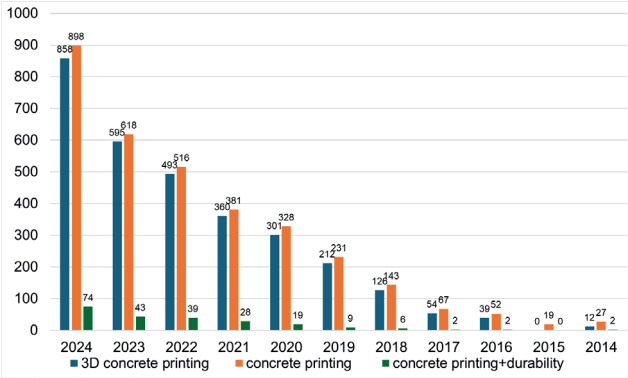


Figure 1. Dynamics of distribution of publications by keywords

The analysis of sample 3 allowed us to conclude that additive construction production or 3D concrete printing is actively developing, but requires solving the problems of interlayer adhesion, anisotropy of mechanical properties and durability. At the same time, considerable attention is paid to sustainable development using 3D concrete printing [1-15], problems of interlayer adhesion [16-25], and issues of anisotropy [26-29]. There are separate publications that pay attention to the durability of printing using geopolymer composites [30-32], but there are no issues of studying durability depending on the printing method yet.

The relevance of studying the durability of 3D concrete printing structures is due to the rapid development of this area in the modern construction industry and the need for scientific justification of their operational reliability. In recent years, 3D concrete printing (3DCP) technology has demonstrated significant potential for transforming traditional approaches to the construction of buildings and structures, offering such advantages as reduced construction times, reduced waste, and design flexibility, which makes it possible to create complex architectural and space-planning forms. However, the widespread adoption of this technology is hampered by insufficient study of the long-term behavior of printed structures in real operating conditions, especially when exposed to aggressive environmental factors. Of particular importance is the study of interlayer adhesion as a critical factor determining the mechanical characteristics and durability of structures. The durability of structures made of fine-grained concrete, which includes materials for 3DCP, is generally beyond doubt, but it is in the contact zones between successively applied layers that stresses can concentrate and potential destruction sites can form. The existing shortage of experimental data on the behavior of 3DCP structures under cyclic temperature and humidity exposure, typical for cold climate zones, requires comprehensive studies aimed at establishing a correlation between the technological parameters of printing, the structural features of the material and its resistance to external influences during operation. Obtaining such data is important both for improving the additive construction technology itself and for developing a regulatory framework governing the operation of structures manufactured using this technology. In this regard, the purpose of this study is to investigate the effect of the printing method of multilayer products and structures on the nature of degradation under conditions of accelerated model aging.

MATERIALS AND METHODS

The experimental part of the study was carried out using the material for additive construction production 3D4Art. The main physical and mechanical characteristics of the material used were de-

termined based on the Research Institute of Construction Materials and Technologies of the National Research University Moscow State University of Civil Engineering, considering the requirements of GOST R 59096-2020. The results of standard material tests are presented in Table 1.

Table 1. Results of testing a batch of material used for additive construction production

№	Name of the indicator	Unit of measurement	Test method	Test result
1	Humidity	%	GOST 8735-88 p. 10	0,29
2	Grain size (largest size of filler grains)	мм	GOST 8735-88 p. 3	5
3	Grain size (content of grains of the largest size)	%	GOST 8735-88 p. 3	0,03
4	Bulk density	кг/м^3	GOST 8735-88 p. 9.3	1382,23
5	Mobility by cone flow	мм	GOST R 58277-2018 p. 5	135
6	Water holding capacity	%	GOST R 58277-2018 p. 6	98
7	Start of setting	min	GOST 30744-2001, p. 6	100
8	End of setting	min	GOST 30744-2001, p. 6	110
9	Bending strength	MPa	GOST 310.4-81 p. 2.2	4,1
10	Compressive strength (GOST 310.4)	MPa	GOST 310.4-81 p. 2.2	34,6
11	Effective thermal conductivity (thermal conductivity coefficient)	W/m*K	GOST 7076-99 GOST 12730.2-2020 p. 6.1	0,442
12	Water resistance grade by the "wet spot" method	–	GOST 12730.5-2018 p. 4	W20

To implement the study, control programs were prepared for three types of parallelepiped-shaped products:

1. The first version of the product for printing layers oriented in one direction along one axis. The height of the finished product was 400 mm, which corresponds to 20 layers with the format of each layer being 50 mm in width and 20 mm in height. The length of each layer reached 450 mm, considering the rotary part (Figure 2).

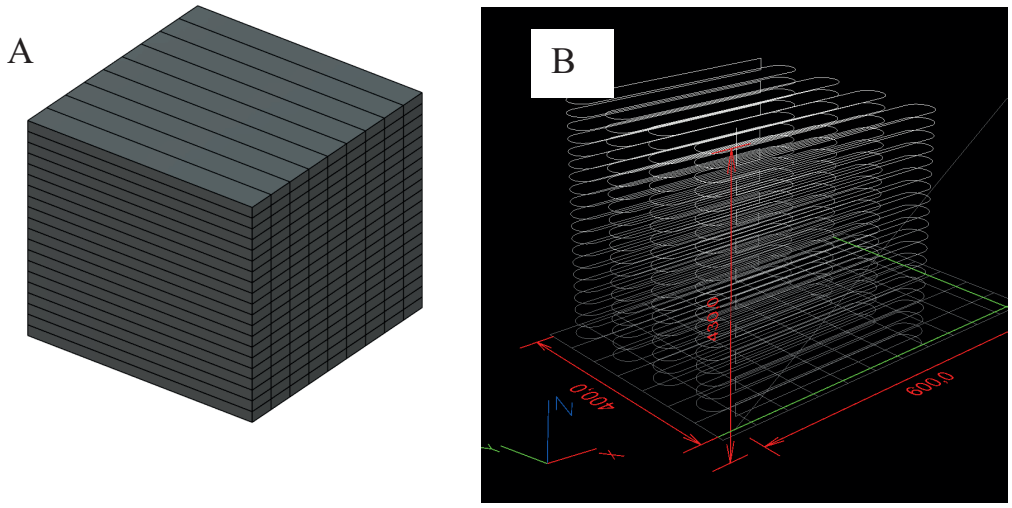


Figure 2. Visualization of the first version of the product. A – 3D model. B – visualization of the control program

2. The second version of the product was also a parallelepiped with the following parameters: height 400 mm, width and length 450 mm. However, in this case, the sequence and direction of printing layers alternated. Thus, one layer was printed along the X axis, and the next one along the Y axis (Figure 3).

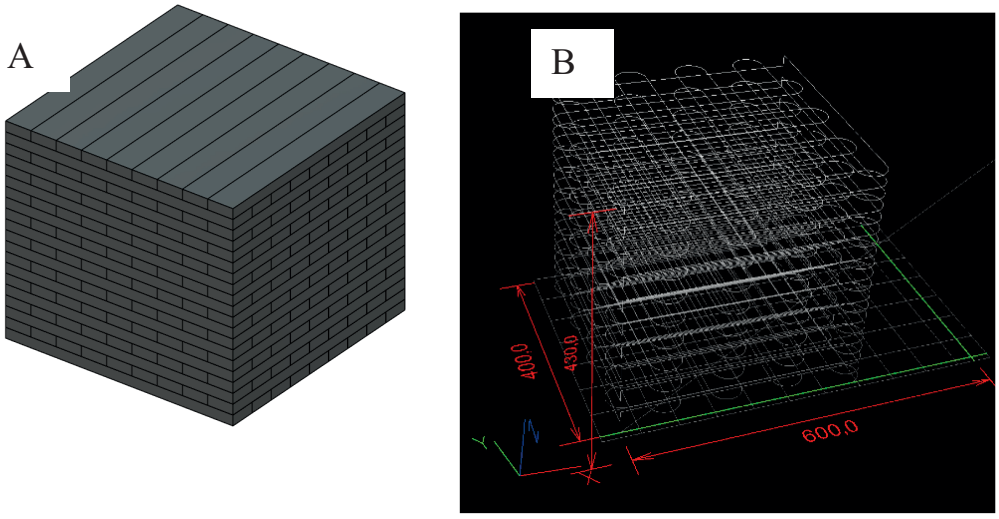


Figure 3. Visualization of the second version of the product. A – 3D model. B – visualization of the control program

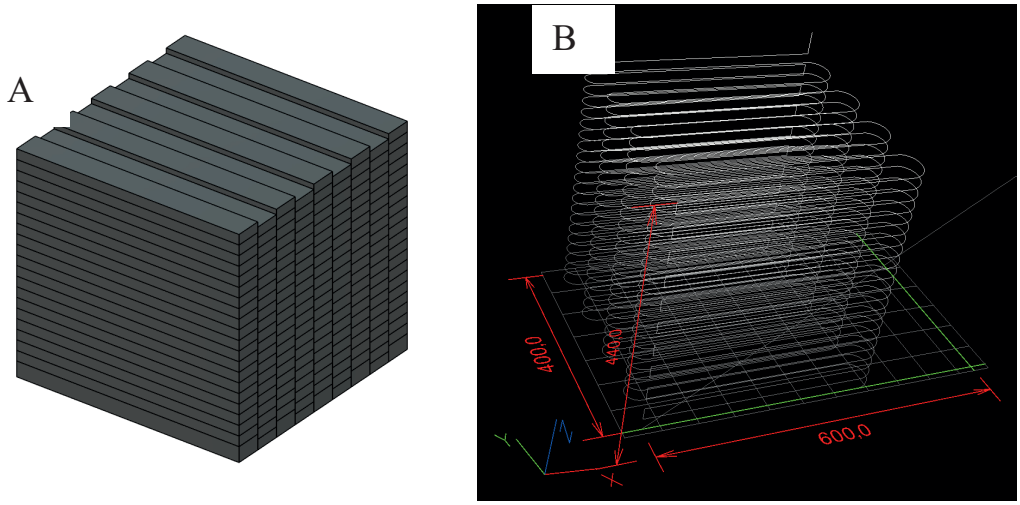


Figure 4. Visualization of the third version of the product. A – 3D model. B – visualization of the control program

The third version of the product is characterized by a variable height of layer printing. Thus, when printing layers in contact with the base of the print field (floor), the layer height alternated sequentially: 3 cm and 2 cm. Subsequent layers were printed with a height difference between adjacent layers (1 cm) formed in this way, but with the same height of each layer (2 cm). This approach ensured a tight fit of adjacent layers to each other in the contact zone (Figure 4).

As a result, three different strategies for forming the geometry of solid products using 3DCP were tested. The first option involved printing layers in one direction, the second - alternating directions, and the third - a variable height of layers to improve adhesion between them.

Despite the fact that in real practice, the technology of 3DCP is mainly used for the construction of permanent formwork for enclosing or (less often) supporting structures with a thickness of, as a rule, one or two layers - studying the durability of such structures requires a special approach that takes into account the specifics of layer-by-layer formation of the material. Since 3DCP involves sequential application of layers, interlayer boundaries become potentially vulnerable zones where stresses can concentrate, microcracks can form, and delamination can occur under the influence of external factors. In this regard, the use of multilayer samples for studying aging processes seems methodologically justified, since it allows artificially increasing the number of interlayer contacts and thereby accelerating the manifestation of degradation processes under cyclic climatic influences, such as freezing and thawing in combination with sprinkling. Despite the apparent discrepancy between the multilayer structure of the studied samples and the single-layer configuration of most real building elements, the proposed methodology provides a reliable basis for predicting the durability of 3DCP structures, since it allows for a targeted study of the weakest zones of the material and modeling its degradation processes in an accelerated mode.

The 3DCP products were manufactured using a portal-type construction 3D printer. The X axis is the axis along which the nozzle of the construction 3D printer's print head moves during layer-by-layer extrusion of the material. During the optimization of the model for printing multilayer products, the parameters were adjusted so that when laying adjacent layers, their maximum adhesion was achieved without the occurrence of sagging. This considers the selected width of the printed layer and the extrusion speed.

All products were manufactured under identical temperature and humidity conditions corresponding to room temperature and humidity, in the same laboratory room.

The photographs below demonstrate the process of printing a multilayer product in the form of a parallelepiped with layer-by-layer laying of the mixture in one direction and the appearance of the finished product (Figure 5).



Figure 5. Printing of a parallelepiped-shaped product with layer-by-layer laying of the mixture in one direction and the appearance of the finished product

Similarly, the process of printing a parallelepiped-shaped product with layer-by-layer laying of the mixture in perpendicular directions is demonstrated below (Figure 6), as well as with different printing heights of the layers (Figure 7).



Figure 1. Printing of a parallelepiped-shaped product with layer-by-layer laying of the mixture in perpendicular directions and the appearance of finished products



Figure 7. Printing of a parallelepiped-shaped product with layer-by-layer laying of the mixture and different printing heights of the layers

In addition to the products printed in one run, an additional series of three products with layer bonding was printed, on which a cold joint was simulated. For this, the product was printed to the middle of the height, after which a pause of at least 6 hours was made, and after this pause the remaining part of the product was printed. This approach is designed to simulate long pauses in the operation of a construction 3D printer that may occur at a construction site. One product with a cold joint serve as a control, while the other two were coated with a primer based on styrene-acrylic polymer dispersion (Figure 8a) and concrete contact (Figure 8b) using a paint brush to assess the effectiveness of the influence of various methods of cold joint treatment on ensuring interlayer adhesion (Figure 9). In this case, the compositions were applied to one product immediately after printing the first half, and to the others - before printing the second part.



a) applying primer



b) concrete contact application process

Figure 2. Cold seam processing



Figure 9. Printing process over a processed cold seam

In addition, monolithic samples of the same dimensions are manufactured. After reaching the age of 28 days, the products are placed in a large climatic chamber for temperature and humidity loading (Figure 10). Every 10 block cycles of temperature and humidity loading are recorded and the defects that have arisen in the products are described. The tests involve the application of cyclic climatic effects to the product under test in accordance with the requirements of GOST R 55943-2018. One block cycle (24 hours) consists of two climatic cycles (cycle A and cycle B) each lasting 12 hours (720 minutes) (Figure 11 - Figure 12), following each other.



Figure 3. Placing products in a large climate chamber

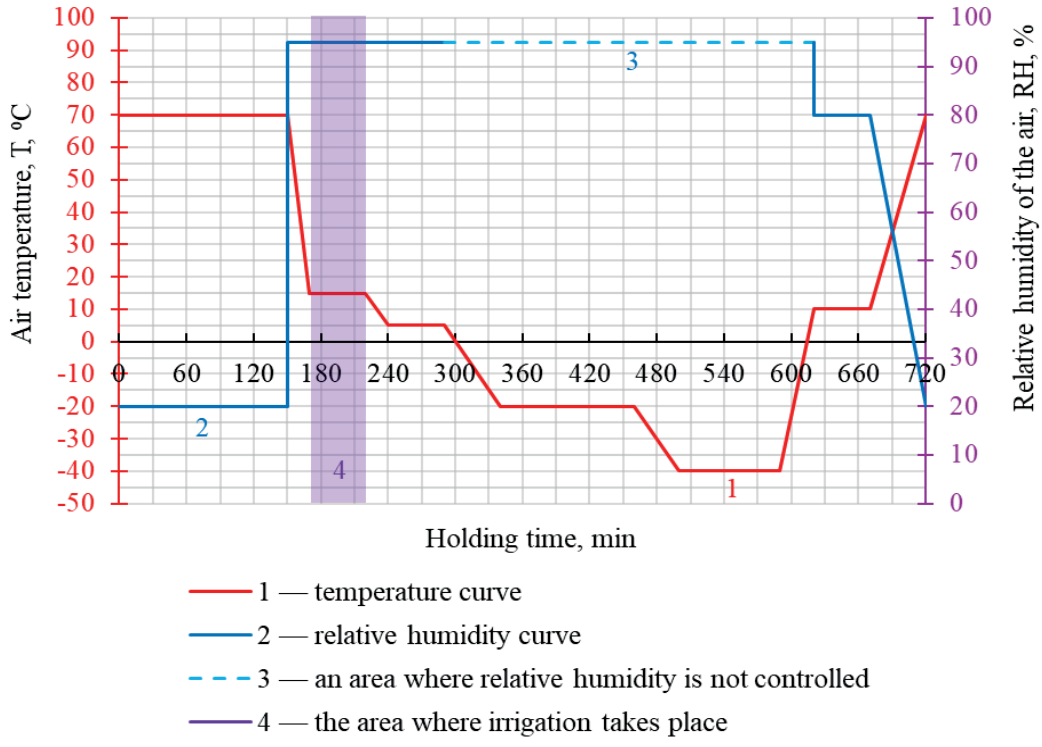


Figure 4. Climate cycle A

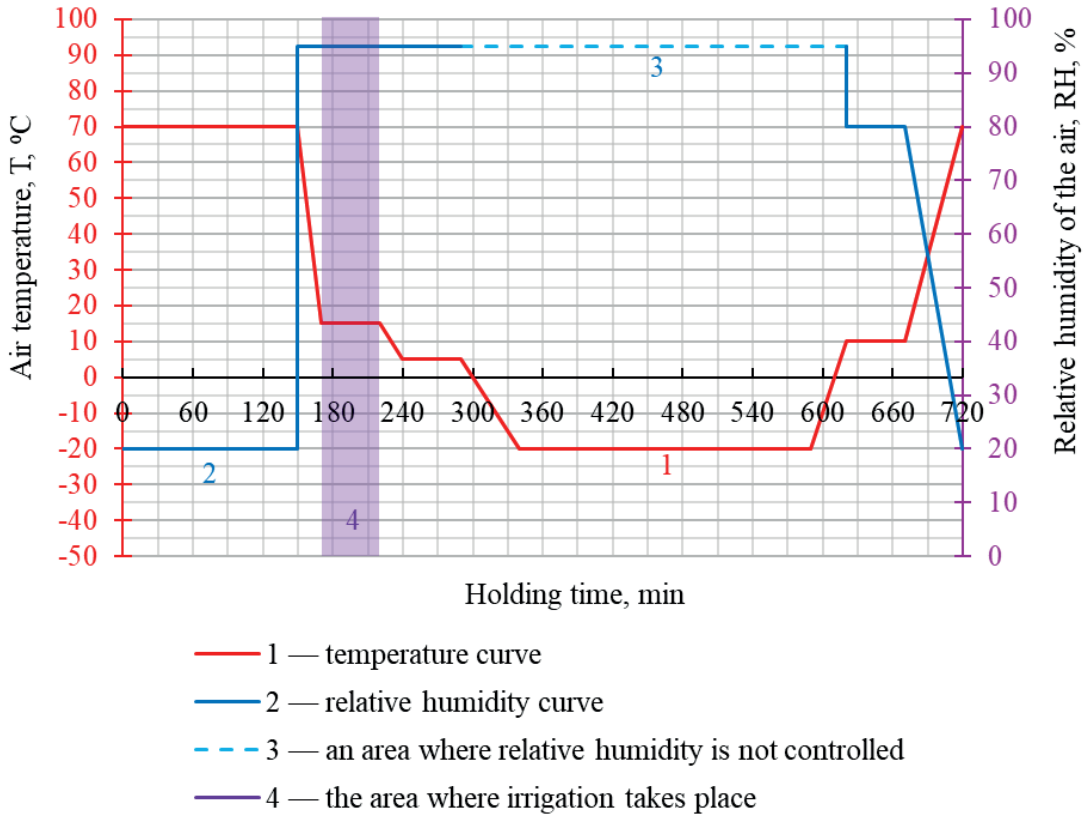


Figure 5. *Climate cycle B*

RESULTS OF THE STUDY OF THE INFLUENCE OF THE PRINTING METHOD OF MULTILAYER PRODUCTS AND STRUCTURES ON THE NATURE OF DEGRADATION UNDER CONDITIONS OF ACCELERATED MODEL AGING

In the part of the experimental study described in this article, the effect of the printing method for multilayer products and structures on the nature of degradation under accelerated model aging conditions was assessed visually by the nature of crack development and the width of their opening. The results of the visual assessment of the samples after climatic influences are presented in the form of photographs.

Before conducting climatic tests according to GOST R 55943-2018, each of the seven test samples was visually inspected for defects. Visual inspection was carried out on 5 faces with codes A - D (A - front face; B - left side face; B - back face; G - right side face; D - horizontal face above). Each sample was assigned a unique code (Table 2).

Table 2. Codes assigned to samples

Sample name	Sample code
Control sample of 3D printing with a cold seam	1
Monolithic sample	2
Sample of 3D printing with a cold seam with primer applied before printing the second part	3
Sample of 3D printing with a cold seam with primer applied im-	4

mediately after finishing printing the first part	
Sample of 3D printing with different layer heights	5
Sample of 3D printing with cross layers	6
Sample of 3D printing with cross layers	7

Based on the results of the inspection prior to the climatic tests, it was established that:
– the 3D printing sample with a cold seam with code 1 has one horizontal crack in the layer in the center of face A with pigmentation (Figure 13); isolated vertical cracks on faces B and C; there are no defects on faces G and D;
– the monolithic sample with code 2 has: a vertical crack 12.5 cm long, a horizontal hairline (less than 0.1 mm) crack 4 cm long in the center of the face, a diagonal hairline crack 7 cm long and a horizontal interlayer hairline crack 5 cm long on face A; face B was not inspected due to lack of access; a vertical hairline crack 12 cm long in the center of face C; there are no defects on faces G and D;
– the 3D printing sample with a cold seam with primer applied before printing the second part with code 3 has multiple vertical cracks in the layers along the edges of faces A, B and G (Figure 14); there are no defects on faces B and D;
– the 3D printing sample with a cold seam with primer applied immediately after finishing printing the first part with code 4 has single vertical cracks in the layers along the edges of faces A, B and G; there are no defects on faces B and D;
– the 3D printing sample with different layer heights with code 5 has multiple vertical cracks in the layers of the edges of faces A, B and G; single vertical cracks in the layers along the edges of face B; there are no defects on face D;
– the cross-layer 3D print sample with code 6 has: multiple vertical cracks in the layers of faces A, B, C and G (Figure 15); there are no defects on face D;
– the parallel-layer 3D print sample with code 7 has multiple vertical cracks in the layers of the edges of faces A, B and G; single vertical cracks in the layers along the edges of face B; there are no defects on face D.



Figure 13. Horizontal crack with pigmentation



Figure 14. Vertical cracks along the ribs

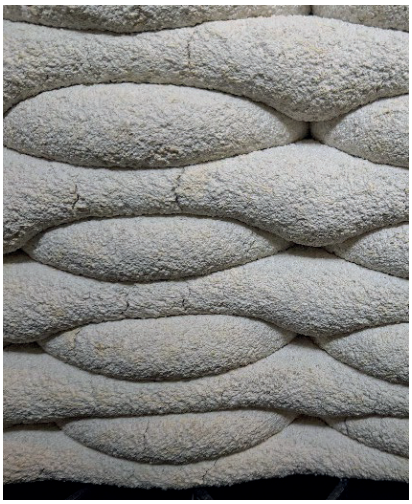


Figure 15. Vertical cracks

After the inspection, the climatic effects were activated. The first intermediate inspection was carried out after one block cycle of climatic effects. Then the inspection and photo recording of the samples was carried out every 5 block cycles, until the result of 100 block cycles was achieved. According to the results of the inspection after the first block cycle, it was found that the samples with markings 1, 3 and 4 in the wet state are covered with numerous hair cracks forming a "spider web", which is not observed in the dry state, no other defects were found. After 5 block cycles, the "spider web" was found on all samples (Figure 16 - Figure 17).



Figure 16. Multiple hairline cracks "spider web" on sample with code 5



Figure 17. Multiple hairline cracks "spider web" on sample with code 2

In addition to hairline cracks after 1 block cycle, a vertical crack was found in the middle of face G on sample code 3, with its transition to face D (Figure 18).

As a result of the tests, samples were photographed every 5 cycles. Below is a general assessment of the development of defects in samples with different codes.

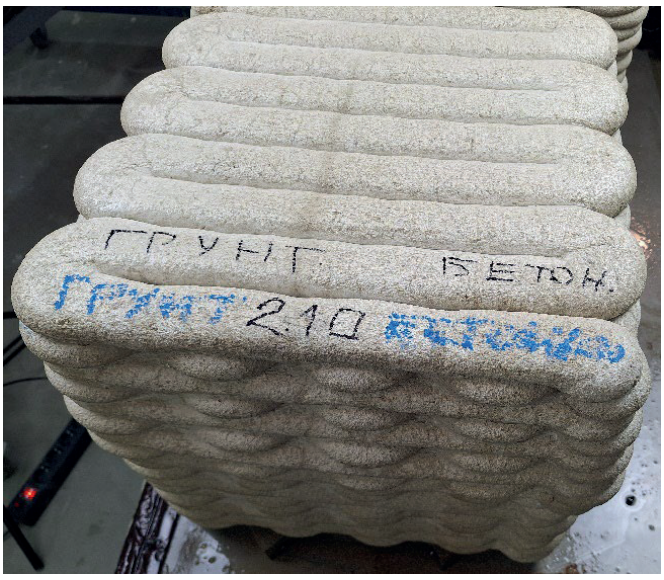


Figure 18. Vertical crack along faces G and D

Sample code	Evaluation of defect development	Conclusion based on the results of 100 cycles of model aging
1	In the period from 1 to 100 block cycles of climatic impacts: after the 5th block cycle, the appearance of a crack with an opening of more than 0.1 mm is observed, passing along the middle of the faces G and D; after 15 block cycles, yellow-red efflorescence was noticed on all faces of the sample; from the 15th to the 100th block cycle, the appearance of new visible damage was not observed, but more significant efflorescence was noticed with a change in the color of the sample and a greater opening of the crack along the faces G and D to a thickness of more than 0.1 mm	The sample has: one horizontal layer crack in the center of face A with white and reddish efflorescence along the edge and multiple hairline cracks; single vertical layer cracks and multiple hairline cracks along faces B, C and G; one crack in the middle of face D with white efflorescence along the edge; yellowish-reddish efflorescence and significant color change
2	In the period from 1 to 100 block cycles of climatic influences: after the 5th block cycle, the appearance of a "web" of hairline cracks is observed; after 10 block cycles, yellow-red efflorescence was observed on all edges of the sample; from the 10th to the 100th block cycle, the appearance of new visible damage was not observed, but more significant efflorescence was observed with a change in the color of the sample	The sample has a vertical crack 12.5 cm long, a horizontal hairline crack (less than 0.1 mm) 4 cm long in the center of the face, a diagonal hairline crack 7 cm long and a horizontal interlayer hairline crack 5 cm long on face A; face B was not inspected due to lack of access; a vertical hairline crack 12 cm long in the center of face C; there are no defects on faces G and D; yellowish-red formations and significant color change
3	In the period from the 1st to the 100th block cycle of climatic impacts: after the 40th block cycle, yellow-red efflorescence was observed on all faces of the sample; after the 65th block cycle, a crack was found in the lower part of face A, which is a continuation of the crack formed after the 1st block cycle; after the 75th block cycle, the appearance of a vertical crack in the middle of face B with an opening of more than 0.1 mm is observed; from the 75th to the 100th block cycle, the appearance of new visible damage was not observed, but more significant efflorescence was observed with a change in the color of the sample and a greater opening of the crack along faces G and D to a thickness of more than 0.1 mm (Figure 19 - Figure 20).	The sample with the application of primer before printing the second part has multiple vertical cracks in the layers along the edges of faces A, B, C and D; a crack with an opening of more than 0.1 mm along faces A, B and D; one crack on face D with an opening of more than 0.1 mm, adjacent to the edges of faces B and D; yellowish-red formations and a significant change in color
4	In the period from 1 to 100 block cycles of climatic impacts: after 10 block cycles, one	The sample with the application of the primer immediately after the

Sample code	Evaluation of defect development	Conclusion based on the results of 100 cycles of model aging
	crack is observed in the middle of faces A and D, extending to the cold joint; after 15 block cycles, yellow-red efflorescence was observed on all faces of the sample; from 15 to 100 block cycles, the appearance of new visible damage was not observed, but more significant efflorescence was observed with a change in the color of the sample and a greater opening of the crack along faces G and D to a thickness of more than 0.1 mm.	end of printing of the first part with the code 4 has single vertical cracks of the layers along the edges and multiple hairline cracks on faces A, B and G; multiple hairline cracks along the entire face B; one crack on face D with an opening of more than 0.1 mm and multiple hairline cracks; yellowish-red formations and a significant change in color.
5	In the period from 1 to 100 block cycles of climatic influences: after the 5th block cycle, the appearance of a "web" of hairline cracks is observed; after the 35th block cycle, yellow-red efflorescence was noticed on all edges of the sample; from the 35th to the 100th block cycle, the appearance of new visible damage was not observed, but more significant efflorescence with a change in the color of the sample was noticed.	The sample has: multiple vertical cracks in the layers of the ribs and multiple hairline cracks on faces A, B and D; single vertical cracks in the layers along the ribs and multiple hairline cracks on face B; multiple hairline cracks on face D; yellowish-red formations and significant color change
6	In the period from the 1st to the 100th block cycle of climatic impacts: after the 5th block cycle, the appearance of a "web" of hairline cracks is observed; after the 20th block cycle, the appearance of a vertical crack along face A with white efflorescence is observed, and yellow-red efflorescence is also noted on all faces of the sample; from the 20th to the 100th block cycle, the appearance of new visible damage was not observed, but more significant efflorescence was noted with a change in the color of the sample and a greater opening of the crack along face A to a thickness of more than 0.1 mm with more significant white efflorescence.	The sample has multiple vertical cracks in the layers of faces A, B, C, D and E; one vertical crack in the middle of face C with white efflorescence along the edge and an opening of more than 0.1 mm; two vertical cracks in the middle of face D with white efflorescence along the edge and an opening of more than 0.1 mm; yellowish-red formations and a significant change in color
7	In the period from 1 to 100 block cycles of climatic impacts: after the 5th block cycle, the appearance of a "spider web" of hairline cracks is observed; after 15 block cycles, yellow-red efflorescence was observed on all edges of the sample; from the 15th to the 100th block cycle, the appearance of new visible damage was not observed, but more significant efflorescence with a change in the color of the sample was noted.	The specimen has multiple vertical cracks in the layers of the ribs and multiple hairline cracks on faces A, B and D; single vertical cracks in the layers along the ribs and multiple hairline cracks on face B; multiple hairline cracks on face D; yellowish-reddish precipitates and significant discoloration

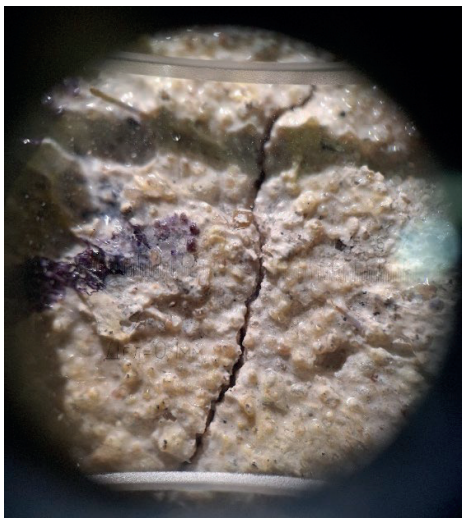


Figure 19. Crack on face D after 30 cycles

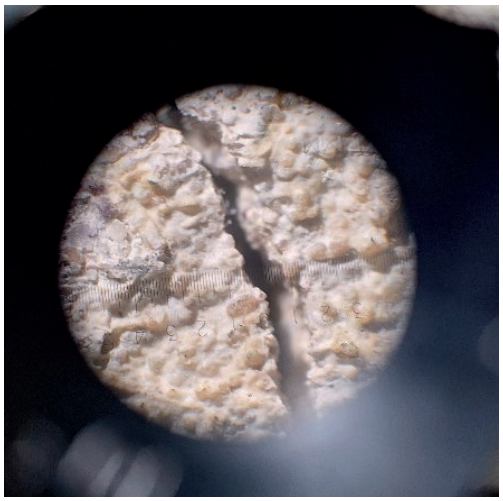


Figure 20. Crack on face D after 100 cycles

Summary results of visual assessment of samples after climatic impacts

The conducted studies revealed significant differences in degradation of 3D-printed samples and a monolithic analogue under cyclic climatic influence. The key differences are in the features of crack formation, the dynamics of defect development and resistance to external influences. The monolithic sample (code 2) demonstrated the least tendency to crack formation. Despite the presence of hairline cracks and single defects, their development during testing was minimal. In contrast, all 3D-printed samples, especially with a cold seam (codes 1, 3, 4), showed intense crack formation, mainly in the zones of interlayer contacts. The most pronounced defects were observed in samples with a cold seam, where cracks reached an opening of more than 0.1 mm, and were also accompanied by the formation of efflorescence.

Samples with cross-layer stacking (code 6) and variable layer height (code 5) showed better stability compared to samples printed in one direction (code 7). However, even they were inferior to the monolithic sample in terms of resistance to climatic influences. This confirms that interlayer boundaries remain a weak link in 3D-printed structures, despite the optimization of printing strategies. The use of a primer and concrete contact to improve adhesion in the cold joint zone (codes 3, 4) did not lead to a significant increase in durability. On the contrary, in some cases the treatment even contributed to an increase in the number of cracks, which may be due to additional stresses at the layer interface. During the removal of samples that had undergone 100 cycles of accelerated model aging from the climatic chamber, it was established that all samples for which the creation of a cold seam was modeled (codes 1,3,4) did not have interlayer adhesion and were freely separated in the zone where the cold seam was modeled (Figure 21).



Figure 21. Free separation of the sample by the cold seam modeling zone after 100 cycles of accelerated model aging in a climatic chamber

CONCLUSIONS

The conducted study allowed us to obtain several conclusions that may be relevant for the further development of 3DCP technology and assessment of the durability of structures created in this way. In particular, the obtained results demonstrated that monolithic samples manufactured in the traditional way have a significantly higher resistance to cyclic climatic effects compared to 3D-printed analogues. This confirms that the layer-by-layer formation of the structure is a critical factor determining its durability. Accelerated model aging in a climatic chamber shows that it is the interlayer contact zones that become the main sources of degradation, where stresses are concentrated and cracks develop. At the same time, none of the developed printing methods (parallel, cross-laying of layers, variable layer height) allowed us to completely neutralize this effect, although cross-laying showed slightly better results. The use of a primer and concrete contact to improve adhesion in the technological break zone did not give the expected positive effect. In some cases, this even led to an increase in the number of defects, which requires a revision of existing approaches to the processing of interlayer connections. The data obtained indicates that solving the problem of durability of 3DCP structures requires simultaneous optimization:

– composition of building mixtures (with an emphasis on improving adhesion characteristics);

– technological printing parameters (extrusion speed, temperature conditions);

– design solutions (stress distribution in interlayer contact zones).

This study has identified several promising areas for future research:

– development of new methods for assessing interlayer adhesion at the construction site;

– study of long-term behavior of structures under real operating conditions;

– creation of specialized regulatory and technical documents for assessing the durability of building products and structures manufactured using 3DCP technology.

The findings obtained are of fundamental importance for understanding the degradation processes of layered building materials, as well as of practical value for the industry, indicating the need for further improvement of additive construction production technologies. The solution to the identified problems will facilitate a wider implementation of 3D printing in construction practice while ensuring the required level of reliability of the structures being erected.

ACKNOWLEDGMENTS

The research was conducted as part of the development program for 2025-2036 of Moscow State University of Civil Engineering under the framework of strategic academic leadership program "Priority 2030."

REFERENCES

1. **de Brito, J., Kurda, R.** (2021) The past and future of sustainable concrete: A critical review and new strategies on cement-based materials, *Journal of Cleaner Production*, no. 281, doi: 10.1016/j.jclepro.2020.123558
2. **Flatt, R.J., Wangler, T.** (2022) On sustainability and digital fabrication with concrete, *Cement and Concrete Research*, vol. 158, 2022, doi: 10.1016/j.cemconres.2022.106837
3. **Rollakanti, C.R., Prasad, C.V.S.R.** (2022) Applications, performance, challenges and current progress of 3D concrete printing technologies as the future of sustainable construction – A state of the art review, *Materials Today: Proceedings*, vol. 65, 995-1000, doi: 10.1016/j.matpr.2022.03.619
4. **Su, J., Ng, W.L., An, J., Yeong, W.Y., Chua, C.K., Sing, S.L.** (2024) Achieving sustainability by additive manufacturing: a state-of-the-art review and perspectives,

Virtual and Physical Prototyping, vol. 19 doi: 10.1080/17452759.2024.2438899

5. **Capêto, A.P., Jesus, M., Uribe, B.E.B., Guimarães, A.S., Oliveira, A.L.S**. (2024) Building a Greener Future: Advancing Concrete Production Sustainability and the Thermal Properties of 3D-Printed Mortars, *Buildings,* vol. 14, doi: 10.3390/buildings14051323
6. **Mohan, M.K., Rahul, A.V., De Schutter, G., Van Tittelboom, K.** (2022) Salt Scaling Resistance of 3D Printed Concrete, *RILEM Bookseries,* vol. 37, pp. 188-193 doi: 10.1007/978-3-031-06116-5_28
7. **Habibi, A., Buswell, R., Osmani, M., Aziminezhad, M. (2024)** Sustainability principles in 3D concrete printing: Analysing trends, classifying strategies, and future directions, *Journal of Building Engineering*, vol. 98, 2024, doi: 10.1016/j.jobe.2024.111354
8. **Spurina, E., Sinka, M., Ziemelis, K., Bajare, D. (2023)** The effects of 3D printing on frost resistance of concrete, *Journal of Physics: Conference Series*, vol. 2423, doi: 10.1088/1742-6596/2423/1/012037
9. **Sheng, W., Wang, Y. (**2022) Fatigue behavior and abrasion resistance of prefabricated pavement textures assisted with 3D printing technology, *Green and Intelligent Technologies for Sustainable and Smart Asphalt Pavements - Proceedings of the 5th International Symposium on Frontiers of Road and Airport Engineering*, IFRAE 2021, pp. 266-271, doi: 10.1201/9781003251125-43
10. **Rollakanti, C.R., Venkata Siva Rama Prasad, C., Joe, A.** (2022) Digital Concrete for Sustainable Construction Industry: A State-of-the-Art Review, *Lecture Notes in Civil Engineering*, vol. 233, pp. 183-195, doi: 10.1007/978-981-19-0189-8_16
11. **Kallayil, A., Patadiya, J., Kandasubramanian, B., Adamtsevich, A., Kchaou, M., Aldawood, F.K.** (2025) Adaptive Smart Materials in Architecture: Enhancing Durability and Sustainability in Modern Construction, *ACS Omega*, doi: 10.1021/acsomega.4c04943
12. **Mohamed, O., Mishra, A., Isam, F.** (2025) An overview of 3D printed concrete for building structures: Material properties, sustainability, future opportunities, and challenges, *Structures,* vol. 78, doi: 10.1016/j.istruc.2025.109284
13. **Loporcaro, G., Scott, A., Palermo, A.** (2024) Sustainable Resilience for 3D concrete printed homes in New Zealand: a three-year research government funding overview, *fib Symposium,* pp. 757-768, 2024
14. **Jain, A., Varma, R.K., Prahsant, G.K., Gupta, R., Betteka, A.,** (2024) Innovative Sustainable Construction For Mars Colonization Through In-Situ Resource Utilization (ISRU), *Proceedings of the International Astronautical Congress*, IAC, vol. 2, pp. 703-709, doi: 10.52202/078364-0081
15. **Patil, M.G.M., Nayaka, R., Scholar, F.S.R.** (2024) Digital Transformation for Sustainable and Resilient Infrastructure: Current Progress and Future Potentia, *2024 IEEE Conference on Engineering Informatics, ICEI 202*4, doi: 10.1109/ICEI64305.2024.10912434
16. **Ma, G., Salman, N.M., Wang, L., Wang, F.** (2020) A novel additive mortar leveraging internal curing for enhancing interlayer bonding of cementitious composite for 3D printing, *Construction and Building Materials*, vol. 244, doi: 10.1016/j.conbuildmat.2020.118305
17. **Moelich, G.M., Kruger, P.J., Combrinck, R.** (2021) The effect of restrained early age shrinkage on the interlayer bond and durability of 3D printed concrete, *Journal of Building Engineering*, vol. 43 doi: 10.1016/j.jobe.2021.102857
18. **Yao, H., Xie, Z., Li, Z., Huang, C., Yuan, Q., Zheng, X.** (2022) The relationship between the rheological behavior and interlayer bonding properties of 3D printing cementitious materials with the addition of attapulgite, *Construction and Building Mate-*

rials, vol. 316, doi: 10.1016/j.conbuildmat.2021.125809

19. **Babafemi, A.J., Kolawole, J.T., Miah, M.J., Paul, S.C., Panda, B**. (2021) A concise review on interlayer bond strength in 3D concrete printing, *Sustainability (Switzerland),* vol. 13, doi: 10.3390/su13137137
20. **Şahin, H.G., Mardani, A.** (2023) Mechanical properties, durability performance and interlayer adhesion of 3DPC mixtures: A state-of-the-art review, *Structural Concrete,* vol. 24, pp. 5481-5505 , doi: 10.1002/suco.202200473
21. **Skibicki, S., Szewczyk, P., Majewska, J., Sibera, D., Ekiert, E., Chung, S.-Y., Sikora, P.** (2024) The effect of interlayer adhesion on stress distribution in 3D printed beam elements, *Journal of Building Engineering,* vol. 87, doi: 10.1016/j.jobe.2024.109093
22. **Tian, Z., Wang, L., Zhang, X., Zhou, X., Hu, Y.** (2020) Formation Mechanism and Improvement Solutions for Weak Interlayer Surfaces of 3D Printing Concrete, *Bulletin of the Chinese Ceramic Society,* vol. 39, pp. 2052-2058
23. **Rui, A., Wang, L., Ma, G.** (2023) Effect of Interlayer Water Film on Interfacial Characteristics of 3D Printed Concrete, *Bulletin of the Chinese Ceramic Society*, vol. 42, pp. 2281-2289
24. **Salman, N.M., Ma, G., Ijaz, N., Wang, L.** (2021) Weak inter-layer bonding in extrusion 3D concrete printing: A comparative analysis of mitigation techniques*, IOP Conference Series: Materials Science and Engineering*, vol. 1028, doi: 10.1088/1757-899X/1028/1/012003
25. **Lin, Y., Yan, J., Sun, M., Han, X., Tang, B.** (2024) Interlayer cohesion in 3D printed concrete: The role of width-to-height ratio in modulating transport properties and pore structure, *Journal of Building Engineering*, vol. 98, doi: 10.1016/j.jobe.2024.111009
26. **Surehali, S., Tripathi, A., Nimbalkar, A.S., Neithalath, N.** (2023) Anisotropic chloride transport in 3D printed concrete and its dependence on layer height and interface types , Additive Manufacturing, vol. 62, doi: 10.1016/j.addma.2023.103405
27. **Rui, A., Wang, L., Lin, W., Ma, G.** (2023) Experimental study on damage anisotropy of 3D-printed concrete exposed to sulfate attack, *Construction and Building Materials*, vol. 407, doi: 10.1016/j.conbuildmat.2023.133590
28. **Li, Y.-F., Yao, L., Wang, L., Ma, G.-W.** (2021) Study on Mechanical Anisotropy and Meso Damage Mechanism of 3D Printing Concrete, Gonglu Jiaotong Keji, *Journal of Highway and Transportation Research and Development*, vol. 38, pp. 81-89, doi: 10.3969/j.issn.1002-0268.2021.05.010
29. **Li, C., Ren, Q., Zhang, Y., Yang, Z., Jiang, Z.** (2024) Anisotropy of Hardened Properties of 3D Printing Concrete and Its Dependence on Resting Time, Jianzhu Cailiao Xuebao, *Journal of Building Materials*, vol. 27, pp. 675-684, doi: 10.3969/j.issn.1007-9629.2024.08.002
30. **Zhong, H., Zhang, M.** (2023) Engineered geopolymer composites: A state-of-the-art review, *Cement and Concrete Composites,* vol. 135, doi: 10.1016/j.cemconcomp.2022.104850
31. **Qin, L., Yan, J., Zhou, M., Liu, H., Wang, A., Zhang, W., Duan, P., Zhang, Z. (2023)** Mechanical properties and durability of fiber reinforced geopolymer composites: A review on recent progress// Engineering Reports, vol. 5, doi: 10.1002/eng2.12708
32. **Li, Z., Li, J., Lu, W., Zhang, Y.** (2025) Research Progress and Application Prospects of Plant Fibers in Geopolymer Concrete: A Review//Materials, vol. 18doi: 10.3390/ma18102342

СПИСОК ЛИТЕРАТУРЫ

1. **de Brito, J., Kurda, R.** The past and future of sustainable concrete: A critical re-

view and new strategies on cement-based materials// Journal of Cleaner Production, vol. 281, 2021, doi: 10.1016/j.jclepro.2020.123558

2. **Flatt, R.J., Wangler, T.,** On sustainability and digital fabrication with concrete // Cement and Concrete Research, vol. 158, 2022, doi: 10.1016/j.cemconres.2022.106837
3. **Rollakanti, C.R., Prasad, C.V.S.R.,** Applications, performance, challenges and current progress of 3D concrete printing technologies as the future of sustainable construction – A state of the art review//Materials Today: Proceedings, vol. 65, pp. 995-1000, 2022, doi: 10.1016/j.matpr.2022.03.619
4. **Su, J., Ng, W.L., An, J., Yeong, W.Y., Chua, C.K., Sing, S.L.,** Achieving sustainability by additive manufacturing: a state-of-the-art review and perspectives//Virtual and Physical Prototyping, vol. 19, 2024, doi: 10.1080/17452759.2024.2438899
5. **Capêto, A.P., Jesus, M., Uribe, B.E.B., Guimarães, A.S., Oliveira, A.L.S.,** Building a Greener Future: Advancing Concrete Production Sustainability and the Thermal Properties of 3D-Printed Mortars// Buildings, vol. 14, 2024, doi: 10.3390/buildings14051323
6. **Mohan, M.K., Rahul, A.V., De Schutter, G., Van Tittelboom, K.,** Salt Scaling Resistance of 3D Printed Concrete// RILEM Bookseries, vol. 37, pp. 188-193, 2022, doi: 10.1007/978-3-031-06116-5_28
7. **Habibi, A., Buswell, R., Osmani, M., Aziminezhad, M.,** Sustainability principles in 3D concrete printing: Analysing trends, classifying strategies, and future directions//Journal of Building Engineering, vol. 98, 2024, doi: 10.1016/j.jobe.2024.111354
8. **Spurina, E., Sinka, M., Ziemelis, K., Bajare, D.,** The effects of 3D printing on frost resistance of concrete// Journal of Physics: Conference Series, vol. 2423, 2023, doi: 10.1088/1742-6596/2423/1/012037
9. **Sheng, W., Wang, Y.,** Fatigue behavior and abrasion resistance of prefabricated pavement textures assisted with 3D printing technology //Green and Intelligent Technologies for Sustainable and Smart Asphalt Pavements - Proceedings of the 5th International Symposium on Frontiers of Road and Airport Engineering, IFRAE 2021, pp. 266-271, 2022, doi: 10.1201/9781003251125-43
10. **Rollakanti, C.R., Venkata Siva Rama Prasad, C., Joe, A.,** Digital Concrete for Sustainable Construction Industry: A State-of-the-Art Review// Lecture Notes in Civil Engineering, vol. 233, pp. 183-195, 2022, doi: 10.1007/978-981-19-0189-8_16
11. **Kallayil, A., Patadiya, J., Kandasubramanian, B., Adamtsevich, A., Kchaou, M., Aldawood, F.K.,** Adaptive Smart Materials in Architecture: Enhancing Durability and Sustainability in Modern Construction //ACS Omega, 2025, doi: 10.1021/acsomega.4c04943
12. **Mohamed, O., Mishra, A., Isam, F.,** An overview of 3D printed concrete for building structures: Material properties, sustainability, future opportunities, and challenges//Structures, vol. 78, 2025, doi: 10.1016/j.istruc.2025.109284
13. **Loporcaro, G., Scott, A., Palermo, A.,** Sustainable Resilience for 3D concrete printed homes in New Zealand: a three-year research government funding overview// fib Symposium, pp. 757-768, 2024
14. **Jain, A., Varma, R.K., Prahsant, G.K., Gupta, R., Betteka, A.,** Innovative Sustainable Construction For Mars Colonization Through In-Situ Resource Utilization (ISRU)// Proceedings of the International Astronautical Congress, IAC, vol. 2, pp. 703-709, 2024, doi: 10.52202/078364-0081
15. **Patil, M.G.M., Nayaka, R., Scholar, F.S.R.,** Digital Transformation for Sustainable and Resilient Infrastructure: Current Progress and Future Potential//2024 IEEE Conference on Engineering Informatics, ICEI 2024, 2024, doi: 10.1109/ICEI64305.2024.10912434
16. **Ma, G., Salman, N.M., Wang, L., Wang, F.,** A novel additive mortar leveraging in-

ternal curing for enhancing interlayer bonding of cementitious composite for 3D printing//Construction and Building Materials, vol. 244, 2020, doi: 10.1016/j.conbuildmat.2020.118305

17. **Moelich, G.M., Kruger, P.J., Combrinck, R.,** The effect of restrained early age shrinkage on the interlayer bond and durability of 3D printed concrete//Journal of Building Engineering, vol. 43, 2021, doi: 10.1016/j.jobe.2021.102857
18. **Yao, H., Xie, Z., Li, Z., Huang, C., Yuan, Q., Zheng, X.,** The relationship between the rheological behavior and interlayer bonding properties of 3D printing cementitious materials with the addition of attapulgite//Construction and Building Materials, vol. 316, 2022, doi: 10.1016/j.conbuildmat.2021.125809
19. **Babafemi, A.J., Kolawole, J.T., Miah, M.J., Paul, S.C., Panda, B**., A concise review on interlayer bond strength in 3D concrete printing//Sustainability (Switzerland), vol. 13, 2021, doi: 10.3390/su13137137
20. **Şahin, H.G., Mardani, A.,** Mechanical properties, durability performance and interlayer adhesion of 3DPC mixtures: A state-of-the-art review// Structural Concrete, vol. 24, pp. 5481-5505, 2023, doi: 10.1002/suco.202200473
21. **Skibicki, S., Szewczyk, P., Majewska, J., Sibera, D., Ekiert, E., Chung, S.-Y., Sikora, P.,** The effect of interlayer adhesion on stress distribution in 3D printed beam elements//Journal of Building Engineering, vol. 87, 2024, doi: 10.1016/j.jobe.2024.109093
22. **Tian, Z., Wang, L., Zhang, X., Zhou, X., Hu, Y.,** Formation Mechanism and Improvement Solutions for Weak Interlayer Surfaces of 3D Printing Concrete//Bulletin of the Chinese Ceramic Society, vol. 39, pp. 2052-2058, 2020
23. **Rui, A., Wang, L., Ma, G.,** Effect of Interlayer Water Film on Interfacial Characteristics of 3D Printed Concrete//Bulletin of the Chinese Ceramic Society, vol. 42, pp. 2281-2289, 2023
24. **Salman, N.M., Ma, G., Ijaz, N., Wang, L.,** Weak inter-layer bonding in extrusion 3D concrete printing: A comparative analysis of mitigation techniques// IOP Conference Series: Materials Science and Engineering, vol. 1028, 2021, doi: 10.1088/1757-899X/1028/1/012003
25. **Lin, Y., Yan, J., Sun, M., Han, X., Tang, B.,** Interlayer cohesion in 3D printed concrete: The role of width-to-height ratio in modulating transport properties and pore structure//Journal of Building Engineering, vol. 98, 2024, doi: 10.1016/j.jobe.2024.111009
26. **Surehali, S., Tripathi, A., Nimbalkar, A.S., Neithalath, N.,** Anisotropic chloride transport in 3D printed concrete and its dependence on layer height and interface types //Additive Manufacturing, vol. 62, 2023, doi: 10.1016/j.addma.2023.103405
27. **Rui, A., Wang, L., Lin, W., Ma, G.,** Experimental study on damage anisotropy of 3D-printed concrete exposed to sulfate attack// Construction and Building Materials, vol. 407, 2023, doi: 10.1016/j.conbuildmat.2023.133590
28. **Li, Y.-F., Yao, L., Wang, L., Ma, G.-W.,** Study on Mechanical Anisotropy and Meso Damage Mechanism of 3D Printing Concrete, Gonglu Jiaotong Keji//Journal of Highway and Transportation Research and Development, vol. 38, pp. 81-89, 2021, doi: 10.3969/j.issn.1002-0268.2021.05.010
29. **Li, C., Ren, Q., Zhang, Y., Yang, Z., Jiang, Z.,** Anisotropy of Hardened Properties of 3D Printing Concrete and Its Dependence on Resting Time, Jianzhu Cailiao Xuebao//Journal of Building Materials, vol. 27, pp. 675-684, 2024, doi: 10.3969/j.issn.1007-9629.2024.08.002
30. **Zhong, H., Zhang, M.,** Engineered geopolymer composites: A state-of-the-art review// Cement and Concrete Composites, vol. 135, 2023, doi: 10.1016/j.cemconcomp.2022.104850

31. **Qin, L., Yan, J., Zhou, M., Liu, H., Wang, A., Zhang, W., Duan, P., Zhang, Z.,** Mechanical properties and durability of fiber reinforced geopolymer composites: A review on recent progress// Engineering Reports, vol. 5, 2023, doi: 10.1002/eng2.12708

32. **Li, Z., Li, J., Lu, W., Zhang, Y.,** Research Progress and Application Prospects of Plant Fibers in Geopolymer Concrete: A Review// Materials, vol. 18, 2025, doi: 10.3390/ma18102342

Aleksey O. Adamtsevich Head of Research institute of Construction materials and technologies of the National Research Moscow State University of Civil Engineering; 129337, Russia, Moscow, Yaroslavskoe shosse, 26. E-mail: AdamtsevichAO@mgsu.ru ; ORCID: 0000-0003-4878-2737

Адамцевич Алексей Олегович, кандидат технических наук, директор НИИ Строительных материалов технологий Национального исследовательского Московского государственного строительного университета, 129337, Москва, Ярославское ш. ,д.26; e-mail: AdamtsevichAO@mgsu.ru ; ORCID: 0000-0003-4878-2737

Andrey P. Pustovgar Scientific director of Research institute of Construction materials and technologies of the National Research Moscow State University of Civil Engineering; 129337, Russia, Moscow, Yaroslavskoe shosse, 26. PustovgarAP@mgsu.ru ; ORCID: 0000-0002-0480-2401

Пустовгар Андрей Петрович, кандидат технических наук, доцент, Научный руководитель НИИ Строительных материалов технологий Национального исследовательского Московского государственного строительного университета, 129337, Москва, Ярославское ш. ,д.26; e-mail: PustovgarAP@mgsu.ru ; ORCID: 0000-0002-0480-2401

Liubov A. Adamtsevich Candidate of Technical Sciences, Associate Professor, Head of the Research Laboratory of Energy Efficiency, Ecology and Sustainable Construction of the National Research Moscow State University of Civil Engineering; 129337, Russia, Moscow, Yaroslavskoe shosse, 26. E-mail: AdamtsevichLA@mgsu.ru.

Адамцевич Любовь Андреевна, кандидат технических наук, доцент, заведующая научно-исследовательской лаборатории Энергоэффективности, экологии и устойчивого строительства Национального исследовательского Московского государственного строительного университета, 129337, Москва, Ярославское ш. ,д.26; e-mail: AdamtsevichLA@mgsu.ru ; ORCID: 0000-0002-5843-0076M

Yuriy I. Markov Engineer of Research institute of Construction materials and technologies of the National Research Moscow State University of Civil Engineering; 129337, Russia, Moscow, Yaroslavskoe shosse, 26. E-mail: MarkovYI@mgsu.ru

Марков Юрий Игоревич, инженер НИИ Строительных материалов технологий Национального исследовательского Московского государственного строительного университета, 129337, Москва, Ярославское ш., д.26